Stress corrosion crack growth in porous sandstones

Ira O. Ojala

B.Sc. Geophysics (London) 1998

M.Sc. Geophysics (Dunelm) 1999

Thesis submitted for the degree of

Doctor of Philosophy

University of Edinburgh

2003

ABSTRACT

Stress corrosion crack growth occurs when the chemical weakening of strained crack tip bonds facilitates crack propagation. I have examined the effect of chemical processes on the growth of a crack population by carrying out triaxial compression tests on Clashach and Locharbriggs sandstones at temperatures of 25-80°C and at strain rates of 10^{-5} to 10^{-8}/s. The axial strain, permeability, acoustic emission (AE) activity and the pore fluid chemistry were monitored continuously during these tests. Rock strength is reduced in the presence of water and on the application of a slower strain rate. Elastic modulus also decreases with decreasing strain rate. Microstructural observations indicate that microfracturing is more pervasive in the slow strain rate tests in comparison to the high strain rate tests. Damage parameters derived from the AE data predict the stress-strain curves adequately. The accumulation of damage is more rapid in the slow strain rate tests than in the high strain rate tests. The exit pore fluid silica (Si) concentrations correlate with the main microfracturing domains of the stress-strain curve. In the strain hardening phase of the Locharbriggs tests the Si concentrations and AE damage increase exponentially. The small reactive surface area and the temperature dependence of the Si concentration in the Locharbriggs tests suggest that silica is dissolving actively from the growing crack tips and that reaction rates contribute towards this signal. The Locharbriggs Si signal and damage parameters are strongly correlated by a power law relationship. The observed strain rate and environment dependence of mechanical properties of Locharbriggs sandstone can be uniquely attributed to crack growth by the stress corrosion mechanism. In the Clashach tests the damage accumulation is best described by a power-law. The AE activity of both sandstones exhibits clear fore- and aftershock sequences that are well modelled by the Omori law with a power law exponent that is close to unity. The Clashach Omori decay parameter correlates with test temperature, indicating a faster decay of aftershock activity at a higher temperature. The permeability evolution also displays a distinct strain rate dependence. At high strain rates permeability correlates with microcrack damage. At slow strain rate the fluid flow properties correlate with mean effective stress or pore fluid ion concentrations. These observations suggest that brittle fracturing, chemical reaction and hydraulic properties of porous sandstones are strongly coupled processes in the crust.

Declaration

I declare that this thesis has been composed solely by myself and that it has not been submitted, either in whole or in part, in any previous application for a degree. Except where otherwise acknowledged, the work presented is entirely my own.

Ira O. Ojala
August 2003

Acknowledgements

Firstly, I would like to thank my supervisors Ian Main, Bryne Ngwenya and Stephen Elphick for a cracking project idea and swift reading through of my chapters. Many thanks for Philip Meredith and Peter Sammonds for introducing me to the fascinating study of rock physics as an undergraduate. Big thanks to Alexander Hart and Robert Brown for their good humour and kind help with the rock deformation apparatus. Thanks to Gavin Brown, Nichola Cayzer, Sabrina Colombo, Lorna Eades, Mike Hall, Alex Jackson, Denis McLaughlin and Nick Odling for general assistance.

My brief stay in KB, Edinburgh would not have been so enjoyable without the fab company my friends: Allan, Andy, Bridget, Bärbel, Chris, Dave, Fahad, Gavin, Guy, Lynette, Magi, Mark, Rich, Robin, Sarah, Sonja, Stuart, Theo, Tim. Thanks for fun nights out with a bit of zumhei. Lots of thanks to everyone else too.

This work was funded by the Edinburgh University Faculty of Science, the Finnish cultural foundation and the Väisälä foundation. Some of it was also funded by my mum. Thanks to mum and dad for their support throughout the years and for my sister Sini for many interesting discussions.

Contents

1 Introduction **1**

1.1 Thesis organisation 5

2 Crack growth and reaction rate theory **7**

2.1 Introduction 7

2.2 Dynamic crack growth 8

2.2.1 Crack as a stress concentrator 8

2.2.2 Griffith's energy balance principle 10

2.2.3 Obreimoff's experiment 13

2.2.4 Irwin's modification of the Griffith concept 15

2.2.5 Criteria for dynamic fracture 17

2.2.6 Shortcomings of the LEFM approach 18

2.2.7 Conclusion 19

2.3 Kinetic crack growth 19

2.3.1 The effect of pore fluid on crack growth 19

2.3.2 Subcritical crack growth 20

2.3.3 Stress corrosion crack growth 21

2.3.4 Experimental data on quartz and quartz-rich rocks 27

2.3.5 Theoretical models and crack growth constitutive equations 33

2.3.6 Conclusion 38

2.4 Kinetics of the quartz-water system 39

2.4.1 Introduction 39

2.4.2 General expression for the dissolution and precipitation of silica 39

2.4.3 Theoretical rate equations for dissolution and precipitation of silica 41

2.4.4 Previous laboratory studies 45

2.4.5 Factors influencing silica dissolution 47

2.4.6 Are laboratory rates representative of real weathering rates? 54

2.4.7 Conclusion 57

2.5 Stress corrosion by active dissolution 57

2.6 Summary 60

3 Methodology **63**

3.1 Introduction 63

3.2 The triaxial test 64

3.3 Test Materials 65

3.3.1 Lithologies 65

3.3.2 Preparation of the test specimen 67

3.3.3 Sample characterisation 67

3.4 Deformation Rig 68

3.5 Typical test 71

3.5.1 Sample stack 71
3.5.2 Test procedure 71
3.5.3 AE monitoring 74
3.5.4 Permeability measurement and calculation 78
3.5.5 Pore fluid analysis 80
3.5.6 Post test analysis 81
3.5.7 Data reduction 82
3.6 Calibration tests 82
3.6.1 Control test for fluid flow 82
3.6.2 Control test for chemical analysis 83
3.6.3 Control test for permeability measurement 84
3.7 Summary 86

4 Mechanical Data **87**

4.1 Introduction 87
4.2 Compressive strength 88
4.3 Semi-empirical fracture criteria 90
4.4 The effect of environmental variables on the strength of rocks . . 92
4.4.1 Introduction 92
4.4.2 The effect of aqueous environment 94
4.4.3 Temperature effect 95
4.4.4 Strain rate effect 95
4.5 Results 98
4.6 Microstructural observations 109

4.7 Comparison to other studies 110

4.8 Conclusion 116

5 Quantification of Damage **117**

5.1 Introduction 117

5.2 Previous AE work 118

5.2.1 Historical perspective 118

5.2.2 AE Event rate statistics 119

5.2.3 Stress corrosion and AE event rate 121

5.2.4 Characteristic frequency-magnitude scaling of AE data . . 122

5.2.5 Hypocentre mapping and polarity studies 125

5.2.6 AE source parameters inferred from the dislocation theory of seismic source 126

5.2.7 Quantification of damage using the AE catalogue 130

5.2.8 Deformation rate dependence of AE 132

5.3 AE data 133

5.3.1 Introduction 133

5.3.2 General characteristics of the AE data 134

5.3.3 AE source parameters 141

5.3.4 Temporal evolution of the AE event rate 145

5.3.5 Extraction of damage parameters from the AE catalogue . 151

5.3.6 Correlation of AE damage with stress 154

5.4 Discussion 156

5.5 Conclusion 160

6 Stress corrosion crack growth **163**

6.1 Introduction 163

6.2 The pore fluid chemistry in the Locharbriggs tests 164

6.2.1 The geochemical signal 164

6.2.2 The silica signal and its correlation with AE damage . . . 170

6.3 Clashach sandstone pore fluid chemistry 174

6.4 Crack growth constitutive equations 178

6.5 Accumulation of damage and Si dissolution 182

6.6 Discussion 191

6.7 Conclusions 197

7 Strain rate dependence of Permeability **199**

7.1 Introduction 199

7.2 The importance of permeability 200

7.3 Previous Observations 202

7.4 Results 206

7.4.1 Relationship between initial permeability and porosity . . 206

7.4.2 The effect of loading rate on permeability evolution 209

7.4.3 Relationship between permeability, stress, strain and temperature 212

7.4.4 Relationship between permeability and AE data 215

7.4.5 Relationship between permeability and chemical reaction . 218

7.5 Discussion 222

7.6 Conclusion 229

8 Discussion **231**

8.1 Data synthesis 231

8.1.1 Introduction 231

8.1.2 Stress corrosion crack growth 231

8.1.3 The effect of test temperature 236

8.1.4 The strain rate effect 238

8.2 Potential applications 242

8.2.1 General applications 242

8.2.2 The resemblance of earthquake and AE foreshocks 243

8.2.3 Temperature dependence of Omori decay parameter 244

8.2.4 Geochemical precursors of earthquakes 245

8.2.5 The weakness of crustal faults 247

8.2.6 The origin of silica for quartz cement 247

8.2.7 Crack growth on the Moon 248

8.3 Outstanding questions 248

8.4 Recommendations for future work 249

9 Conclusions **253**

Bibliography **278**

A Instructions for loading a rock sample **279**

A.1 Preparing the Cell 279

A.2 Preparing the sample stack 279

A.3 Pressurising the rock sample to hydrostatic conditions 281

A.4 Pressurising the ram 282

A.5 Filling the pump 283

A.6 Stopping a test 283

B Preparation of standard solutions **285**

B.1 Making standards for silica analysis 286

C ICP-AES **289**

C.1 Introduction 289

C.2 The ICP-AES instrument 291

C.3 Analysis 294

List of Figures

1.1 The axial strain and differential stress as a function of time for a constant load test on Locharbriggs sandstone. 4

2.1 A schematic diagram of how a stress concentration arises at a crack tip. 9

2.2 A plate containing an elliptical hole that is subjected to applied tension 11

2.3 The mica experiment of *Obreimoff* (1930) 14

2.4 The three modes of crack opening. 17

2.5 Chemically induced bond rupture. 22

2.6 Schematic picture of the proposed reaction between water and the strained Si-O-Si bond at the crack tip. 23

2.7 Schematic picture that relates crack growth velocity v to the stress intensity factor K. 24

2.8 The distinction between continuous and episodic crack growth in the quartz-water system. 26

2.9 A log-log plot of stress intensity factor versus crack velocity for several quartz-rich rocks. 31

2.10 Influence of temperature on subcritical tensile crack growth rate in synthetic quartz. 32

2.11 Schematic illustration of possible kinetic crack growth scenarios. . 36

2.12 Schematic illustration of the dissolution process in deionised water. 42

2.13 The effect of sample preparation on the dissolution behaviour of alkali feldspar. 46

2.14 Experimentally determined quartz dissolution rates at 300°C solutions of various silica concentrations. 48

2.15 Quartz dissolution rates in pure water from 25°C to 300°C. 51

2.16 The solubility of quartz as a function of temperature and pressure 52

2.17 A polyhedral etch pit on a quartz grain. 55

2.18 The measured mass normalised dissolution rate at deionised water as a function of B.E.T. surface area 56

3.1 The stress system in a triaxial test. 65

3.2 A schematic diagram of the deformation rig. 69

3.3 The arrangement of the sample inside the pressure vessel. 72

3.4 The AE waveform and some of the recorded parameters. 75

3.5 The permeameter that was used for the tests. 80

3.6 The flow rate of water out of the pump matched the dial settings. 83

3.7 The flow rate of water out of the Locharbriggs sandstone for the very slow strain rate test at 3×10^{-8}/s. 84

3.8 The amount of dissolved ions from a plastic core. 85

3.9 The differential pressure versus hole area. 86

4.1 The mode of failure observed in a triaxial compression test under a moderate confining pressure. 88

4.2 The complete stress-strain curve for a rock. 89

4.3 The Coulomb criterion expressed in terms of a Mohr diagram. . . 91

4.4 The dependence of differential stress at shear failure on confining pressure 93

4.5 The ultimate strength as a function of strain rate for various rocks. 96

4.6 Strength of micro-grained limestone as a function of strain rate . . 97

4.7 Stress-strain curve for a dry and a water-saturated Locharbriggs sample 100

4.8 Stress-strain curve for a dry and a water-saturated Clashach sample 100

4.9 The failure time for the Locharbriggs specimen as a function of the stress rate and strain rate 101

4.10 The stress-strain curves for Clashach sandstone 103

4.11 The stress-strain curves for Locharbriggs sandstone 104

4.12 Strength of Locharbriggs sandstone as a function of strain rate. . 105

4.13 Strength of Clashach sandstone as logarithmic and a power law function of strain rate. 107

4.14 The elastic modulus of Clashach and Locharbriggs sandstone as a function of strain rate. 108

4.15 Stress drop at failure as a function of specimen strength. 109

4.16 The shear band for the 10^{-6} /s Clashach test. 111

4.17 The shear band for 10^{-8} /s Clashach tests. 111

4.18 The shear band in the 10^{-6} /s Locharbriggs test. 112

4.19 The shear band for the 10^{-8} /s Locharbriggs test. 112

5.1 The inelastic volumetric strain Δ as a function of the cumulative AE event count 119

5.2 The dependence of crack velocity and event rate on on the stress intensity factor K during a wet, tensile, double torsion test on Whin Sill Dolerite. 123

5.3 The the cumulative AE event count F_c as a function of event amplitude 124

5.4 The Haskell source and fault models 127

5.5 The relationship between rupture time L/v_r and rise time τ_r for some earthquakes 130

5.6 The dependence of AE event rate dN/dt on the deformation rate. 133

5.7 The temporal evolution of differential Stress, AE event rate dN/dt and seismic b-value for a Clashach 80° C test that was carried out at a strain rate of 10^{-5} /s 135

5.8 The temporal evolution of Differential Stress, AE event rate dN/dt and seismic b-value for a Locharbriggs 80° C test that was carried out at a strain rate of 10^{-5} /s 136

5.9 The evolution of AE event rate in the four 80°C Clashach tests from 10^{-5} to 10^{-8} /s. 138

5.10 The temporal evolution of the seismic b-value for a 80°C Clashach test at 10^{-6} /s. 139

5.11 There calculated b-values for the entire deformation tests for Locharbriggs sandstone as function of the strain rate. 140

5.12 There is only a slight correlation between the total number of AE events and the specimen strength for the Locharbriggs sandstone. 141

5.13 The AE event duration as a function of event magnitude for the time interval preceding peak stress, strain softening phase and frictional sliding phase for the Locharbriggs 10^{-8}/s test at 80°C. . 143

5.14 The AE event amplitude in dB/20 as a function of energy and rise time for the 25°C Clashach test at 10^{-8}/s. 144

5.15 The procedure for finding the optimum c'-value for fitting the Omori law to the AE data. 146

5.16 The AE event rate, foreshock and aftershock sequences for a 80°C slow strain rate Clashach test 148

5.17 The AE event rate, foreshock and aftershock sequence for a 80°C slow strain rate Locharbriggs test. 149

5.18 The foreshock and aftershock sequences for Clashach sandstone tests that were carried out at a four different strain rates. 152

5.19 The foreshock and aftershock sequences for Locharbriggs sandstone tests that were carried out at a four different strain rates. 153

5.20 The exponent p for the aftershock sequences as a function of test temperature for the Locharbriggs tests at 10^{-7}/s. 154

5.21 The procedure for stress history matching. 155

5.22 The inverted stress-strain curves for a 80°C Clashach test at 10^{-6} /s. 156

5.23 The inverted stress-strain curves for a 80°C Locharbriggs test at 10^{-7} /s. 157

6.1 The stress, AE event rate and exit pore fluid concentration for a slow strain rate Locharbriggs test. 165

6.2 The silica signal in the Locharbriggs tests at 25-80°C. 166

6.3 The variation of Si, Fe, K, Mg and Na in the pore fluid during a slow strain rate Locharbriggs test 167

6.4 The maximum silica concentration as a function of the steady-state value. 169

6.5 The correlation of the pore fluid silica with AE damage 172

6.6 The temperature dependence of the pore fluid silica concentrations 173

6.7 The silica signal in the Clashach 80°C tests at 10^{-5} to 10^{-8} /s . . 175

6.8 The silica signal in the 25-80°C Clashach tests at 10^{-7} /s. 176

6.9 The concentrations of Si, K, Na and Al in the 25°C Clashach test at 10^{-7}/s. 177

6.10 The ratios Si/Al and Si/K in the 40°C Clashach test. 177

6.11 The concentrations of Si, K, Na and Al in the Clashach 10^{-7}/s test. 179

6.12 The differential stress and cumulative AE count as a function of time for the slow strain rate Clashach and Locharbriggs tests. . . 182

6.13 The temporal evolution of damage and silica in the Locharbriggs tests. 183

6.14 The evolution of damage in the 80° Locharbriggs tests. 186

6.15 The temporal evolution of damage in the Locharbriggs test at 10^{-8} /s. 187

6.16 The exponential law (6.18) exponent q as a function of strain rate. 188

6.17 The evolution of damage in the 80° Clashach tests. 189

6.18 The temporal evolution of damage in the Clashach test at 10^{-7} /s. 190

6.19 The power law exponent z (6.8) as a function of strain rate. . . . 190

6.20 The increase in silica concentration in the 80° Clashach test at 10^{-7}/s as a function of time. 191

7.1 The measured permeabilities of various rocks at 25°C under hydrostatic conditions 201

7.2 Pre-failure permeability change ξ as a function of initial porosity for various rock types 203

7.3 The initial permeability as a function of porosity 207

7.4 The evolution of permeability with axial strain for Clashach and Locharbriggs sandstone. 208

7.5 In the 80 °C Clashach tests the evolution of permeability depends on the applied strain rate 210

7.6 The axial permeability as a function of mean effective stress and axial strain for the slow strain rate Locharbriggs tests 214

7.7 The evolution of permeability and stress as a function of time during two high strain rate tests 216

7.8 Permeability as a function of the cumulative AE event number N 217

7.9 The evolution of permeability and silica concentration and differential stress and cumulative AE event count for a Clashach sandstone 80 °C test that was carried out at strain rate of 3.3×10^{-8} /s. . . 219

7.10 The evolution of permeability and silica concentration for a Clashach sandstone test conducted at a strain rate of 3.3×10^{-8} /s. 220

7.11 The concentration of dissolved ions as a function of permeability for Clashach sandstone 223

7.12 The evolution of dissolved silica and permeability for a slow strain rate Locharbriggs test. 224

7.13 The concentration of silica as a function of permeability in Locharbriggs sandstone. 224

8.1 A schematic diagram of the temporal evolution of hydraulic, microseismic and geochemical properties during brittle deformation in a weakly cemented sandstone. 233

8.2 A schematic diagram of the temporal evolution of hydraulic, microseismic and geochemical properties during brittle deformation in a well-cemented sandstone. 234

C.1 The major components of a multi-element ICP-AES system. . . . 290

C.2 A simple cross-flow nebuliser. 291

C.3 Co-axial design of an ICP torch. 292

C.4 The generation of atomic emission in an ICP instrument. 294

List of Tables

2.1 Some experimentally determined parameters for stress corrosion crack growth in quartz, sandstones and other quartz-rich rocks. . 28

2.2 Some quartz dissolution rates measured in previous studies. 49

2.3 The effect of various environmental variables on silica dissolution rate. 50

3.1 Some characteristics of the two Scottish sandstones that were used for this study. 66

3.2 The conversion factors for the logging software. 70

3.3 The estimated errors for the axial pressure (Ram), confining pressure (P_{conf}), differential pressure (dP) and LVDT measurements. 73

3.4 The recording parameters for AE monitoring. 77

4.1 Mechanical data 99

4.2 Linear and areal crack densities 110

5.1 Mechanical and AE data for the flow-through tests on Clashach and Locharbriggs sandstones. 142

5.2 The Omori law fits to the AE event rate dN/dt. 147

5.3 Omori law fits to the AE event rate dN/dt 150

6.1 Chemical and AE data for the Locharbriggs tests 169

6.2 The composition of the exit pore fluid in the Clashach tests. . . . 179

6.3 The ratios of Si/Al, Si/K and Si/Ca in the Clashach tests. 180

6.4 The fitted values for the exponential formula (6.18) for the Locharbriggs tests. 184

6.5 The fitted values to the exponential formula (6.18) for the Locharbriggs tests. 192

6.6 The fitted values to the power law (6.8) Clashach tests. 193

7.1 Mechanical and permeability data for the flow-through tests on Clashach and Locharbriggs sandstones. 207

7.2 Various parameters relating to the fault geometry in the Clashach tests. 212

7.3 For the slow strain rate tests, permeability k can be expressed in terms on increasing stress and strain 213

7.4 Permeability of the intact rock specimen scales linearly with respect to the exit ion concentrations for the Clashach sandstone 80°C test 221

7.5 The concentration of dissolved ions as a function of permeability for Locharbriggs sandstone during the initial compaction phase . . 221

8.1 A summary of the scaling relationships that have been observed in this study. 235

8.2 A summary of the effect of decreasing strain rate on rock properties, as observed in this study. 239

B.1 The standards that were used for the calibration of the ICP instrument. 286

Glossary of symbols and abbreviations

Symbol	Description	Equation no.
a	constant	5.5
a_i	activity of species i	2.33
A	environmental molecule	2.14
$A(\omega)$	far field amplitude spectrum	5.8
A_f	fault area	5.9
A_h	cross-sectional area for fluid flow	3.3
A_i	interfacial area	2.33
A_{max}	maximum AE amplitude for a test	table 5.1
A_s	crack surface area	2.7
A'	constant	5.17
b	seismic b-value	5.5
b_f	b-value minimum	table 5.1
b_t	b-value for a whole test	5.22
B	crack tip molecule	2.14
B^+	activated state	2.15
c	crack half length	2.1
c'	constant	5.1
c^*	constant	5.14
c^+	constant	6.9
c_c	critical crack length	2.5
C	constant	7.2
C_i	pore fluid concentration of species i	7.8
C_{ss}	steady state silica concentration	6.1

C_{Si}	pore fluid outlet silica concentration	6.1
C_{max}	maximum silica concentration	6.2
C_0	specimen strength	figure 4.2
d	constant	5.15
d_c	crack tip diameter	2.51
d_f	thickness of a flake	2.6
dP	differential pressure	3.3
dN/dt	AE event rate	5.4
D	damage parameter, equal to χ'	5.20
D_e	power law exponent	5.15
D_p	pore diameter	6.4
E	cumulative AE event energy	6.5
E_0	initial stiffness	5.18
E_e	AE event energy	5.23
E_m	Elastic modulus	2.4
E'	modified stiffness	5.18
E^*	apparent activation energy	2.17
E^+	stress-free activation energy	2.19
f_{AE}	frequency of an AE event	3.2
f_{ij}	angular function of crack tip stress field	2.8
f_T	resonant frequency of an Ae transducer	section 3.5.3
F_c	cumulative frequency of AE events	5.5
F_i	frequency of AE events	5.4
F'	scaling factor	5.18
g	radius of curvature of a crack	2.1
G	mechanical energy release rate	2.7
G_c	crack extension force	2.12
G_e	Gibbs free energy	2.21
G_I	mechanical energy release rate for mode I	2.10
h	Planck constant $6.63 * 10^{-34} Js$	2.40
h_g	thickness of a glass wedge	2.6
H	activation enthalpy	2.16
H'	scaling factor	5.19
j_1	empirical constant	table. 6.5
j_2	empirical constant	table. 6.6

j_3	empirical constant	table. 6.3
k	permeability	3.3
$k(C')$	permeability at the onset of dilatancy	7.1
k_{min}	lowest recorded permeability of the intact specimen	7.4
k_{peak}	permeability at peak stress	7.1
k_0	initial permeability	7.3
k_1	empirical constant	table 5.2.
k_-	precipitation constant	2.33
k'_-	apparent precipitation constant	2.35
k_+	dissolution constant	2.34
k'_+	apparent dissolution constant	2.36
k_b	Boltzmann constant $1.38 * 10^{-23} JK^{-1}$	2.40
K_i	stress intensity factor of mode i	2.8
K_{eq}	equilibrium constant	2.37
K_0	initial value of the stress intensity factor	2.16
K_c	fracture toughness	2.12
l_s	sample length	3.3
l_1	constant	2.19
l_2	constant	2.19
l_0	initial length of test specimen	3.5
L	fault length	5.8
M_c	critical threshold for amplitude measurement	5.6
M_f	mass of fluid	2.35
M_0	seismic moment	5.9
M_s	seismic surface wave magnitude	5.12
$M(t)$	linear ramp function	figure 5.4
$\dot{M}(t)$	far field displacement pulse	figure 5.4
m	AE event magnitude	5.5
m_c	critical threshold for AE amplitude measurement	5.5
n	subcritical crack growth index	2.16
n_c	number of cracks	5.16
n'	effective stress corrosion index	5.4
n_i	number of moles of species i	2.33
N	cumulative AE event frequency	6.5
N_0	background AE frequency	5.4

N_a	moles of reactive sites on the mineral surface	2.41
N_e	AE event count for a certain time interval	5.6
N_f	AE events up to failure	table 5.1
N_L	average distance between Si-O-Si bridging bonds	2.50
N_p	AE events up to peak stress	table 5.1
N_t	total number of recorded AE events	table 5.1
p	Omori exponent for aftershocks	5.1
p'	Omori exponent for foreshocks	5.2
p_c	pressure parameter	4.4
P_c	pressure	2.51
P_{conf}	confining pressure	section 3.4
P_{eff}	effective pressure	section 2.3.1
P_p	pore pressure	section 2.3.1
P_w	partial pressure of water	2.19
q	exponent of an exponential law	6.18
Q	activity quotient	2.37
Q_f	fluid flow rate	3.3
r	radial distance from a crack tip	2.8
r_z	process zone size	section 2.2.6
r_-	dissolution rate	2.33
r_+	precipitation rate	2.34
r_d	quartz dissolution rate in term of silicic acid release	2.37
r_h	hydraulic radius	7.2
R_c	crack resistance	2.7
R	Universal gas constant 8.31 J/(mol K)	2.16
R_a	aftershock event rate	5.1
R_f	foreshock event rate	5.2
R_p	plastic work term	2.13
s	average fault slip	5.8
s_n	normalised reactive surface area	6.3
s_v	specific surface area	6.4
S	surface area parameter	5.25
t	time	5.1
t_f	failure time	6.8
t_m	time of the main shock	5.1

T	temperature	2.16
T_m	melting temperature	section 4.1
T_0	natural period of a recording instrument	section 5.2.6
$u(t)$	far field displacement pulse	figure 5.4
u_i	displacement	2.9
U	total energy	2.2
U_e	strain energy	2.2
U_m	mechanical energy	2.2
U_s	surface energy	2.2
w	fault width	5.8
W	work done by external forces	2.2
v	crack growth velocity	2.16
v'	local corrosion velocity	2.25
v_0	pre-exponential term	2.16
v_0'	pre-exponential term	2.17
v_r	rupture velocity	5.12
v_R	Rayleigh wave velocity	6.18
V	volume	5.16
V_m	molar volume of a solid	2.19
V_ϕ	pore volume	3.4
V_{rock}	volume of a rock sample	6.3
V^+	activation volume	2.19
x	power law exponent	6.5
X	number of environmental species	2.15
X_{H_2O}	fraction of sites at crack tip accessible to water	2.41
Y	yield point	4.2
Y_1	constant	2.11
z	power law exponent	6.8
zum	constant	6.12
Z	atomic number	section C.2
α_1	empirical constant	2.17
α_2	empirical constant	2.18
α_3	empirical constant	2.52
β_1	empirical constant	5.21
β_2	empirical constant	5.21

β_3	empirical constant	7.8
β_4	empirical constant	7.8
γ	free surface energy per unit area	2.4
γ_0	surface energy in a vacuum	2.23
$\gamma*$	effective surface energy	2.23
γ_a	activity coefficient of adsorbed species	2.40
γ^+	activity coefficient of intermediate species	2.40
γ_i	activity coefficient of species i	2.35
γ_1	stress sensitivity parameter	7.3
γ_2	strain sensitivity parameter	7.3
Γ_i	surface conc. of adsorbed species	2.22
δ	fault slip	table 7.2
Δ	volumetric strain	fig. 5.1
ΔC_{Si}	change in silica concentration	6.1
ΔG^+	Standard Gibbs free energy for activation	2.49
ΔH^+	Standard activation enthalpy	2.40
Δk	change in permeability	7.6
Δk_f	permeability increase at failure	table 7.2
Δl	piston displacement	3.5
ΔS^+	Standard activation entropy	2.40
ΔV	change in volume	2.51
$\Delta\varepsilon$	strain drop at failure	table 7.2
$\Delta\sigma$	stress drop at failure	4.12
$\Delta\tau$	shear stress drop at failure	table 7.2
ε	axial strain	3.5
$\dot{\varepsilon}$	strain rate	4.5
ε_f	strain at specimen failure	table 4.1
ε_Y	yield strain	table 4.1
ζ	tortuosity	7.2
η	viscosity	3.2
θ	fault angle	4.2
θ_1	angle measured form crack plane	2.8
Θ	azimuth angle	5.8
ϑ_1	empirical constant	5.3
ϑ_2	empirical constant	5.3

λ	wavelength	section C.2
μ	rigidity of a medium	5.9
μ_i	chemical potential of species i	2.22
μ_m	probability of fracture	5.21
μ_s	coefficient of internal friction	4.2
ξ	empirical parameter	7.1
ρ_b	bulk density	3.1
ρ_s	average density	3.1
σ_{ij}	component of stress tensor	2.8
$\dot{\sigma}$	stress rate	5.21
σ_a	applied stress	2.1
σ_b	95% confidence limit for calculating the b-value	5.7
σ_c	crack tip stress	2.1
σ_{eff}	effective mean stress	7.3
σ_F	critical stress	2.5
σ_{max}	maximum compressive stress	4.4
σ_n	normal stress	4.2
σ_y	yield stress	table 4.1
σ_0	initial stress	7.3
σ_1	maximum stress	4.1
σ_2	intermediate stress	4.1
σ_3	minimum stress	4.1
σ_4	constant	4.4
Σ	surface in an elastic medium	section 5.2.6
Σm_i	sum of all events above m_c	5.6
τ_r	rise time	5.8
τ_d	rupture duration	5.8
τ_s	shear stress	4.2
τ_0	cohesive shear strength of a material	4.2
τ_t	residence time	3.4
ϕ	angle of internal friction	4.2
ϕ_i	interconnected porosity	6.4
ϕ_p	porosity	7.2
ϕ_T	total porosity	3.1
φ	constant	6.9

χ	damage parameter	5.16
χ'	working damage parameter	5.20
ψ	constant	4.4
ω	angular frequency	5.8
$(*)^+$	reactive intermediate	2.31

Chapter 1

Introduction

Gutta cavat lapidem (Dripping water hollows out a stone)
Ovid

The Earth is as smooth as a billiard ball. To us humans, this may not be apparent at first, given the height of the mountains or the depth of the seas. However, at a closer inspection this turns out to be a valid analogue. Relative to the radius of the earth (6378 km) the great Challenger deep in the Marianas trench (11.5 km) is comparable to the small irregularities (0.05 mm) that can be found on the surface of a 5.7 cm billiard ball. So the Earth is quite literally as smooth as a billiard ball.

The Earth is so smooth because its crust is weak over very long time scales (*Feynman*, 1963). It cannot support great structures. The apparent weakness of crustal rocks is caused by the ubiquitous presence of water (*Hickman et al.*, 1995). Fluids have been directly sampled in super-deep drill holes. Similarly, surface exposures of metamorphic rocks that once resided deep in the crust indicate large fluxes of fluids. These observations suggest the existence of porous rocks and fractures up to 15 km depth in the crust (*Sornette*, 1999).

In the temperature and pressure conditions of the upper crust rocks deform in a dominantly brittle manner by the growth and coalescence of cracks. Water can influence the brittle deformation properties of rocks in two ways. Firstly, the presence of pressurised fluids weakens and embrittles rocks by reducing the effective confining pressure (*Paterson*, 1978). Secondly, the chemical activity of water facilitates the slow and stable subcritical growth of cracks at stresses much

lower than that required for dynamic rupture. This mechanism is termed stress corrosion crack growth (*Anderson and Grew*, 1977; *Atkinson*, 1982). Subcritical crack growth by stress corrosion is probably the dominant mechanism of fracture nucleation in the upper crust (*Scholz*, 1968b; *Anderson and Grew*, 1977; *Barnett and Kerrich*, 1980; *Atkinson*, 1982; *Atkinson and Meredith*, 1987a; *Meredith et al.*, 1990; *Renshaw and Pollard*, 1994; *Dove*, 1995). The characteristic time, rate and environment dependence of the mechanical properties of rocks can also be ascribed to the subcritical growth of cracks (*Costin*, 1987). It is therefore very important in assessing the long-term evolution of hydrocarbon reservoirs, hydrothermal deposits, deep aquifers and waste repositories. Stress corrosion crack growth is also the likely cause of time-dependent earthquake phenomena (*Scholz*, 1968b; *Das and Scholz*, 1981).

This thesis presents research into the chemical role of pore water in advancing fracture growth in porous sandstones that can be considered analogues to North Sea reservoir rocks. The idea for this project came from a recent experimental study by *Ngwenya et al.* (2000), who demonstrated that the formation of a fault in a quartz-rich sandstone is associated with an elevated concentration of silica in the sample pore fluid. They attributed this geochemical signal to the enhancement of reactivity caused by microfracturing. The aim for this project is to quantify the extent by which this geochemical signal and microfracturing activity are correlated during a laboratory rock deformation test.

There are several reasons why one could expect a geochemical signal to be associated with a standard rock deformation test. During such *triaxial compression test* the growth of axial microcracks is expected to increase both fresh and total surface area of the rock sample (*Tapponier and Brace*, 1976). Experimental studies on the dissolution of silicates have demonstrated that the dissolution of silica depends on the available surface area in contact with the fluid (*Rimstidt and Barnes*, 1980; *Dove and Crerar* 1990). Dissolution could also occur preferentially from areas of high contact pressures, such as crack tips, due to their higher solubility. During the rock fracture experiments a constant flow of distilled water was pumped through the rock sample in order to monitor any such changes.

The triaxial compression tests of *Ngwenya et al.* (2000) were carried under a constant load. It was anticipated that such loading condition would also be used in my tests. However, the normal variation in the laboratory temperatures were too large to sustain a constant load on the rock sample. Even after the installation of a heater the diurnal temperature variations were noticeable, as illustrated in figure 1.1. Due to the 24-hour cycle in the laboratory temperatures, the rock sample experienced cyclic stressing. It was not possible to determine whether the sample failed due to cyclic stressing or constant loading conditions. In fact, constant load tests typically involve the measurement of such small strains that temperature effects on the specimen and loading apparatus can cause considerable difficulties (*Jaeger and Cook*, 1976: *Lockner*, 1993b). Hence, I decided to carry out a series of tests at a constant deformation rate. This kind of arrangement provides another way of studying the time dependent fracturing properties of rocks in the laboratory.

In this thesis I will show that the brittle microfracturing that precedes the dynamic failure of a rock sample during a triaxial compression test is associated with a distinct geochemical signal. Dissolution of silica dominates this signal since both sandstones used in this study are mainly composed of quartz grains. In the Locharbriggs tests silica concentrations and microcrack damage are strongly correlated by a power-law relationship. Hence, the observed environment and strain rate dependence of rock strength can be uniquely attributed to time-dependent crack growth by the stress corrosion mechanism.

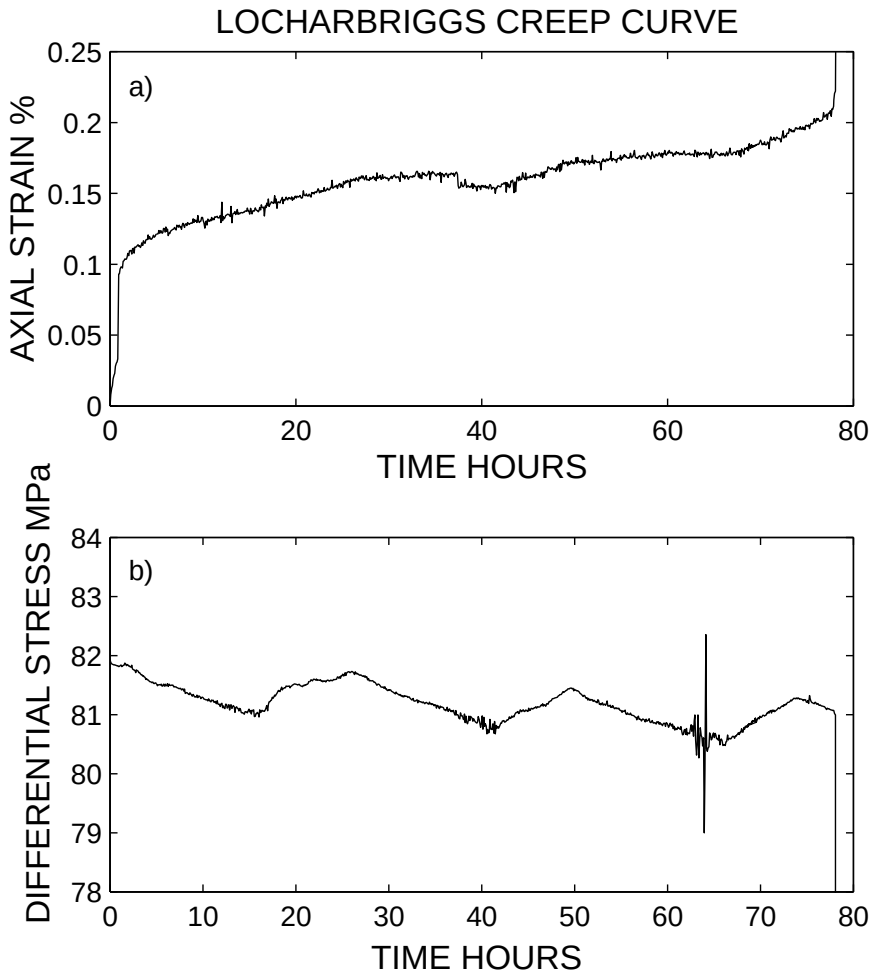

Figure 1.1. The (a) axial strain and (b) differential stress as a function of time for a constant load (creep) test on Locharbriggs sandstone. Because of temperature variations in the laboratory, the applied load fluctuated throughout the test. Hence, the rock sample experienced cyclic stressing. The thermal fluctuations are also evident in the recorded strain data. It is not clear whether the rock sample failed due to cyclic stressing or because of time-dependent creep. The answer to this question is non-unique. Hence, I decided to carry out experiments at a constant deformation rate rather than under a constant load.

1.1 Thesis organisation

The results of this study into the time dependent brittle deformation properties of sandstones are arranged into nine chapters. Chapter 2 provides a background to crack growth and reaction rate theory, with particular reference to fracturing in the quartz-water system. Chapter 3 describes the experimental apparatus. The mechanical data gathered during these tests are presented in chapter 4. Chapter 5 deals with the AE technique: the way by which the *small noises* emitted by the growing cracks can be monitored indirectly (*Obert and Duvall*, 1942). The geochemical signal that accompanies brittle deformation is described in chapter 6. Finally, chapter 7 presents the permeability data collected during this experimental suite. Each results chapter contains a discussion section and chapter 8 presents a synthesis of the main findings of this study. The conclusions are listed in chapter 9. Two publications have been prepared from the work so far (*Ojala et al.*, 2003, 2004).

Chapter 2

Crack growth and reaction rate theory

Crack propagation, the progression of consecutive bond breaking events, is identical to a chemical reaction. Krausz (1978)

2.1 Introduction

Cracks are ubiquitous in the earth's crust. They control the mechanical and physical properties of rocks. The temperature and pressure conditions of the upper crust are such that rocks deform in a dominantly brittle fashion, hence the name schizosphere (literally, broken part) (*Scholz*, 1990). The term 'brittle' refers to cracks of atomic sharpness that propagate mainly by bond rupture processes (*Lawn*, 1993). Such breaking of bonds can be induced by mechanical stress or by chemical attack. In the earth's crust, however, both of these processes act together in order to advance fracture growth. Crustal rocks are saturated with water, which can adsorb into the crack walls and help to overcome the energy barrier required for bond rupture. In this chapter I will outline the conditions for crack propagation in terms of key fracture mechanics concepts and then proceed to describe slow fracture growth in a chemically reactive environment. Due to the success of chemical kinetics in accounting for environmentally assisted fracture

growth in rocks, the final section deals with reaction kinetics from a purely chemical standpoint. I will concentrate on the fracturing and dissolution of quartz in the presence of water, since quartz is the dominant mineral of the sandstones used for this study.

2.2 Dynamic crack growth

2.2.1 Crack as a stress concentrator

The theoretical strength of a solid is equal to the stress required to break the bonds across a lattice plane (*Scholz*, 1990). At 5-10 GPa, the theoretical strength is much more than the strength of real materials, including rocks. For instance, the strength of the sandstones used for this study varies from 77.7 to 173.4 MPa, which represents only 1.6 to 3.5 % of their theoretical strength. This discrepancy arises from the fact that all materials contain defects. A microcrack is an example of a line defect, that can propagate in response to an applied stress and hence produce yielding in a rock (*Scholz*, 1990). However, a microcrack will propagate under an applied stress that is much lower than the theoretical strength, because geometrical irregularities can raise the local stress. Hence, the theoretical strength of a material is only met locally.

The idea of a crack as a stress concentrator is illustrated in figure 2.1, in which a smooth plate or bar is subjected to an uniform tensile stress σ_a (*Gordon*, 1976). The vertical lines are stress trajectories, that represent the typical paths by which stress is handed from one molecule to another. If the stress trajectories are interrupted by a hole or a crack (fig. 2.1.b) the forces have to go around the crack and they become crowded together. Hence, at the crack tip there is more force per unit area and the local stress is high. It can also be seen from figure 2.1.b that a long thin crack produces severe crowding and hence the local stress concentration is high.

In mathematical terms, a microcrack can be approximated by an ellipse that is made relatively long and thin. The stresses around a circular and an elliptical hole were calculated by Kirsch in Germany in 1898 and Kolosoff in Russia in 1910,

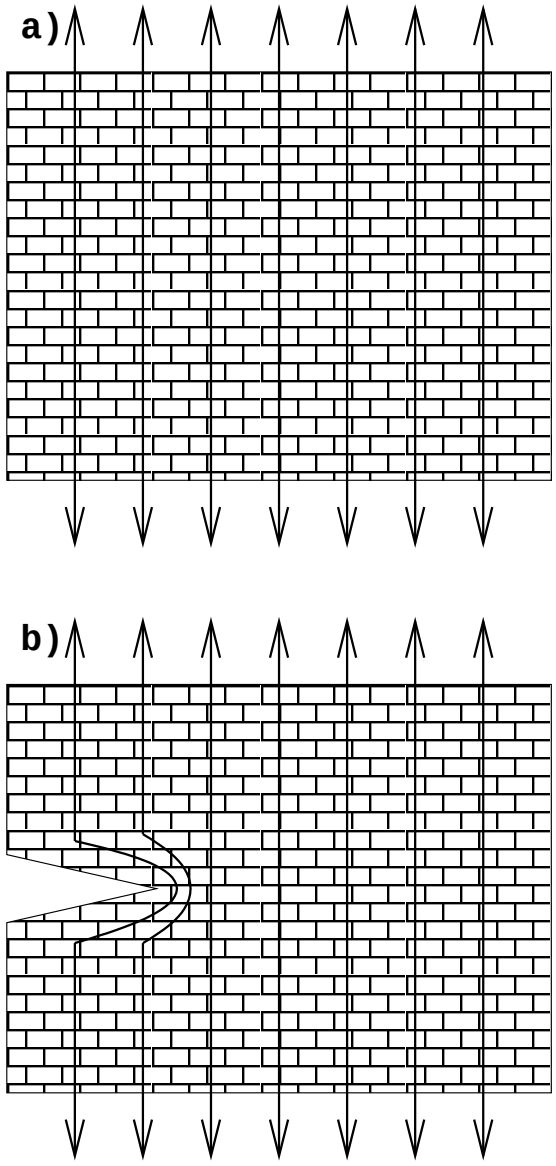

Figure 2.1. A schematic diagram of how a stress concentration arises at a crack tip. In (a) uniform plate is subjected to an uniform tensile stress σ_a. In a smooth plate the stress trajectories are straight. In a cracked plate (b) the the stress trajectories are interrupted by the hole. Hence, the stress trajectories must go around the crack. They become crowded together and give rise to a stress concentration at the tip of the crack. Redrawn from *Gordon* (1976).

respectively (*Timoshenko*, 1953; *Gordon*, 1976). However, the concept of stress concentration was first introduced to English shipbuilding circles by *Inglis* (1913). He calculated the stresses around an elliptical hole in order to explain why cracks in ships' hulls always initiated in the corners of hatchways and other openings (*Gordon*, 1976). For a plate that contains an elliptical hole with semi-axes b,c, subjected to uniform applied tension σ_a the stress concentration ratio is given by (*Lawn*, 1993):

$$\frac{\sigma_c}{\sigma_a} = 1 + 2\left(\frac{c}{g}\right)^{1/2} \tag{2.1}$$

where σ_c is the crack tip stress, c is half length of the crack and g is the radius of curvature of the crack. Equation (2.1) suggests that stress concentration depends on the shape of the hole, rather than its size. Hence, it is incapable of explaining why larger cracks propagate more readily than smaller ones (*Lawn*, 1993).

2.2.2 Griffith's energy balance principle

Griffith (1920) approached the problem of crack propagation in terms of an energy balance rather than force or stress. While Inglis's stress concentration is a plausible mechanism for crack propagation, Griffith recognised that a continuous supply of strain energy is a pre-requisite for creating new crack surface (*Gordon*, 1976). The Griffith concept can be explained in terms of an elastic body containing a crack of length $2c$ under a constant applied stress σ_a (figure 2.2.a). The total energy U of such a system is given by (*Scholz*, 1990):

$$U = U_m + U_s = (-W + U_e) + U_s \tag{2.2}$$

where W is the work done by the external forces, U_e is the strain energy stored in the system, U_s is the energy required for creating new surfaces and U_m is the total mechanical energy of the system. Clearly, the energy required to propagate a

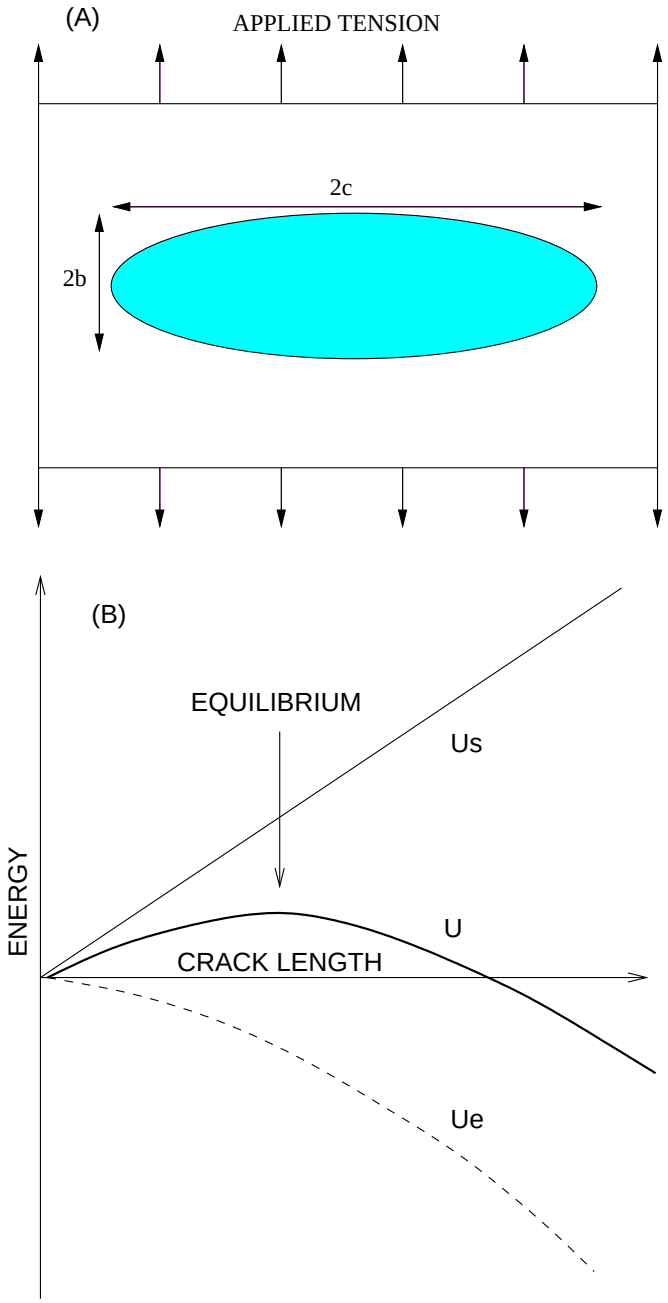

Figure 2.2. (a) A plate containing an elliptical hole with semi-axes b, c that is subjected to applied tension. (b) The total energy of the system U is a function of the strain energy U_e and the fracture surface energy U_s. The equilibrium configuration is unstable. Redrawn from *Scholz* (1990).

crack needs to come from somewhere else in the system. Therefore, the combined term in parenthesis, known as the mechanical energy term, decreases as the crack proceeds (fig 2.2.b). The decrease in U_e can be attributed to relaxation of the material adjacent to the newly created crack surfaces (*Gordon*, 1976). In contrast, U_s increases with crack extension since cohesive forces must be overcome in creating new surface area (*Lawn*, 1993). At equilibrium, there exist a balance between the surface and mechanical terms, and hence

$$\frac{dU}{dc} = 0 \tag{2.3}$$

This is the *Griffith energy balance principle*. Whether the crack will propagate or retract is expressed by the negative or positive sign of (2.3), respectively. In the case of a rod in uniform tension, the total energy of the system is given by

$$U = -U_e + U_s = -\left(\frac{\pi c^2 \sigma_A^2}{E_m}\right) + 4c\gamma \tag{2.4}$$

where σ is the applied stress, E_m is the elastic modulus, and γ is the free surface energy per unit area. By combining (2.4) with (2.3) we get the critical stress σ_F and the critical crack length $c = c_c$

$$\sigma_F = \left(\frac{2E_m\gamma}{\pi c_c}\right)^{1/2} \tag{2.5}$$

As shown in figure 2.2.b, the energy of the system is at maximum at equilibrium and hence the configuration is unstable (*Scholz*, 1990). Consequently, if the applied stress σ_A is less than σ_F the crack is likely to remain at its original size c_0: however, if $\sigma_A > \sigma_F$ the crack will propagate spontaneously, without limit (*Scholz*, 1990; *Lawn*, 1993). On the other hand (2.5) also defines c_c, the critical crack length for each stress component in the material (*Gordon*, 1976). At $c > c_c$ the crack is producing more energy than it is releasing and thus it may run away

in a catastrophic manner. In other words, (2.5) explains why longer cracks are more likely to propagate than shorter ones.

2.2.3 Obreimoff's experiment

The boundary condition for Griffith crack configuration (fig. 2.2) was that of a constant stress, resulting in unstable equilibrium. In contrast, *Obreimoff* (1930) carried out a cleavage test on mica under constant displacement rate control. He used a glass wedge inserted under a thin mica flake, that was still attached to its parent block, in order to drive a crack along the cleavage plane (fig. 2.3.a). In his test setup the work done on the system equals zero. From (2.3), by using $U_s = 2c\gamma$ and from elementary beam theory $[U_e = E_m d_f^3 h_d^2/(8c^3)]$, the equilibrium crack length c_c is given by

$$c_c = \left(\frac{3E_m d_f^3 h_g^2}{16\gamma} \right)^{1/4} \tag{2.6}$$

where d_f and h_g are the thicknesses of flake and the glass wedge, respectively (*Lawn*, 1993). Figure 2.3.b highlights the stable equilibrium configuration resulting from the constant displacement rate boundary condition of the Obreimoff experiment. The energy terms U, U_s and U_e are also depicted in figure 2.3.b.

More importantly, Obreimoff was the first person to carry out a detailed study on the effect of test environment on crack propagation rates in laboratory conditions (*Scholz*, 1990; *Lawn*, 1993). From (2.6) he calculated the surface energy γ in a vacuum (p=100 μ Pa) and he found that it was over ten times as much as in ambient atmosphere (p=100 kPa). Furthermore, the crack did not attain its equilibrium length immediately, but crept for few seconds and several days in air and vacuum, respectively. This observation suggests that chemical kinetics may also play a role in fracture propagation rates. With his experiment Obreimoff confirmed what French champagne makers had known for years: they never used the same bottle twice and thus saved many good bottles of champagne from destruction by chemical weakening of glass (*Anderson and Grew*, 1977). As

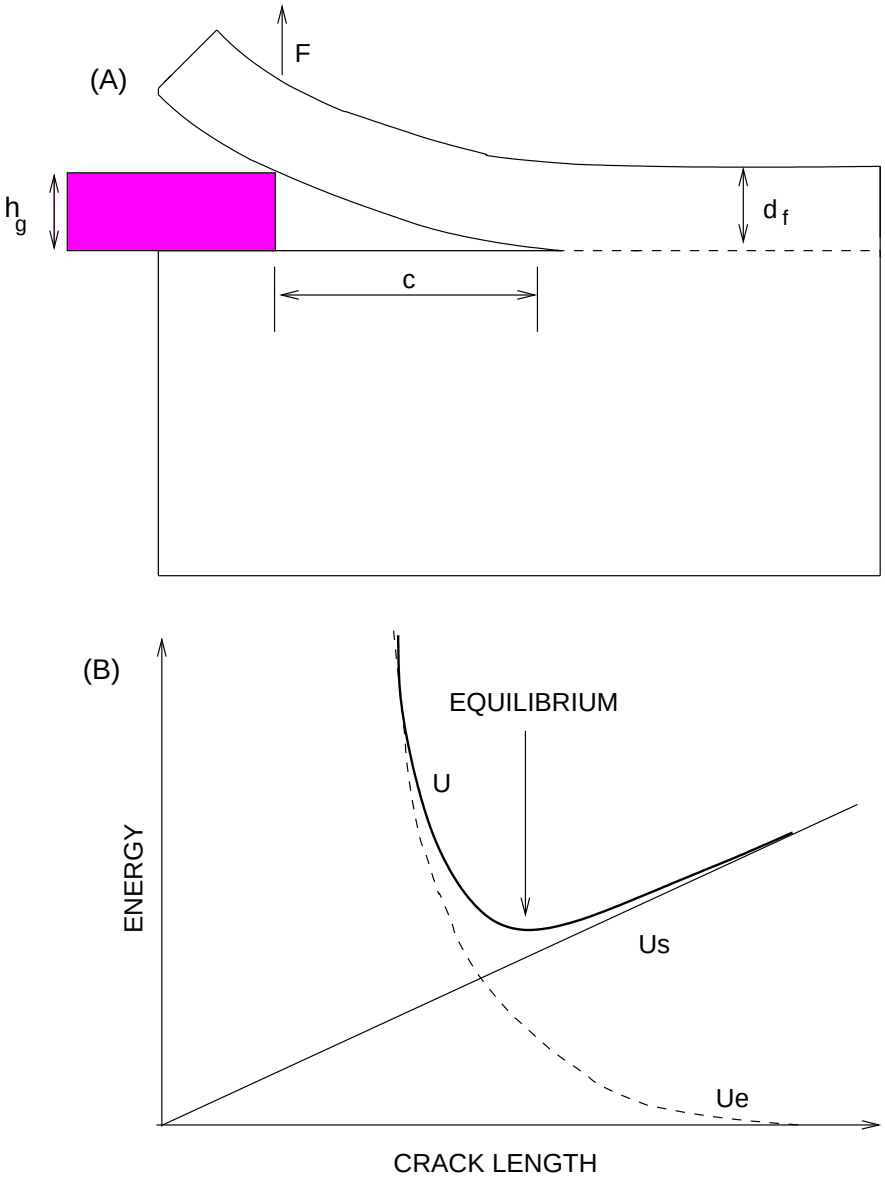

Figure 2.3. The mica experiment of *Obreimoff* (1930). (a) Glass wedge with thickness h_g was inserted to drive a mica cleavage flake with thickness d_f. (b) The system energy U is a function of surface energy U_s and the internal strain energy U_e. The equilibrium configuration is stable. Redrawn from *Scholz*, (1990).

well as Obreimoff they too had observed the dramatic effect that time and test environment can have on material strength.

2.2.4 Irwin's modification of the Griffith concept

Griffith's analysis was insufficient since it omitted important forms of energy dissipation, such as the generation of heat and acoustic emission, that occur during crack propagation. Nevertheless, the energy balance approach of Griffith provided a solid foundation for the development of a new concept called *fracture mechanics* by Irwin and his contemporaries in the 1950's (*Lawn*, 1993). Fracture mechanics is concerned with the stress field around a crack, represented by a narrow slit in a linear elastic medium, and the conditions under which it may propagate to form a macrocrack (*Meredith*, 1990; *Scholz*, 1990). It relates the macroscopic strength of a material to the intrinsic one by formulating a relationship between the applied stresses and crack tip stresses (*Scholz*, 1990).

Irwin modified the Griffith equation for crack growth energetics (2.2) by balancing the mechanical and surface terms against increase in crack surface area A_s

$$\frac{dU}{dA_s} = \frac{dU_m}{dA_s} + \frac{dU_s}{dA_s} = -G + R_c \tag{2.7}$$

where G is the mechanical energy release rate per unit surface area and R_c is crack resistance that describe the crack driving and resistance forces, respectively (*Irwin*, 1958; *Ewalds and Wanhill*, 1991). Hence, for a crack to propagate, G must be at least equal to R_c. Since R_c is a constant, G must exceed a critical value G_c for unstable crack propagation to occur.

Due to practical problems associated with the energy approach, Irwin introduced the stress intensity factor K that describes the crack tip force field. Assuming a flat and perfectly sharp crack, with traction free walls, the near-field approximation to the crack tip stress σ_{ij} and displacement u_i fields are given by by (*Irwin*, 1958, *Scholz*, 1990):

$$\sigma_{ij} = \frac{K_i}{(2\pi r)^{1/2}} f_{ij}(\theta_1) \tag{2.8}$$

$$u_i = \left(\frac{K_i}{2E_m}\right)\left(\frac{r}{2\pi}\right)^{1/2} f_i(\theta) \tag{2.9}$$

where i and j are the components of the stress tensor, r is the radial distance form the crack tip, θ_1 is the angle measured from the plane of the crack, E_m is the elastic modulus and $f_{ij}(\theta)$ is a well defined function that depends on the loading geometry (*Ewalds and Wanhill*, 1991; *Lawn*, 1993). K is the stress intensity factor that depends on the crack opening mode. The three crack opening modes are illustrated in figure 2.4 from *Guéguen et al.* (1990). Hence, K_I, K_{II} and K_{III} refer to the tensile, in-plane shear and anti-plane shear modes of crack tip displacement. The superposition of the three basic modes can be used to describe any general case of crack tip displacement and stress field. For plane stress conditions, the stress intensity factor K_I for mode I crack propagation is related to G_I by

$$G_I = \frac{K_I^2}{E_m} \tag{2.10}$$

where E_m is the Young's modulus for the material (*Lawn*, 1993). Due to such equivalence of parameters the condition for unstable crack propagation can be expressed using critical values K_c or G_c. The critical value K_c is termed fracture toughness.

For experimental determination of fracture mechanics parameters and in modelling of crack systems, stress intensity analysis can be simplified by arranging a two-dimensional crack tip stress field and uniform loading in a finite body (*Meredith*, 1990; *Ewalds and Wanhill*, 1991; *Lawn*, 1993). For such a system, the stress intensity factor K for a two-dimensional crack of any mode is given by

$$K = Y_1 \sigma_A (\pi c)^{1/2} \tag{2.11}$$

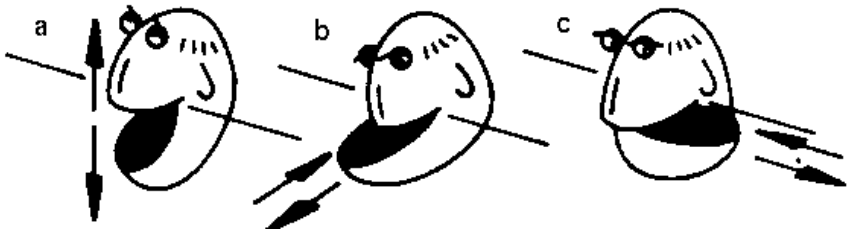

Figure 2.4. The three modes of crack opening. (a) tensile, (b) in-plane shear and (c) anti-plane shear. From *Guéguen et al.* (1990).

where σ_A is the remotely applied stress, c is the crack half length and Y is a constant related to crack tip geometry.

2.2.5 Criteria for dynamic fracture

Linear elastic fracture mechanics (section 2.2.4) predicts that an isolated planar crack with traction free walls will propagate dynamically once a critical condition is met at the crack tip (*Meredith*, 1990). Such critical condition can be expressed in terms of a fracture toughness K_c or crack extension force G_c. Since the growth of a crack requires the creation of two new crack surfaces, G_c equals

$$G_c = 2\gamma \tag{2.12}$$

where γ is the specific surface energy of the solid. During dynamic fracturing, the running crack typically divides the test specimen into two or more parts (*Lawn*, 1993). Therefore it can be considered to be catastrophic. The the fracture propagation velocity may approach the speed of sound in the medium (*Lawn*, 1993). However, due to inertial effects the terminal velocity is generally considered to be less than equal to the Rayleigh wave velocity in the material (*Aki and Richards*, 1980). Alternatively, dynamic rock fragmentation can result from impact or stress wave loading, in which case the material response depends on the duration of the loading pulse (*Lawn*, 1993). Such a condition for dynamic fracturing is important in evaluating the effects of impact cratering or explosives

on rocks (*Grady and Kipp*, 1987). However, in this study I am only concerned with the critical condition defined by G_c. Crack propagation at a critical value G_c is an example of an equilibrium law for crack propagation.

2.2.6 Shortcomings of the LEFM approach

The mechanical behaviour of real materials deviates from the assumptions of linear elastic fracture mechanics. For instance, the definition of the stress intensity factor (2.8) includes a singularity at the crack tip, since it assumes a perfectly sharp crack. However, no material can support infinitely large strains. The existence of a singularity also violates the small strain assumption that is implicit to the LEFM approach (*Scholz*, 1990; *Lawn*, 1993). In fact, K can be used to describe the crack tip stress field only when the the region of the inelastic behaviour, known as the *process zone*, is small compared to the macrocrack length and the size of the test specimen. It is generally believed that the LEFM approach holds when $r_z/2c < 0.02$, where r_z is the process zone size and $2c$ is the macrocrack length or any dimension of the test specimen (*Knott*, 1973).

Experimental evidence (*Swanson*, 1984; 1987) suggests that when it comes to real materials, the assumption of small-scale inelasticity is commonly violated. In fact, metre-sized specimen of Westerly granite would be required in order to assume small-scale inelasticity (*Swanson*, 1987). Hence, various process zone models have been developed to describe this region of inelastic behaviour (*Dugdale*, 1960; *Barenblatt*, 1962; *Lawn*, 1993, *De With*, 2002). Alternatively, non-linear crack tip processes may be incorporated into the LEFM approach by considering an effective crack length (*Labuz et al.*, 1985) or and effective stress intensity factor (*Meredith*, 1990).

Furthermore, experimentally defined values for the fracture surface energy of minerals (*Atkinson*, 1984) and rocks (*Murrell*, 1990) are generally higher than theoretically determined values. This discrepancy can be attributed to energy dissipative (heat generation, acoustic emission) and inelastic processes (subsidiary microcracking, crack deflection). The Irwin-Orowan extension (*Irwin*, 1958) takes this into account by introducing a plastic work term R_p so that

$$G_c = R_c = 2\gamma + R_p \tag{2.13}$$

where R_c is the crack resistance energy. Although γ is actually much smaller than R_p it cannot be ignored when considering crack tip energetics (*Lawn*, 1993). However, in practice the specific processes that contribute to G_c are not generally known. Typically, these processes do not have a great practical importance since G can be determined as long as G_c is measured outside the non-linear zone (*Rice*, 1978; *Scholz*, 1990).

2.2.7 Conclusion

The Griffith-Irwin fracture mechanics provides a thermodynamically plausible model for dynamic crack propagation. However, the LEFM approach does not provide a physically realistic mechanism for crack extension. Real materials are likely to have a non-linear zone ahead of the crack tip that relaxes the singularity assumed by LEFM. This non-linear zone can be incorporated into LEFM principles by considering effective fracture mechanics parameters. In addition, the LEFM assumes that brittle fracture properties are governed by in-vacuo surface energies. This is clearly non-physical as fracture growth in crustal rocks takes place in a chemically active environment. The effect of reactive environment on crack propagation rates is discussed in the next section.

2.3 Kinetic crack growth

2.3.1 The effect of pore fluid on crack growth

The existence of fluids in the earth's crust has been proved to at least 15 km depth in super-deep drill holes (*Sornette*, 1999). The presence of water affects the brittle deformation properties of rocks in two important but separate ways. The poroelastic effect results from changes in pore fluid pressure that affect the local

effective pressure (*Paterson*, 1978). If the fluid pressure P_p is fully communicated within the pore space of the rock, the effective pressure P_{eff} that controls the mechanical properties of rocks is reduced by the amount of P_p Secondly, chemical weakening of crack tip bonds may facilitate crack propagation. This mechanism is termed stress corrosion crack growth (*Anderson and Grew*, 1977; *Atkinson*, 1982, 1984). It is one of the mechanisms by which subcritical crack growth may operate.

2.3.2 Subcritical crack growth

Classical fracture mechanics postulates that a crack will propagate when a critical value K_c or G_c is exceeded at the crack tip (section 2.2.5). However, experimental evidence for glass (*Wiederhorn*, 1967), minerals (*Scholz*, 1972), and rocks (*Atkinson*, 1982, 1984; *Atkinson and Meredith*, 1987a,b) demonstrates that crack growth can occur at values of K below K_c. This kind on fracture behaviour is termed subcritical crack growth since it occurs below critical values of K or G. While dynamic fracture is associated with fast, catastrophic crack propagation, subcritical crack growth is characteristically slow and quasi-static. Due to the slow velocities in the nm/s to m/s range, subcritical crack growth can also be referred to as kinetic crack growth (*Lawn*, 1993). Therefore the theory of chemical kinetics is especially suited for analysing the time dependent aspects of crack growth (*Krausz and Eyring*, 1975) that are commonly ascribed to slow crack growth in the subcritical range (*Costin*, 1987).

Although subcritical crack growth has been observed in a vacuum (*Wiederhorn et al.*, 1974; *Lawn*, 1993), it is especially common in reactive chemical environments and at elevated temperatures. Several atomic scale mechanisms that may contribute towards subcritical crack growth include atomic diffusion, dissolution, ion exchange, microplasticity, stress corrosion and cyclic fatigue (*Atkinson*, 1984; *Atkinson and Meredith*, 1987a). However, crack growth in the crustal environment is dominated by the chemical effects of water. Stress corrosion crack growth is likely to be the most important cause of delayed failure (*Das and Scholz*, 1981, *Costin*, 1987) and seismic anisotropy (*Crampin et al.*, 1981) in the upper crust. It is maybe due to its importance in the crustal setting that subcritical crack growth and stress corrosion fracturing in particular have received considerable

attention in the literature (*Charles and Hillig*, 1962; *Martin*, 1972; *Scholz*, 1972; *Anderson and Grew*, 1977; *Krausz*, 1978; *Rice*, 1978; *Wiederhorn*, 1978; *Dunning et al.*, 1980, 1984, 1994; *Atkinson and Meredith*, 1981; *Das and Scholz*, 1981; *Sano et al.*, 1981; *Atkinson*, 1982, 1984; *Meredith and Atkinson*, 1983; *Freiman*, 1984; *Kirby*, 1984; *Segall*, 1984; *Darot and Guéguen*, 1986; *Atkinson and Meredith*, 1987a, 1987b; *Renshaw and Pollard*, 1994; *Dove*, 1995; *Schultz*, 2000; *de With*, 2002). Excellent reviews of the topic have been provided by *Anderson and Grew* (1977), *Atkinson* (1982), *Atkinson and Meredith* (1987a).

2.3.3 Stress corrosion crack growth

In the most general sense, stress corrosion fracturing is slow crack growth that can be attributed to the combined effects of stress and a corrosive environment. Other workers (*Anderson and Grew*, 1977) have specified that stress corrosion is environment induced slow crack growth that occurs under sustained stress. Figure 2.5 is a schematic representation of chemically induced rupture (*Lawn*, 1993). An environmental molecule A reacts dissociatively with the intact crack tip bond B to produce two terminal groups A-B

$$(A-A)+(-B-B-)\rightarrow(-BA\cdot AB-) \tag{2.14}$$

Each event described through (2.14) ruptures the crack tip bond, produces new crack surface area and exposes the new crack tip bond for the next incoming molecule. Hence, the general expression for stress corrosion can be written as (*Atkinson and Meredith*, 1987a)

$$XA+B\rightleftharpoons B^{+}\rightleftharpoons Products \tag{2.15}$$

where X is the number of environmental species and B^{+} denotes the activated state. It is interesting to note that the form of the general expression (2.15) is

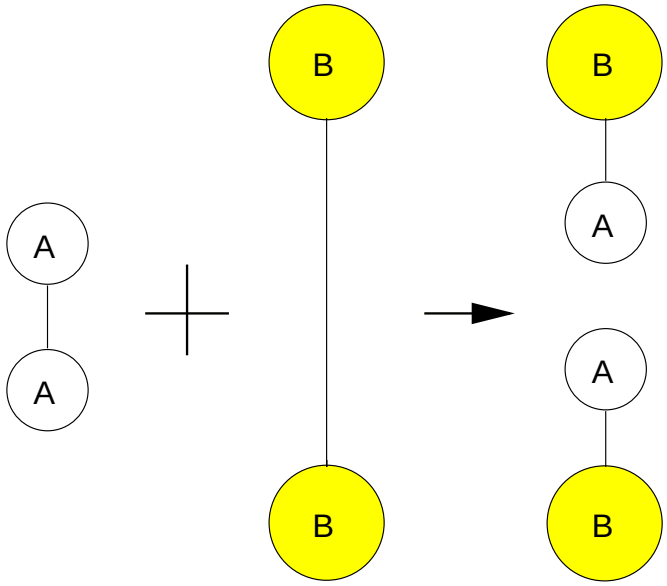

Figure 2.5. Chemically induced bond rupture. An environmental molecule A reacts dissociatively with crack tip molecule B to produce terminal bonds A-B-. Redrawn from *Lawn* (1993).

identical to the equation that describes the dissolution of quartz into water (2.30). The similarities between silica dissolution and the slow fracturing of quartz in the presence of water will be discussed further in section 2.5.

Experimental evidence for slow crack growth in quartz (*Darot and Guéguen*, 1986) has confirmed that the size of the activation area for crack propagation is 1.3 Å, which is close to the spacing of the Si-O bonds, 1.6 Å. Their observations suggest that the elementary process for slow crack growth in the quartz-water system is the breaking of bonds. An elegant model for the bond weakening process by water has been put forward by *Michaelske and Freiman* (1982). Their model is based on the idea that the strained Si-O bonds at crack tips can react more readily with water because of a strain-induced decrease in the overlap between atomic orbitals. The water molecule has three hybrid orbitals and two of these link oxygen and hydrogen atoms. The third hybrid orbital and the p_z orbital remain alone. Therefore, hydrogen bonding is formed between H and the O atom from SiO_2 and covalent bonding is formed between OH and Si. The three-step model of *Michaelske and Freiman* (1982) involving (a) adsorption, (b) reaction and (c) separation is illustrated in figure 2.6. Firstly, (a) environmental water molecule

attaches itself to the bridging Si-O-Si bond at the crack tip with the lone electron pair orbitals on the oxygen of the water molecule O_W aligned towards the silicon. This kind of alignment occurs due to the charge characteristics of the system. In the second step (b) the O_W donates an electron to one of the silicons and a proton to the linking O_{Si}. Hence, two new bonds are formed, Si-O_W and H-O_{Si}. Subsequently (c) the weak hydrogen bond between O_W and the transferred hydrogen creates Si-OH surface groups on each fracture surfaces. While a similar mechanism for silica dissolution has been proposed by *Budd* (1961), the model of *Michaelske and Freiman* (1982) does not include the removal of material from the fracture surface.

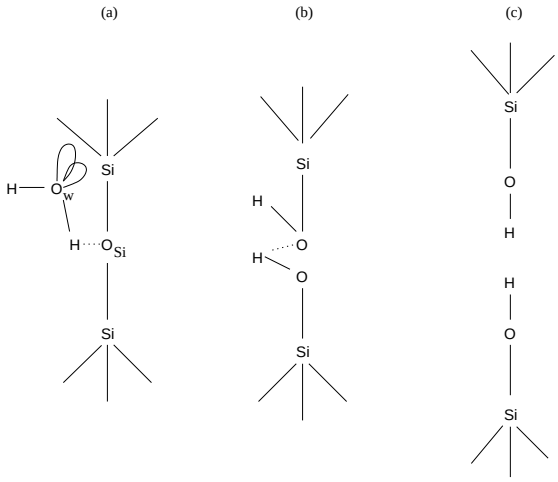

Figure 2.6. Schematic picture of the proposed reaction between water and the strained Si-O-Si bond at the crack tip. Redrawn from *Michaelske and Freiman* (1982).

A majority of theoretical models for stress corrosion crack growth are based on empirical fits to laboratory data. It is therefore instructive to first consider the general features that have been observed in laboratory studies. In a typical test a single macrocrack, which emanates from a pre-existing notch, is allowed to propagate in a quasi-static manner. These studies often utilise a double torsion type testing machine. Hence, The appropriate crack growth parameters v and K can be determined from load relaxation data and specimen geometry. The most common way for displaying crack growth data is to plot crack velocity v versus K or $\log K$. Alternatively, G or $\log G$ may also be used (*Darot and Guéguen*, 1986).

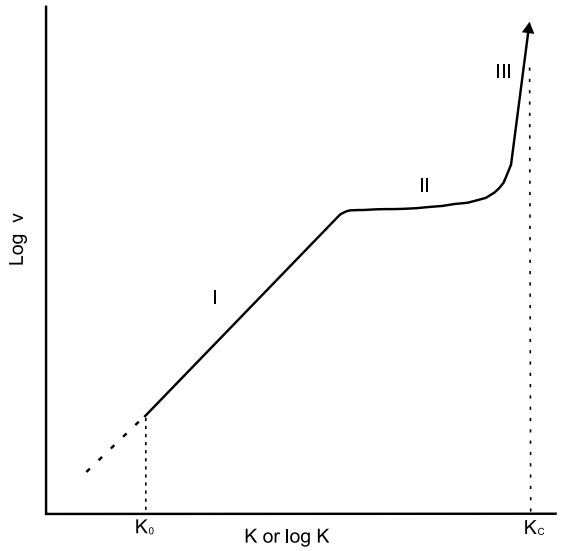

Figure 2.7. Schematic picture that relates crack growth velocity v to the stress intensity factor K. Redrawn from *Lockner* (1993b).

Much of the early experimental work on stress corrosion crack growth dealt with static fatigue (or delayed failure) due to stress corrosion in glasses and ceramics (*Anderson and Grew*, 1977). Delayed failure in glass was first reported by Grenet in 1899, who observed that '*glass could statically support a given weight for a time and then would fail*' (*Anderson and Grew*, 1977). Eighty years later, Wiederhorn (1967) observed a characteristic trimodal pattern in crack growth by stress corrosion mechanism in glass. Since the pioneering work of *Wiederhorn* (1967) stress corrosion crack growth has been traditionally interpreted in terms of these three regions (figure 2.7). In region I the crack growth velocity is controlled by the rate of chemical reactions at the crack tip. In region II v is controlled by the transport of reactive species to the crack tip. In region III v is controlled by mechanical rupture and it is relatively insensitive to the chemical reaction. *Wiederhorn et al.* (1982) have proposed models for the diffusion velocity and stress aided reaction in regions II and III, respectively. However, not all of the three regions are observed for a material in a given environment. Typically, only region I type behaviour is observed for rocks (*Atkinson*, 1982).

Stress corrosion crack growth is characterised by its notable dependence on the applied load (figure 2.7) and therefore many kinetic laws of crack growth

describe crack growth velocity as a function of K or G (*Anderson and Grew*, 1977; *Atkinson*, 1982; *Atkinson and Meredith*, 1987a). The most commonly used empirical expressions for region I behaviour are the *Charles* (1958) power law and the exponential law of *Wiederhorn and Bolz* (1970) and *Lawn* (1993). These can be written, respectively, as

$$v = v_0 \exp\left(\frac{-H}{RT}\right)\left(\frac{K}{K_0}\right)^n \tag{2.16}$$

$$v = v_0' \exp\left(\frac{-E^* + \alpha_1 K}{RT}\right) \tag{2.17}$$

$$v = v_0' \exp\left(\alpha_2 G\right) \tag{2.18}$$

where H is activation enthalpy, R is the gas constant, T is temperature, K is stress intensity factor, K_0 is the threshold stress intensity for subcritical crack growth, n is the subcritical crack growth index, E^* is the apparent activation energy, G is the strain energy release rate, v_0, v_0' are pre-exponential factors and α_1, α_2 are empirical constants. While the exponential form (2.17) is derived from reaction rate theory for propagation of a single crack (*Charles and Hillig*, 1962; *Wiederhorn and Boltz*, 1970; *Lawn*, 1993), the power law form (2.16) is consistent with the growth of multiple cracks in a stochastic granular medium (*Main*, 1999). Other workers have suggested an exponential dependence on G (2.18) rather than K: they based their argument on reaction rate theory (*Darot and Guéguen*, 1986), adsorption theory (*Dunning et al.*, 1984) and the quasi-static growth of Griffith cracks (*Rice*, 1978). A wide range of experimental data fit both exponential (*Wiederhorn*, 1978) and power-law forms (*Atkinson*, 1982; 1984, *Meredith and Atkinson*, 1983; *Swanson*, 1984). The subcritical crack growth index n generally takes values 30-60 for polycrystalline rocks (*Atkinson and Meredith*, 1987b). Due to such strong dependence of v on K or G it may be impossible to distinguish between (2.16), (2.17) and (2.18) over a narrow range of K or G values (*Meredith*, 1990).

It is also clear from figure 2.7 that stress corrosion crack growth occurs at value of K above some threshold value K_0. While a finite stress corrosion limit has been observed for soda-lime, borosilicate glasses (*Michaelske*, 1983; *Freiman*, 1984) and quartz crystals (*Dunning et al.*, 1994) it is not clear whether all materials behave

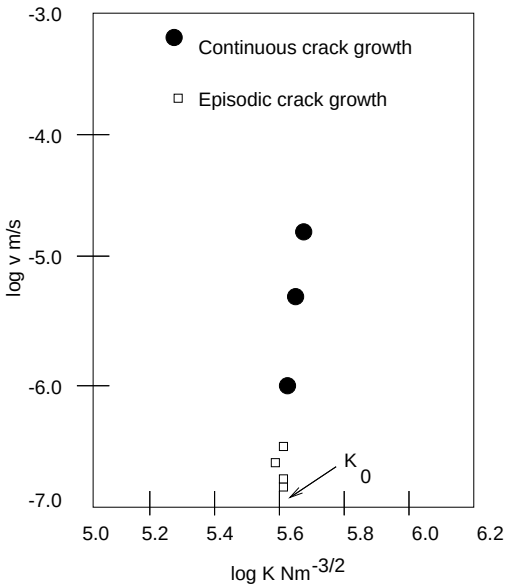

Figure 2.8. The distinction between continuous and episodic crack growth in the quartz-water system. *Dunning et al.* (1994) defined stress corrosion limit K_0 at a point when slow crack growth in quartz turned from episodic to continuous. Redrawn from *Dunning et al.* (1994).

this way. Although K_0 is a very important parameter for modelling earthquake precursors, aftershocks (*Narteau et al.*, 2003) and the long term strength of rocks, it is very difficult to obtain a reliable measure of this parameter in laboratory conditions. In fact, '*minimum crack growth rates depend primarily on the patience of the observer*' (*Speidel and Hyatt*, 1972) and slow rack growth tests can be *literally* very time consuming. For instance, crack propagation in alloys has been measured at velocities as slow as 10^{-11} m/s which corresponds to one cm per year. It is unlikely that laboratory observations can be made at a slower rate than that. In fact, *Dunning et al.* (1994) suggested that K_0 for quartz occurs when crack growth turns episodic at a velocity of 3.5×10^{-7} m/s. The episodic crack growth that was observed by *Dunning et al.* (1994) is illustrated in figure 2.8. It has been suggested that the ratio of critical values for quasi-static and dynamic crack growth K_0/K_c in quartz could be as low as 0.15 (*Parks*, 1984; *Segall*, 1984).

Although the earth's crust is pervaded by fractures it is not rubble. This fact suggests that there is a limit for stress corrosion crack growth in rocks (*Atkinson and Meredith*, 1987a). The existence of a finite threshold for crack propagation

is also predicted by various models. In the *Charles and Hillig* (1962) model K_0 occurs when dissolution equals the crack growth velocity. The *Orowan* (1944) model predicts crack healing when G is less than 2γ, where γ is the solid-fluid interface energy. Similarly, the *Lawn* (1993) model predicts crack healing when $G < R_0$, where R_0 is the surface tension of the solid. However, the only laboratory observations of crack healing in quartz and calcite were obtained at high temperatures (*Brantley et al.*, 1990) and in the absence of chemically reactive fluids (*Dunning et al.*, 1994). In the low temperature regime crack healing has been observed by *Obreimoff* (1930) and *Lawn et al.* (1987) for mica and glass, respectively. It has been pointed out (*Dunning et al.*, 1994), however, that these experiments were '*somewhat special*' because of experimental apparatus of Obreimoff and due to the near-vacuum conditions of the *Lawn et al.* (1987) tests. A different mechanism could be responsible for fracture propagation in the near-vacuum tests of *Lawn et al.* (1987). However, *Elias and Hajash* (1992) observed healed microcracks as indicated by fluid inclusion trails in quartz sand that had been compacted (constant P_{eff}) at high temperatures. So far no stress corrosion limit has been measured for rocks.

2.3.4 Experimental data on quartz and quartz-rich rocks

The majority of the existing data on subcritical crack growth in geological materials deals with slow fracture growth in quartz. This is perhaps not surprising since quartz makes up 20-30 % of the continental crust (*Skinner and Porter*, 1995). Quartz is also the major constituent of the rocks used in this study. In fact, the early studies of *Martin* (1972), *Scholz* (1972) and *Martin and Durham* (1975) all dealt with static fatigue in quartz. Although *Martin* (1972) and *Scholz* (1972) did not report their data in terms of v or K, they observed that the fracturing process depends on temperature, partial pressure of water and crystallographic orientation. The first study to report stress corrosion data on quartz in terms of v and K was by *Atkinson* (1979). Unlike *Dunning et al.* (1994) he observed no evidence for a stress corrosion limit even at crack velocities as slow as 10^{-9} m/s. Since then, slow crack growth in quartz has been studied by *Atkinson* (1980), *Dunning et al.* (1980; 1984; 1994), *Atkinson and Meredith* (1981), *Meredith and Atkinson* (1982), *Miller and Dunning* (1985) and *Darot and Guéguen* (1986).

Table 2.1. Some experimentally determined parameters for stress corrosion crack growth in quartz, sandstones (SST) and other quartz-rich rocks. *Winter* (1983) used a single edge-notch bending beam method and *Holder et al.* (2001) used a dual torsion type apparatus. All of the other studies were carried out by using the double cantilever beam technique. Both *Winter* (1983) and *Holder et al.* (2001) reported higher stress corrosion indices for crack growth in air in comparison to water saturated sandstone samples. The specimen with the higher proportion of quartz cement had a higher n-value in the tests of *Holder et al.* (2001).

Material	Environment	T °C	ΔH kJ/mol	n	Study
Quartz	water	20-80	52.5	12.0	Atkinson (1979)
	vapour	90-240	108		Martin (1972)
	vapour	20-50	46-100		Scholz (1972)
	vapour	20	-	18	Meredith and
		100	-	16	Atkinson (1982)
		200	-	12	
Scioto SST	air	20		35	Holder et al.
		20		52	(2001)
	water	20		25	
		20		36	
Ruhr SST	air	22	-	63-151	Winter (1983)
	water	22	-	8-11	
Tennessee SST	air	20	-	17	Atkinson (1982)
	water	20	-	14	
	water	60	-	26	
Arkansas Novaculite	water	20-80	70	25	Atkinson (1980)
Mojave Quartzite	water	20	-	39	Atkinson (1984)

Table 2.1 presents a compilation of some of the experimentally determined parameters for mode I subcritical crack growth in quartz and quartz-rich rocks. The relatively high activation enthalpies for quartz (52.5 kJ/mol) and Arkansas novaculite (70 kJ/mol) suggest that the kinetics of crack growth in water are controlled by bond breaking mechanism in these materials (section 2.4.2). The subcritical crack growth index is 12 and 8-39 for quartz and quartz-rich rocks, respectively, in the presence of water. The n-values of *Winter* (1983) appear quite different from those determined in the other studies. This may be due to the different testing apparatus used in his experiments (*Atkinson and Meredith*, 1987b). For all of the other studies listed in table 2.1., the values of n are consistently higher for quartz bearing rocks than for quartz crystals. This observation may reflect the higher microstructural complexity of the rock with respect to a pure crystal. Numerous studies have observed a lower susceptibility for crack growth in geological materials with increasing microstructural complexity (*Atkinson*, 1984; *Swanson*, 1984; *Atkinson and Meredith*, 1987a). Furthermore, both *Winter* (1983) and *Holder et al.*, (2001) reported lower n-values in the presence of water relative to that in air. The observations of *Holder* (2001) also suggest that the amount of quartz cementation may increase the n-value.

Laboratory studies of subcritical crack growth in quartz and quartz-rich rocks have demonstrated the dependence of crack growth rate on temperature (*Scholz*, 1972; *Martin*, 1972; *Atkinson*, 1979; *Meredith and Atkinson*, 1982; *Atkinson*, 1984; *Darot and Guéguen*, 1986), partial pressure of water (*Scholz*, 1972; *Martin*, 1972), humidity (*Scholz*, 1972; *Atkinson*, 1979), pH (*Atkinson and Meredith*, 1981; *Dunning et al.*, 1994), crystallographic orientation (*Scholz*, 1972; *Atkinson*, 1979, 1984) and the presence of solutes (*Dunning et al.*, 1980; 1994).

The temperature dependence of crack growth rates in quartz and Arkansas novaculite is consistent with theoretical models of stress corrosion crack growth as a thermally assisted process (*Charles and Hillig*, 1962; *Krausz*, 1978; *Dove*, 1995). In his static fatigue tests on quartz *Scholz* (1972) observed that the mean fracture time was strongly reduced at a higher temperature. In a similar set of experiments, *Martin* (1972) observed an increase in crack velocity with increasing temperature. The result of *Martin* (1972) is in good agreement with the double torsion tests of *Atkinson* (1979), *Meredith and Atkinson* (1983) and *Darot and Guéguen* (1986). All of these studies reported a positive temperature (T=20-80

°C) dependence of crack velocity for particular values of K or G. A similar trend was observed for Arkansas novaculite by *Atkinson* (1979).

However, crack growth data for quartz and quartz-rich rocks do not display a temperature dependent n-value predicted by *Wiederhorn and Boltz* (1970) equation (2.17). Instead, quartz (*Meredith and Atkinson*, 1982; *Darot and Guéguen*, 1986), Arkansas Novaculite (*Atkinson*, 1979) and Mojave quartzite (*Atkinson*, 1984) exhibit a constant n on a $v-K$ plot. These trends are illustrated in figure 2.9 from *Atkinson* (1984). Only Mojave quartzite displays a trimodal $v-K$ dependence (fig. 2.7) for the range of environmental conditions studied. However, cracks in the impure Tennessee sandstone appear to support higher K in water at 60° than they do at 20°C. This discrepancy could be caused by uncertainties in the testing method (*Atkinson*, 1984; *Atkinson and Meredith*, 1987b) or due to heterogeneities in the test specimen. If there was a threshold crack velocity $v*$ due to dissolution, one might expect this velocity to increase with increasing temperature for quartz rich rocks. This is due to the normal temperature dependence of silica solubility (*Atkinson and Meredith*, 1987a). However, the threshold stress intensity is likely to be independent of temperature (*Krausz*, 1978). To date, there have been no laboratory measurements of a stress corrosion limit in quartz-rich rocks.

Increase in humidity (*Scholz*, 1972; *Atkinson*, 1979) and the partial pressure of water (*Martin*, 1972; *Martin and Durham*, 1975) increases both crack velocities and the value of n, as illustrated in figure 2.9 from *Atkinson and Meredith* (1987a). The subcritical crack growth index n is approximately three times greater in a vacuum (fig. 2.10a) than in water vapour pressure of 300 Pa (fig. 2.10b). This observation is consistent with the general theory of stress corrosion crack growth (*Hillig and Charles*, 1965) and the *Wiederhorn* (1969) equation given by

$$v = v_0' \, l_1 P_w^{l_2} \exp\left(\frac{E^+ - V^+\sigma - \gamma V_m/g}{RT}\right) \tag{2.19}$$

where P_w is the partial pressure of water, E^+ is the stress free activation energy, V^+ is the activation volume, σ is stress, γ is the surface energy of the solid, V_m is the molar volume of the solid, g is the radius of curvature of a crack tip and

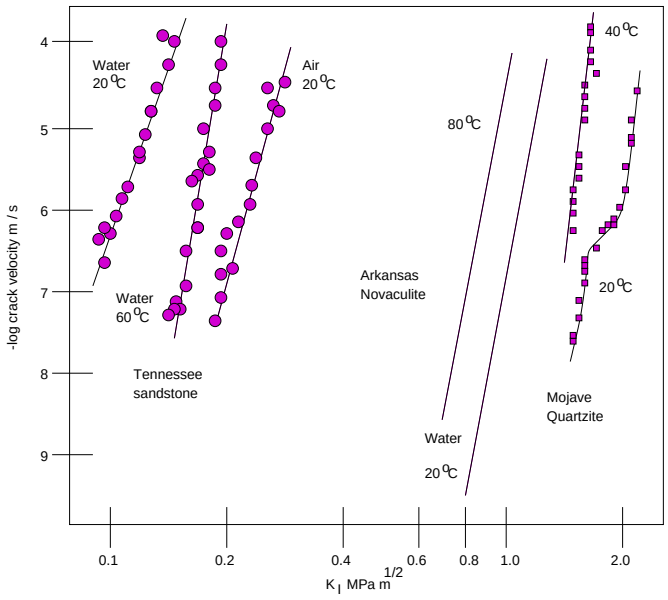

Figure 2.9. A log-log plot of stress intensity factor versus crack velocity for several quartz-rich rocks. Redrawn from *Atkinson* (1984).

l_1 and l_2 are constants. Equation (2.19) is similar to the empirical equations presented by *Martin* (1972) and *Scholz* (1972). An increase in crack velocities with increasing partial pressure of water is also predicted by a recent model by *Dove* (1995) that is based on reaction rate theory. The effect of increasing partial pressure of water is to increase reaction frequency and hence, crack velocity, due to the improved access of water molecules to the reactive crack tip (*Dove*, 1995).

There appears to be some conflicting evidence on the effect of pH on crack propagation rates in quartz. *Atkinson and Meredith* (1981) conducted double torsion tests on quartz in 2 N of HCl and NaOH solutions. In relatively high pH environment quartz was weaker while a low pH environment strengthened quartz with respect to its strength in water. In their tests, weakening of material was interpreted as a decrease in K required to propagate a crack at a particular velocity. Hence, *Atkinson and Meredith* (1981) proposed that the weakening of quartz in a high pH environment is controlled by the chemical composition of the new crack surfaces. The results of *Atkinson and Meredith* (1981) are in good agreement with the observations of *Wiederhorn and Johnson* (1973) for silica glass. However, *Dunning et al.* (1994) have presented some conflicting evidence

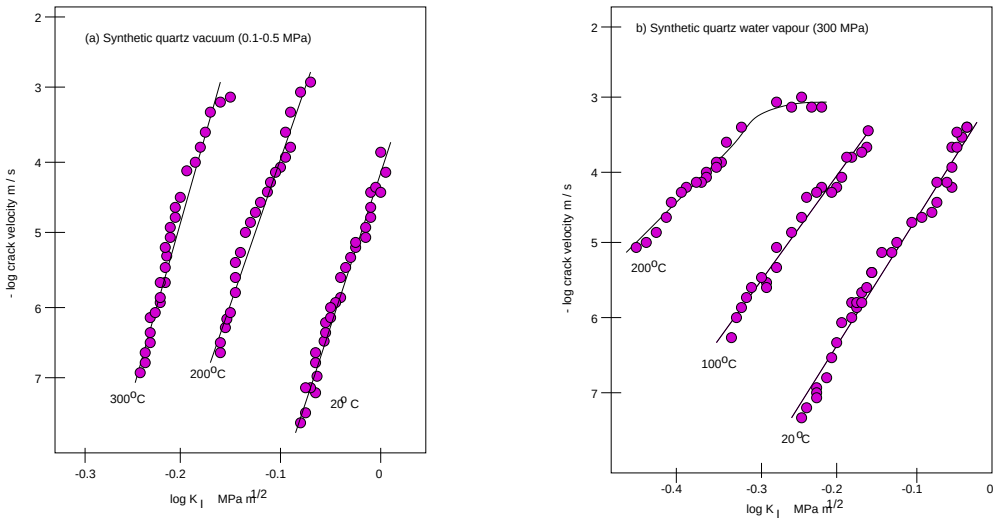

Figure 2.10. Influence of temperature on subcritical tensile crack growth rate in synthetic quartz. Redrawn from *Atkinson and Meredith* (1987a). The data presented here is from *Meredith and Atkinson* (1982).

on the pH dependence of crack growth in quartz. They used a double cantilever beam apparatus, which could explain the differing observations (*Atkinson and Meredith*, 1987b). In the tests of *Dunning et al.* (1994) acidic solutions at pH=2 strengthened quartz relative to its strength in water, while crack growth rates were variable at high pH values. At a high pH of 11.4 the crack growth behaviour was different depending on the particular base used for the test. The dissolution rate of quartz, however, was identical in all of these tests, within the experimental error of 10 ppm. Furthermore, SEM studies of crack flanks did not reveal any evidence of smoothing or blunting of crack tips that might be indicative of dissolution. Hence, *Dunning et al.* (1994) concluded that pH level alone is not a direct indicator of crack growth behaviour in quartz. It is important to note, however, that an experimental error of 10 ppm for Si dissolution represents a high error margin. In the same study, *Dunning et al.* (1994) reported a slight decrease in the strength of quartz in the presence of $AlCl_3$, while the addition of other salts ($NaCl$, $CaCl_2$) did not alter crack growth behaviour appreciably.

While the static fatigue tests of *Martin and Durham* (1975) did not observe any effect of crystallographic orientation on crack growth rates, the majority of crack growth studies on quartz suggest otherwise (*Scholz*, 1972; *Atkinson*, 1979, 1984).

For instance, *Atkinson* (1984) reported higher fracture velocities for a given stress intensity factor in the direction of z when compared to velocities perpendicular to z. This observation can be explained by the smaller bond density N_L in the z-direction with respect to the direction perpendicular to z (*Dove*, 1995). In light of these observations one could expect the fastest subcritical crack growth velocity parallel to any lineations in geological materials (*Anderson and Grew*, 1977).

There are also numerous other variables that could affect crack growth rates, but whose effect on fracture rates in quartz or quartz-rich rocks have not been observed. For instance, one might expect an increase in crack propagation rates associated with a lower viscosity of the pore fluid due to the improved access of fluid to the crack tip (*Anderson and Grew*, 1977). The effect of other environmental variables, such as pressure, on crack growth rates is likely to be more complicated. Pressure can affect a water saturated quartz rock in three ways, namely, by acting upon the stress tensor of the solid, the mechanical properties of the fluid or the chemical reactions between the fluid and the crack (*Anderson and Grew*, 1977; *Atkinson*, 1984; *Atkinson and Meredith*, 1987a). Hence, it is likely that: '*pressure could well increase crack velocity in one situation and decrease it in another*' (*Anderson and Grew*, 1977).

2.3.5 Theoretical models and crack growth constitutive equations

The constitutive models for subcritical crack growth can be broadly subdivided into lattice trapping theories (*Lawn*, 1993), thermodynamic models (*Rice*, 1978, *Darot and Guéguen*, 1986), reaction rate theories (*Charles and Hillig*, 1962) and process zone theories (*Evans and Graham*, 1975, *Meredith and Atkinson*, 1987a). Slow crack growth in a vacuum can be explained by using lattice trapping theories, that relate the crack tip structure to fracture propagation rates (*Meredith and Atkinson*, 1987a; *Lawn*, 1993). In modelling crack growth at a chemically active environment, thermodynamic or reaction rate theories are frequently used.

The classic *Griffith* (1920) theory for fracture does not predict stable crack growth by the stress corrosion mechanism. It cannot explain any kinetic aspects of crack growth nor can it deal with the reversibility of cracks against healing (*Rice*, 1978).

Nevertheless, the Griffith condition can be modified to account for the effect of the test environment on crack propagation rates. In such a model some of the energy required to form a new surface is supplied by chemical reaction and hence any time dependence of the fracturing process can be attributed to chemical reaction rate or to the diffusion of environmental species onto the crack surface (*Anderson and Grew*, 1977). *Rice* (1978) has shown that the requirement for non-negative entropy production leads to the modification of the Griffith fracture criteria to the form

$$(G - 2\gamma)v \geq 0 \tag{2.20}$$

where γ is the surface free energy of the solid and v is the crack velocity. The surface free energy γ equals the energy needed to produce a unit of new surface by a reversible process resulting in an equilibrium surface (*Parks*, 1984):

$$\gamma = \left[\frac{\delta G_e}{\delta A_s}\right]_{p,T} \tag{2.21}$$

where G_e is the Gibbs free energy and A_s is the surface area. Hence, the Griffith criterion $G = 2\gamma$ corresponds to crack growth with no entropy production, which may not be possible in real materials. The thermodynamic surface free energy is likely to be less than the fracture surface energy due to dissipative processes and the failure to achieve true equilibrium surface (*Parks*, 1984).

Experimental studies have demonstrated that hydrogen species that are adsorbed to quartz surfaces can lead to significant reductions in the surface free energy (*Parks*, 1984; *Kronenberg*, 1994). The reduced γ permits crack propagation at a lower stress level (*Dunning et al.*, 1984). This surface energy reduction is described through the Gibbs adsorption equation

$$d\gamma = -\sum_{i=1}^{N} \Gamma_i d\mu_i \tag{2.22}$$

where the sum extend over all interacting species i, μ_i is the chemical potential of species i and Γ_i is the surface concentration of the adsorbed species i (*Darot and Guéguen*, 1986). Hence, in the presence of one interacting species the effective surface energy $\gamma*$ is given by

$$\gamma* = \gamma_0 - \int_{-\infty}^{\mu} \Gamma(\mu) d\mu \tag{2.23}$$

where γ_0 is the surface free energy in a vacuum (*Darot and Guéguen*, 1986). Consequently, in a chemically active environment the requirement of non-negative entropy production rate is given by

$$(G - 2\gamma*)v \geq 0 \tag{2.24}$$

The resulting thermodynamically admissible relations for kinetic crack growth (2.20 and 2.24) are illustrated in figure 2.11. In a chemically inert environment rapid crack growth occurs at $G > 2\gamma$ but fast healing takes place if $G < 2\gamma$ (2.11.a). However, in a chemically reactive environment, kinetic crack growth occurs at $2\gamma* < G < 2\gamma$ and at $G < 2\gamma*$ cracks may heal or remain unchanged. There are no quantitative fracture rate models based on the thermodynamic approach described above (*Dove*, 1995).

There are, however, various quantitative models for stress corrosion that are based on reaction rate theory. Whether or not this phenomenon justifies declaring brittle fracture merely *a special branch of chemical kinetics* (*Krausz and Eyring*, 1975; *Krausz et al.*, 1978) remains questionable. It is more likely that the success of chemical fracture theories relies on their ability to account for majority

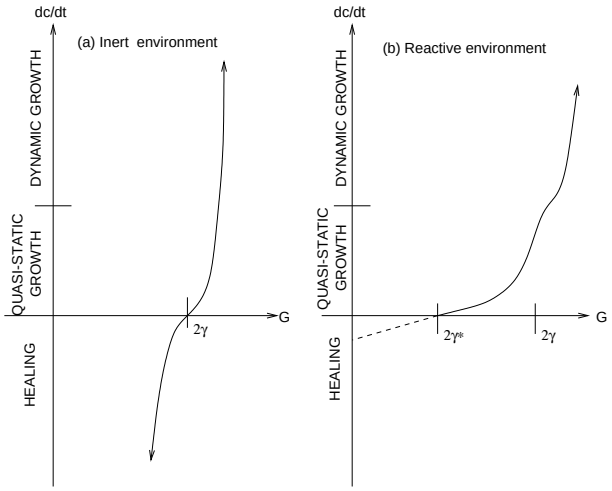

Figure 2.11. Schematic illustration of possible kinetic crack growth scenarios. dc/dt is the crack velocity, G is the crack extension force and γ is the surface free energy. (a) In an inert environment fast crack growth occurs at $G > 2\gamma$ and fast healing takes place if $G < 2\gamma$. (b) In a reactive environment quasi-static crack growth occurs at $2\gamma* < G < 2\gamma$ and at $G < 2\gamma*$ cracks may heal or remain unchanged. Redrawn from *Segall* (1984).

of experimental observations on subcritical crack growth (*Wiederhorn*, 1967; *Wiederhorn and Boltz*, 1970; *Atkinson*, 1982). Some of the earliest models were developed by *Charles* (1958), *Elliott* (1958) and *Charles and Hillig* (1962) in order to explain static fatigue in glass. The *Charles and Hillig* (1962) general theory of stress corrosion was later extended to account for fracture in brittle crystalline solids (*Hillig and Charles*, 1965). The three assumptions implicit in the *Charles and Hillig* (1962) equation are (1) the transport of reactant does not control the reaction rate (2) the reaction between the solid and the fluid depends on the applied stress (3) the activation energy displays an Arrhenius (2.44) type dependence on temperature and it decreases with increasing stress (*Anderson and Grew*, 1977). Their equation is given by

$$v' = v_0' \exp\left(\frac{-E^+ + \sigma V^+ + \gamma V_m/g}{RT}\right) \tag{2.25}$$

where v' is the local corrosion velocity, v'_o is a pre-exponential term, E^+ is a stress-free activation energy, γ is the interfacial surface energy, V_m is the molar volume of the solid, V^+ is the activation volume and g is the radius of curvature of the crack tip. Note that Wiederhorn (1969) obtained his equation (2.19) by simply including a partial pressure term in (2.25). Subsequently, *Wiederhorn and Boltz* (1970) expressed (2.25) by assuming that for a two-dimensional Griffith crack

$$\sigma = \frac{2K_I}{(\pi g)^{1/2}} \tag{2.26}$$

$$E^* = E^+ + \gamma V_m/g \tag{2.27}$$

where E^* is the apparent activation energy (*Anderson and Grew*, 1977). Combining (2.25), (2.26) and (2.27) gives the crack velocity

$$v = v'_0 \exp\left(\frac{-E^* + 2\,V^+ K_I/(\pi g)^{1/2}}{RT}\right) = v'_0 \exp\left(\frac{-E^* + \alpha_1 K}{RT}\right) \tag{2.28}$$

Hence, the *Charles and Hillig* (1962) formula predicts the *Wiederhorn and Boltz* (1970) empirical equation (2.17) assuming that

$$\alpha_1 = \frac{2\,V^+}{(\pi\,g)^{1/2}} \tag{2.29}$$

The *Wiederhorn and Boltz* (1970) equation (2.17) fits a wide range of experimental data and it is therefore considered to be a standard constitutive equation for subcritical crack growth (*Anderson and Grew*, 1977; *Wiederhorn*, 1978; *Atkinson and Meredith*, 1987a).

All of the above theories for subcritical crack growth deal with crack tip processes in a semi-continuum. They operate in a microscopic level and assume linear elastic behaviour (*Meredith and Atkinson*, 1987a). However, crack growth in polycrystalline materials is likely to be greatly influenced by cracks and pores,

grain boundary effects and due to the existence of a process zone. In fact, the extension of a macrocrack may be dominated by the process zone ahead of the crack tip, and not by the specific micromechanism responsible for subcritical crack growth. A comprehensive description of subcritical crack growth in rocks should therefore include both microscopic and macroscopic aspects of crack propagation. It is maybe due to the complexity of the system involving thermally activated microscopic processes at crack tip as well as microstructural properties ahead and behind the crack tip that no such unifying model exists.

2.3.6 Conclusion

Experimental evidence suggest that cracks can propagate at a value of K below K_c. This is termed subcritical crack growth. The dominant micromechanism contributing to slow crack growth in a chemically reactive environment is likely to be stress corrosion. Kinetic crack growth rates are characterised by their extreme sensitivity to applied load and test temperature, humidity, pH and other environmental variables. In particular, the presence of water can lower the stress required to propagate fracture through adsorption of of molecules onto the crack walls. For this reason, stress corrosion crack growth is typically interpreted in terms of models that are based on reaction rate theory. Typically, these models do not consider the formation of distinct corrosion products during crack propagation. This is quite surprising since crack advance creates new surface area and silica dissolution rates depend on the contact area between fluid and the mineral. In the next section I will discuss the process of chemical dissolution in more detail.

2.4 Kinetics of the quartz-water system

2.4.1 Introduction

In the previous section I concentrated on the chemical and mechanical theories for subcritical crack growth by the stress corrosion mechanism. In this section I will describe the additional effect of chemical dissolution that may contribute actively to crack growth. Alternatively, dissolution may occur passively on the newly created crack surface area behind the crack tip. Like cracks, quartz is also ubiquitous in the earth's crust. In pure form it makes up 12 % of the rocks in the crust and in total, silicate minerals comprise 90% of crustal rocks. The central role of silica dissolution in terrestrial weathering was appreciated as early as 1884 (*Dana*, 1884), who published a paper on the 'decay of quartzyte' (*Dove*, 1999). It is now thought that the combination of quartz with water dominates virtually all water-rock systems in the crust. This is the reason why the dissolution properties of silica have received considerable attention in the literature (*Henderson et al.*, 1970; *Kamiya and Shimokata*, 1976; *Rimstidt and Barnes*, 1980; *Brantley et al.*, 1986; *Schwartzentruber et al.*, 1987; *Knauss and Wolery*, 1988; *Brady and Walther*, 1990; *Dove and Crerar*, 1990; *Dove and Elston*, 1992; *Berger et al.*, 1994; *Dove*, 1994; *Tester et al.*, 1994; *O'Day et al.* 1996; *Dove and Nix*, 1997; *Dove*, 1999;*Icenhower and Dove*, 2000; *Gautier et al.*, 2001; *Kay*, 2001;*Carroll et al*, 2002). The results of such solution chemistry experiments are typically interpreted in terms of kinetic or equilibrium models of surface complexation (*Dove*, 1994; *Tester et al.*,1994; *Dove and Nix*, 1997; *Schulz and White*, 1999). In this section I will discuss the dissolution behaviour of unfractured quartz using kinetic and equilibrium formulations, before proceeding to show how such conditions relate to the kinetic crack growth.

2.4.2 General expression for the dissolution and precipitation of silica

The reaction rates between minerals and water are either controlled by the transport of species to or away from the surface or by bond breaking and formation

at the mineral surface. Hence, these reactions can be termed either diffusion or surface controlled (*Lasaga*, 1984). For silica dissolution, the transition from surface to diffusion limited reaction occurs at $300°C$ for geologically reasonable conditions (*Casey*, 1987). At temperatures below $300°C$ the rate limiting step (the slowest step) is the breaking of bonds, because the activation energy E_a for the bond breaking reaction is considerably higher (45.5 kJ/mol) than the E_a for diffusion of aqueous species (20 kJ/mol)(*Lasaga*, 1984; *Dove and Rimstidt*, 1994). Large activation energies suggesting reaction rate control by the bond breaking mechanism have also been observed in experimental studies (see *Dove and Rimstidt*, 1994 for review). However, the reaction rate for bond breaking increases rapidly with temperature. Therefore, at some cross-over temperature material is released into the solution faster than it can diffuse away from the surface. This temperature depends on the system geometry and the fluid flow rate (*Dove and Rimstidt*, 1994).

It is important to know the thermodynamic properties of the system before proceeding to investigate its reaction kinetics. This is why the equilibrium solubility relationship between the mineral phase and the solution forms the basis of the kinetic analysis of silica dissolution and precipitation. The overall forward and reverse reaction of quartz with deionised water is given by

$$SiO_2(s) + 2H_20(l) \leftrightarrow H_4Si0_4(aq) \tag{2.30}$$

where the dissolution and precipitation proceeds by equal rates, in accordance with the transition state theory (*Lasaga*, 1981, 1990; *Dove*, 1999). The dissolution (2.37) and precipitation (2.38) are given by

$$SiO_2 + 2H_2O = (*)^+ = H_4SiO_4 \tag{2.31}$$

$$H_4SiO_4 = (*)^+ = SiO_2 + 2H_2O \tag{2.32}$$

where the species marked by a plus represents the intermediate steps (*Rimstidt and Barnes*, 1980). The particular form of the reactive intermediate $(*)^+$ may

depend on temperature, pressure or solution composition (*Dove and Crerar*, 1990). However, insofar the composition of $(*)^+$ is unknown (*Dove*, 1999).

2.4.3 Theoretical rate equations for dissolution and precipitation of silica

Based on a purely thermodynamic approach, *Rimstidt and Barnes* (1980) derived a rate equation for dissolution (2.34) and precipitation (2.33) of silica given by

$$r_- = \frac{dn_{H_4SiO_4}}{dt} = A_i k_- a_{H_4SiO_4} \tag{2.33}$$

$$r_+ = \frac{dn_{H_4SiO_4}}{dt} = A_i k_+ a_{Si0_2} a^2_{H_20} \tag{2.34}$$

where $dn_{H_4SiO_4}$ is the number of moles of H_4SiO_4, A_i is the interfacial area (m^2), k_+ and k_- are the dissolution and precipitation constants, respectively. In addition, *Rimstidt and Barnes* (1980) quantified the extent of the system through the A_s/M_f ratio, where M_f is the mass of water (in kg) in the reactor. Hence, they included the effect of the measuring system on the measured rates by defining apparent rate constants k'_- (2.35) and k'_+ (2.36) such that

$$k'_- = \frac{A_s}{M_f} \gamma_{H_4Si0_4} k_- \tag{2.35}$$

$$k'_+ = \frac{A_s}{M_f} \gamma_{H_4Si0_4} a_{SiO_2} (a_{H_20})^2 k_+ \tag{2.36}$$

where $\gamma_{H_4Si0_4}$ is the activity coefficient of H_4Si0_4 and a_{SiO_2} and a_{H_20} are the activities of quartz and water, respectively. Hence, they derived a first order expression for quartz dissolution rate r_d in terms of silicic acid release, given by

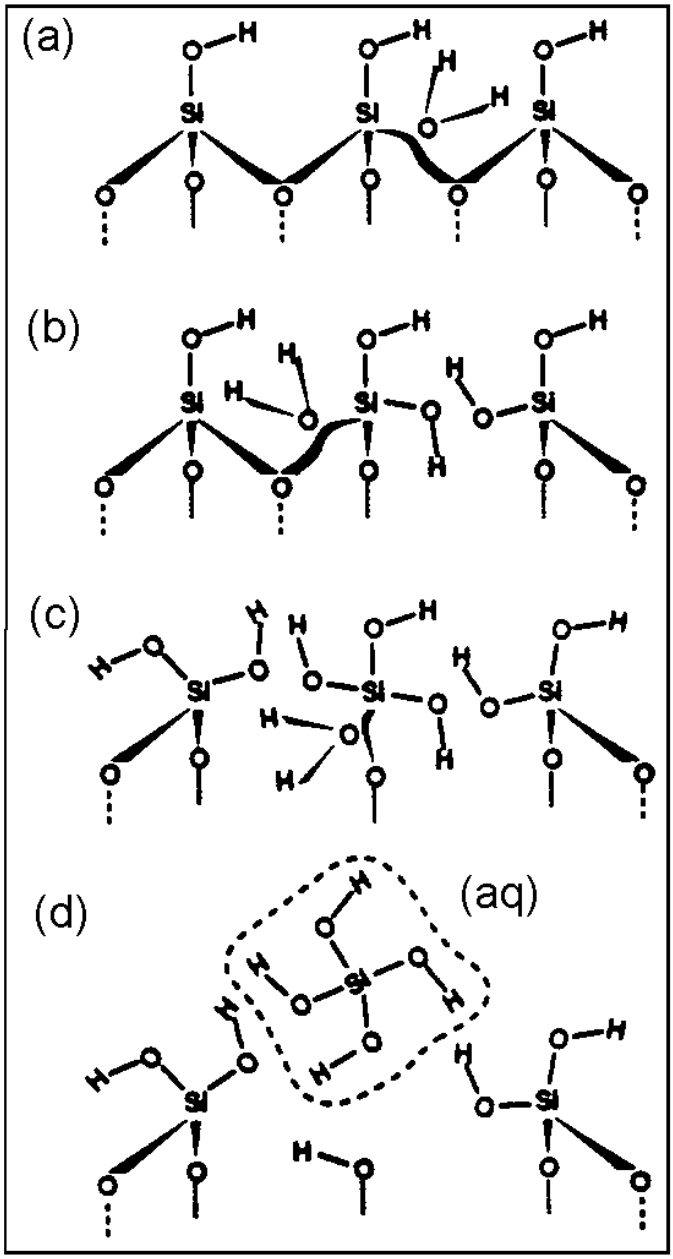

Figure 2.12. Schematic illustration of the dissolution process in deionised water. From *Dove and Crerar* (1990).

$$r_d = k'_+(1 - Q/K_{eq}) \quad (2.37)$$

$$Q = \frac{a_{H_4Si0_4}}{a_{Si0_2}a^2_{H_20}} \quad (2.38)$$

where Q is the activity quotient of the system and K_{eq} is the equilibrium constant.

Alternatively, mineral-water reaction rates can be considered in terms of reactants, i.e. surface site densities and interfacial solvent behaviour. This is the approach taken by *Dove and Rimstidt* (1994), who formulated a kinetic expression for silica dissolution and precipitation reaction rates based on transition state theory TST (*Lasaga*, 1981, 1990). They assumed that the rate limiting step for quartz dissolution is the breaking of Si bonds by H_2O given by

$$> Si - O - Si < + H_2O = (> Si - O - Si < \cdot H_2O)^+ \rightarrow 2(> Si - O - H) \quad (2.39)$$

This rate limiting step is illustrated in figure 2.12 from *Dove and Crerar* (1990), who suggested that the breakage of the first Si-O-Si bond is the most energetic and therefore the rate limiting step. It is important to note that this mechanism (fig. 2.12) differs from that in figure 2.6 by releasing silica into solution. *Dove and Rimstidt* (1994) used the TST formulation of a rate constant that describes the frequency by which an adsorbed water molecule binds to a the silica surface in order to form an activated complex. The apparent rate constant k'_+ is given by

$$k'_+ = \left(\frac{k_bT}{h}\right)\left(\frac{\gamma_a}{\gamma^+}\right)\left(\exp\frac{\Delta S^+}{R}\right)\left(\exp\frac{-\Delta H^+}{RT}\right) \quad (2.40)$$

where $\frac{k_bT}{h}$ is frequency factor, $\frac{\gamma_a}{\gamma^+}$ are the activity coefficients for adsorbed H_2O and intermediate species, ΔS^+ is the standard activation entropy and ΔH^+ is the standard activation enthalpy. In (2.40) the apparent rate constant k_+ is given

in units of s^{-1}. However, in a typical test the BET (Brunauer-Emmett-Teller) surface area (*Brunauer et al.*, 1938) is known and the experimental data gives the dissolution rate per unit surface area. The apparent rate constant k'_+ can be linked to the rate constant k_+ via

$$k_+ = \frac{X_{H_2O} N_a}{(a_{SiO_2})(a_{H_2O})^2} k'_+ \tag{2.41}$$

where X_{H_20} is the mole fraction of sites accessible to water molecules and N_a is the moles of reactive sites on the mineral surface. Substituting (2.40) for k'_+ gives the rate constant for the reaction of water molecules with quartz

$$k_+ = \frac{X_{H_2O} N_a}{(a_{SiO_2})(a_{H_2O})^2} \left(\frac{k_b T}{h}\right) \left(\frac{\gamma_a}{\gamma^+}\right) \left(\exp \frac{\Delta S^+}{R}\right) \left(\exp \frac{-\Delta H^+}{RT}\right) \tag{2.42}$$

where k_+ is the fundamental rate constant and it is given in its usual units of $molm^{-2}s^{-1}$. Since, by definition, the activities of a pure solvent a_{SiO_2} and pure crystalline solid a_{SiO_2} both equal one (*Dove and Rimstidt*, 1994) equation (2.42) can be further simplified to

$$k_+ = X_{H_2O} N_a \left(\frac{k_b T}{h}\right) \left(\frac{\gamma_a}{\gamma^+}\right) \left(\exp \frac{\Delta S^+}{R}\right) \left(\exp \frac{-\Delta H^+}{RT}\right) \tag{2.43}$$

In analysing experimental data, the standard activation enthalpy ΔH^+ can be determined directly from the slope of an Arrhenius plot of $\ln k_+$ versus inverse temperature. The Arrhenius relationship predicts that $\ln k_+$ is a linear function of the inverse temperature $1/T$ and it is given by

$$\ln k_+ = \ln A - \left(\frac{E_a}{R}\right) \left(\frac{1}{T}\right) \tag{2.44}$$

where A is a pre-exponential factor. Hence, by combining (2.43) and (2.44) we get

$$\Delta H^{+} = E_a \tag{2.45}$$

On the other hand, the pre-exponential factor A can be determined from the intercept on an Arrhenius plot. It is composed of the remaining terms in (2.49) so that

$$A = X_{H_2O} N_a \left(\frac{k_b T}{h}\right) \left(\frac{\gamma_{ads}}{\gamma^{+}}\right) \left(\exp \frac{\Delta S^{+}}{R}\right) \tag{2.46}$$

According to the *Dove and Crerar* (1990) model given by (2.43) any increase or decrease in the dissolution rate are isolated within (2.46), since the slope of an Arrhenius plot is constant. Hence, these changes must be attributed to changes in X_{H_2O}, $\left(\frac{\gamma_{ads}}{\gamma^{+}}\right)$, or ΔS^{+}. However, the determination of ΔS^{+} or X_{H_2O} is not straight forward using present experimental techniques. In a recent study, *Schlegel et al.* (2002) observed that the number of adsorbed water molecules equalled the number of reactive sites on pristine quartz crystals. Quantification of the accessibility of H_2O molecules to the reactive sites in a natural rock sample is likely to be a more punishing task.

2.4.4 Previous laboratory studies

The reaction kinetics of the dissolution and precipitation of quartz and other silica polymorphs have been investigated in the laboratory by using a variety of experimental apparatus, including a conventional batch reactor (*Rimstidt and Barnes*, 1980; *Brady and Walther*, 1990), a flow-through reactor (*Franklin et al.* 1994; *Dewers and Hajash*, 1995; *Carroll et al.*, 2002) and a hydrothermal mixed-flow reactor (*Dove and Crerar*, 1990; *Dove*, 1994, 1999, *Gautier et al.*, 2001).

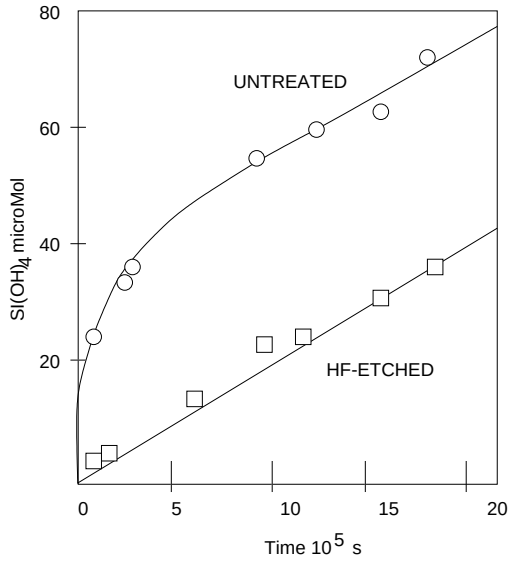

Figure 2.13. The effect of sample preparation on the dissolution behaviour of alkali feldspar. In preparing the sample, the grinding process creates small particles that adhere to the run material. These small particles cause the transient parabolic trend in the untreated sample. The particles can be removed by HF etching, which results in linear behaviour. Redrawn from *Holdren and Berner* (1979).

Recently, *Icenhower and Dove* (2000) combined the use of all these reactor types in one study.

The importance of the water-mineral interface in controlling mineral dissolution was recognised as early as 1956 by *De Vore* (1956). Since then, various surface analysis techniques have been employed in studying the surface features generated by dissolution-precipitation reactions. Some of the more modern techniques that can be used to image surface structures include SEM (e.g. *Dewers and Hajash*, 1995; *Gautier et al.* 2001), in situ X-ray reflectivity, ex-situ atomic force spectroscopy (*Schlegel et al.* 2002) and NMR analysis under magic-angle-spinning conditions (*Carroll et al.* 2002). The aims of these studies have invariably been to quantify the rates for dissolution-precipitation reactions, to pinpoint the different factors that influence silica-water reactions and to image the resulting surface features.

In a typical study a batch of silica powder of known surface area and size fraction is placed in a container of known mass of distilled water. (e.g. *Brady and*

Walther, 1990). Quartz grains are ground to a powder, the size of the grains are determined by sieving and the surface areas are usually measured by using the BET method. During the course of the experiment the mixture of quartz and water is continuously shaken or stirred in order to remove any temperature or concentration gradients. At regular intervals, small samples of the reacted fluid are analysed for the concentration of dissolved silica (Si). Subsequently, Si concentration is plotted as a function of time in order to determine the reaction rate. While early studies observed a parabolic release of silica, suggesting the formation of a leached layer (*Wollast*, 1967), more recent studies have confirmed that any non-linearity in the concentration versus time curve stems from the sample preparation (*Holdren and Berner*, 1979), except at very low pH (*Lasaga*, 1984). Namely, the grinding process produces fine particles that adhere to the surfaces of the run material. The removal of such particles can be accomplished by using specific cleaning methods, such as etching with HF, after which linear kinetics are observed. This effect is illustrated in figure (2.13) from *Holdren and Berner* (1979) that shows the constant release rate of silica obtained after the cleaning procedure. However, exhaustive cleaning has its downside, too. Sample preparation by grinding and cleaning may cause the loss of reactive sites, thus reducing the measured reaction rates (*Holdren and Speyer*, 1987: *Kay*, 2001).

2.4.5 Factors influencing silica dissolution

Early studies of quartz dissolution, such as the famous *Rimstidt and Barnes* (1980) equation (2.44), assumed a first order behaviour in the dissolution rate of quartz. However, this wasn't proven experimentally until fairly recently. *Berger et al.* (1994) studied quartz dissolution rates at 300°C deionised water that contained 1-10 mmol of silica. They found a linear dependence between the solution silica concentration and reaction rate, that is illustrated in fig (2.14a). However, in the presence of small sodium or lead concentrations, the rate law deviated from linearity (b,c) due to the adsorption of both H_4SiO_4 and cations at the silica surface (*Dove and Rimstidt*, 1994).

Table 2.2. presents a compilation of some of the quartz dissolution rates into distilled water that have been observed in previous studies. The discrepancies in the measured dissolution rates are typically attributed to differences in sample

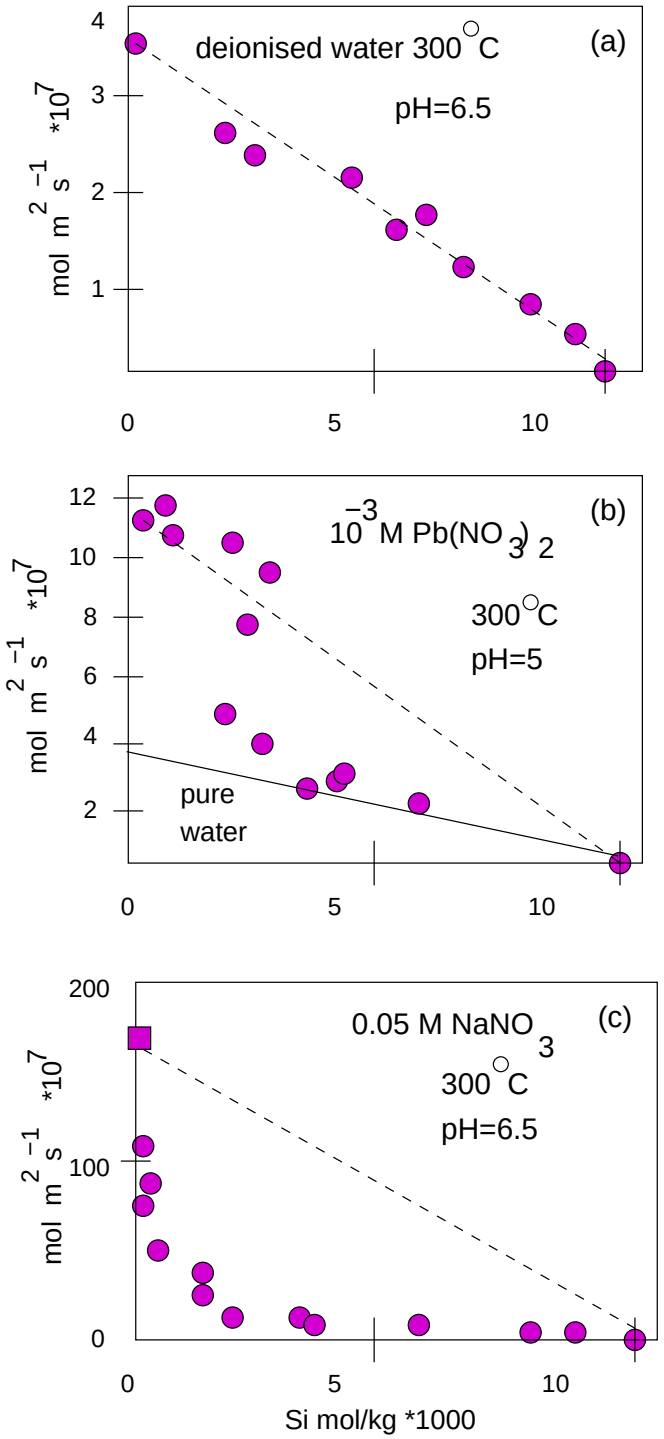

Figure 2.14. Experimentally determined quartz dissolution rates at 300°C solutions of various silica concentrations. Dotted lines are the calculated rates from (2.37). (a) deionised water (b) 10^{-3} molal $Pb(NO_3)_2$ (c) 0.05 molal $NaNO_3$. From *Berger et al.* 1994.

Table 2.2. Some quartz (QTZ) dissolution rates measured in previous studies. (*) This dissolution rate was calculated from the geometric surface area. The corresponding rate for BET surface area for the same experimental run equals $10^{-8.61}$. All of the other studies have normalised their dissolution rates against the BET surface area.

Study	Material	T °C	log rate k_+ $molm^{-2}s^{-1}$
Brady and Walsh (1990)	Arkansas hot spring QTZ	25	-11.90
Icenhower and Dove (1999)	Corning glass (amorphous)	40	-11.36
		60	-10.75
		80	-9.96
Kay (2001)	Clashach SST	25	-10.0
		50	-9.55
		90	-8.61
Franklin et al. (1994)	Brazilian hydrothermal QTZ	100	-9.98
Dove (1999)	Arkansas hot spring QTZ	200	-8.41
Gautier et al. (2001)	Natural QTZ grains	200	-8.61
			-8.26(*)

material, its preparation or due to the experimental apparatus. The starting material can affect the measured rates since the extent of the reactive surface area is likely to depend on crystal history (*Helgeson et al.*, 1984). However, the origin of the quartz grains used in different studies is not commonly specified. If the reactive surface area is considerably different from the BET surface area, run material is likely to have a significant effect on the measured reaction rates.

The effect of sample preparation was investigated by *Dove* (1999), who took extra care to minimise sample contamination. Hence, the measured dissolution rates were consistently lower for the same run material as those of *Dove and Nix* (1997). The apparent reaction rates can also be affected by the type of reactor used in the study. Recently, *Icenhower and Dove* (2000) reported systematically higher dissolution rates for a flow-through reactor when compared to the dissolution rates in a mixed-flow reactor for the same run material. Similarly, *Brady and Walther* (1990) reported consistently higher Si concentrations for the ICP method when compared to simple colorimetry.

Laboratory studies have demonstrated that silica-water reaction rates depend on test temperature (*Brady and Walther*, 1990; *Dove and Crerar*, 1990; *Dove*

Table 2.3. The effect of various environmental variables on silica dissolution rate.

Variable	Effect	Range	Example study
Mechanism	breaking of bonds	T<300°C	Berger et al. (1994)
Temperature	Arrhenius law	T=25-300°C	Dove and Rimstidt (1994)
Alkali cations	rate increase	-	Dove and Crerar (1990)
Trivalent metals	rate decrease	-	Dove and Rimstidt (1994)
Organic acids	rate increase	-	Bennett (1991)
pH	rate increase	$pH > 6$	Brady and Walther (1990)
particle size	solubility increase	-	Rimstidt and Barnes (1980)

and Rimstidt, 1994; *Icenhower and Dove*, 2000), sample surface area (*Rimstidt and Barnes*, 1980; *Holdren and Speyer*, 1987; *Dove and Rimstidt*, 1990; *Gautier et al.*, 2001), the presence of electrolytes (*Dove and Crerar*, 1990; *Dove and Rimstidt*, 1994; *Dove*, 1999), organic acids (*Bennett*, 1991; *Franklin et al.*, 1994) and the solution pH (*Henderson et al.*, 1970; *Knauss and Wolery*, 1988; *Schwartzentruber et al.*, 1987, *Brady and Walther*, 1990; *Dove*, 1994; *Carroll et al.*, 2002). Particle size may also affect reaction rates, since small particles have higher solubility (*Rimstidt and Barnes*, 1980; *Dove and Rimstidt*, 1994). Increase in test temperature or pressure increases reaction rates, while the presence of trivalent metals may inhibit rates. Accelerated reaction rates are also observed in the presence of organic acids or alkali cations. The effect of various environmental variables on dissolution rates are summarised in table 2.3.

Quartz dissolution rates increase with increasing temperature (table 2.2.). A compilation of the measured dissolution rates as a function of temperature is presented in figure (2.15) from *Dove and Rimstidt* (1994). These data suggest that at temperatures from 25-300 °C quartz dissolution rates are described by an exponential Arrhenius type dependence (2.44) on temperature. Both BET and geometric surface areas can be used to estimate the reaction rates. Such temperature dependence allowed *Rimstidt and Barnes* (1980) to derive empirical expressions for the dissolution of quartz (2.47) and the precipitation of all quartz phases (2.48) given by

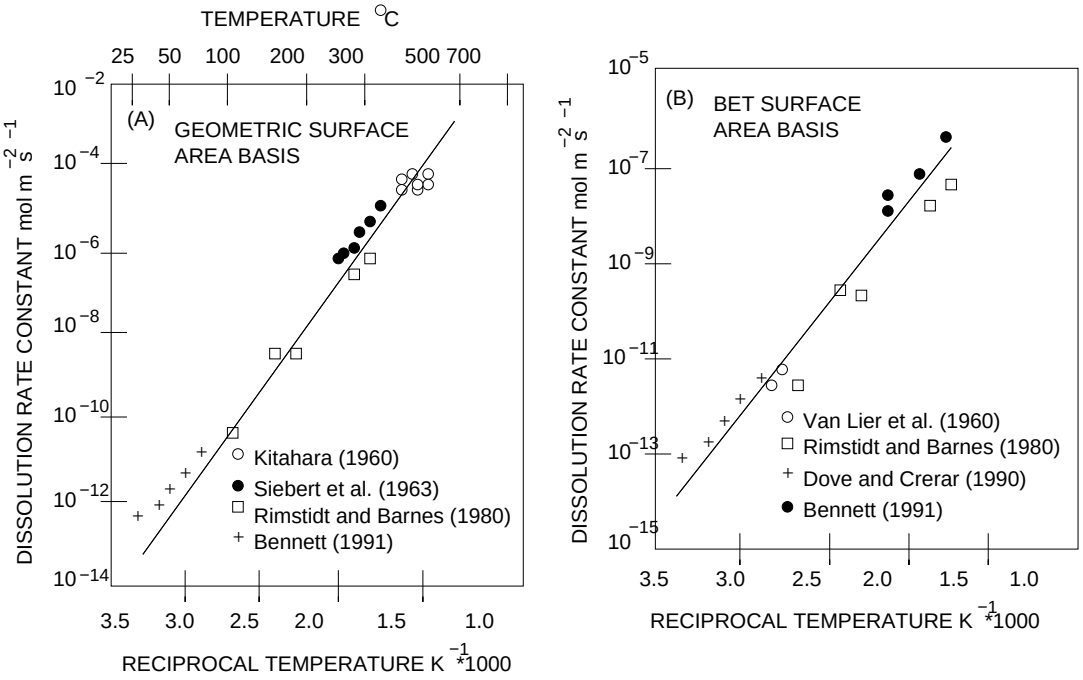

Figure 2.15. Quartz dissolution rates in pure water from 25°C to 300°C. Either (a) geometric surface area or (b) BET surface area can be used in the rate calculation. From *Tester et al.* (1994)

$$\log k_{+(quartz)} = 1.174 - 2.2028 \times 10^{-3}T - 4158/T \quad (2.47)$$

$$\log k_{-(all\,phases)} = -0.707 - 2598/T \quad (2.48)$$

where the rate constants k_+ (s^{-1}) and k_- (s^{-1}) are given as a function of temperature T (K). It is due to this temperature dependence that quartz dissolution becomes more important at T=70-100°C which corresponds to 2-3 km depth (*Bjørlykke*, 1999).

The dissolution rates of quartz also display a positive pressure dependence. In purely thermodynamic terms, the effect of increasing pressure is to increase quartz solubility. Figure (2.15) from *Dove and Rimstidt* (1994) that was calculated based on the quartz solubility equation of *Fournier and Potter* (1982) illustrates this effect. Increasing pressure increases water density thus resulting in crowding of

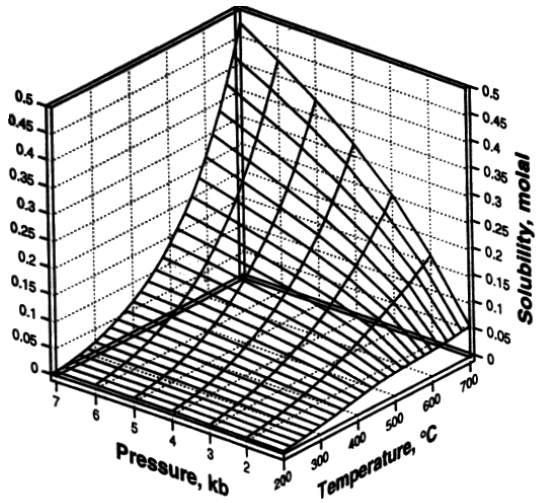

Figure 2.16. The solubility of quartz as a function of temperature and pressure calculated from the *Fournier and Potter* (1982) formula. From *Dove and Rimstidt* (1994).

water molecules close to the OH groups. Consequently, the number of encounters between H_4SiO_4 and H_2O increases, which enhances quartz solubility.

The presence of alkali cations markedly increases quartz dissolution rates above that measured in pure water (*Kamiya and Shimokata*, 1976; *Dove and Crerar*,1990; *Dove and Nix*, 1997; *Dove*, 1999). This is an important observation since the compositions of natural waters are dominated by low concentrations of cations such as sodium (Na), calcium (Ca), magnesium (Mg) and potassium (K) (*Berner and Berner*, 1996; *Miretzky et al.*, 2001). In previous studies, both sodium and potassium (*Dove and Crerar*, 1990; *Bennett*, 1991) as well as magnesium and calcium (*Dove and Nix*, 1997) have been observed to increase quartz dissolution rates. However, this rate enhancing effect decreases with decreasing temperature. At low temperatures of 25-70 °C low concentrations of sodium or potassium increase dissolution rates only by a factor of 5 to 8 (*Bennett*, 1991; *Dove and Crerar*, 1994), while the rate-enhancing effect may be as high as a factor of 40 to 100 in hydrothermal conditions (*Dove and Nix*, 1997; *Dove*, 1999). At near neutral pH this rate-enhancing trend is also cation dependent in the order of pure water$< Mg^{2+} < Ca^{2+} \approx Li^{+} \approx Na^{+} \approx K^{+} < Ba^{2+}$ (*Dove and Nix*, 1997). Recently, *Dove* (1999) carried out a study of quartz dissolution in

the presence of a variety of dissolved cations ($Mg^{2+}, Ca^{2+}, Ba^{2+}$and Na^{+}). They observed that the dissolution rates were a nonlinear function of the cation concentrations in solution and these rates were limited by the cation with the smallest rate-enhancing effect. For instance, small concentrations of magnesium were observed to limit the overall dissolution rate in a manner that was disproportionate to its bulk concentration. Hence, *Dove* (1999) developed a model that suggests the dominance of Mg^{2+} and Ca^{2+} in regulating quartz dissolution rates despite their low concentrations in natural waters. Since the experimentally determined activation energies are of similar magnitude in pure water and in the presence of alkali cations, the rate increase may be attributed to the number of sorbed cations on the Si-O surface structures (*Dove*, 1999).

In contrast, the presence of trivalent metals such as aluminium (Al^{3+}) and iron (Fe^{3+}) may actually decrease quartz dissolution rates. For instance, aluminium can decrease quartz dissolution rates by three to eight orders of magnitude (*Hurd*, 1973; *Dove*, 1994). To date there have been no studies on the combined effect of the rate-enhancing alkali cations and rate-inhibiting trivalent metals on quartz dissolution rates. It would be interesting to know whether these two effects might cancel out in solution chemistries relevant to earth environments.

There appears to be some conflicting evidence on the effect of pH on quartz dissolution rates. Some workers (*Brady and Walther*, 1990; *Dove and Rimstidt*, 1994) have reported a dissolution rate minimum near the zero point of net proton charge, which corresponds to $pH = 2$ for quartz. Dissolution rates increase for solutions that are more acidic or basic than this minimum. Other workers (*Knauss and Wolery*, 1988; *Carroll et al.*, 2001) have observed pH independent dissolution below pH=6. At higher pH values, dissolution rates increased with decreasing acidity. Empirical equations relating test temperature and pH to the measured reaction rates have been presented by *Dove* (1994) and *Carroll et al.* (2002).

In general, an increase in surface area per unit volume leads to an increase in the reaction rate. Since experimental techniques vary, most reaction rates are normalised to the BET surface area of the run material. Hence, in calculating Si dissolution rates a direct proportionality between reaction rates and BET surface area is assumed (*Rimstidt and Barnes*, 1980; *Schott et al.*, 1981; *Brady and Walther*, 1990; *Dove and Crerar*, 1990; *Berger et al.*, 1994; *Dove*, 1999, *Yokoyama and Banfield*, 2002). Furthermore, *Dove and Rimstidt* (1994) showed that both

geometric and BET surface areas can be used equally well in calculating quartz dissolution rates (figure 2.16). However, other workers have criticised the ongoing habit of normalising dissolution rates against BET surface area (*Grandstaff*, 1978; *Holdren and Speyer*, 1987; *Gautier et al.*, 2001). In fact, the reactive surface area may be considerably different from the total surface area due to non-uniform distribution of high energy sites such as defects. Assuming preferential dissolution at high energy sites, differences in dislocation densities can be used to explain the variability in the measured Si dissolution rates (table 2.2). However, the degree of non-uniformity in the density of defect sites on quartz surfaces remains questionable. Early studies (*Lasaga and Blum*, 1986; *Blum et al.*, 1988) suggested that the effect of dislocation density on quartz dissolution rates is very small. However, the formation of etch pits (negative crystals) and the rounding of grains are the most common morphological changes resulting from dissolution: both phenomena suggest preferential dissolution from high energy sites (*Dove and Rimstidt*, 1994; *Lee et al.*, 1998; *Gautier et al.*, 2001; *Tuncay et al.*, 2002). A typical etch pit formed during a quartz dissolution experiment is illustrated in figure 2.17 from *Gautier et al.* (2001). In their tests the mass normalised dissolution rates varied only within a factor of 1.27 while the BET surface areas increased by a factor of 5.6, as illustrated in figure 2.18. They proposed that the walls of an etch pit remain unreactive throughout a typical test and hence contribute negligibly to the measured dissolution rates. However, the geometric surface areas were consistently proportional to the mass normalised dissolution rates. Hence, the results of *Gautier et al.* (2001) cast doubt on the validity of any study that is based on BET surface area. Geometric surface areas have also been successful in predicting dissolution rates from sandstone cores (*Kieffer et al.*, 1999).

2.4.6 Are laboratory rates representative of real weathering rates?

Weathering of mineral assemblages by the chemical action of aqueous species is one of the most important processes that affect the surface of the earth (*Kirby*, 1984; *Lasaga*, 1984; *Kronenberg et al.*, 1994). Knowledge of chemical weathering rates is required for modelling geochemical cycling of elements as well as in

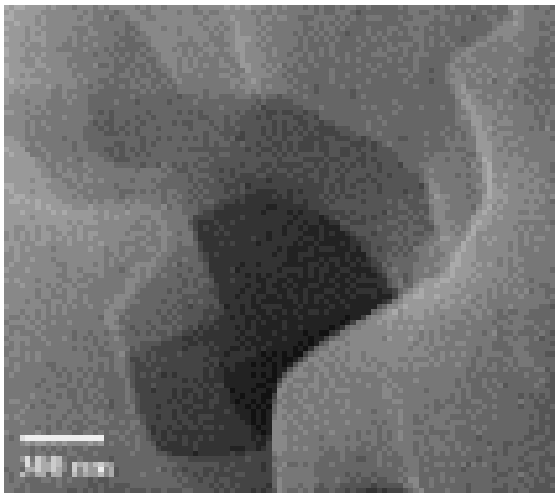

Figure 2.17. A polyhedral etch pit on a quartz grain. The scale bar is 300 nm. From *Gautier et al.* (2001).

estimating the durability of materials, both natural and synthetic (*Yokoyama and Banfield*, 2002). Since the release of ions determines the composition of natural waters, weathering rates are also linked to the global atmosphere interactions, and hence to the global climate (*Berner*, 1995). Yet, field estimates of mineral dissolution rates are typically five times less than the measured laboratory rates (*White and Brantley*, 1995). For instance, *Yokoyama and Banfield* (2002) reported three orders of magnitude difference in the Si release rate from crushed rhyolite powder and a field site of the same volcanic rocks. These observations suggest that the laboratory dissolution rates from crushed rock do not represent weathering from a real rock.

The discrepancies in laboratory and field rates are typically attributed to differences in the surface condition of minerals, in estimating the surface area, solution chemistry, temperatures or due to the heterogeneous distribution of water in the field (*White and Brantley*, 1995). Laboratory studies of silica dissolution are frequently carried out using distilled water, although it is well known that the presence of electrolytes increases Si dissolution rates and induces non-linearity in the form of the rate law (*Dove and Crerar*, 1990; *Berger et al.*, 1994; *Dove and Rimstidt*, 1994; *Dove*, 1999). Natural waters, in turn, may contain up to 50 % by weight of dissolved solids (*Rose and Burt*, 1979; *Miretzky et al.*, 2001), including cations or organic acids that are known to increase Si dissolution rates (*Dove*

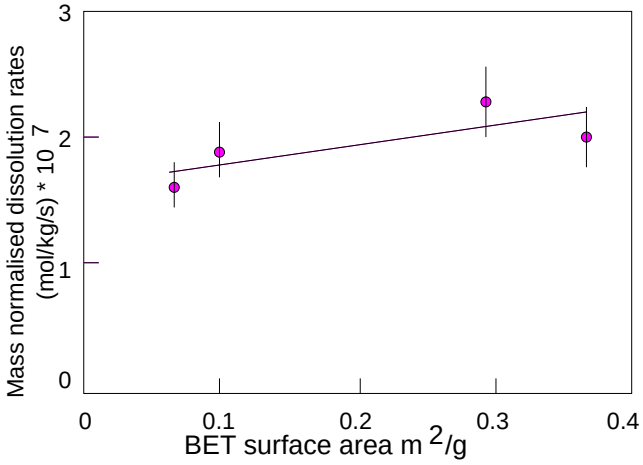

Figure 2.18. The measured mass normalised dissolution rate at deionised water at 200 °C a function of B.E.T. surface area. From *Gautier et al.* (2001)

and Crerar, 1990). On the other hand, surface waters may also contain trivalent metals that may inhibit dissolution rates (*Dove and Rimstidt*, 1994). However, the combined effect of rate-enhancing cations, organic acids and rate inhibiting metals on quartz dissolution rates remains unknown.

Since quartz dissolution experiments are typically carried out using grains of known size fraction, most laboratory samples are freshly ground materials with no previous exposure to surface waters. The surface conditions of natural materials are quite different, since they have been exposed to weathering for millions of years. If sites of high energy are the loci for attack during weathering, these sites are likely to dominate the measured dissolution rates in the laboratory. However, it is possible that such high energy sites have largely weathered away from natural rock surface, thus leaving behind more stable host crystals. This might explain why laboratory dissolution rates are typically higher than the field estimates. Hence, laboratory rate estimates should be treated as upper limits for the individual minerals being investigated (*Yokoyama and Banfield*, 2002). There does not appear to be any clear consensus of the main cause of the disparity in the laboratory and field rates. Instead, '*...differences between lab and field reaction rates [of silica] may be attributable to presently unrecognised geochemical controls*' (*Dove and Rimstidt*, 1994). Clearly, more work is required to investigate this effect.

2.4.7 Conclusion

The system involving silica (in the form of quartz or silicate minerals) and water is likely to dominate fluid-rock interactions in the crust. Hence, both theoretical modelling and experimental investigation of the dissolution-precipitation reactions in the quartz-water system is well documented. Theoretical modelling of silica dissolution can be carried out from a purely thermodynamical point of view or in terms of reaction kinetics. These models have highlighted the importance of surface area, temperature and accessibility of water in controlling silica reactivity. Both theoretical models and experimental observations have suggested that, during crack propagation, bond breaking is the rate limiting step controlling silica dissolution at low temperatures. Previous laboratory experiments have also demonstrated the dependence of quartz reaction rate on temperature, surface area, the presence of electrolytes, organic acids, solution pH and particle size. However, the measured Si dissolution rates reported in different studies are quite variable due to differences in sample material, its preparation or the particular surface area that is used for the rate calculation. In fact, geometric surface area may approximate the actual reactive surface area better than BET surface area. This observation invalidates most quartz dissolution rates that appear in the literature. Furthermore, due to differences in dislocation densities, solution chemistry or the availability of water laboratory rates do not correspond directly to dissolution from a real rock.

2.5 Stress corrosion by active dissolution

In a chemically reactive environment the dominant micromechanism responsible for slow fracture growth in rocks is either stress corrosion or dissolution. In fact, some authors do not differentiate between these two mechanisms, but suggest that for *true stress corrosion* the rate of crack tip advance equals the rate of dissolution (*Dunning et al.*, 1994). It is questionable, however, whether *true stress corrosion* takes place in any geologically reasonable situation (*Darot and Guéguen*, 1986; *Dunning et al.*, 1994). One might expect that the fracture growth in quartz proceeds faster than Si dissolution rate due to the low solubility of quartz in water at the temperatures of the upper crust ($T < 80 - 100°C$). True stress corrosion

is more likely to occur in a system that consist of high solubility minerals, such as calcite (*Atkinson and Meredith*, 1987a).

In purely mechanistic terms subcritical crack growth approximates dissolution since both processes involve the relatively slow fracturing of chemical bonds (*Atkinson and Meredith*, 1987a; *Dove*, 1995). This kind of kinetic crack growth cannot be explained adequately by using conventional fracture mechanics parameters. Stress corrosion crack growth in glasses, ceramics and rock has been traditionally interpreted in terms of constitutive models that are based on reaction rate theory (*Orowan*, 1944; *Charles and Hillig*, 1962; *Wiederhorn and Boltz*, 1970, *Krausz and Eyring*, 1975; *Anderson and Grew*, 1977; *Atkinson and Meredith*, 1987a). It is easier to derive the reaction rate constants from experimental data than to pin down the precise microscopic mechanism responsible for subcritical crack growth. Previous deformation studies and chemical solution experiments also highlight the similarity of the dissolution reactions to slow fracture growth. In the quartz-water system, both fracture and dissolution rates exhibit a marked dependence on test temperature, pressure, solution pH, crystallographic orientation and the presence of electrolytes.

Recently, *Dove* (1995) developed a quantitative model for subcritical crack growth that can explain a number of experimental observations regarding the dependence of fracture rates on the chemical environment. Her model is based on the theory of chemical kinetics and the transition state formulation of an apparent rate constant k'_+ given by

$$k'_+ = \frac{k_b T}{h} \left(\frac{\gamma_a}{\gamma^+} \right) \left(\frac{\Delta - G^+}{RT} \right) \tag{2.49}$$

where $\frac{k_b T}{h}$ is the natural lattice frequency, k_b is the the Boltzmann constant, h is the Planck constant, γ_a and γ^+ are the activity coefficients for the adsorbed and the intermediate species, respectively, ΔG^+ is the standard Gibbs free energy for activation, R is the universal gas constant, and T is temperature. It is assumed that (2.49) controls both silica dissolution and crack growth rate. In order to relate the microscopic dissolution rate to the macroscopic crack growth velocity, (2.49) can be rewritten in terms of the fraction of reactive sites at the crack tip

X_{H_2O} accessible to water molecules and the length of each crack increment N_L to give the crack velocity v

$$v = X_{H_2O}\, N_L\, k'_+ = X_{H_2O}\, N_L\, \frac{k_b\, T}{h} \left(\frac{\gamma_a}{\gamma^+}\right) \left(\frac{\Delta - G^+}{RT}\right) \tag{2.50}$$

Since k'_+ has units of (1/s) and N_L is the distance between Si-0-Si bridging bonds in metres, (2.50) gives the crack velocity in (m/s). Equation (2.50) assumes that the crack velocity is directly proportional to the reaction rate, which depends on $\Delta\, G^+$ and the accessibility of water to the reactive sites. It is therefore very similar to the *Charles and Hillig* (1962), *Scholz* (1972) and *Freiman* (1984) kinetic formulae for crack propagation. Furthermore, $\Delta\, G^+$ can be expressed as

$$\Delta\, G^+ = \Delta\, H^+ + P_c\, \Delta V - T\, \Delta S^+ = \Delta\, H^+ - T\, \Delta S^+ - \frac{K_I\, \Delta\, V}{(\pi\, d_c)^{1/2}} \tag{2.51}$$

where $P_c = -K_I\, (\pi\, d_c)^{-1/2}$ is the pressure at the crack tip, $\Delta\, H^+$ is the standard activation enthalpy, $\Delta\, S^+$ is the standard activation entropy and $\Delta\, V$ is the volume change (*Wiederhorn et al.*, 1980, *Dove*, 1995). Furthermore, α_3 can be defined as

$$\alpha_3 = (\pi\, d_c)^{-1/2}\, \Delta V \tag{2.52}$$

Hence, combining (2.50), (2.51) and (2.52) gives

$$v = X_{H_2O}\, N_L\, \frac{k_b\, T}{h} \left(\frac{\gamma_a}{\gamma^+}\right) \exp\left(\frac{\Delta\, S^+}{R}\right) \exp\left(\frac{-\Delta\, H^+ + \alpha_3\, K_I}{RT}\right) \tag{2.53}$$

which is yet another way to express the *Wiederhorn and Boltz* (1970) empirical equation (2.17) assuming that $\Delta H^+ \propto E^*$ and

$$v_0' = X_{H_2O}\, N_L\, \frac{k_b T}{h} \left(\frac{\gamma_a}{\gamma^+}\right) \exp\left(\frac{\Delta S^+}{R}\right) \tag{2.54}$$

Equation (2.53) assumes that the rate limiting step for fracture and silica dissolution is the reaction of the Si-O-Si bond with molecular water. However, at high pH environments both fracture (*Charles*, 1958; *Atkinson*, 1979; *Atkinson and Meredith*, 1981) and Si dissolution are governed by breaking of bonds due to chemical reaction involving ionised water. Hence, the overall fracture or dissolution rate at any pH environment is likely to be determined by both water and hydroxide ion promoted mechanisms (*Charles*, 1958; *Dove*, 1994; 1995). Furthermore, this model can can account for the dependence of crack velocity on humidity, temperature, pH, crystallographic orientation and the presence of salts.

2.6 Summary

Conventional fracture mechanics predicts that a crack will propagate once a critical stress intensity factor K_c has been attained at the crack tip. Such critical condition results in dynamic crack growth at a velocity that equals the Rayleigh wave velocity in the medium. However, in a chemically active environment cracks may propagate at a value of K below K_c. This kind of crack propagation is termed subcritical crack growth. It is characteristically slow and quasi-static. In the presence of water the most likely mechanism for subcritical crack growth is stress corrosion. It occurs due to the chemical weakening of the strained crack tip bonds.

Experimental observations demonstrate that stress corrosion crack growth depends on humidity, temperature pH and the presence of salts. The passive dissolution of silica also exhibits a similar dependence on environmental parameters. This is perhaps not so surprising since the growth of cracks increases both fresh and total surface area for silica dissolution. Hence, one might expect that silica could be dissolving actively from the growing crack tips or passively from the crack walls behind the tip. In fact, a recent model by *Dove* (1995) suggests that both

silica dissolution and crack growth rate are governed by the same rate constant. *Dove's* model considers silica release as an essential part of the stress corrosion fracture process.

The motive for this study is to investigate whether the growth of a crack population in a chemically active environment is associated with a clear geochemical signal. In the next section I will explain the methodology that I used to tackle this problem.

Chapter 3

Methodology

This turkey found that, on his first morning at the turkey farm, he was fed at 9 a.m. However, being a good inductivist, he did not jump to conclusions. He waited until he had collected a large number of observations ... and he made these observations under a wide variety of circumstances, on Wednesdays and Thursdays ... Finally his inductivist conscience was satisfied and he carried out an inductive inference to conclude: 'I am always fed at 9 a.m.'. Alas, this conclusion was shown to be false in no uncertain manner when, on Christmas eve, instead of being fed, he had his throat cut.
A. Chalmers (1982) elaborating on the famous story of B. Russell

3.1 Introduction

In the previous chapter I considered some of the experimental results of slow crack growth in quartz that were obtained by using a double torsion type test apparatus. Such testing configuration has the advantage that both v and K can be determined for a single mode I crack. However, it is well known that macroscopic fracture of real rocks is preceded by the growth of several microcracks (*Mogi*, 1962; *Scholz*, 1968a,c; *Tapponier and Brace*, 1976). Furthermore, the brittle deformation properties of rocks are characterised by their notable dependence on deformation rate (*Serdengecti and Boozer*, 1961; *Sangha and Dhir*, 1972; *Lankford*, 1981; *Sano et al.*, 1981, 1982), temperature (*Serdengecti and Boozer*, 1961) and test environment (*Sano et al.*, 1981; *Masuda*, 2001). At low homologous temperatures ($T < T_m$) and in the presence of a chemically active environment

the main mechanism for time-, rate and environment dependent deformation in crystalline rocks is stress corrosion crack growth (*Costin*, 1987). Hence, the study of time and environment properties of brittle deformation provides an alternative way to investigate stress corrosion crack growth in rocks. Time dependent aspects of rock deformation can be studied in the laboratory by carrying out a series of constant stress (creep) or constant strain rate tests (*Jaeger and Cook*, 1976). In this study constant strain rate tests were used to simulate *in-situ* conditions. Furthermore, the overburden stress was assumed to be compressive, consisting of three principal stresses.

3.2 The triaxial test

There are three main reasons for investigating the mechanical properties of rocks under a triaxial stress state. Firstly, triaxial stress is considered to be the best way to simulate the stress imposed by the overlying rocks. A triaxial test involves a homogeneous distribution of stresses and thus the interpretation of the test results is relatively easy. Perhaps the most important reason is that rock failure is greatly influenced by both normal and shear stress components. It is therefore not surprising that the mechanical properties of rocks are typically studied under compressive regime with non-zero minimum, intermediate and maximum stresses, σ_3, σ_2, and σ_1, respectively (*Jaeger and Cook*, 1976; *Paterson*, 1978). This is also the approach taken in my study.

Figure 3.1 illustrates the stress system in a typical triaxial test. Compressive stresses σ_1, σ_2 and σ_3 are defined to be positive, as it is customary to do in both geological and rock mechanics literature. The intermediate stress is always equal to one of the principal stresses and hence the *conventional triaxial test* depicted in in figure 3.1 is not actually a true triaxial, but an axisymmetric triaxial test. A test in which all three principal stresses are varied is termed a *a true triaxial test* (*Paterson*, 1978) in order to distinguish it from a conventional triaxial test. Although highly desirable, it is notoriously difficult to achieve a *true triaxial* stress state in laboratory conditions and therefore conventional triaxial tests are still widely used in rock mechanics testing (*Paterson*, 1978; *Jaeger and Cook*, 1976). Had a true triaxial stress state been used for my tests, one could expect

the failure plane to be oriented parallel to σ_2 (*Paterson*, 1978; *Crawford et al.*, 1995). It has also been reported that increasing σ_2 has a strengthening effect on both Locharbriggs and Clashach sandstone (*Main et al.*, 1994; *Crawford et al.*, 1995) as well as on other rock types (*Chang and Haimson*, 2000; *Haimson and Chang*, 2000, 2001).

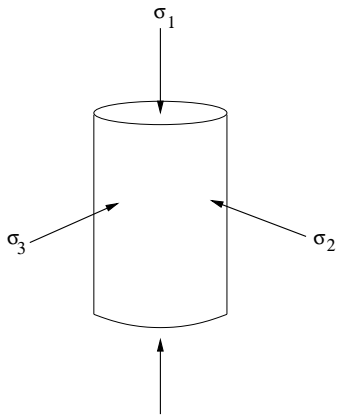

Figure 3.1. The stress system in a triaxial test. σ_3 is the confining pressures. In the conventional triaxial test $\sigma_3 = \sigma_2 < \sigma_1$. Redrawn from Paterson (1978).

3.3 Test Materials

3.3.1 Lithologies

The experiments were carried out on two Permian aeolian sandstones. Both of these sandstones were chosen for this study because of their simple mineralogy and their relative homogeneity in the core scale. Their mechanical and hydraulic behaviour have also been well characterised in previous studies (*Crawford et al.*, 1995; *Ngwenya et al.*, 1995, *Mair*, 1997; *Crawford*, 1998; *Main et al.*, 2000; *Mair et al.*, 2000; *Ngwenya et al.*, 2000, 2003). An extensive mineralogical characterisation of both of these sandstones has been carried out by *Crawford et al.* (1995) by using a combination of X-ray diffraction, polarised light microscopy and electron microscopy. Some of their observations are summarised in table 3.1.

Table 3.1. Some characteristics of the two Scottish sandstones that were used for this study. From *Crawford et al.* (1995)

Rock type	Source	Age	Lithology	Mineralogy	ϕ_T	ϕ_I
Clashach sandstone	Elgin, Scotland	Permian	Pale-fawn medium-coarse grained well-sorted arenite	89% quartz 11% K-feldspar	16%	10%
Locharbriggs sandstone	Dumfries, Scotland	Permian	Red medium-coarse grained	86% quartz 13%feldspar 1 % hematite	22%	16%

The Clashach specimen were sourced from a commercial quarry near Hopeman village in the Elgin area of NE Scotland. Stratigraphically this rock belongs to the Hopeman sandstone, which outcrops in Permo-triassic aeolian outliers on the shores of the Moray Firth basin (*Lovell*, 1983; *Crawford*,1998). Because of its simple mineralogy and reasonable homogeneity at the core plug scale it is widely used within the UK scientific community as the nearest equivalent to Berea sandstone (*Crawford et al.*, 1995; *Ngwenya et al.*, 1995; *Crawford*, 1998). It can also be considered as a good analogue for a North Sea reservoir rock since it has offshore equivalents in the form of the finer grained Smithbank formation of the Inner Moray Firth (*Fisher and Mudge*, 1990; *Ngwenya et al.*, 1995). It is a pale-fawn, well-sorted, medium to coarse grained (0.5-1mm) subarkosic arenite(*Crawford et al*, 1995; *Ngwenya et al.*, 1995). It is composed of sub-rounded quartz grains (90%) and fresh to altered K-feldspar (10%). Some trace amounts of muscovite, apatite, zircon (*Liakopoulou-Morris et al.*, 1994), dolomite and kaolinite (*Ngwenya et al.*, 1995) have also been reported. The Clashach samples are characterised by pervasive cementation due to secondary quartz overgrowths.

Fresh blocks of Locharbriggs sandstone were obtained from a working quarry in Dumfries, SW Scotland. This sandstone is analogous to the Penrith sandstone studied by *Fowles and Burley* (1994). Locharbriggs sandstone is reddish brown and it consists of sub-rounded quartz (83%), feldspar (16%), hematite (1%) and minor amounts of illite (*Crawford et al.*, 1995). It has a mean grain size of 100 μm. Locharbriggs sandstone is relatively weakly cemented with a diagenetic assemblage that is characterised by hematite and illite coatings on quartz surfaces. Both Clashach and Locharbriggs sandstones are widely used as a building stone

in the UK because of their excellent weathering properties. In particular, the Museum of Scotland and the Balmoral hotel in Edinburgh are made out of Clashach and Locharbriggs sandstones, respectively.

3.3.2 Preparation of the test specimen

Cylindrical samples measuring approximately 80 mm in length and 38 mm in diameter were cut from fresh sandstone blocks by using a diamond coring drill. The Clashach block did not show any clear fabric and thus the rock cores were drilled at two directions perpendicular to each other. In contrast, the block obtained from the Locharbriggs quarry had a distinct lamination that was oriented parallel to one of the block faces. Hence, for the Locharbriggs sandstone oriented cores were drilled at three perpendicular directions. The specimen ends were ground parallel and flat to produce precise right-angled cylinders. The length to diameter ratio was over 2:1 and hence in the recommended range for rock mechanics testing (*Paterson*, 1978). For instance, a homogeneous distribution of stresses can no longer be assumed if the length to diameter ratio is around one. The diameter of the test specimen was exactly the same as the platen diameter in order to minimise end effects (*Paterson*, 1978).

3.3.3 Sample characterisation

Three measurements of sample diameter and length were used to estimate the exact dimensions of each test specimen. Subsequently, the initial porosities of each specimen were estimated using two different techniques: the density and the Archimedes method. The density method allows the estimation of the total porosity ϕ_T from the difference between bulk density ρ_b and the average density of the solid constituents ρ_s (*Guéguen and Palcianskas*, 1994). The total porosity is given by

$$\phi_T = 1 - \rho_b/\rho_s \tag{3.1}$$

For example, a 3.8 cm diameter and 8 cm long cylindrical specimen weighing 184.6 g has a volume of 90.7 cm^3 and hence the bulk density is 2.04 g/cm^3. Assuming that the rock is composed entirely from quartz grains with ρ_s=2.65 g/cm^3, (3.1) gives a total porosity of 23%. Alternatively, the interconnected porosity can be determined by using the Archimedes method, which compares the weights of dry and water saturated specimen. If the wet weight of our example rock core is 199.3g, the interconnected porosity ϕ_I is 16%. The difference between the average total and interconnected porosities of both rock samples were typically 6 %. The interconnected Clashach porosities varied from 10-12%, while the porosity ϕ_I of Locharbriggs sandstone was higher at 15-17%. Having determined both total and interconnected porosities, each sample was oven dried in order to remove excess moisture.

3.4 Deformation Rig

Figure 3.2 shows a schematic representation of the deformation rig. The upper circuit, which includes the main 100 tonne ram, is used to apply an axial load to the cylindrical sample. The lower circuit describes the confining pressure system. Both hydraulic circuits are buffered with bladder accumulators in order to maintain a constant confining pressure or end load, when required. Since the confining pressure P_{conf} system has a hand pump attached to it, the P_{conf} is manually pumped at the start of each test. Hydraulic oil is used as the confining medium.

The main ram, which is used to apply a differential pressure, has an ISCOTM syringe pump connected to its back end. Hence, the ram can be lowered at a constant rate by setting the pump to deliver hydraulic oil at a constant speed, calculated from the cross-sectional area of the piston. This arrangement provides a way of carrying out a constant displacement rate test. Appendix A includes more detailed instructions of how to operate the rig. The pressure vessel that hosts the sample during a typical deformation test is a standard Hoek Cell. The cell body can be heated by using two band heaters, that are placed on both sides of the central confining pressure inlet port. Similarly, the platens contain cartridge heaters next to the fluid port and a separate thermocouple for

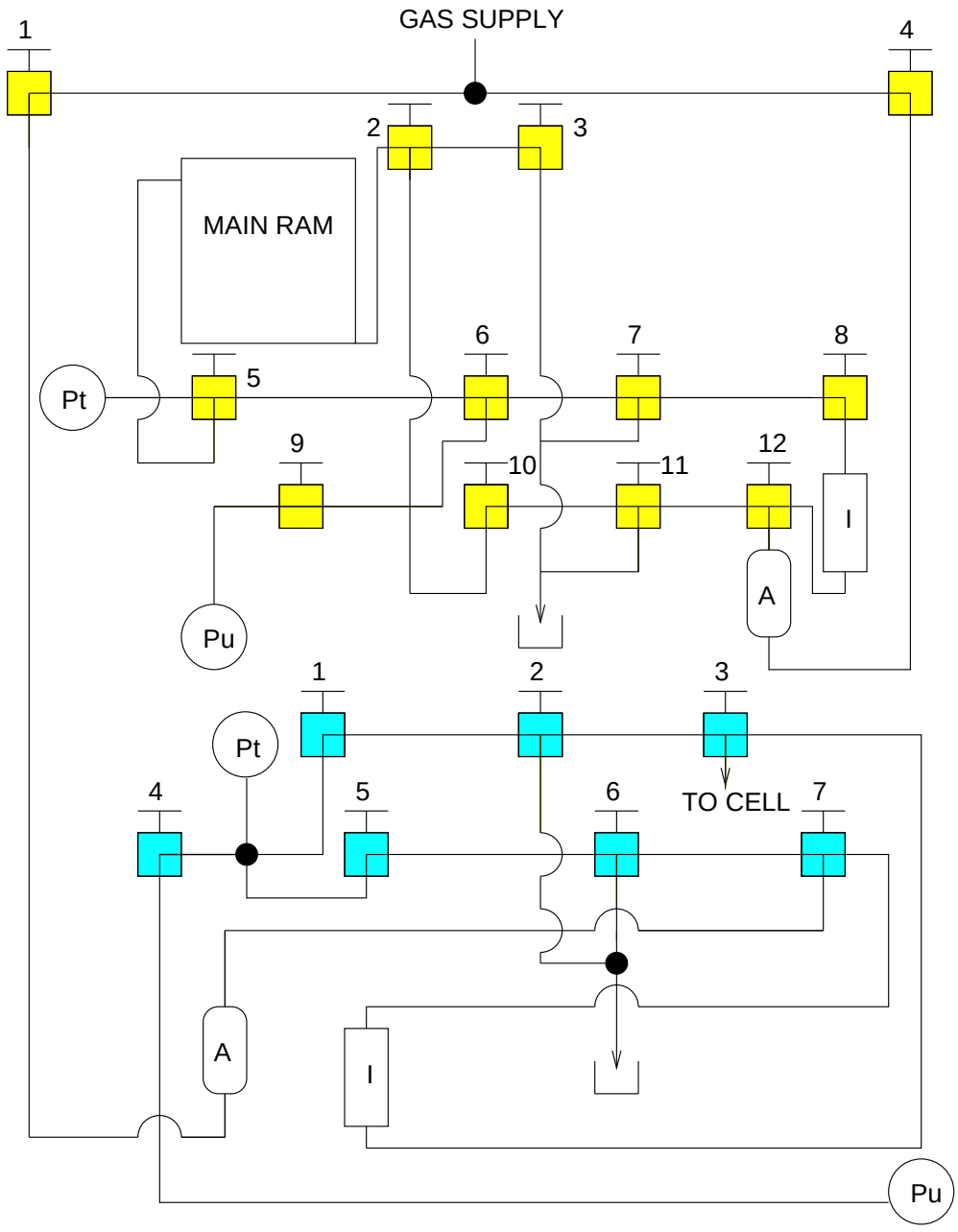

Figure 3.2. A schematic diagram of the deformation rig. Pt indicates a pressure transducer, I is an intensifier, A is an accumulator and Pu is a pump.

Table 3.2. The conversion factors for the logging software. LVDT stands for the externally mounted linear differential transformer, which measures the axial strain on the test specimen.

Parameter	Reading	SI units	Imperial units
Ram pressure	1 V	184.8 MPa	26800 psi
Confining pressure	1 V	6.891 MPa	1012.56 psi
Differential pressure	1 V	2.068 MPa	30 psi
LVDT	5.929	6.4 mm	0.025 in

temperature control. This kind of arrangement of heaters allows the test specimen to be heated to a required temperature during a test.

An external differential transformer (LVDT) monitors the piston displacement and hence provides a measure of the axial strain on the specimen. The output of the LVDT and the transducers measuring the confining pressure, differential pressure and axial load are logged by a PC through a Keithley data card. In acquiring data the Testpoint software was set to take 200 readings every 0.5 s (400 Hz) and average them out to give a final reading, that can be displayed on the computer screen or saved to a file. Testpoint software displays/saves the recorded values in Volts, and the readings can be converted to S.I. units by using the conversion factors listed in table 3.2. Any uncertainty in the measurement is ultimately caused by the transducer sensitivity, since any time lag due to the logging software is negligible.

The fluid ports in the platens allow for continuous flow of fluid through the specimen as it is being deformed. The percolating fluid enters the rock via the lower platen and it leaves the specimen from the upper platen. An ISCOTM syringe pump delivers the fluid at a constant velocity. The laboratory temperature is controlled by a free-standing heater with a thermostat. The bottom part of the deformation rig is also insulated with perspex sheets.

3.5 Typical test

3.5.1 Sample stack

Prior to a deformation test, a heat shrink made of thin polythene was placed around the test sample in order to preserve the post test gauge and deformation characteristics. Subsequently, the sample was placed inside a rubber sleeve to isolate it from the confining fluid and to prevent mixing of the confining and pore fluids. The rubber sleeve was placed inside a standard Hoek cell and a sample stack was assembled. Detailed instructions of how to prepare a sample stack are included in appendix A.

The sample stack consists of two steel mushroom shaped platens that were in contact with the upper and lower ends of the sample. In order to reduce the effect of a bending interface and to reduce any lateral movement (*Jaeger and Cook*, 1976), the platen ends were exactly the same size as the sample ends. End effects were minimised by inserting a steel spacer and a melinex sheet between the platens and the sample ends, as shown in figure 3.3. Melinex is a very strong polyester with low friction properties. It is therefore an ideal material for preventing any sideways movement due to end friction that could have inhibited shear localisation (*Scott et al.*, 1994). For the flow through tests a two mm hole was cut in the middle of the melinex sheet in order to allow for fluid flow through the sample. The steel spacer also had a two millimeter concentric hole. In addition, the movement of larger rock particles that might have blocked the hydraulic system was prevented by placing a nylon sheet at both ends of the specimen next to the melinex sheet (figure 3.3).

3.5.2 Test procedure

The samples were deformed in a conventional triaxial testing apparatus (section 3.4) under flow-through conditions at constant flow rate. Initially, the jacketed sample was heated to the appropriate temperature and loaded to hydrostatic conditions. The confining pressure was fixed within the brittle regime at 13.5 MPa and the pore fluid back-pressure was 0.1 MPa. In order to remove highly

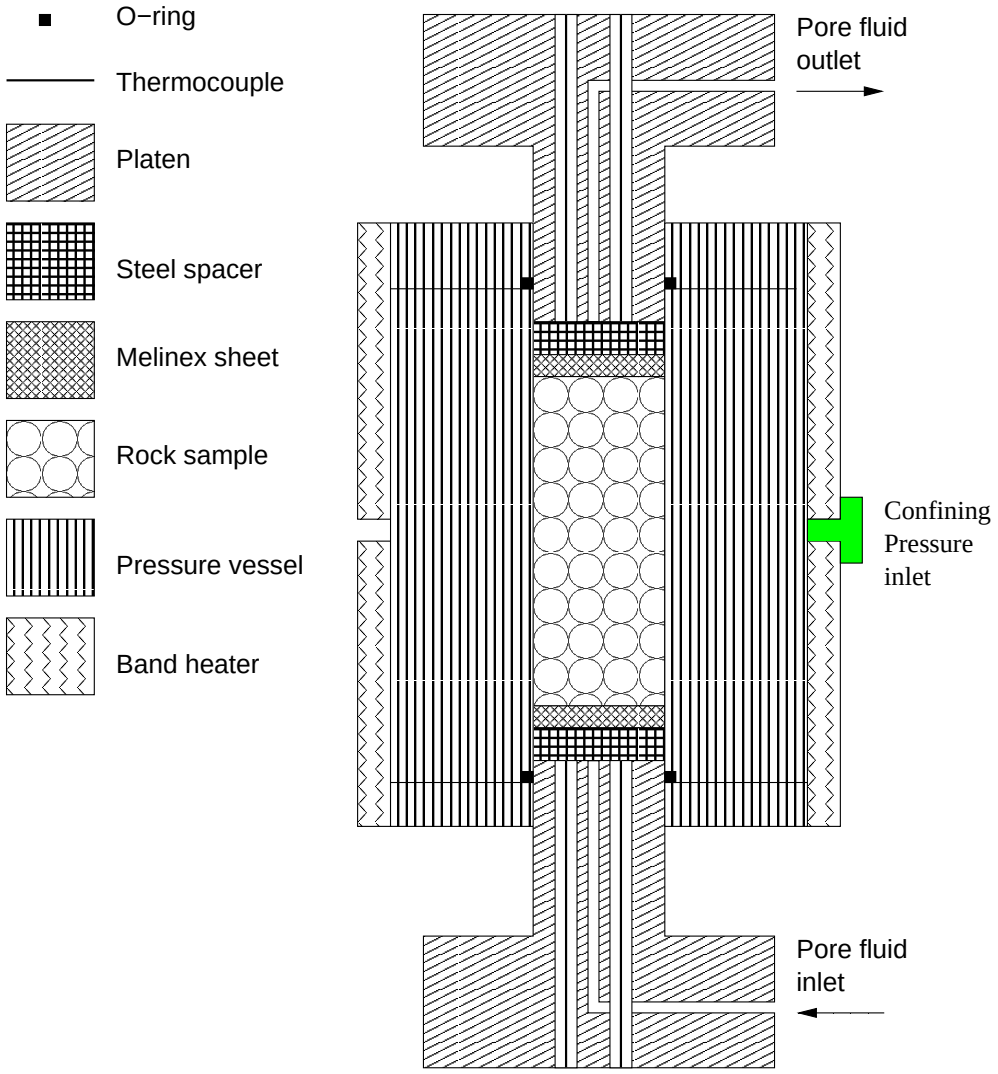

Figure 3.3. The arrangement of the sample inside the pressure vessel. A heat shrink and a rubber sleeve, that are not shown in figure also surrounded the sample. The platens contain both cartridge heaters and thermocouples for temperature control.

Table 3.3. The estimated errors for the measured values for axial pressure (Ram), confining pressure (P_{conf}), differential pressure (dP) and LVDT. The errors were estimated from the background noise level for the slow strain rate tests. They represent the sensitivity of the recording transducer.

Rock	$\dot{\varepsilon}$ /s	Ram %	P_{conf} %	dP %	LVDT
Clashach	10^{-7}	± 0.3	± 0.5	± 5.0	±0.3
Clashach	10^{-8}	± 1.0	± 0.5	± 7.0	±0.3
Locharbriggs	10^{-7}	± 0.2	± 0.5	± 2.5	±0.3
Locharbriggs	10^{-8}	± 1.0	± 0.5	± 2.2	±0.2

reactive fine particles the specimen was then flushed with distilled water for 24 hours at constant fluid flow rate Q_f = 0.2 ml/min. This is also the flow rate of water for the dynamic loading tests. The value of Q_f was dictated by the need to deliver an accurate and constant flow rate. Unfortunately, low Q_f value combined with short sample length resulted in linear flow velocities of 6.6 cm/h that were too high for the solution to reach equilibrium with the minerals in the rock specimen (*Ngwenya et al.*, 2000).

The time and temperature dependence of brittle deformation was investigated by carrying out compressional dynamic loading tests at different loading rates (1.2×10^{-4} to 1.5×10^{-1} MPa/s) and at temperatures of 25 − 80°C. The four different deformation rates used correspond to strain rates ranging from 10^{-5} to 10^{-8} s^{-1} during the linear elastic phase of deformation. In addition, both wet, flow through tests and dry tests were carried out in order to investigate the effect of test environment on rock strength. The test conditions are listed in table 4.1.

The uncertainty in the recorded values for the axial load (Ram), confining pressure (P_{conf}), differential pressure (dP) and axial displacement (LVDT) was estimated for the background noise in the test data for the slow loading rate tests. The percentage errors, that are likely to be caused by the gauge sensitivity, are listed in table 3.3. These errors were estimated from the raw data that was recorded in Volts, before converting the readings to pressure or displacement. The error for the Ram, P_{conf} and LVDT readings was ± 1 % or less for all the tests. However, the error in the differential pressure reading was considerably higher, ranging from 2.2-2.5 % to 5.0-7.0 % in the Locharbriggs and Clashach tests, respectively. Since

the data for the slow loading rate tests at 10^{-7} to 10^{-8} /s was noisier than that for the high strain rate tests, the values listed in table 3.3. are likely to be the upper limits.

3.5.3 AE monitoring

Although the volumetric strain was not measured, the acoustic emission (AE) technique (Chapter 5) was used as a way of remotely monitoring microcrack growth inside the rock sample. A growing crack acts as a centre of radiation for elastic waves, which propagate through the test specimen. These elastic AE waves can then be recorded by an AE sensor that is cemented on the sample surface (*Lockner*, 1993b).

The AE sensor contains a piezoelectric crystal, which converts movement into an electrical voltage (*Pollock*, 1989). When an elastic wave hits the piezoelectric crystal, it becomes mechanically stressed and delivers and electrical signal to a nearby pre-amplifier. Most AE testing employs resonant type sensors, which have one or more preferred frequencies of oscillation (*Pollock*, 1989). These preferred frequencies dominate the recorded AE signal. Laboratory AE testing on rocks is typically carried out in the 100 kHz to 2 MHz range. This is because the AE source events are controlled by flaws on the scale of the mineral grains (*Scholz*, 1968a; *Lockner*, 1993b).

The signals generated by the AE sensor are pre-amplified in order to provide higher and therefore more useful voltages. Subsequently, the signal is transmitted into the main instrument, where it is further amplified and filtered (*Pollock*, 1989). This is also where the AE signal is detected. The detection of the AE signal is accomplished by a comparator circuit, that generates a digital output pulse whenever the AE signal exceeds a fixed threshold voltage, as illustrated in figure 3.4 (*Pollock*, 1989). This voltage is proportional to the amplitude of the source wave. In this study the amplitude threshold was set at 50 dB, which is 10 dB higher than the amplitude threshold used in previous work. A higher than usual amplitude threshold was chosen with a view of eliminating background noise, especially due to the constant flow of water through the test specimen. Furthermore, the 50 dB limit was deemed appropriate in order to ensure adequate

disk space for data storage, especially for the very slow strain rate tests that lasted for several days (see also section 5.3.3).

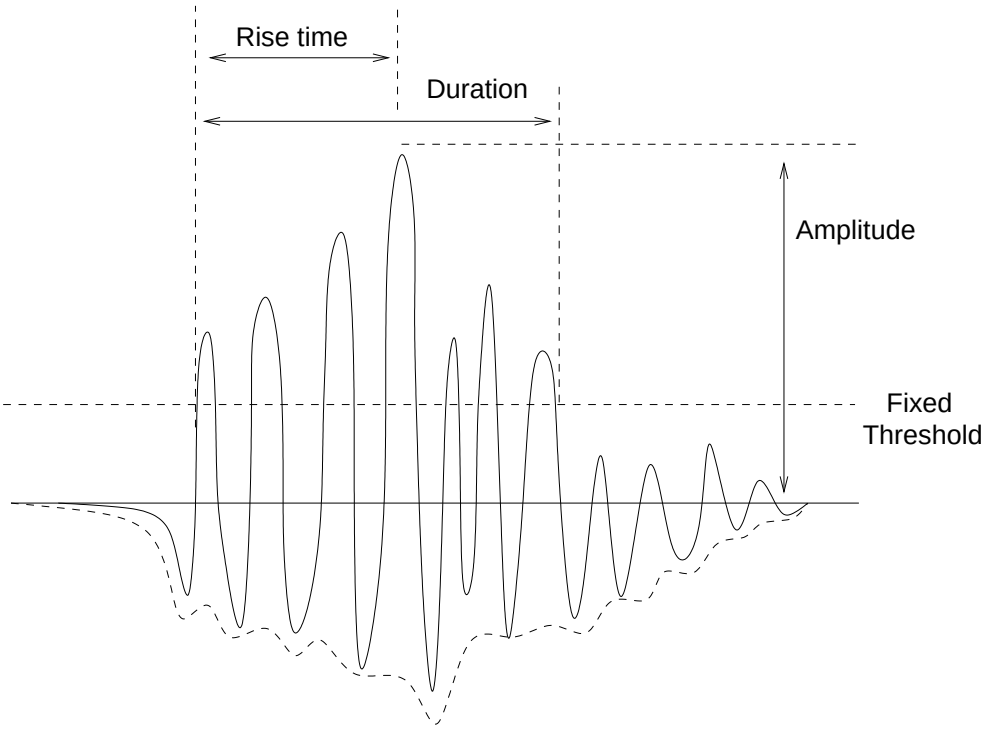

Figure 3.4. The AE waveform and some of the recorded parameters. Each AE signal that crosses a fixed amplitude threshold of 50 dB defines an AE hit. For each hit, the time, duration and amplitude were recorded. The rise time was defined as the time to the peak amplitude of the hit. The AE energy was calculated from the area under the signal envelope.

In my tests the AE activity was measured by a Panametrics wide-band piezoelectric transducer, which operates in a frequency range of 100 kHz to 1 MHz with a resonant frequency of 125 kHz. The resonant frequency of the AE transducer is somewhat lower than the expected frequency range of source events from 0.2 mm grains (table 3.1). The frequency f_{AE} of an emission signal from an extensional or a shear dislocation crack can be estimated from

$$f_{AE} \propto \frac{1}{(c/v_r + c/v_s)} \tag{3.2}$$

where c is crack length, v_r is rupture velocity and v_s is the propagation velocity of the signal (*Ohnaka and Mogi*, 1982). Hence, one could expect a 500 kHz emission signal from the fracturing of a 200 μs grain if v_r=v_s= 2000 m/s. This AE frequency is higher than the typical frequency range that was measured in my tests, since the lower and higher cutoffs for the AE data were set at 10 and 400 kHz, respectively (table 3.4). However, such filter limits represent sensible cut-off frequencies for a 125 kHz transducer. Furthermore, *Ohnaka and Mogi* (1982) demonstrated that the temporal evolution of AE activity proceeds in a similar fashion in the low (30 kHz), intermediate (250-400 kHz) and high frequency (1 MHz) range. This occurs as a result of the broad spectrum of frequencies that characterise AE waves. It is important to note that equation (3.2) is only an estimate of the emission frequency resulting from the growth of a single crack. The macroscopic failure of real rocks is preceded by the growth of several cracks of varying sizes. Assuming that cracks grow subcritically, the velocity v_r for crack propagation is likely change with increasing stress, since the local stress intensity K is a function of the applied stress σ_A (equation 2.11): such increase in crack velocity with K is illustrated in figure 2.7. Similarly, the propagation velocity v_s of the AE signal decreases as the sample dilates (*Guéguen and Palciauskas*, 1994). All of these factors contribute towards the emission frequency given by equation (3.2). As a consequence, the AE waveforms that accompany sample deformation during a typical test are likely to contain a wide spectrum of frequencies. It is anticipated that a more detailed study involving different frequency AE sensors would be required in order to examine his question further.

The AE transducer was clamped to the surface of the platen. In order to ensure a good contact with the transducer and the platen, Sainsbury's runny honey was used as a couplant. The output of the AE sensor was amplified by 40 dB with a Panametrics pre-amplifier and recorded with MISTRAS acoustic emission system. The MISTRAS system contains acoustic emission signal processor (AEDSP) boards that digitise the information contained in each threshold crossing AE signal, otherwise known as an AE hit.

The recording of AE hits is controlled by adjustable hardware settings (*Pollock*, 1989). Peak definition time (PDT) defines the time that the system will wait for a new maximum in a hit signal before defining the previous maximum as the maximum amplitude of the entire hit. PDT should be long enough to include any

Table 3.4. The recording parameters for AE monitoring.

Parameter	Range
Amplitude Threshold	Fixed 50dB
Pre-amplifier gain	40dB
Peak definition time (PDT)	200 μ s
Hit definition time (HDT)	800 μ s
Hit length (HLT)	1000 μ s
Transducer resonant frequency	125 kHz
Filter low	10 kHz
Filter high	400 kHz
Sample rate	1 MHz
Pre trigger	300 μ s

precursors. A reasonable estimate of the PDT can be obtained by dividing the sensor spacing by the speed of the fastest wave through the specimen.

Hit definition time (HDT) is the time within which the recording system will define counts belonging to the same event. Having detected a count the system will wait for a period of time defined by the HDT: if no counts are detected during this time, the system assumes that the hit signal has come to an end. There are two ways of defining a correct HDT. A reasonable value can be obtained by dividing the sample length l_s by the speed of the typical AE wave. Alternatively one could estimate HDT from $20/f_T$, where f_T is the resonant frequency of the AE sensor. For some recording systems, such as MISTRAS used here, HLT must be at least twice as long as the PDT.

Finally, hit lockout time (HLT) is the time that the system will wait after the end of a hit without recording any new data. HLT's of less than 300 μs are meaningless for the particular recording system that was used for my tests. This is because the minimum time for the MISTRAS system to complete data measurements and transfer the results to the output buffer equals 300 μs.

The hardware setting that were used for my tests are listed in table 3.4. It is quite possible that the PDT, HLT and HLT were too long in duration relative to what one might anticipate for the sample assembly that was used in my tests. For instance, the time for a typical AE wave to travel through the rock specimen

and the loading platen equals 100 μs, assuming a velocity of 2000 m/s in the sandstone and 6000 m/s in steel. Hence, a more reasonable estimate for the PDT, HDT and HLT could be 50, 100 and 300 μs, respectively. However, this problem was not noted until after a few tests had already been carried out. Therefore I decided to continue using these parameters in order to allow the comparison of different test results. Furthermore, it was not possible to measure the speed of the AE waves through laboratory test specimen by using the available equipment, and therefore to establish a correct value for PDT, HDT and HLT for the test assembly. However, the relatively long PDT, HDT and HLT that were used for my tests could have caused some short duration events to be recorded as one long duration event. This could be the reason why the total event count in my tests (table 5.1) is less than that reported in previous studies. On the other hand, some summing up of individual events would be expected to occur during the extremely high event rates that precede specimen failure. This is because of the finite time of 300 μs that the measuring system requires to process data.

The most widely used signal measurement parameters include the time of an AE hit, the number of counts (number of threshold crossings), rise time (time to peak amplitude), duration, energy (measured area under rectified signal envelope) and amplitude. These signal measurement parameters and their relation to the AE waveform is illustrated in figure 3.4 from *Pollock* (1989). The signal parameters that were measured in my tests are rise time, duration, energy and amplitude. These data were exported in ascii format from the MISTRAS system to UNIX machines for further analysis. I wrote several MATLAB codes for analysing and displaying the AE data.

3.5.4 Permeability measurement and calculation

Permeability is a measure of how easily fluid flows though a material. At sufficiently low flow rate (<1 m/s) the water permeability k of a rock is given by Darcy's law (*Darcy*, 1856; *Guéguen and Palcianskas*, 1994)

$$k = \frac{Q_f \, \eta \, l_s}{A_h \, dP} \tag{3.3}$$

where Q_f is the flow rate, A_h is the cross-sectional area for fluid flow, η is the dynamic viscosity, dP is the differential pressure and l_s is the length of the flow path. Hence, permeability can be measured in the laboratory by arranging either a constant flow rate or a constant pressure gradient across a rock sample. These two methods of permeability measurement are called the steady-state and the pulse transient method. The steady-state method can be used for measuring the permeability of high porosity rocks, because it is relatively straight forward to arrange and to maintain a constant flow of water through a porous rock (*Kieffer et al.*, 1999; *Zhu and Wong*, 1999; *Main et al.*, 2000a, 2000b). However, the pulse transient method of *Brace et al.* (1968) is the most commonly used technique for measuring permeability. It can be used to determine the permeability of all rock types, including tight, low porosity rocks (*Brace et al.*, 1968; *Zoback and Byerlee*, 1975; *Liakopoulou-Morris et al.*, 1994; *Popp et al.*, 2001).

It is quite possible that the pulse-transient method is more representative of crustal conditions than the steady-state method. Many geological settings, such as sedimentary basins or active fault systems, have distinct fluid pressure compartments (*Hickman et al.*, 1995). Hence, the existence of pressure gradients is likely to be the dominant cause of fluid flow in the crust. However, in all of my tests a constant flow of distilled water was pumped through the test specimen in order to monitor the temporal evolution of pore fluid chemistry. Such boundary condition implies a constant Q_f is equation (3.3). Hence, I used the steady-state technique of measuring permeability (chapter 7) in my tests. A single stroke ISCO^{TM} syringe pump delivered a constant flow rate to the upstream (bottom) end of the sample, as shown in figure 3.4. The pressure difference dP across the sample was measured by using a high sensitivity Validyne DP 360 differential pore pressure transducer ($\pm$ 300 psi). Each test was carried out under drained conditions with the downstream end open to atmosphere. The exit pore fluid on the downstream (top) end of the sample was directed to an auto-sampler.

Permeability k (in m^2) was calculated from (3.3) taking into account sample shortening during the test. At $\pm$7 % the error in the permeability measurement is greater than that of the differential pressure or axial strain (table 3.3) but still within the acceptable error margin of previous work on rock permeability. For instance, *Zhu and Wong* (1999) reported uncertainties of up to $\pm$15 % in their tests on porous sandstones. The error in my permeability measurements is large

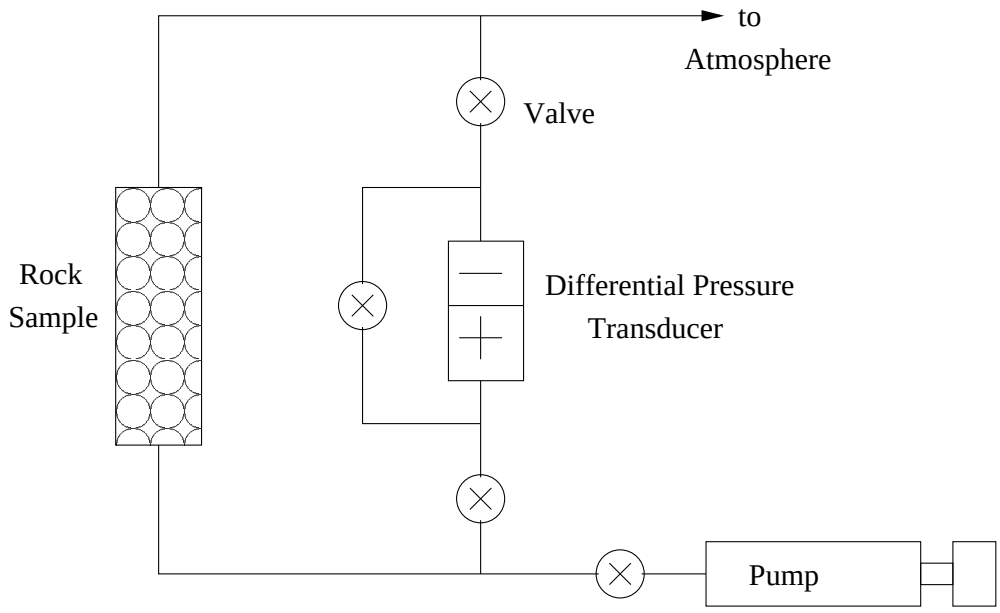

Figure 3.5. The permeameter that was used for the tests.

due to the relatively poor sensitivity of the differential pressure gauge. However, in analysing the permeability data (Chapter 7) the emphasis is on the relative permeability values and the temporal evolution of sample permeability rather than the actual numerical value.

3.5.5 Pore fluid analysis

The evolution of fluid chemistry was assessed by analysing the amount of dissolved ions in the exit pore fluid throughout the experiments. The exit pore fluid was directed to an auto-sampler loaded with test tubes. The samples were acidified by using 1 % HCl in order to reduce adsorption of dissolved species onto container walls and to stop mineral precipitation. The pore fluid samples were analysed after the tests for the concentration of Al, Ca, Fe, K, Mg, Na and Si by using an inductively coupled plasma source (Appendix B&C). The analysis was carried out for these particular ions in order to quantify the extent of chemical dissolution from quartz, feldspar, illite and diagenetic iron grains in the rock sample. In order to obtain enough sample (5 ml) for analysis of dissolved species sampling rates

of 30 min and 1 hour were used. Hence, a clear geochemical signal could only be recorded for the slow strain rate tests at 10^{-7} and 10^{-8}/s.

The sampling times for the exit pore fluid were corrected for the residence time τ_t, which describes the average time a fluid element resides inside the rock sample. Assuming constant porosity ϕ and constant fluid flow rate Q_f the residence time is given by

$$\tau_t = \frac{V_\phi}{Q_f} \tag{3.4}$$

where V_ϕ is the pore volume. In analysing the results, each chemical sample was plotted at a time when it resided half-way inside the rock sample. For a 8 cm long cylindrical sample with a 3.8 cm diameter and 16 % interconnected porosity, the calculated pore volume equals 14.5 cm^3. Since a constant flow rate of 0.2 ml/min was used for all the tests, the average residence time given by (3.4) is 73 minutes. However, this is only an approximation, since τ_t decreases during compactive stage and increases during dilatancy. Assuming 1% variation in rock porosity due to compactive/dilatant processes, the error in τ_t is 5 min, which represents only 0.5 % of the total duration of the 10^{-7} /s tests.

3.5.6 Post test analysis

Microstructural analysis was carried out in order to compare the deformation styles produced in high and slow strain rate tests and in different test lithologies. Hence, thin and polished sections were prepared near mid-length of the rock cores in a direction parallel to the shear band. The analysis was carried out by using an optical microscope and a scanning electron microscope at a magnification of 200×. The linear density of cracks was determined from the number of cracks along five 9.6 mm long traverses inside four 0.8×9.6 mm^2 mosaics of SEM micrographs. The traverse direction and the long direction of the mosaic were aligned parallel to the direction of σ_3. Only transgranular cracks oriented within 45 degrees of the direction of maximum compressive stress were included in the crack count. This is because both grain boundary cracks and transgranular cracks oriented at high

angles to σ_1 could have formed or been significantly altered during decompression (*Zhang et al.*, 1994). In total, 198 and 289 cracks were counted for the 80°C 10^{-6} and 10^{-8}/s Locharbriggs samples. For the Clashach sandstone the corresponding values were 190 and 204, respectively. In addition, areal crack densities were determined inside the SEM mosaics. Both inter-granular cracks and cracks of all orientations were included in the areal crack count.

3.5.7 Data reduction

The confining pressure and the axial stress were calculated by using the conversion factors listed in table 3.2. The stress calculation assumes that the sample diameter remains constant during an experiments. The axial strain ε was computed from

$$\varepsilon = \frac{\Delta l}{l_0} \tag{3.5}$$

where Δl is the piston displacement and l_0 is the initial specimen length. In practice, this was accomplished by creating text files from the logged data. Subsequently, I wrote several matlab functions and programs that could be used in analysing and displaying the data.

3.6 Calibration tests

3.6.1 Control test for fluid flow

The calculation of permeability (3.3) assumes a constant flow rate of fluid through the sample. It is therefore essential to check that the fluid flow in and out of the sample is indeed constant. Hence, calibration tests were carried out by using distilled water as a permeant.

The pump output was checked by measuring the volumetric outflow rate at different dial settings. The pump output for 10 min was directed to a test tube

of known weight. Subsequently, the test tube containing the sample was weighed in order to determine the sample volume. The results of the calibration test confirmed that the pump output matched the dial settings, as illustrated in figure 3.6.

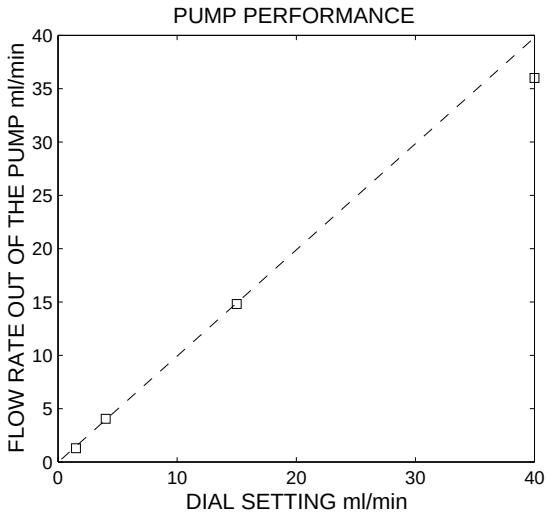

Figure 3.6. The flow rate of water out of the pump matched the dial settings.

The mean flow rate for water out of the rock sample was determined from the weight of the chemical samples. Prior standard deformation tests, the test tubes were weighed and then placed in the auto sampler. Since the exit pore fluid was sampled at regular intervals for chemical analysis, the flow rate out of the rock could be calculated. Figure 3.6 shows the measured flow rates for the slow strain rate Locharbriggs test. The flow rate out of the rock equalled the inflow rate at 0.2 ml/min. However, since the syringe pump volume was 500 ml, it needed to be refilled every day. At the refilling times, flow rate decreased, as indicated by letter P in figure 3.7. Specimen failure (F) did not lead to appreciable changes in the mean outflow rate, but increased variability may indicate fines migration.

3.6.2 Control test for chemical analysis

In order to eliminate artifacts that might be produced by reactions in the experimental apparatus, a control test was carried out under constant hydrostatic

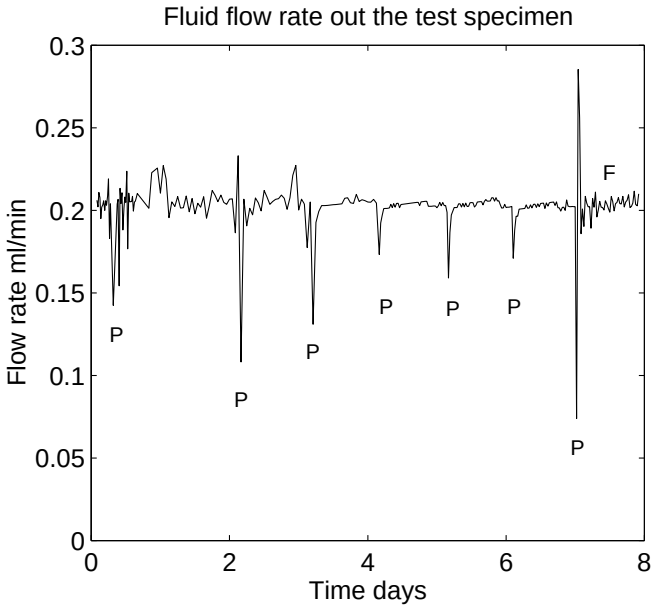

Figure 3.7. The flow rate of water out of the Locharbriggs sandstone for the very slow strain rate test at 3×10^{-8}/s. P indicates times when the pump was refilled and the flow rate decreased. F indicates sample failure time.

pressure of 13.5 MPa for the duration of one week. Throughout the test, distilled water was directed through a plastic cylinder with an axial 2 mm diameter hole. The flow rate of water was 0.2 ml/min and hence the same as for the rock deformation tests. The exit water was sampled at regular intervals and analysed for the concentration of Al, Ca, Fe, K, Mg, Na and Si by using an inductively coupled plasma source (Appendix 3). Test results indicated that there was very little dissolution of silica and iron from the stainless steel apparatus, as shown in figure 3.8. Quite interestingly, the stainless steel EN57 that was used for making the apparatus also contains up to 1 % of silica. However, any dissolution from the test apparatus was negligible and hence all our results can be attributed to chemical dissolution from the rock core.

3.6.3 Control test for permeability measurement

The effect of the cross sectional area for fluid flow A_h to the measured differential pressure (dP) across the test specimen was investigated by subjecting an intact

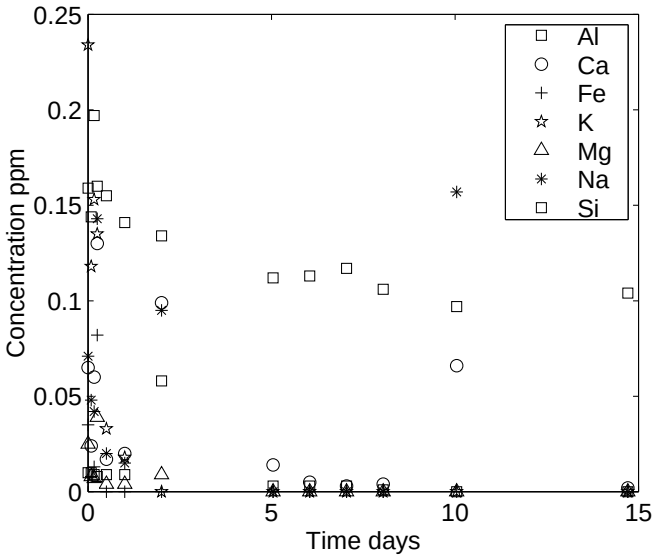

Figure 3.8. The amount of dissolved ions from a plastic core. The silica and iron could originate from the test apparatus, while the small amount of other elements represents the measurement error of $\pm$ 0.1 ppm.

rock sample to a hydrostatic pressure of 13.5 MPa. The cross-sectional area through which the fluid enters the rock specimen was varied by using metalling end pieces with different hole sizes between the sample and the loading platen. Both P_{conf} and axial stress were set at 13.5 MPa and dP was measured at a constant flow rate of 0.2 ml/min. The differential pressure increased with decreasing hole size, as illustrated in figure 3.9. Hence, the cross sectional area of the 2 mm diameter metallic end piece was used for calculating permeability according to (3.3). This procedure yielded permeability values in the expected range for sandstones (10^{-12} to 10^{-14} m^2), as shown in table (7.1). It is anticipated that a more systematic testing program should be carried out in order to investigate the effect of platens and end pieces on the percolation of fluid through a rock core during a triaxial compression test.

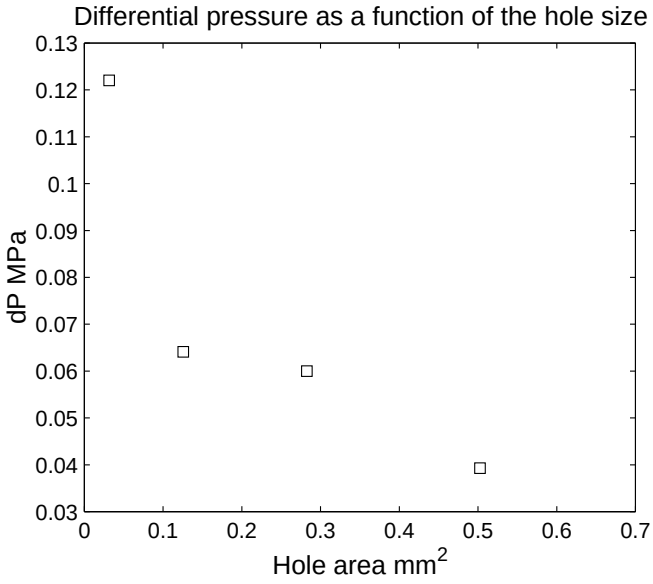

Figure 3.9. The differential pressure versus hole area. Initial calibration revealed that the differential pressure is a function of the hole size. However, $A_h \times dP$ does not remain constant as predicted by (3.3).

3.7 Summary

Triaxial test provides a means by which the *in situ* conditions can be simulated. In this study, triaxial tests were carried out at different strain rates in order to investigate time dependent aspects of rock deformation. The effect of test environment and temperature was also investigated. The tests were conducted on cylindrical sandstone cores. During each test, axial strain, differential stress, differential pressure, acoustic emission activity, the chemical content of the pore fluid and the axial permeability were measured continuously and contemporaneously. The recorded mechanical data (Chapter 4), acoustic emission activity (Chapter 5), geochemical data (Chapter 6) and fluid flow properties (Chapter 7) will be discussed in the following chapters.

Chapter 4

Mechanical Data

All this brings us to the question of stresses and strains, words which the layman is apt to regard as alarming, distressing and confusing. This is perhaps partly because the words may conjure up the idea of a wilderness of mathematics but probably more because these words have been borrowed or stolen by non-scientists to describe the mental condition of human beings.
J.E. Gordon (1976)

4.1 Introduction

A triaxial test culminates in the failure of the rock sample. The simplest way to interpret the results of such a test is to regard specimen failure as a discrete event that occurs at a particular stress without any significant prior warning (*Paterson*, 1978). Such an approach does not reveal anything about the physical mechanisms responsible for brittle deformation. However, a carefully designed laboratory rock testing programme can tell us a great deal about how various environmental factors affect rock strength. In this chapter I will consider the effect of test environment, strain rate and temperature on the purely mechanical behaviour of the rock samples. Subsequently, I will examine some of the microstructures that were generated in the rock deformation tests.

4.2 Compressive strength

The triaxial compression test (section 3.2) can be used to determine the macroscopic strength of a rock sample. If a modest confining pressure is used, the specimen fails along a shear surface that is oriented at an acute angle $\theta < 45°$ to the direction of σ_1. This kind of failure mode is illustrated in figure 4.1. It is characterised by shearing movement along the fracture plane. It has been suggested that this shear plane should be called a fault, because of its similarity to geological faulting (*Griggs and Handin*, 1960). However, other workers prefer to call it a shear fracture and restrict the term fault to geologic use (*Jaeger and Cook*, 1976; *Paterson*, 1978). In this study I will use the term *fault* to describe this kind of failure mode.

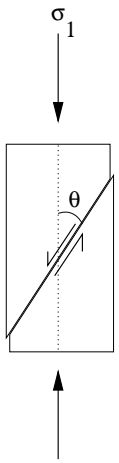

Figure 4.1. The mode of fracture observed in a triaxial compression test under a moderate confining pressure. The failure mode resembles a geological fault, that is oriented at an angle θ to the direction of maximum compressive stress σ_1.

The mechanical data for a triaxial compression test are displayed in the form of a stress-strain curve. Figure 4.2. illustrates the shape of a stress-strain curve for a compressive strength test under a modest confining pressure. The stress-strain dependence is typically interpreted in terms of three or four microfracturing domains (*Brace et al.*, 1966; *Jaeger and Cook*, 1976; *Scholz*, 1990; *Guéguen and Palcianskas*, 1994). Phase I is slightly concave upwards, indicating increasing stiffness of the test specimen. Such behaviour is caused by the compaction of favourably oriented cracks lying at high angles to σ_1. This phase is not very

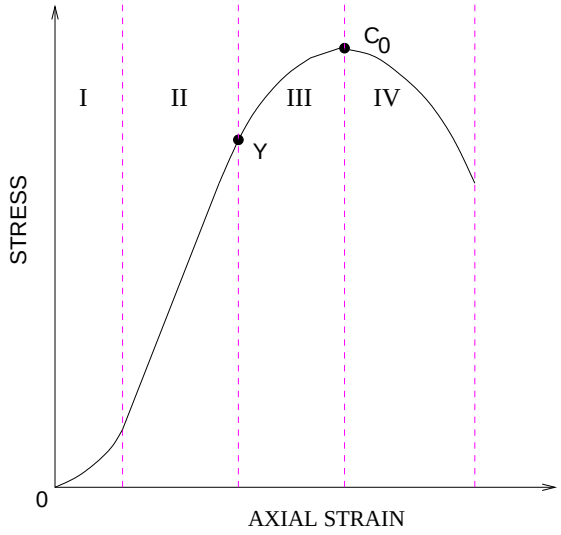

Figure 4.2. The complete stress-strain curve for a rock sample subjected to triaxial compression. Four distinct microfracturing domains can be identified in such a curve (I-IV). Y indicates the yield point and C_0 is the rock strength. Redrawn from *Jaeger and Cook* (1976).

pronounced in triaxial tests because many of the cracks are already closed at the start of the test due to the application of a confining pressure. The following linear elastic phase (II) is marked by a constant slope of the stress-strain curve. This slope gives the elastic modulus E_m for the specimen. The transition from elastic to *ductile* behaviour occurs at the *yield point* Y at about half to two thirds of the maximum stress value at C_0. The rock sample is ductile since it can sustain permanent deformation without losing its ability to resist load (*Jaeger and Cook*, 1976). In this strain hardening phase (III) the slope of the stress-strain curve decreases progressively, reaching zero at C_0. The stiffness of the rock sample decreases due to the growth of cracks oriented parallel or sub-parallel to σ_1 (*Tapponier and Brace*, 1976). The growth of cracks causes the rock to dilate: this rheological property is termed *dilatancy* (*Brace et al.*, 1966; *Scholz*, 1990). The deviatoric stress at C_0 defines the material *strength*. The following strain softening phase (IV) can only be recorded with a stiff machine or a servo controlled machine with a short response time. If a conventional soft loading machine is used, the instability associated with brittle failure terminates the test. During this stage the slope of the stress-strain curve is usually negative and its magnitude is a measure of the brittleness of the material. The rock is in a *brittle* state, since its ability

to resist load decreases with increasing strain (*Jaeger and Cook*, 1976). Although the macroscopic failure of the rock sample occurs progressively throughout the brittle stage, in practical testing a catastrophic failure and an associated stress drop $\Delta\sigma$ is often observed (*Jaeger and Cook*, 1976). Specimen failure is followed by frictional sliding along the newly created fault.

4.3 Semi-empirical fracture criteria

The Griffith energy balance concept can only predict material strength in the case of a homogeneous elastic material under tensile loading (*Paterson*, 1978; *Scholz*, 1990). The models for tensile failure are based on the propagation of a single crack. Since failure in compression is controlled by a population of microcracks, such weakest link theories are not applicable to compressive loading (*Costin*, 1987). Rock fracture under general stress conditions is typically expressed in terms of the three principal stresses in the form

$$\sigma_1 = f(\sigma_2, \sigma_3) \tag{4.1}$$

which is known as the criterion of failure (*Paterson*, 1978). Semi-empirical failure criteria, that pre-date the *Griffith* approach described in section 2.2, are often used. One such criterion is the *Coulomb* (1773) equation given by

$$\tau_s = \tau_0 + \sigma_n \tan\,\phi = \tau_0 + \mu_s \sigma_n \tag{4.2}$$

where τ_s and σ_n are the shear and normal stresses resolved on any plane within the material, whose cohesive shear strength is τ_0 (*Paterson*, 1978; *Scholz*, 1990). The parameter μ_s is called the coefficient of internal friction and ϕ is the angle of internal friction. Equation (4.2) is frequently used as a criterion for rock fracture and it can be termed the Coulomb, Navier-Coulomb or Coulomb-Mohr criterion (*Paterson*, 1978). It describes the straight line envelope on a Mohr diagram,

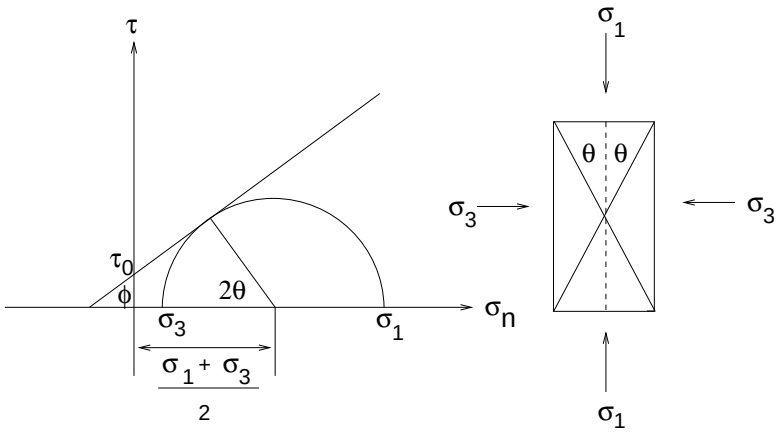

Figure 4.3. The Coulomb criterion expressed in terms of a Mohr diagram. The Coulomb criterion for fracture(4.2) is the equation of the straight line. The right hand side shows the angular relationship between the principal stresses and the fracture planes. Redrawn from *Scholz* (1990).

which is illustrated in figure 4.3. Hence, failure occurs in two conjugate planes that are oriented at acute angles

$$\theta = 45^\circ - \phi/2 \tag{4.3}$$

on both sides of σ_1 and they have an opposite sense of shear (*Jaeger and Cook*, 1976; *Scholz*, 1990).

The results of triaxial compression tests are in good agreement with the Coulomb criterion (*Jaeger and Cook*, 1976), as illustrated in figure 4.4. If the rock fails by shear fracturing, the maximum differential stress $\sigma_{max} = \sigma_1 - \sigma_3$ preceding failure is linearly related to the pressure parameter p_c that equals σ_3 under compressive loading. Under tensile loading p_c=σ_1. Over a moderate range of confining pressures, σ_{max} takes the form

$$\sigma_{max} = \sigma_1 - \sigma_3 = \sigma_4 + p_c \tan \psi \tag{4.4}$$

where σ_4 is a constant that equals the uniaxial compressive strength if (4.4) holds down to zero confining pressure (*Paterson*, 1978). The parameter tan ψ is also a constant that usually takes values between 1 and 10. However, it should be noted that the Coulomb criterion is strictly empirical, since the coefficient of internal friction cannot be viewed as a real friction coefficient (*Handin*, 1969; *Paterson*, 1978). This is because the failure surface is not yet present at the ultimate stress (*Scholz*, 1990). Nevertheless, μ_s takes values from 0.5 to 1.5 (*Sangha and Dhir*, 1975) and it therefore lies in the range of empirically determined friction coefficients for rocks (*Paterson*, 1978).

However, many studies have also observed a non-linear relationship between $\sigma_1 - \sigma_3$ and p_c. In such case the differential stress at failure is a curve that is concave towards the confining pressure axis (fig 4.4.b). There are various reasons that could explain such non-linearity. For instance, a curved plot may be an indication that the brittle-ductile transition is being approached. On the other hand, some theoretical considerations such as the modified Griffith theory (*Paterson*, 1978) predict a non-linear pressure dependence without invoking a change of deformation mechanism. Perhaps the most intriguing suggestion is that an increase in p_c leads to a progressive increase in the degree by which cracks are closed. Hence, a change in slope in the Mohr envelope is observed (*Mogi*, 1972). However, the Coulomb relation (4.2) remains an important failure criteria because of its mathematical simplicity (*Paterson*, 1978).

4.4 The effect of environmental variables on the strength of rocks

4.4.1 Introduction

Most rock deformation tests have involved the axial compression of cylindrical samples at different temperatures, confining and pore fluid pressures (*Cook*, 1981). Such studies are motivated by the need to quantify the individual contributions of various environmental parameters to the mechanical properties of rocks (*Gretener*, 1981). The test specimen are typically housed in a jacket in order to prevent

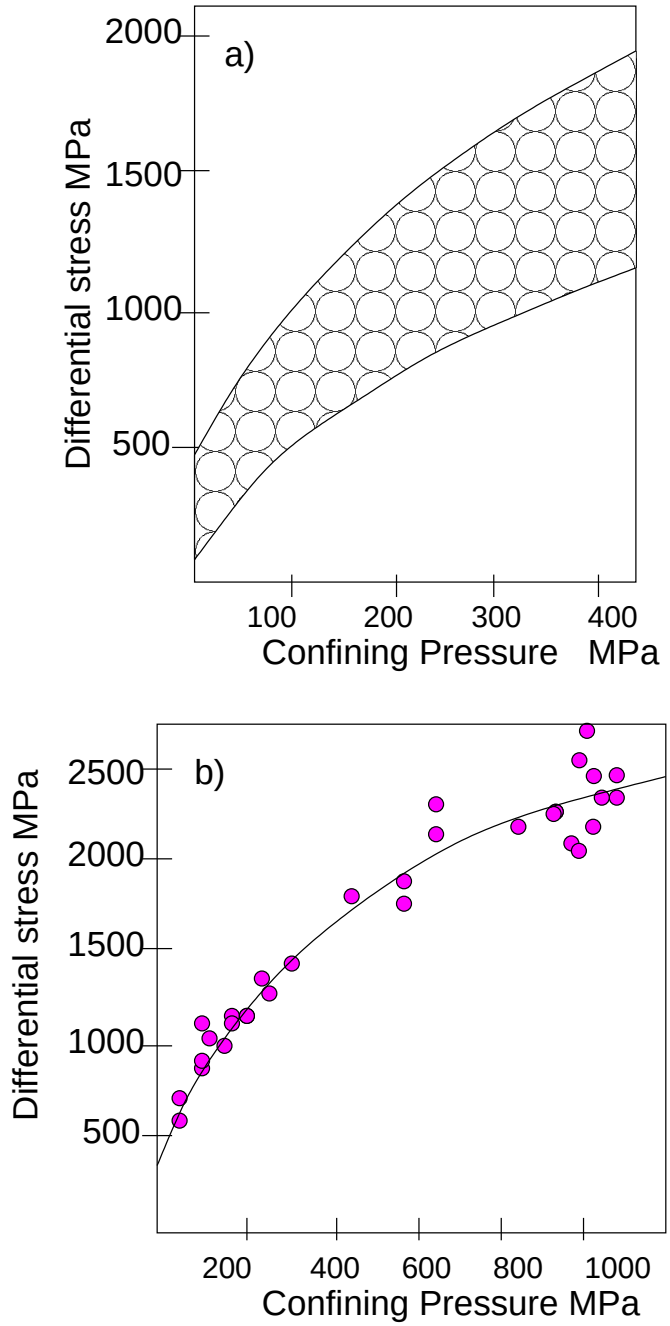

Figure 4.4. The dependence of differential stress at shear failure on confining pressure (a) in various igneous rocks (b) in granite, illustrating non-linearity. Redrawn from *Paterson* (1978).

confining fluid from entering the rock sample (*Becker*, 1893). The effect of confining pressure on rock strength and ductility has been known for over a century (*Adams and Nicolson*, 1901; *Von Karman* 1911). An increase in strength with increasing P_c has also been observed for both sandstones used in this study (*Crawford et al.*, 1995). Hence, in my tests the confining pressure was kept constant at 13.5 MPa. The aim of the testing procedure was to investigate the effect of test environment, temperature and deformation rate on the mechanical properties of Clashach and Locharbriggs sandstones. These variables have also been shown to affect the brittle deformation properties of rocks in previous studies.

4.4.2 The effect of aqueous environment

In section 2.3 I considered the effect of water on crack growth rates in quartz and quartz rich rocks. A similar water weakening effect is the likely cause of the observed reduction in rock strength in the presence of aqueous solutions (*Hirschwald*, 1912; *Terzaghi*, 1945; *Murrell*, 1965; *Paterson*, 1978; *Masuda*, 2001). Water decreases the strength of rocks even when it is adsorbed from the atmosphere relative to that obtained after careful drying (*Paterson*, 1978). Some of the earliest observations of the special weakening effect of water were by *Griggs & Bell* (1938) and *Griggs* (1940). They discovered that quartz, calcite, gypsum and marble were weaker in the presence of aqueous solutions (*Kirby*, 1984). Subsequently, *Serdengecti and Boozer* (1961) carried out triaxial compression tests on Berea sandstone. In their tests, both ultimate and yield strength were less for a water saturated specimen relative to oil-saturated samples. *Boozer et al.* (1963) also reported a similar weakening effect in the presence of various surface active liquids (*Paterson*, 1978). The effect of humidity on rock strength was studied by *Sano et al.* (1981). They showed that an increase in humidity and test temperature decreased the uniaxial compressive strength of Oshima granite in a systematic manner. In a recent study, *Feng et al.* (2001) observed a 24 and 38 % reduction in the uniaxial compressive strength of granite in distilled water and Yangtze river water, respectively, relative to that in air. The effect of water chemistry on rock strength is likely to be attributed to differences in the surface energy of minerals when wetted with the fluid (*Boozer et al.*, 1963, *Dunning et al.*, 1980).

4.4.3 Temperature effect

The effect of test temperature on rock strength was already evident in the early tests of *Adams & Nicolson* (1901) and *Griggs* (1936). In general, rock strength decreases and ductility increases with increasing temperature (*Heard*, 1976; *Cook*, 1981). At high temperatures above 500°C most rocks become extremely ductile and the constituent crystals deform in a plastic manner (*Jaeger and Cook*, 1976). However, in the purely brittle regime, little effect is observed. For instance, *Blacid et al.* (1981) did not observe any systematic changes in the strength of Galesville sandstone in their triaxial compression tests at 37-204°C. A similar result was obtained for Berea sandstone and Pala gabbro at temperatures of 26-149°C by *Serdengecti and Boozer* (1961). They could not determine a distinct temperature effect on rock strength within the accuracy of the measurements. Although there is some tendency for the angle θ to increase with temperature (*Handin*, 1966), this effect may merely reflect the approaching brittle-ductile transition (*Paterson*, 1978).

4.4.4 Strain rate effect

The strength of rocks depends on the applied loading rate (*Paterson*, 1978; *Costin*, 1987). A reduction in rock strength associated with decreasing strain rate has been observed in Solenhofen limestone (*Robertson*, 1955; *Serdengecti and Boozer*, 1961; *Lankford*, 1981), Yule marble (*Turner et al.*, 1956), marble and granite (*Mogi*, 1959; 1962), Pala gabbro (*Serdengecti and Boozer*, 1961), Laurencekirk sandstone (*Sangha and Dhir*, 1972), Berea sandstone (*Serdengecti and Boozer*, 1961; *Peng*, 1973), Oshima granite (*Sano et al.*, 1981; 1982) and Indian granite (*Masuda*, 2001). Figure 4.5 from *Sano et al.* (1981) illustrates the power-law scaling of strength versus strain rate for various rocks. The power law exponent equals $n/(n+1)$ and hence n varies from 32 to 62 for these rocks (*Sano et al.*, 1981). However, it is questionable whether a power law should be used at all, since the variation in rock strength is less than an order of magnitude.

Sano et al. (1982) observed over 50 MPa reduction in the uniaxial compressive strength of Oshima granite as the axial or dilatant strain rate decreased by five orders of magnitude ($\dot{\varepsilon}$=10^{-3} to 10^{-7} /s). In contrast, the strength of Laurencekirk

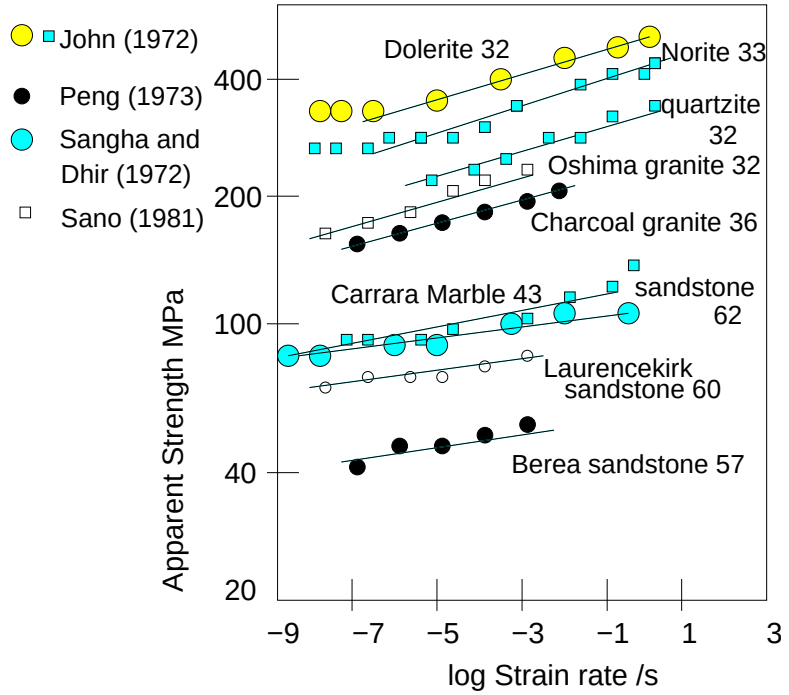

Figure 4.5. The ultimate strength as a function of strain rate for various rocks. Rock strength is often assumed to obey power law scaling with the applied strain rate. The number next to the rock type indicates the stress corrosion index. Redrawn from *Sano et al.* (1981).

sandstone decreased just 4 MPa as the axial strain rate varied from 10^{-4} to 10^{-9}/s (*Sangha and Dhir*, 1972). While both *Sano et al.* (1982) and *Sangha & Dhir* (1972) carried out their tests on dry specimen, a similar strain rate effect has also been observed for both oil (*Serdengecti and Boozer*, 1961) and water saturated specimen (*Sano et al.*, 1981, *Masuda*, 2001). However, wet specimens display a greater strain rate sensitivity than ones saturated with air (*Masuda*, 2001). Furthermore, the loading configuration may also modify the strain rate effect. *Sangha and Dhir* (1975) found a smaller strain rate effect for sandstones that were loaded under triaxial stress state when compared to rocks deformed under uniaxial compression. While most studies have investigated the effect of loading rate under compressive stresses, strain rate rate effect has also been observed under tensile loading (*Turner et al.*, 1956).

The reduction in rock strength with decreasing strain rate is not predicted by the Griffith theory (*Mogi*, 1962, *Scholz*, 1968a; *Sano et al.*, 1981). *Mizutani et*

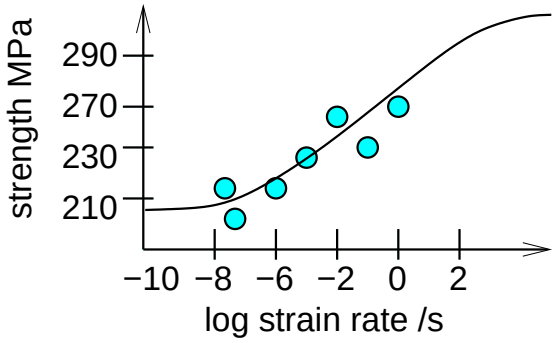

Figure 4.6. Strength of micro-grained limestone (Soultz micrite) as a function of strain rate under uniaxial compression. The experimental data shows considerable scatter. The solid line shows the failure strength prediction after the wing crack model of *Kemeny and Cook* (1987). Redrawn from *Reuschlé et al.* (1989).

al. (1977) demonstrated that subcritical crack growth due to stress corrosion plays a major role in the strain rate effects on strength. They predicted an exponential decrease in rock strength with strain rate based on the assumption of subcritical crack growth by the stress corrosion mechanism. Their work was later criticised by *Sano et al.* (1981) who pointed out that one critical flaw theory cannot be used to predict rock properties, since many microfractures are observable prior to macroscopic failure (*Tapponier and Brace*, 1976). *Sano et al.* (1981) demonstrated both theoretically and experimentally that rock strength is a power law function of strain rate. However, both *Lankford* (1981) and *Sano et al.* (1981) used a power law dependence of crack velocity on K (2.16) and therefore it is not surprising that both arrived in a power law formula. In fact, the data of *Sano et al.* (1981) could be equally well described assuming a direct proportionality between strength and the logarithm of the strain rate. A logarithmic reduction in rock strength has been predicted (*Mogi*, 1962; *Segall*, 1984) and observed for granite and andesite (*Mogi*, 1962; *Masuda*, 2001). *Reuschlé et al.* (1989) used the wing crack model of *Kemeny and Cook* (1987) in order to predict the failure strength of limestone, as illustrated in figure 4.6. Their calculations suggest that the relationship of strength to the applied strain rate is sigmoidal rather than a simple power or an exponential law. Their model calculations suggest that at a strain rate above 10^{+1} /s or below 10^{-9} /s slow crack growth no longer has any effect. The lower limit for subcritical crack growth defined the conditions user

which delayed failure no longer occurs. Therefore it is a very important parameter in strength and time-to-failure predictions (*Atkinson and Meredith*, 1987a).

4.5 Results

Table 4.1 shows the testing conditions and a compilation of the mechanical data obtained during triaxial compression tests on Clashach and Locharbriggs sandstones. The effect of the test environment was first quantified by loading a water saturated and an air-dry Clashach and Locharbriggs specimen under otherwise identical conditions. In the presence of water rock strength was reduced by 6 and 11 % for Clashach and Locharbriggs sandstone, respectively. Figure 4.7 shows typical stress-strain curves for the dry and the wet test on Locharbriggs sandstone. The non-linear part of the stress-strain curve began earlier at 58.1 MPa for the wet specimen compared with 61.8 MPa for the dry specimen. Similarly, the yield strain was less for the dry than the wet specimen (table 4.1). In addition, the strain hardening phase was more pronounced in the presence of water. Figure 4.8 illustrates the stress-strain curves for the dry and wet Clashach tests. At 131.2 MPa, the wet yield stress of Clashach sandstone was considerably less than the σ_y for the dry specimen (153.3 MPa). The corresponding yield strains were 1.5% and 1.9% for the wet and the dry tests, respectively. The general shape of the Clashach stress-strain curve did not change appreciably in the presence of water.

The effect of strain rate and temperature on rock strength was investigated by carrying out wet, flow-through tests at 80°C using different loading rates. The specimen failure time t_f is a power law function of the stress rate $\dot{\sigma}$ and strain rate $\dot{\varepsilon}$ with an r-squared value of 0.999, as illustrated in figure 4.9. Hence, both strain rate and stress rate can be considered equally good indicators of the loading rate used for the tests.

The stress strain curves for the Clashach and Locharbriggs tests are shown in figures 4.10 and 4.11, respectively. Clashach sandstone was stronger and more brittle than Locharbriggs sandstone. In contrast, the Locharbriggs tests displayed well developed strain softening and hardening phases. The Clashach strength varied from 122.6 to 169.3 MPa, while the peak stress of Locharbriggs sandstone ranged from 77.7 to 81.2 MPa for the 80°C wet tests at 10^{-5} to 10^{-8} /s. The

Table 4.1. Mechanical data for the triaxial tests. Type indicates the test environment, σ_{max} is the peak stress, ε_f is the axial strain at failure, E_m is the elastic modulus, σ_y is the yield stress, ε_Y is the yield strain and θ is the fault angle. C and L stand for Clashach and Locharbriggs specimen, respectively.

Rock Type	$\dot{\varepsilon}$ 1/s	Type	T °C	σ_{max} MPa	ε_f %	E_m MPa	σ_y MPa	ε_Y %	θ degrees
C	3.1×10^{-5}	wet	80	168.5	2.33	9254	125.8	1.47	26
C	2.7×10^{-5}	wet	80	162.8	2.29	9400	131.2	1.51	34
C	2.9×10^{-5}	dry	80	173.4	2.46	8997	153.3	1.90	26
C	3.2×10^{-6}	wet	80	169.3	2.43	7983	142.3	1.95	33
C	2.5×10^{-7}	wet	25	166.7	2.47	9035	137.4	1.72	26
C	2.2×10^{-7}	wet	40	140.4	1.52	10874	104.4	1.00	30
C	2.7×10^{-7}	wet	60	161.2	1.80	9310	155.4	1.84	25
C	3.3×10^{-7}	wet	80	134.6	2.14	7512	112.2	1.60	39
C	3.3×10^{-8}	wet	80	122.6	2.22	7096	103.2	1.62	26
L	3.0×10^{-5}	wet	80	81.2	1.96	6219	60.3	1.01	35
L	3.1×10^{-6}	dry	80	90.3	1.95	6193	61.8	1.08	26
L	3.2×10^{-6}	wet	80	80.8	1.95	6155	58.1	0.96	31
L	3.3×10^{-7}	wet	25	81.3	2.08	5252	56.6	0.98	40
L	2.8×10^{-7}	wet	40	77.8	1.88	5749	60.0	1.14	34
L	3.3×10^{-7}	wet	40	82.3	2.21	5649	55.7	1.10	35
L	3.1×10^{-7}	wet	60	81.4	2.12	5401	59.6	1.25	37
L	3.4×10^{-7}	wet	80	79.9	2.26	5467	53.9	1.15	36
L	2.8×10^{-8}	wet	80	77.7	2.11	5306	62.3	0.72	39
L	3.1×10^{-8}	wet	80	90.5	1.94	5360	69.1	1.23	36

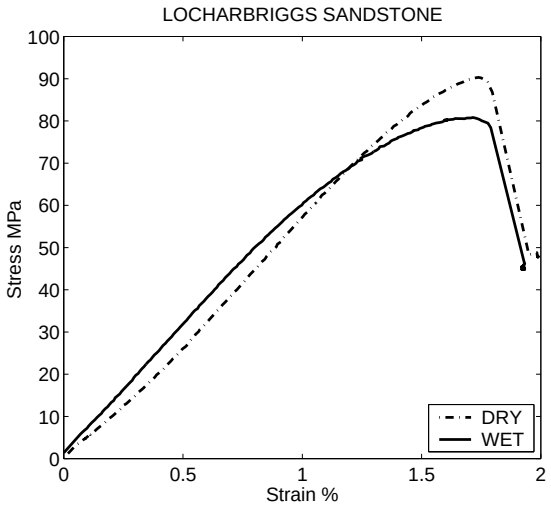

Figure 4.7. Stress-strain curve for a dry and a water-saturated Locharbriggs sample that were loaded under otherwise identical conditions. The water-saturated sample is considerably weaker than the dry one.

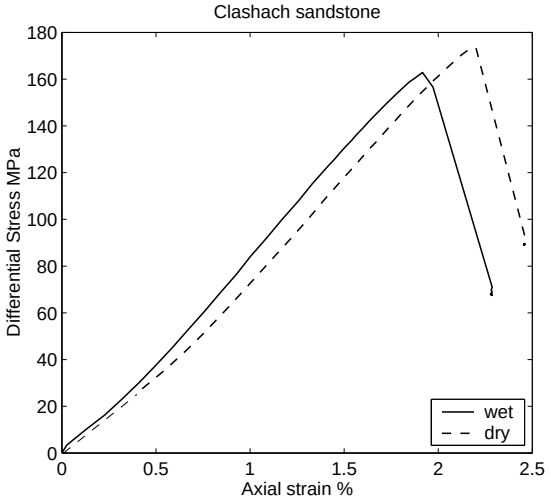

Figure 4.8. Stress-strain curve for a dry and a water-saturated Clashach sample that were loaded under otherwise identical conditions. The water-saturated sample is weaker than the dry one.

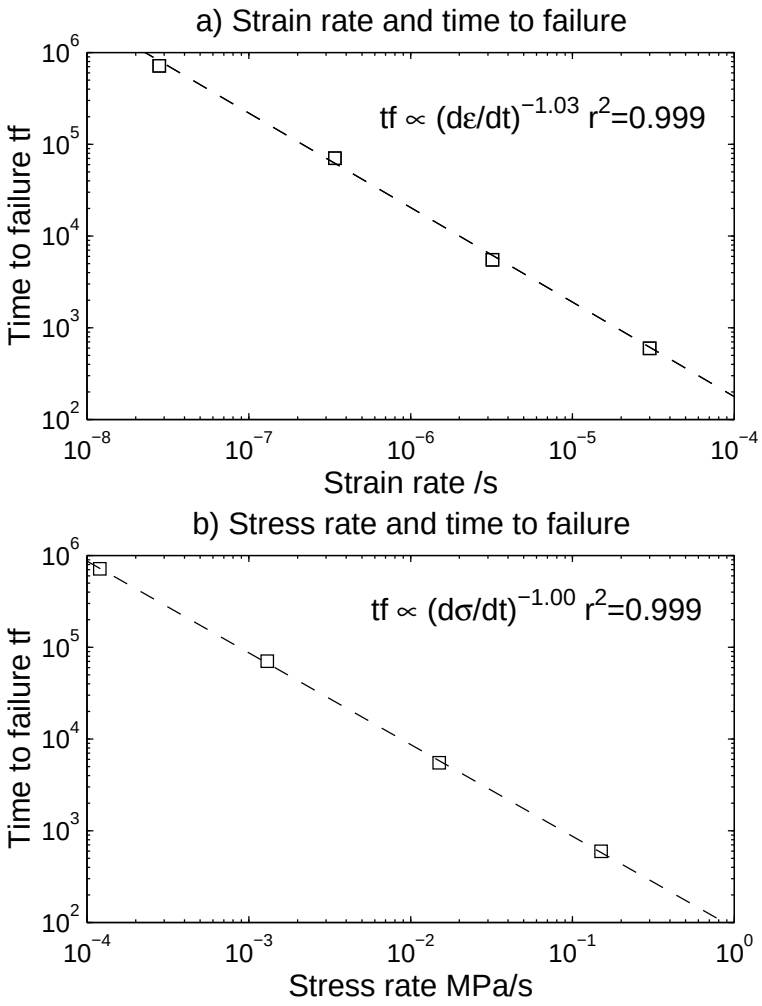

Figure 4.9. The failure time for the Locharbriggs specimen as a function of the (a) strain rate and (b) stress rate.

Clashach sandstone is considerably stronger than Locharbriggs sandstone due to its pervasive quartz cementation (*Wong and Wu*, 1995).

The elastic modulus E_m and the strength σ_{max} of both sandstones decreased with decreasing strain rate (table 4.1). For the Locharbriggs sandstone, the dependence of peak stress σ_{max} on the strain rate $\dot{\varepsilon}$ was found to obey either a power (4.5) or an exponential (4.6) law given by

$$\sigma_{max} = 10^{1.95}\,\dot{\varepsilon}^{0.008} = 89.1\,\dot{\varepsilon}^{\frac{n}{n+1}} \tag{4.5}$$

$$\sigma_{max} = 1.402 \log \dot{\varepsilon} + 88.2 \tag{4.6}$$

with an identical r-squared value of 0.81, as illustrated in figure 4.12. The power law exponent in (4.5) is very small, indicating only a weak dependence of the ultimate strength on the applied strain rate. It corresponds to a stress corrosion index n of 124 (*Sano et al.*, 1981). However, I believe that the use of a power law is not justified here, since the variation in rock strength was only few MPa. In fact, the best fit to the data was obtained by assuming a logarithmic dependence of strength on both strain rate and elastic modulus. The loading rate dependence of the strength of the Locharbriggs sandstone was best predicted by

$$\sigma_{max} = 1.11 \log(\dot{\varepsilon} \times E_m) + 82.4 \tag{4.7}$$

where E_m is the elastic modulus and the r-squared value is 0.90 (fig. 4.12).

The strength of Clashach sandstone decreased by 46.7 MPa as the strain rate was reduced from 10^{-6} to 10^{-8} /s. However, its strength did not decrease systematically with decreasing loading rate. At 10^{-5} /s Clashach strength was 162.8-168.5 MPa while the peak stress at 10^{-6} /s was 169.3 MPa. It is possible that the 10^{-6} /s sample was considerably stronger than the other samples due to normal lithological variation. Alternatively, subcritical crack growth may have a negligible effect at high strain rates of 10^{-5} and 10^{-6} /s. The strain

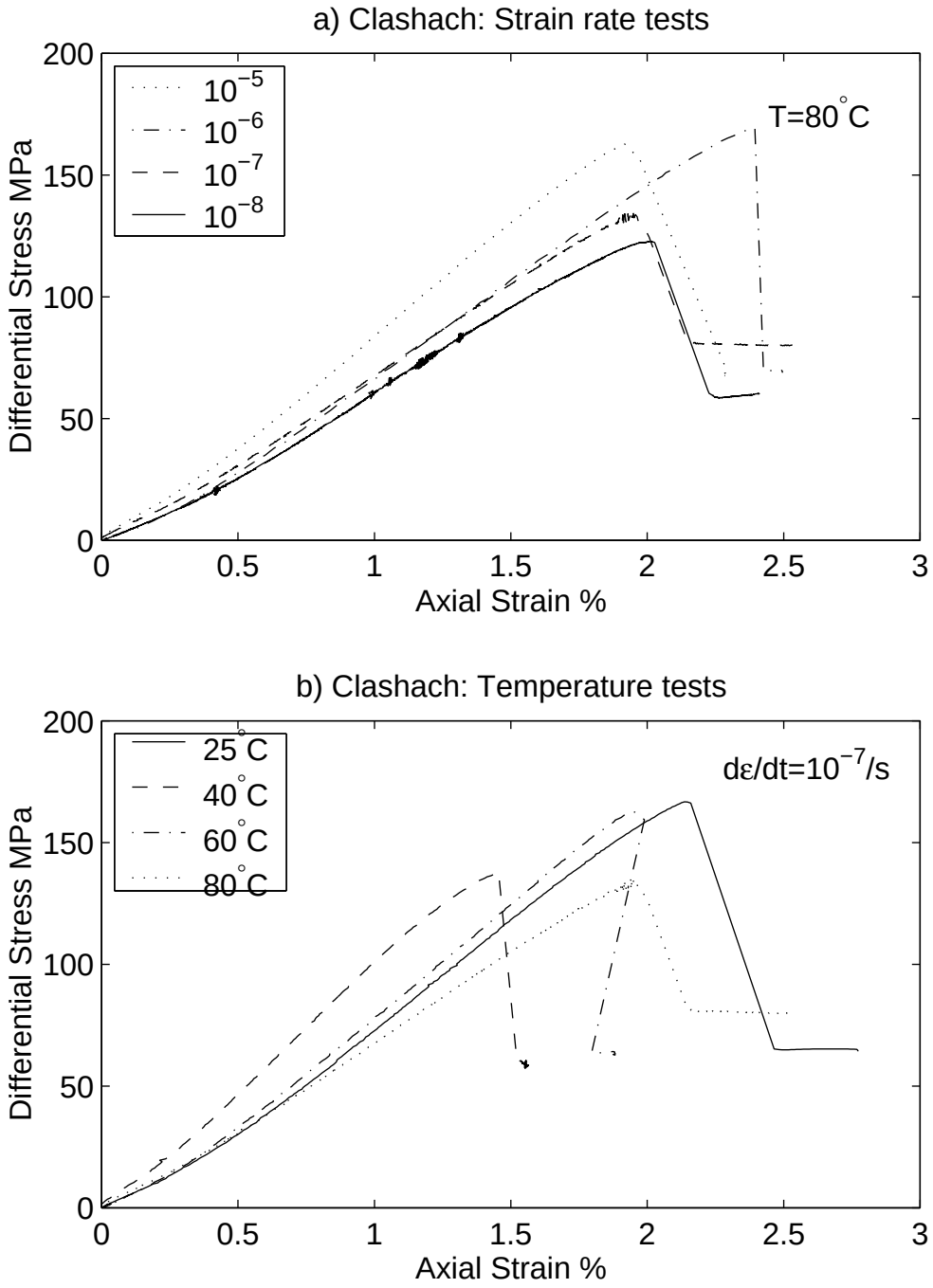

Figure 4.10. The stress-strain curves for Clashach sandstone deformed at (a) a temperature of 80°C with strain rates ranging from 10^{-5} to 10^{-8} /s and (b) strain rate of 10^{-7} at temperatures of 25-80 °C.

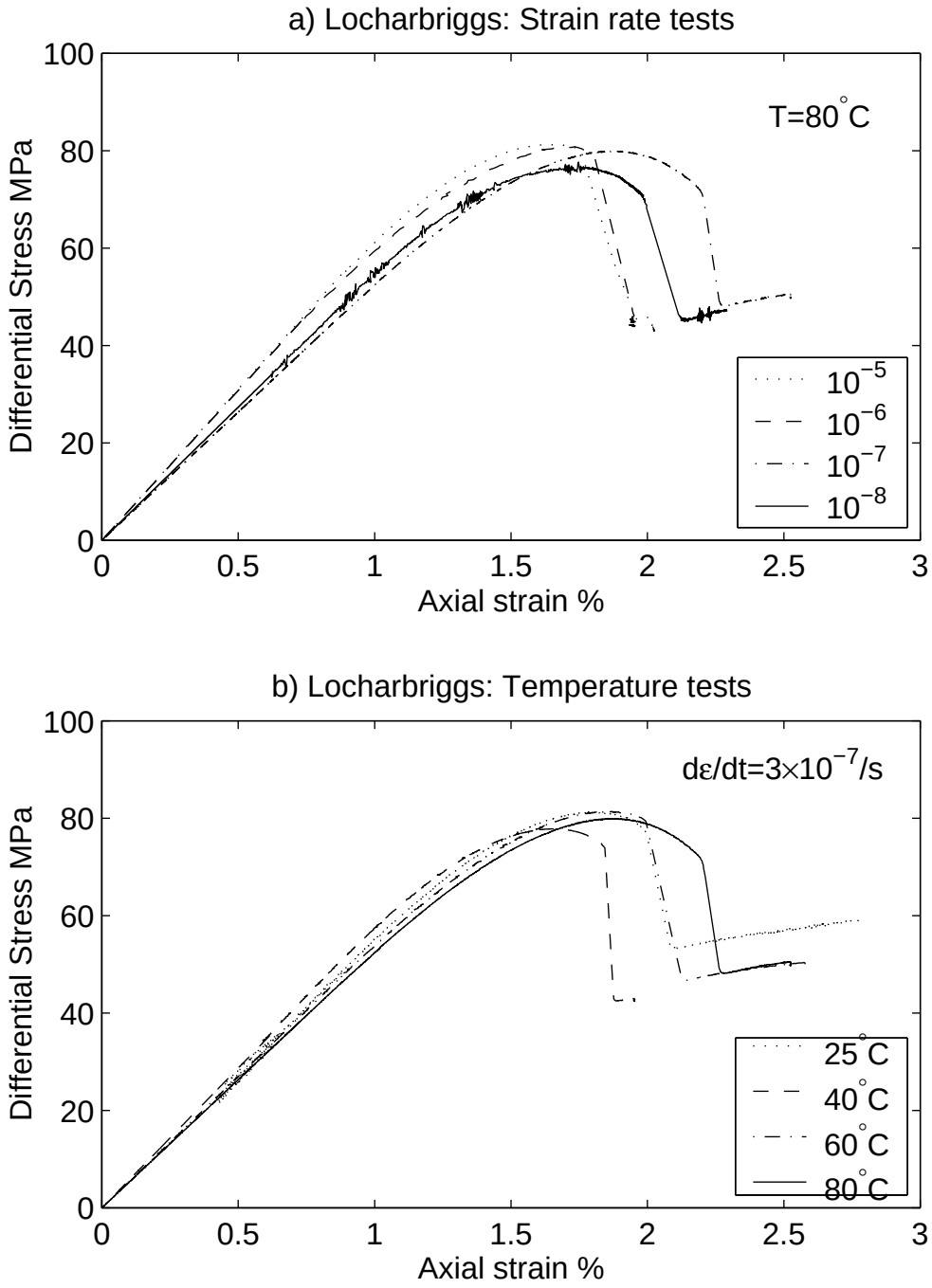

Figure 4.11. The stress-strain curves for Locharbriggs sandstone deformed at (a) a temperature of 80°C with strain rates ranging from 10^{-5} to 10^{-8} /s and (b) strain rate of 10^{-7} at temperatures of 25-80 °C.

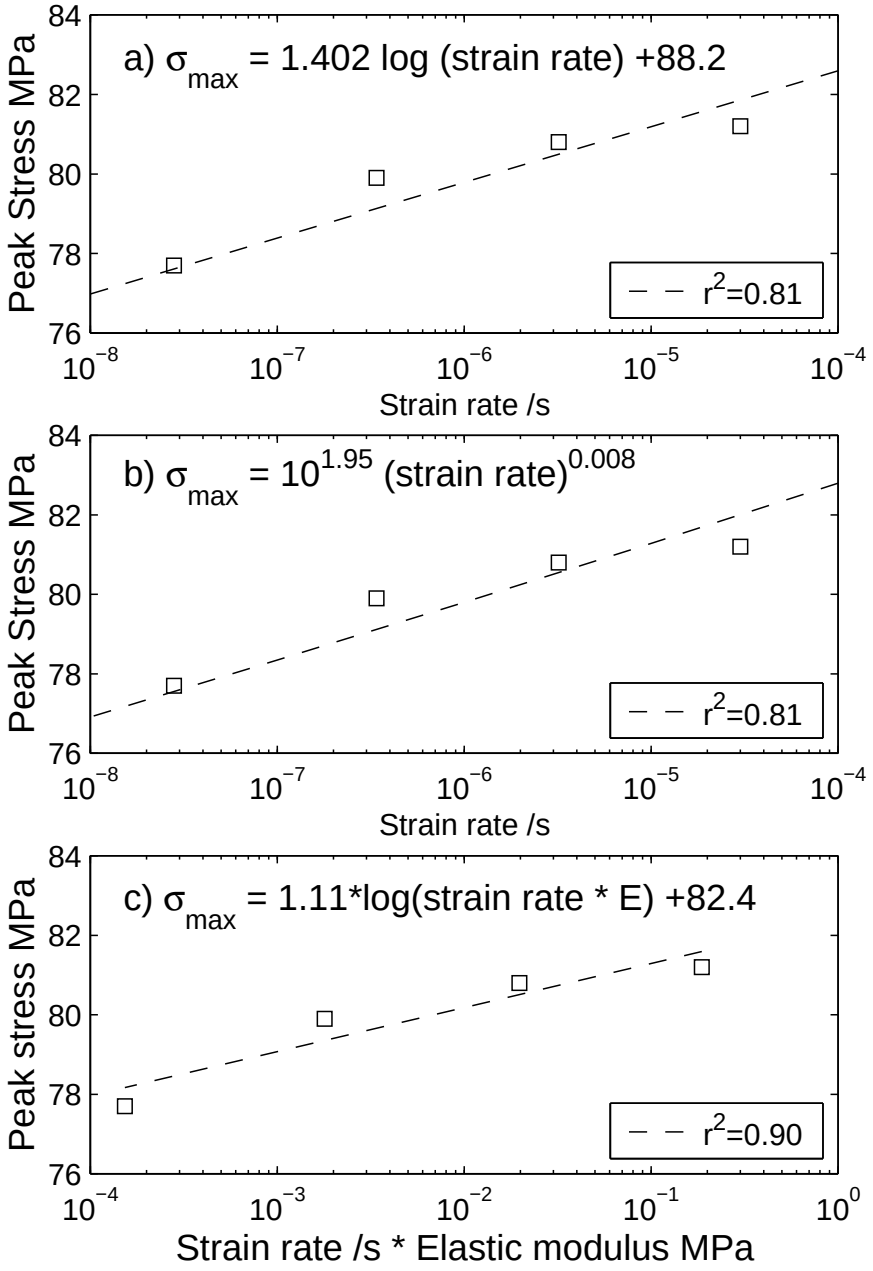

Figure 4.12. Strength of Locharbriggs sandstone as a function of strain rate. Both (a) logarithmic and (b) power law describe the data equally well. However, the best fit to the data was obtained assuming (c) a logarithmic dependence on the product of strain rate and the elastic modulus.

rate dependence of the Clashach peak stress was given by a power (4.8) or an exponential (4.9) law

$$\sigma_{max} = 10^{2.45}\,\dot{\varepsilon}^{0.047} = 281.8\,\dot{\varepsilon}^{\frac{n}{n+1}} \quad (4.8)$$

$$\sigma_{max} = 15.5 \log \dot{\varepsilon} + 240.2 \quad (4.9)$$

With an r-squared value of 0.86 the power law provided a slightly better fit than the exponential law (r^2=0.85), as illustrated in figure 4.13. The slope of the power law relation suggests a value of 21 for the Clashach stress corrosion index. At lower strain rates the pore fluid has more time to reach the crack tips and undergo chemical reactions, which is a plausible explanation for the observed reduction in strength with decreasing strain rate.

The elastic modulus of Clashach and and Locharbriggs sandstone ranged over 7096-9400 MPa and 5306-6219 MPa, respectively for the four strain rates used. Figure 4.14 shows reduction in the elastic modulus with decreasing strain rate. The elastic modulus was a logarithmic function of the strain rate given by

$$E_m = 777.7 \log \dot{\varepsilon} + 12687 \quad (4.10)$$

$$E_m = 339.6 \log \dot{\varepsilon} + 7828 \quad (4.11)$$

for the Clashach and Locharbriggs tests, respectively. The observed reduction in E_m with strain rate suggests more pervasive fracturing in the slow strain rate tests, since the presence of cracks lowers the elastic modulus (*Costin*, 1987). Furthermore, the stress drop at failure also appears to decrease with decreasing strain rate, as illustrated in figure 4.15. This could be an indication of a greater amount of ductile deformation in the slow strain rate tests. However, it appears that the stress drop $\Delta\sigma$ at failure for both Clashach and Locharbriggs specimen is described by an identical equation

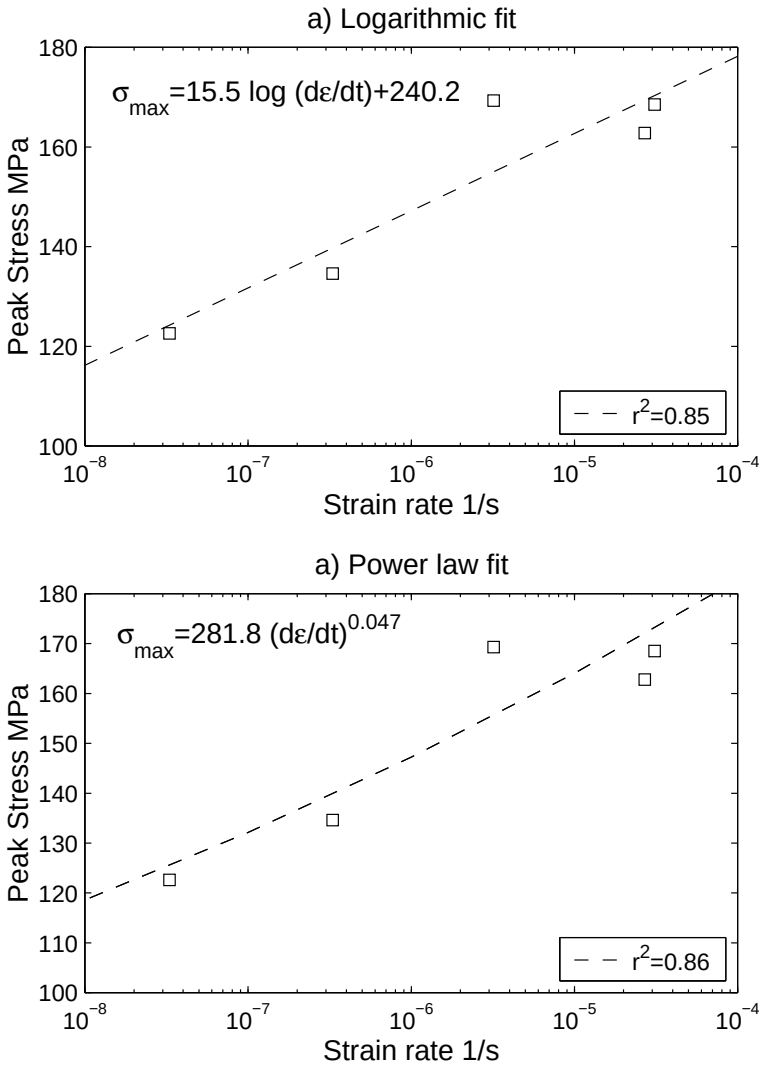

Figure 4.13. Strength of Clashach sandstone as (a) logarithmic and a (b) power law function of strain rate. Power law provides a slightly better fit.

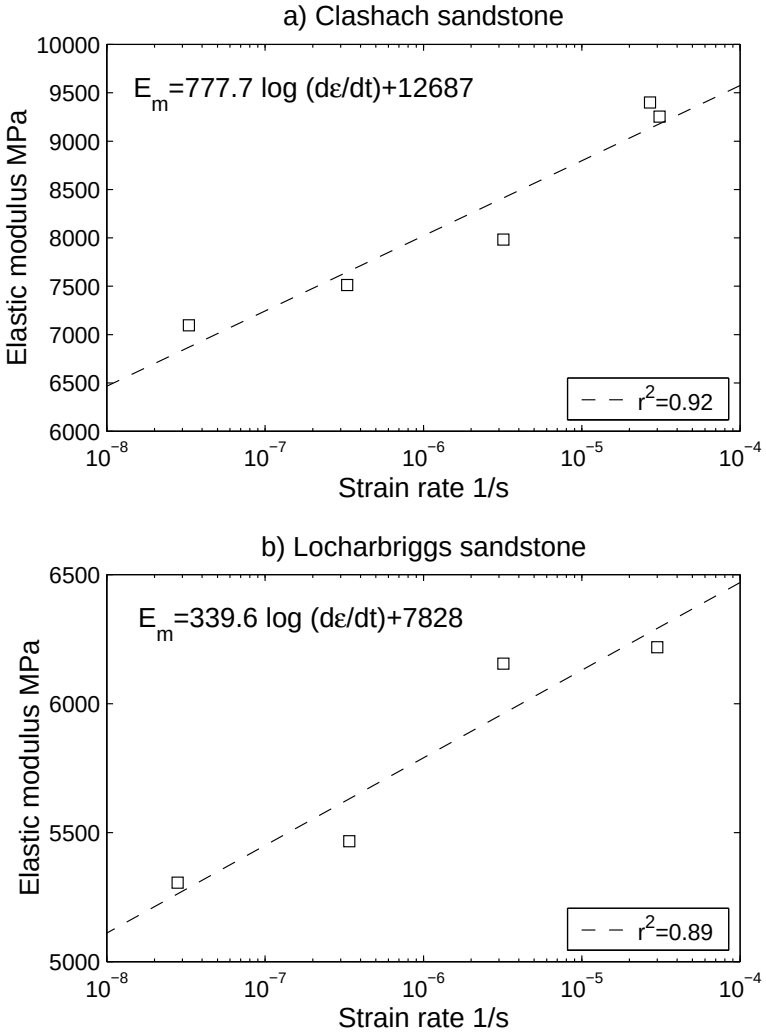

Figure 4.14. The elastic modulus of (a) Clashach and (b) Locharbriggs sandstone as function of strain rate. Note that the elastic modulus of the Locharbriggs sandstone is considerably less than that of the Clashach sandstone.

$$\Delta\sigma = 0.77\sigma_{max} - 35.6 \tag{4.12}$$

where σ_{max} is peak stress at MPa and the r-squared value is 0.92, as illustrated in figure 4.15. This observation implies that stress drop at failure is proportional to specimen strength.

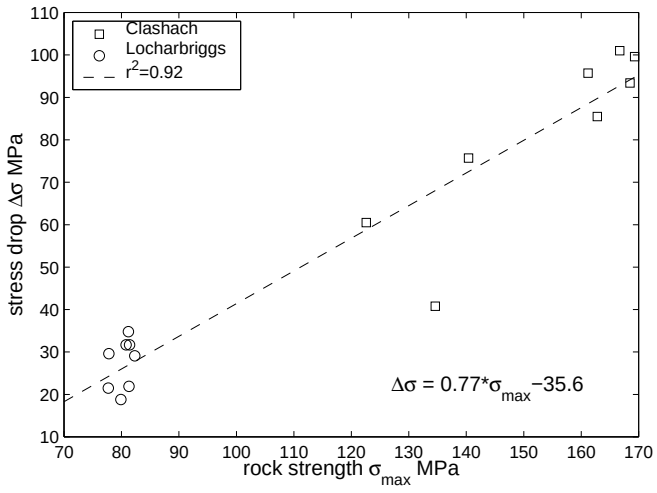

Figure 4.15. Stress drop at failure as a function of specimen strength.

4.6 Microstructural observations

Inter-granular and intra-granular fracturing was pervasive in the deformed specimen. Grain boundary opening was also evident in all deformed samples. Figures 4.16 to 4.19 show the shear band in the 80°C 10^{-6}/s and 10^{-8}/s Clashach and Locharbriggs tests, respectively. The Clashach sandstone has a larger grain size and the fault gouge consisted of partially or wholly fractured grains, indicating cataclasis. In the Locharbriggs sample the shear band contained undeformed grains hence suggesting grain translation and compaction. Among the mineral components, quartz contained a greater proportion of cracks. Oversized pores that contained remnants of feldspar grains were observed for both sandstones

Table 4.2. Linear and areal crack densities

Rock type	$\dot{\varepsilon}$ 1/s	Total crack no linear count	Total crack no areal count	Crack ρ /mm^2	Crack ρ /mm
Clashach	10^{-6}	190	610	79.4	4.0
Clashach	10^{-8}	204	613	79.8	4.3
Locharbriggs	10^{-6}	198	649	84.5	4.1
Locharbriggs	10^{-8}	289	805	105	6.0

deformed at 80°C using fast or slow strain rates. The origin of these features was attributed to the dissolution of feldspar grains. Microcracks were preferentially oriented in the direction of the shear band and maximum compressive stress in the 10^{-6}/s and 10^{-8}/s strain rate Clashach tests, respectively. Locharbriggs sandstone did not display a preferential microcrack orientation, possibly due to extensive grain translation.

The difference in deformation styles of the high and slow strain rate tests was further investigated by counting the microcrack density of the 80°C Clashach and Locharbriggs tests. Microcrack densities were determined from SEM micrographs of deformed samples, as described in section 3.5.6. The resulting linear and areal crack densities are listed in table 4.2. At 6.0/mm the linear crack density was higher for the 10^{-8}/s test than the 4.1/mm for the Locharbriggs 10^{-6}/s test. Similarly, the slow strain rate Clashach test had a higher crack density of 4.3/mm when compared to the high strain rate test with 4.0/mm. Furthermore, the areal crack densities were also higher in the slow strain rate tests. The higher crack densities of the slow strain rate tests could be caused by subcritical crack growth, which is likely to be the dominant mechanism for crack propagation in the slow strain rate tests.

4.7 Comparison to other studies

The results of my experiments demonstrate that the strength of both Locharbriggs and Clashach sandstones is reduced in the presence of water and on the application of a slower loading rate. The time and environment dependence of the mechanical

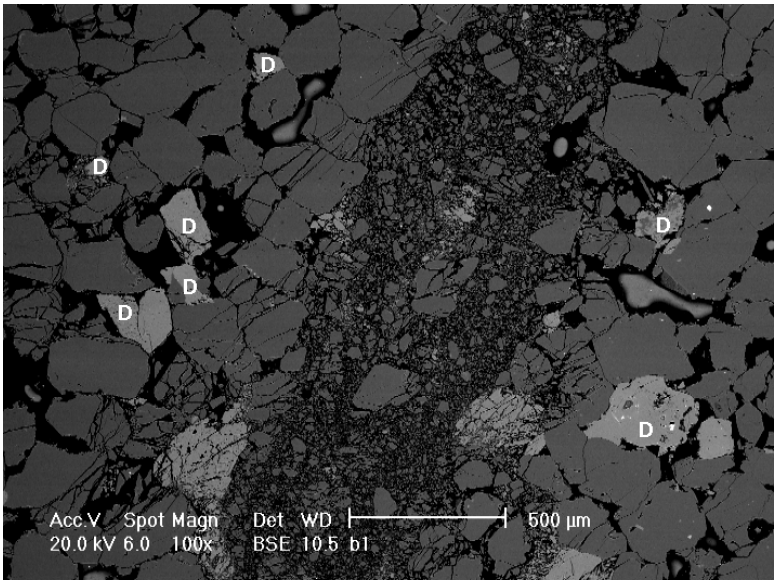

Figure 4.16. The shear band for the 10^{-6} Clashach tests. The microcracks were oriented parallel to the shear band in the 10^{-5}/s sample. The grains that showed signs of dissolution are marked *D*.

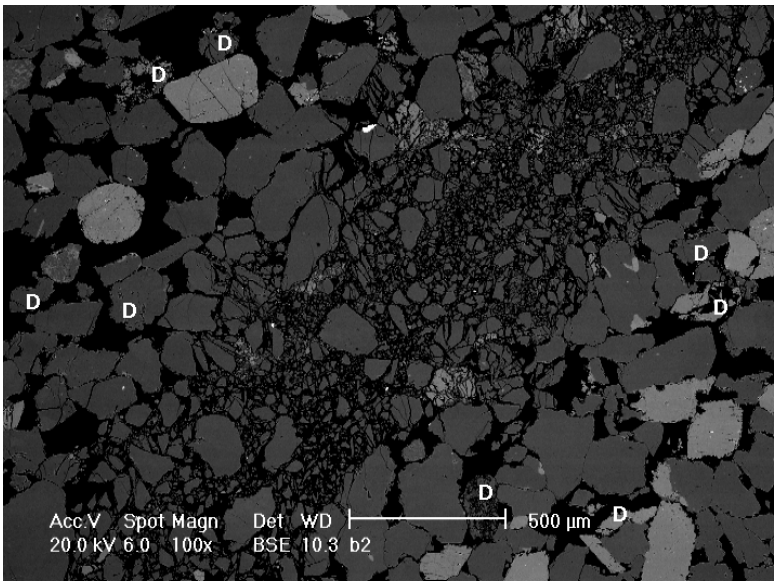

Figure 4.17. The shear band for the 10^{-8} /s Clashach test. The fractures generated in the 10^{-8} /s were aligned in the direction of σ_1. The grains that were being dissolved are labelled *D*.

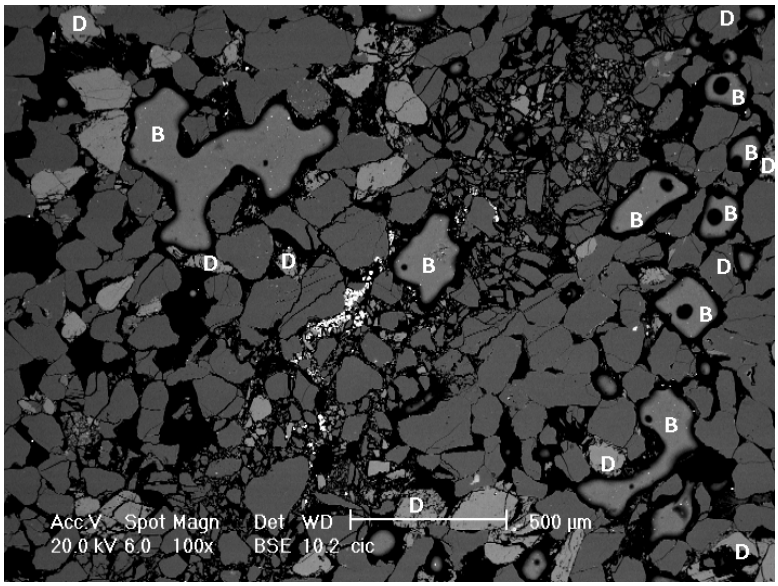

Figure 4.18. The shear band for the 10^{-6} /s Locharbriggs test. The grains that were being dissolved are labelled D. Unfortunately there were also some glue bubbles that are marked with B.

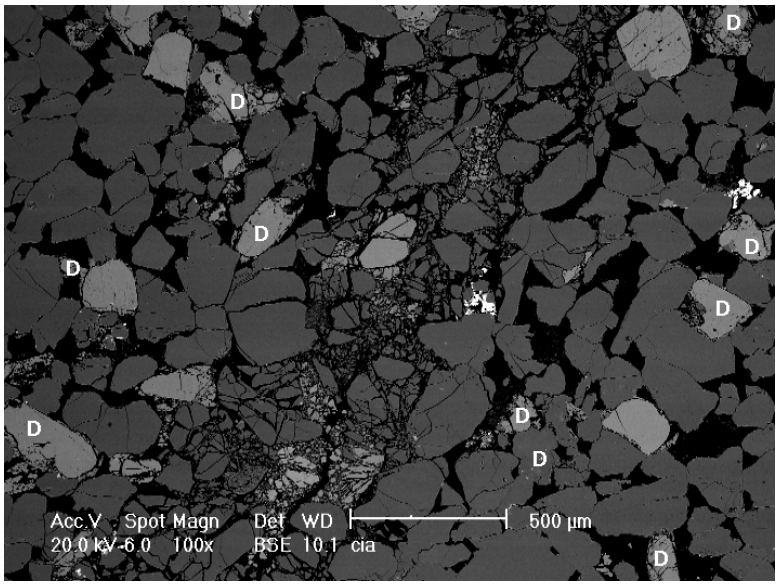

Figure 4.19. The shear band for the 10^{-8} /s Locharbriggs test. The grains that were being dissolved are labelled D.

properties of these sandstones is likely to be caused by subcritical crack growth since the LEFM approach cannot be used to explain the effect of strain rate on rock strength (*Mizutani et al.*, 1977; *Sano et al.*, 1981; *Costin*, 1987). Furthermore, both the stress and strain rates of my tests lie in the region at which subcritical crack growth is considered to operate. At 1.2×10^{-4} to 1.5×10^{-1} MPa/s, the loading rates used for my tests are well below the suggested upper limit 10^5 MPa/s for stress corrosion crack growth (*John*, 1972; *Sano et al.*, 1981). In fact, a reduction of rock strength by subcritical crack growth has been observed at strain rates of 0.1/s or less (*Serdengecti and Boozer*, 1961). The strain rates used for my tests are much slower. They range from 10^{-5} to 10^{-8}/s.

The relationship between specimen strength and applied strain rate can be described by using a power or a logarithmic law. The subcritical crack growth exponent predicted by the power law formulae (4.5 and 4.8) equals 21 and 124 for the Clashach and Locharbriggs sandstones, respectively. Neither of these values lie in the typical range of n=30-60 that has been measured for various rock types using the double torsion apparatus (*Atkinson and Meredith*, 1987b). However, the n-values obtained in my tests are within the experimentally determined range of n=8-151 quartz and quartz rich rocks (table 2.1). It is probably due to the difficulties associated with double torsion tests on rocks (*Swanson*, 1984) that the typical range of the subcritical crack growth index for sandstones is not well constrained by previous experimental studies. For instance, the standard deviations in n obtained by *Swanson* (1984) ranged from 10-35 % of the measured n-value.

The power law provides the best way to describe the effect of strain rate on the strength of the Clashach sandstone. Power-law dependence of strength on the applied strain rate has been previously observed for Oshima granite (*Sano et al.*, 1981; 1982) and fine grained limestone (*Lankford*, 1981). Both of these workers also predicted power-law scaling based on standard constitutive equations for subcritical crack growth. The power law (4.8) gives just 50 MPa for the strength of Clashach sandstone at a crustal strain rate of 10^{-16}/s. Hence, equation (4.8) predicts that the failure strength of the Clashach sandstone is only a third in crustal conditions in comparison to a dry, high strain rate laboratory test. A decrease in rock strength by a factor of two to three has also been suggested in previous studies (*John*, 1972; *Sangha and Dhir*, 1972; *Peng*, 1973, *Sano et*

al., 1981, *Costin*, 1987). However, the logarithmic formula cannot be used to determine the long-term strength of the Clashach sandstone, since (4.8) gives a failure strength of 0 MPa at a geologically reasonable strain rate of 3.2×10^{-16} /s.

Other workers have proposed that subcritical crack growth ceases to have a measurable effect at very slow strain rates. Based on the model of *Kemeny and Cook* (1987), *Reuschlé et al.* (1989) suggested that subcritical crack growth no longer has an effect on the strength of a limestone at a strain rate as high as 10^{-9} to 10^{-10} /s (fig. 4.6). Alternatively, the long term strength of a material could be marked by a 'critical stress' corresponding to the onset of dilation in a rock deformation test (*Bieniawski*, 1966; *Newman and Newman*, 1969). However, *Sangha and Dhir* (1972) showed that the long term strength of Laurencekirk sandstone is likely to be higher than the stress level corresponding to the onset of dilation. At 69 MPa their prediction is in good agreement with my results for the Locharbriggs sandstone. The power (4.5) and logarithmic (4.6 and 4.7) formulae suggest that the strength of Locharbriggs sandstone is 66.4, 65.8 and 68.4, respectively, at a crustal strain rate of 10^{-16}/s. It is not possible to distinguish between the power (4.5) and the logarithmic (4.6) expression for the Locharbriggs tests, since both equations describe the data equally well, with an r-squared value of 0.81. The best prediction of the rock strength is obtained by assuming a logarithmic dependence of a factor involving both strain rate and elastic modulus (r^2=0.90).

The elastic modulus of both sandstones decreases with decreasing loading rate. The relationship of E_m to the applied strain rate can be described by a logarithmic law, which predicts E_m of 244 MPa and 2394 MPa for the Clashach and Locharbriggs sandstones at $\dot{\varepsilon}$=10^{-16}/s. Systematic decrease in another elastic modulus (Young's modulus) with the applied deformation rate has also been observed for Laurencekirk sandstone in the uniaxial compression tests of *Sangha and Dhir* (1972). The decrease in the elastic modulus suggest a greater amount of damage in the slow strain rate tests that is likely to be caused by subcritical crack growth.

It has been suggested that a decrease in strain rate is essentially equivalent to increasing temperature (*Serdengecti and Boozer*, 1961). Both processes are thought to enhance ductility and reduce rock strength. In my tests stress drop at failure decreases with decreasing strain rate. This observation is indicative of a

more ductile deformation style in the slow strain rate tests. However, it appears that the stress drop for both rock types can be described by an identical equation (4.12). Hence the stress drop at sample failure is related to the strength of the rock sample rather than increased ductility at a lower strain rates. In fact, brittle fracturing is likely to dominate the deformation style of both sandstones in the range of temperatures and strain rates used in this study. For instance, failure occurs by brittle faulting in all of my tests. The microstructural observations also suggest a dominance of brittle fracturing in my tests. It is probably due to the relatively small temperature range (55/300=16%) that there are no systematic changes associated with test temperature that can be seen above the 'noise' of sample variability. This observation is consistent with the triaxial compression of *Serdengecti and Boozer* (1961) and *Blacid et al.* (1981) on Berea and Galesville sandstones, respectively. Neither of the studies reported systematic changes in the rock strength in the temperature range of 26 to 204°C. This is probably due to the relative insensitivity of brittle deformation to test temperature (*Paterson*, 1978).

There are no consistent changes in the fault angle θ with test temperature or strain rate. Previous studies have reported an increase in θ with increasing temperature (*Paterson*, 1978) or strain rate (*Sangha and Dhir*, 1972). There is also a tendency for θ to increase with increasing magnitude of principal stresses at failure (*Jaeger and Cook*, 1976). However, in triaxial testing the fault often runs into one platen or diagonally across the specimen (*Jaeger and Cook*, 1976). It is possible that the precise angle of the fault is just an artifact of the loading geometry. In fact, *Paul and Gangal* (1967) suggested that the fault angle is determined by the fact that it runs diagonally across the specimen (*Jaeger and Cook*, 1976). This kind of fault geometry is frequent in the Clashach tests, yielding a fault angle of 26 degrees. However, for all of the wet Locharbriggs tests the fault intersects the circumference of the cylinder away from the sample ends. The fault angles vary from 25 to 40 degrees and hence they are well within the 22-49 degrees that were obtained for these sandstones under true triaxial stress conditions (*Crawford et al.*, 1995). It is interesting to note that *Crawford et al.* (1995) did not observe an increase in θ with increasing confining pressure, although such trend is commonly observed in conventional triaxial testing (*Bésuelle et al.*, 2000). Hence, the angle of the shear band may be related to the loading geometry rather than the test environment.

4.8 Conclusion

The results of triaxial compression tests demonstrate that the strength of Clashach and Locharbriggs sandstone depends systematically on the test environment and applied loading rate. In the presence of water, the strength of Clashach and Locharbriggs sandstones is reduced by 6 and 11 %, respectively. The effect of applied strain rate on the strength of Locharbriggs sandstone is best described by a logarithmic law (r^2=0.90), which predicts an ultimate strength of 68 MPa at crustal strain rate of 10^{-16}/s. In contrast, the peak stress of Clashach sandstone varies considerably. As the strain rate decreases from 10^{-6} to 10^{-8}/s the strength of Clashach sandstone is reduced over 46 MPa. The relationship of the peak stress to the applied loading rate is best described by a power law (r^2=0.86) that predicts a strength of just 50 MPa at 10^{-16}/s. The reduction in rock strength with decreasing strain rate is likely to be caused by subcritical crack growth by the stress corrosion mechanism.

The elastic modulus of Clashach and Locharbriggs also decreases with decreasing strain rate. The relationship of the elastic modulus to the applied loading rate is a logarithmic one, with and r-squared value of 0.89 and 0.92 for the Locharbriggs and Clashach sandstones, respectively. The observed decrease in the elastic modulus suggests a more pervasive fracturing in the slow strain rate tests, possibly due to stress corrosion crack growth.

However, there are no systematic changes in rock strength or ductility associated with test temperature. This is probably due to the small temperature range of 25-80°C. Failure occurs by brittle faulting in all of the tests. The fault angle ranges from 25 to 40 degrees to the direction of maximum compressive stress. Microstructural observations suggest that compressive deformation is accommodated by the growth of intra-granular and transgranular cracks that are oriented in the direction of maximum compressive stress. The growth of these microfractures is the likely cause of the recorded AE activity, that will be discussed in the next chapter.

Chapter 5

Quantification of Damage

It is important that elastic shocks increase remarkably preceding a main rupture of a heterogeneous medium both under increasing stress and constant stress. Mogi (1962)

5.1 Introduction

Rock failure under triaxial compression is preceded by significant departures from purely linear elastic behaviour (*Paterson*, 1978). The inelastic strain hardening and softening phases result from the time-dependent growth of axial microcracks (*Meredith et al.*, 1990). Due to the difficulties in directly observing fracture growth during a typical rock deformation test (*Costin*, 1987), various indirect methods of monitoring crack growth have been developed. One of the most commonly used techniques is recording acoustic emissions (AE). These are wave packets generated by the rapid release of energy within a material. Each wave packet defines an acoustic emission event (*Meredith*, 1990). It is often assumed that an AE event is caused by a propagating crack, although some of the AE generated during rock deformation tests may also come from other irregular structural movements, such as dislocation slip, phase transition or crack faces rubbing together (*Meredith and Atkinson*, 1983, *Costin*, 1987; *Glover et al.*,1995; *Zang et al.*, 1998). However, only a fraction of microfracturing events are likely to be accompanied by a detectable AE (*Lockner*, 1993a, *Zang et al.*, 2000). Generally, these will be the largest events.

Acoustic emission is detected using piezoelectric transducers that are cemented either on the sample surface or on the platens in the deformation apparatus. The majority of the recorded AE events lie between 100 kHz and 1 MHz (*Scholz*, 1968a) and this is also the commonly used frequency band for the recording instruments. It is the frequency content and the typical source dimensions that distinguish AE studies from seismology. In addition, earthquakes are assumed to occur of previously existing faults while AE studies are generally conducted on intact rock samples (*Lockner*, 1993a). On the other hand, both disciplines are concerned with the propagation and detection of elastic waves.

5.2 Previous AE work

5.2.1 Historical perspective

The first measurement of elastic energy released by fracture was reported by F. Kishinoye in 1937 for the purpose of investigating earthquakes (*Mogi*, 1962). For the English speaking audience the small noises that are emitted during compressive loading were introduced by *Obert and Duval* (1942). However, the first major experimental and theoretical study of AE, brittle fracture and its relation to earthquakes was undertaken by *Mogi* (1962), who observed a close correlation between AE energy and inelastic strain as well as the similarity in the statistical behaviour of AE and earthquakes: both phenomena satisfy the *Gutenberg-Richter* (1954) relationship between frequency of occurrence and magnitude (*Mogi*, 1962; 1967). His pioneering work was followed by *Scholz* (1968a,b), who discovered that the cumulative AE event count N is directly proportional to the inelastic volumetric strain, see figure 5.1 after *Sano et al.* (1981). Since then, AE have been detected under a variety of loading conditions, including uniaxial compression (*Mogi*, 1962; *Scholz*, 1968a, 1968c; *Cox and Meredith*, 1993; *Shah and Labuz*, 1995; *Zang et al.*, 1996, 1998), triaxial compression (*Meredith et al.* 1990; *Sammonds et al.*, 1994; *Rao and Kusunose*, 1995; *Lei et al.*, 2000), tensile (*Meredith and Atkinson*, 1983), stress cycling (*Sondergeld and Estey*, 1981), frictional sliding (*Yabe*, 2002), uniaxial creep (*Yanagidani et al.*, 1985; *Hirata*, 1987) and triaxial creep (*Lockner and Byerlee*,

1977; *Rao and Kusunose*, 1985; *Hirata et al.*, 1987; *Satoh et al.* 1996; *Baud and Meredith*, 1997). The commonly recorded AE parameters are event rate (dN/dt), peak amplitude, energy and frequency content of the signals (*Meredith*, 1990). However, some caution is required since the energy and frequency content are likely to be affected by the transducer size and the electronics used (*Costin*, 1987).

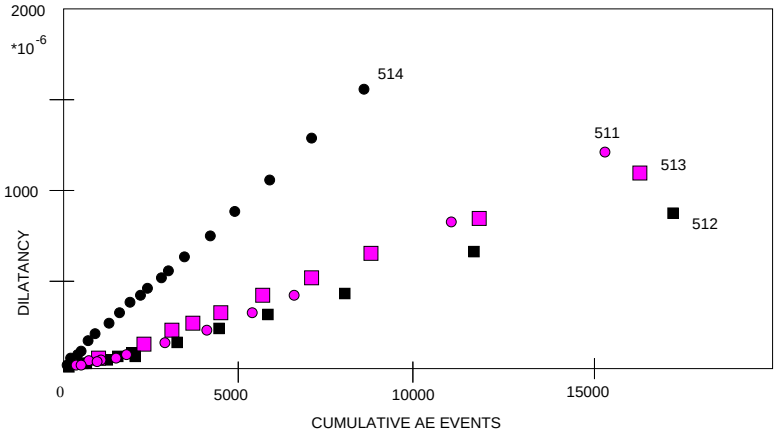

Figure 5.1. The inelastic volumetric strain Δ as a function of the cumulative AE event count. The volumetric strain is a measure of the increase in crack porosity during a deformation test. The AE event count is directly proportional to the increase in volumetric strain. From *Sano et al.* (1981).

5.2.2 AE Event rate statistics

A single transducer, cemented to the sample surface, provides a simple experimental setup for monitoring acoustic emissions in a deforming rock specimen (*Lockner*, 1993a). The number of AE events are logged as a function of time and the maximum amplitude provides an estimate of the event size. Subsequently, the amount of AE events can be used as a measure of the damage caused by microcracking due to the direct proportionality between inelastic volumetric strain and the AE event count N (figure 5.1). A close scrutiny of the temporal evolution of the AE event rate dN/dt or the cumulative event count N is motivated by the similarity between AE after- and foreshock sequences and the equivalent earthquake ones. Although a majority of early AE studies were carried out with

the intention of finding such earthquake precursors, it is generally observed that laboratory rock fracture is dominated by a large number of foreshocks, while the seismicity in the earth's crust is characterised by an abundance of aftershocks (*Main*, 2000). The modified Omori law, that can be used to describe the the time dependence of earthquake and laboratory aftershock rate R_a is given by

$$R_a \propto (c' + t - t_m)^{-p} \tag{5.1}$$

where c' is a constant and t_m is the time of the main shock (*Utsu et al.*, 1995, *Main*, 2000). Similarly, foreshock sequences can be characterised using

$$R_f \propto (c' + t_m - t)^{-p'} \tag{5.2}$$

where p' is the exponent for foreshocks and R_f is the foreshock rate. The estimated p-values for earthquake aftershock sequences range from 0.6 to 2.5 with a median of 1.1 (*Utsu et al.*, 1995).

Laboratory studies have observed a more gradual acceleration of seismic event rate for foreshocks than the few recorded foreshock sequences for earthquakes (*Liankopoulou-Morris et al.*, 1994). This does not leave much hope for successful earthquake prediction based on laboratory AE sequences. Nevertheless, studies of the temporal evolution of AE activity are important in quantifying the damage evolution in a deforming rock sample. In fitting (5.1) or (5.2) to laboratory data it is customary to assume that the fracture of the whole rock specimen corresponds to the main shock. Both exponential and Omori law type power law evolution of R_a and R_f have been observed in previous studies. In their creep tests, *Mogi* (1962) reported an exponential increase in R_f, while *Scholz* (1968b) observed a power law decay in R_a. However, in Mogi's case the whole rock sample was not fractured, which may explain the differing observations. Subsequently, *Hirata* (1987) criticised the approach of Scholz, Mogi and their contemporaries and suggested that the fracture of a rock specimen is analogous to the fracture of a whole tectonic plate. He carried out a constant stress experiment

on Murata basalt and treated individual bursts of AE activity as foreshock-aftershock sequences. The aftershock sequences of Hirata's test underwent a transition from obeying an exponential law given by

$$R_a = \vartheta_1 \exp(-\vartheta_2 t) \tag{5.3}$$

where ϑ_1 is a constant, to obeying Omori's law with decreasing value of ϑ_2 at 2.3-0.3, indicating an increasing heterogeneity of the frictional strength distribution (*Mikumo and Miyatake*, 1979), as the sample approached failure. Hence, in Hirata's experiment the fracture condition gradually changed from exponential to power law type with the evolution of the fracture process. Although not mentioned by *Hirata* (1987), the frequency curve of earthquake aftershocks also undergoes a transition from obeying a power law ($0 < t < 100$ days) to an exponential law ($t > 100$ days) (*Mogi*, 1962). This phenomenon is a direct consequence of the upper and lower cutoffs, that must exist for all power laws in the real world (*Bonnet et al.*, 2001; *Narteau et al.*, 2003): without such limits, aftershocks would go on forever!

5.2.3 Stress corrosion and AE event rate

Alternatively, the AE event rate dN/dt can be considered as a remote measure of the crack growth velocity. Although the rock sample contains numerous microcracks, their behaviour can be viewed analogous to that of a stress corrosion system dominated by a single macrocrack (fig. 5.2), if a fractal distribution of microcracks is assumed (*Main and Meredith*, 1991; *Vinciguerra*, 1999). Numerous studies have observed a direct proportionality between dN/dt and crack growth velocity during stress corrosion crack growth in minerals and rocks (e.g. *Scholz*, 1972; *Meredith and Atkinson*, 1983). It has also been shown that v and dN/dt are related to the stress intensity factor K by an identical functional form given by (*Meredith and Atkinson*, 1983; *Main et al.*, 1993)

$$F_i = \frac{dN}{dt} = N_0 \left(\frac{K}{K_0} \right)^{n'} \tag{5.4}$$

where n' is an effective stress corrosion index, since n and n' are equal within few percent (*Main et al.*, 1992, 1993) and F_i is the frequency of AE events. The power law dependence of dN/dt or crack velocity on the stress intensity factor is illustrated in figure 5.2 after *Main and Meredith* (1991). The parallel lines on this graph indicate that n is proportional to n'.

5.2.4 Characteristic frequency-magnitude scaling of AE data

In addition to its characteristic foreshock-aftershock sequences, AE also exhibits power-law frequency-magnitude relationship, that corresponds to the Gutenberg-Richter law for earthquakes (*Mogi*, 1967; *Meredith and Atkinson*, 1983; *Lockner*, 1993a). In the Gutenberg-Richter relation earthquake magnitudes are expressed with a logarithmic scale of instrumentally recorded magnitudes. Hence, the AE amplitudes reported in dB are first divided by 20 in order to produce a comparable scale. In laboratory conditions AE is monitored above some detection threshold m_c (usually 40 dB) and hence the frequency-magnitude relationship can be written as

$$logF_c = a - b(m - m_c) \tag{5.5}$$

where F_c is the number of events above a critical threshold m_c and b is the seismic b-value (*Main et al.*, 1993). The frequency-magnitude distribution of the AE events in my tests is well characterised by a power-law relationship, as shown in figure 5.3. For a typical deformation test, the temporal evolution of the seismic b-value and the 95 % confidence limit σ_b can be evaluated using the maximum likelihood method of *Aki* (1965) given by

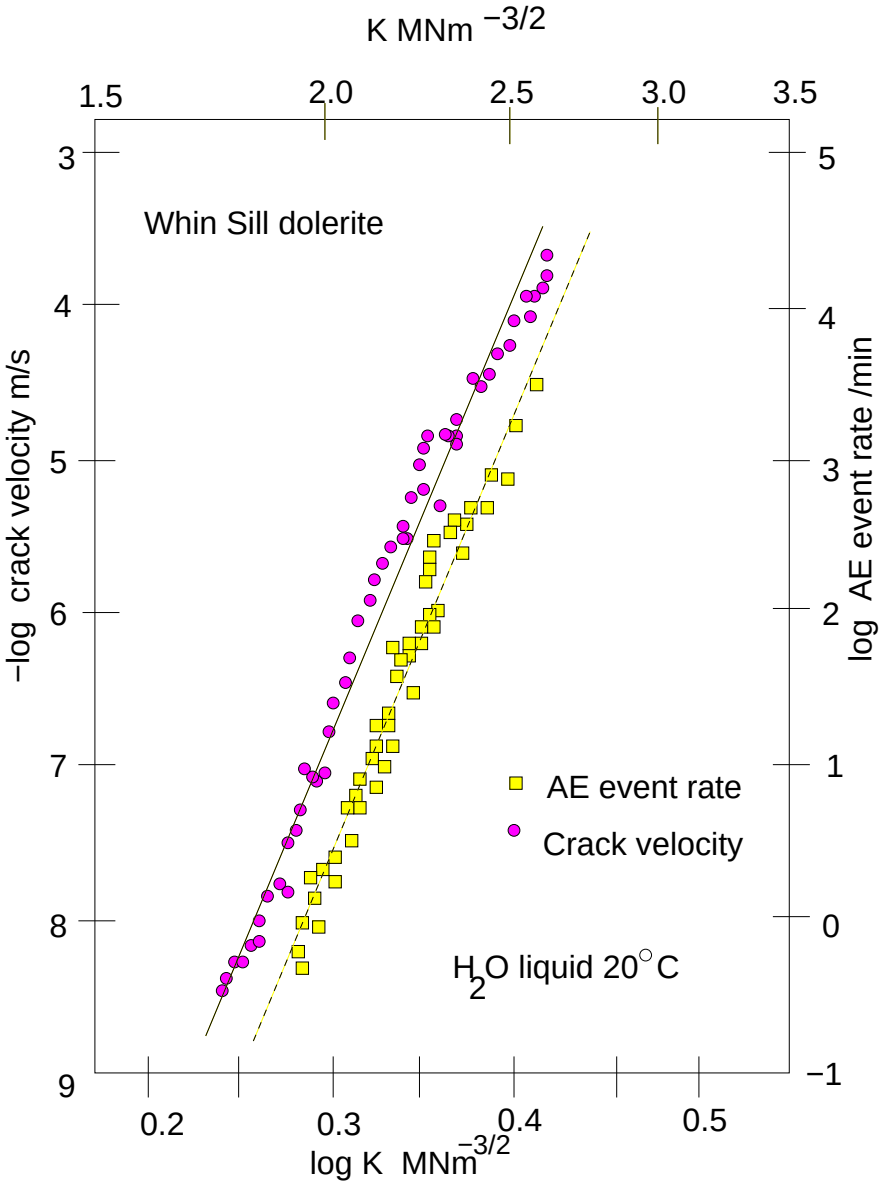

Figure 5.2. The dependence of crack velocity (circles) and event rate (rectangles) on the stress intensity factor K during a wet, tensile, double torsion test on Whin Sill Dolerite. The power law exponent n' (5.4) equals the slope of the straight line on the log-log plot. Redrawn from *Main and Meredith* (1991)

.

$$b = \frac{N_e \log e}{(\Sigma m_i - N_e M_c)} \tag{5.6}$$

$$\sigma_b = 1.96 b / \sqrt{(N_e)} \tag{5.7}$$

where Σm_i is the sum of all event amplitudes above m_c, and M_c is half the amplitude interval less than m_c to take account the finite magnitude increment. N_e is the total event count for the interval considered and σ_b is the standard deviation. The characteristic increase in AE amplitudes prior catastrophic failure is manifested in decreasing b-values as specimen failure is approached (*Main et al.*, 1989; *Meredith et al*, 1990; *Lockner et al.*, 1991; *Main et al.*, 1992; *Sammonds et al.* 1992; *Main et al.* 1993; *Zang et al.*, 1996, 1998, 2000; *Lei et al.*, 2000). In addition, the seismic b-value has been observed to be negatively correlated with stress intensity factor K, indicating a higher proportion of smaller events at lower K values (*Meredith and Atkinson*, 1983).

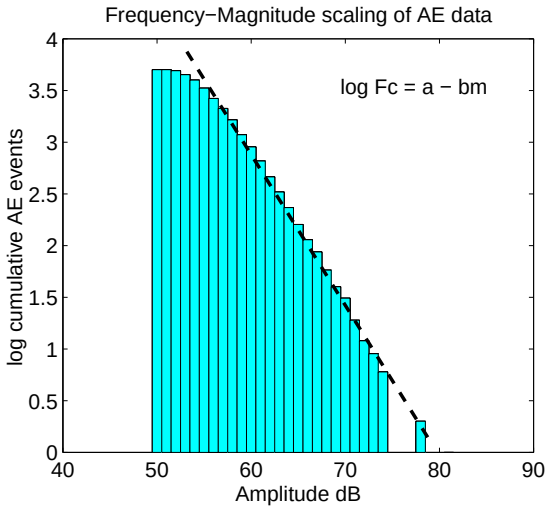

Figure 5.3. The the cumulative AE event count F_c versus event amplitude, which is a measure of the event magnitude, for a Locharbriggs 25°C test that was conducted at a strain rate of 10^{-7} s^{-1}. The cumulative AE event count F_c and the event magnitude show a distinct power law scaling.

5.2.5 Hypocentre mapping and polarity studies

The source physics of AE events have been studied by hypocentre mapping, which involves determining the locations of individual events. Hence, a large enough sample is required in order to accommodate the required amount of AE transducers, which are arranged in an array that is similar to a seismic network (*Sondergeld and Estey*, 1981; *Yanagidani et al.*, 1985; *Hirata et al.*, 1987; *Lockner et al.*, 1991; *Rao and Kusunose*, 1995; *Satoh et al.*, 1996; *Zang et al.*, 1996, 1998, 2000; *Lei et al.*, 2000). Recent advances in AE hypocentre mapping have been reviewed by *Lockner* (1993a), *Kusunose* (1995) and *Lei et al.* (2000). The focal mechanism i.e. the mode of cracking may also be determined by carrying out a moment tensor inversion or a polarity study. The moment tensor inversion uses the first pulse amplitudes (*Shah and Labuz*, 1995; *Lei et al.*, 2000) and a polarity study is carried out on the basis of first pulse signs (*Zang et al.*, 1998; *Lei et al.*, 2000). While early AE studies postulated that a fault is formed by the growth and linkage of microcracks, that emanate from pre-existing damage sites (*Scholz*, 1968c; *Kranz*, 1983), recent AE studies of granite indicate that the microfracturing at or near the yield stress has hardly any effect on the location of the future fault (*Lockner et al.*, 1991; *Lockner and Byerlee*, 1993; *Lei et al.*, 2000).

Polarity studies of AE first motions have yielded important new information on the fracture mode responsible for the recorded AE events. In analysing the AE data the events are characterised as type-S, type-T or type-C depending on whether a positive polarity is recorded on most, some or none of the AE sensors, respectively. Tensile sources generate positive polarities (type-T) at the AE sensors, while shear cracking is the likely source of a type-S event (*Zang et al.*, 1998). Although the growth of tensile microcracks in the direction of maximum compressive stress is the proposed mechanism responsible for sample dilatancy (*Tapponier and Brace*, 1976; *Moore and Lockner*, 1995), several polarity studies have reported an abundance of S-type events in their tests (*Sondergeld and Estey*, 1981; *Yanagidani et al.*, 1985; *Shah and Labuz*, 1995; *Zang et al.*, 1998, 2000; *Lei et al.*, 2000). For instance, *Zang et al.* (1998, 2000) reported that 70 % of AE events were type-S during uniaxial compression in Aue granite. Such controversy can be explained with the 'sliding crack model of axially open microcracks' (*Brace and Bombolakis*, 1963; *Ashby and Hallam*, 1986) since it includes both modes of

cracking (*Yanagidani et al.*, 1985). However, investigation using high resolution scanning electron microscopy (SEM) has not produced any evidence of shear cracks (*Tapponier and Brace*, 1976). In addition, relating the located AE events to microcracks on a thin section is notoriously difficult (*Zang et al.*, 1998).

5.2.6 AE source parameters inferred from the dislocation theory of seismic source

The dislocation model of the seismic source (*Kanamori and Anderson*, 1975) provides a means by which the seismic surface wave magnitude M_s can be related to the fault of length L, width w and area wL. The dislocation model is based on the Haskell source and fault models.

The simplest model of an earthquake source can be regarded as a linear ramp function $M(t)$ of rise time τ_r. The far field displacement pulse $u(t)$ resulting from this *Haskell source* is a boxcar pulse with a duration τ_r (*Shearer*, 1999). The ramp function $M(t)$ and the far field displacement pulse $\dot{M}(t)$=$u(t)$ are illustrated in figure 5.4.a from *Shearer* (1999). The Haskell source (fig. 5.4.a) provides a good description of the far field response of earthquakes that can be approximated by a point source. Furthermore, a fault can be modelled by integrating over individual point source displacements on the fault surface. Lets assume that the a rupture propagates along a fault of length L at a velocity v_r. In such case, the shape of the far field displacement pulse is given by a convolution of two boxcar functions with widths τ_r and τ_d, where τ_d is the rupture duration time (*Shearer*, 1999). This is the *Haskell fault model* and it is illustrated in figure 5.4.b. The far field displacement pulse resulting from such a line source is a trapezoid in the time domain.

The convolution of two boxcar functions in the time domain can be represented by the product of two sinc functions in the frequency domain (*Shearer*, 1999). Hence, the far field amplitude spectrum $|A(\omega)|$ of the Haskell fault model is given by

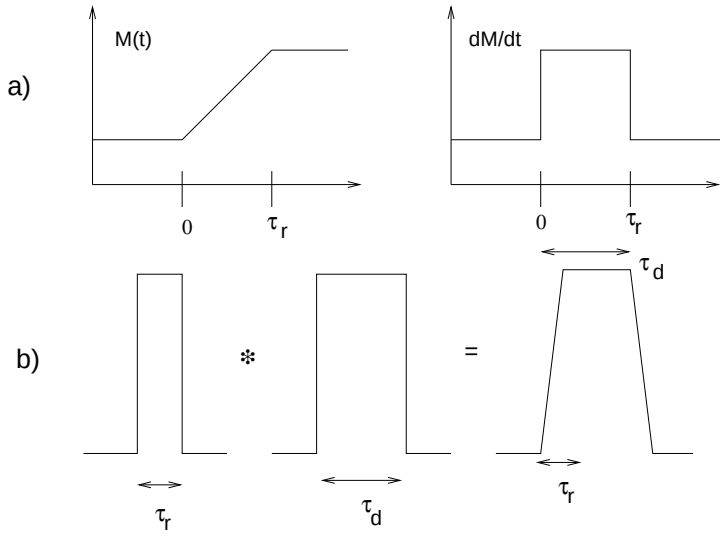

Figure 5.4. (a) The Haskell source model. Haskell source is a linear ramp function $M(t)$ that results in far field displacement pulse $\dot{M}(t)$=$u(t)$. (b) The Haskell fault model. The shape of the far field pulse is a trapezoid that equals convolution of two boxcar functions with widths τ_r (rise time) and τ_d (rupture duration time). Redrawn from *Shearer* (1999).

$$|A(\omega)| \propto \mu s L w |sinc(\omega\tau_r/2)||sinc(\omega\tau_d/2)| \tag{5.8}$$

where s is the average fault slip, w is the width of the fault and τ_d equals L/v_r at an average azimuth $\Theta = \pi/2$. On the other hand, the concept of seismic moment is based on the equivalence of a shear displacement discontinuity and a double couple source (*Kanamori and Anderson*, 1975). Dislocation across a surface Σ in an elastic medium provides a mathematical model of an earthquake fault. Hence, the total moment M_0 can be expressed in terms of the average dislocation s by

$$M_0 = \mu A_f s \tag{5.9}$$

where A_f is the surface area. Subsequently, similarity of the dislocations can be

introduced by assuming a constant strain drop (5.10) and a constant aspect ratio (5.11), given by

$$\frac{s}{L} = \frac{\Delta\sigma}{y} = constant \tag{5.10}$$

$$\frac{w}{L} = constant \tag{5.11}$$

Hence, the seismic moment M_0 can be considered to be proportional to L^3. Moreover, the surface wave magnitude M_s is determined from the logarithm of the surface wave amplitude at $T_0 = 20s$, which is the natural period of the recording instrument. At $\omega = \omega_0 = 2\pi/T_0$ the surface wave magnitude M_s is proportional to $\log|A(\omega)|$,

$$M_s \propto \log\left[sLwF\left(\tau_r, \frac{L}{v_r}\right)\right] = \log\left[sLw|sinc(\omega_0\tau_r/2)||sinc(\omega_0 L/2v_r)|\right] \tag{5.12}$$

at the average azimuth $\Theta = \pi/2$. In equation (5.12) the function $F\left(\tau_r, \frac{L}{v_r}\right)$ takes different asymptotic values depending on the relationship of the rise time τ_r and event duration L/v_r to the natural period of the recording instrument T_0. This is because it is possible to approximate $|sinc\, x|$ as 1 for $x < 1$ and $1/x$ for $x > 1$. Thus, the surface wave magnitude M_s can be related to the fault length L via

$$M_s = \begin{cases} \log L^2 & if\ \tau_r < \frac{T_0}{\pi}\ and\ \frac{L}{v} > \frac{T_0}{\pi} \\ \log L^2 & if\ \tau_r > \frac{T_0}{\pi}\ and\ \frac{L}{v} < \frac{T_0}{\pi} \\ \log L & if\ \tau_r > \frac{T_0}{\pi}\ and\ \frac{L}{v} > \frac{T_0}{\pi} \\ \log L^3 & if\ \tau_r < \frac{T_0}{\pi}\ and\ \frac{L}{v} < \frac{T_0}{\pi} \end{cases} \tag{5.13}$$

Hence, the relationship between τ_r, τ_d and T_0 determine the dependence of M_s on fault length. Figure 5.5 suggests that most earthquakes scale as $M_s \sim L^2$. Combining (5.13) with $M_0 \sim L^3$ yields the general relationship between M_s and M_0

$$\log M_0 \propto \log(L)^3 = c^* m + d \tag{5.14}$$

where c^* is a scaling parameter, that depends on τ_r, τ_d and T_0 while d is proportional to system sensitivity (*Kanamori and Anderson*, 1975). Hence, for events with very long durations compared to the natural period of the recording instrument c^* equals 3, while very short events correspond to c^*=1.0. However, the for most intermediate size earthquakes, c^* is equal to 1.5. The c^*-values 1, 1.5 and 3 correspond to the sensor acting as a strain meter, velocity transducer and an accelerometer, respectively (*Kanamori and Anderson*, 1975). Assuming (5.10) and (5.14), the seismic b-value (5.6) can be related to the power law exponent D_e via

$$D_e = \frac{3b}{c^*} \tag{5.15}$$

In practice, (5.15) has upper and lower bounds of $D_e = 1$ and $D_e = 3$, since microcracks are confined to a volume ($D_e < 3$) and due to the finite crack length (*Main*, 1988, 1991). Traditionally, c^*-values have been inferred from the calculated b-values with these upper and lower bounds. In other words, for $1 < b < 3$ and $1 < D_e < 3$, c^* must equal 3, while $0.5 < b < 1.5$ indicates that c^*=1.5.

Previous laboratory tests have suggested both c^*=1.5 and c^*=3. The double torsion tensile tests of *Meredith and Atkinson* (1983) yielded b-values in the range of $1 < b < 3$, hence suggesting that c^*=3 (*Main et al.*, 1989). On the other hand, majority of triaxial compression tests have observed a b-value in the range of 0.5 to 1 .5, indicating a c^*-value of 1.5 (*Main et al.*, 1989; *Meredith et al.*, 1990; *Main et al.*, 1992; *Sammonds et al.*, 1992, 1994).

Hence, various empirical equations relating seismic parameters (M_o, L, M_s) also have a theoretical basis, namely, the the static crack and dislocation models of earthquake sources *Kanamori and Anderson* (1975). The characteristic power law scaling of the frequency-magnitude relation (5.5) and the temporal evolution of seismic activity (5.1) can be considered indicative of the self-similarity in

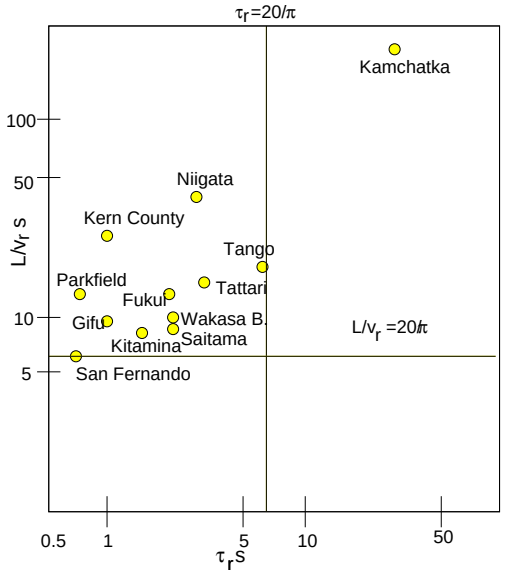

Figure 5.5. The relationship between rupture time L/v_r and rise time τ_r for some earthquakes. The relative values for rupture time and rise time determine the dependence of M_s on L and M_0. From *Kanamori and Anderson* (1975).

the earthquake source function. Since both types of power-law scaling are also observed for AE data one might assume that the source functions for the tensile microcracks, that are the likely sources for the recorded AE activity, are similar to earthquake sources. Hence, fundamental empirical equations of earthquake seismology can be used to infer the AE source parameters from the event data.

5.2.7 Quantification of damage using the AE catalogue

In order to quantify the damage caused by microfracturing, a damage parameter can be extracted from the AE catalogue. For instance, the cumulative event count N can be used as a measure of the damage volume, due to the direct proportionality between N and inelastic volumetric strain (*Scholz*, 1968a; *Sano et al.*, 1981). In general, the volume fraction of cracks can be expressed using the crack density parameter χ that is given by

$$\chi = \frac{n_c < c >^3}{V} = \frac{\Sigma c^3}{V} \tag{5.16}$$

where n_c is the number of cracks with half length c in volume V. *Cox and Meredith* (1993) described a methodology, by which a damage parameter similar to (5.16) can be derived from the AE catalogue. Their definition of a damage parameter χ is based on the dislocation theory of seismic source (*Kanamori and Anderson*, 1975) that relates fault length L to the seismic magnitude m via (5.14). Hence, combining (5.14) and (5.16) gives the damage parameter χ in terms of the recorded AE parameters

$$\chi = \frac{10^{A'}}{V} \Sigma 10^{c^* m} \tag{5.17}$$

where c^* is equals 1.5 for an AE sensor acting as a velocity transducer and m is the event magnitude in dB/20.

In order to test the applicability of (5.17) in describing the the evolution of microcrack damage, χ can be used to calculate the effective Young's modulus by using the dilute crack model of *Walsh* (1965) and the self-consistent model of *Bruner* (1976), as described in *Cox and Meredith* (1993). In the Walsh and Bruner models the ratio of initial stiffness E_0 to its modified value E' is given by (5.18) and (5.19), respectively

$$\frac{E_0}{E'} = 1 + F'\chi' \tag{5.18}$$

$$\ln \frac{E_0}{E'} = H'\chi' \tag{5.19}$$

$$\chi' = \sum_{i=1}^{N} 10^{c^* m} \tag{5.20}$$

where F' and H' are scaling factors and χ' is the working damage parameter. Hence, F' and H' can be determined from the slope of E_0/E' and $\ln E_0/E'$ versus

χ', respectively. Such methodology was used by *Cox and Meredith* (1993) and *Sammonds et al.* (1994) in order to reconstruct the measured stress-strain curves. They observed the superiority of the Bruner model in predicting the constitutive stress-strain behaviour and they attributed this to the better treatment of crack interaction of the *Bruner* (1976) model. In addition, damage was consistently overestimated in the strain softening region due to the isotropic damage parameter (5.20) that was used in the inversion procedure. The use of an anisotropic damage would be more appropriate in describing the high crack densities and crack-to-crack interaction, that are likely to dominate the deformation style in the strain softening phase (*Sammonds et al.*, 1994).

5.2.8 Deformation rate dependence of AE

The theoretical basis for deformation rate dependence of AE activity was set by *Mogi* (1962), who regarded brittle fracturing as a stochastic process. For a constant stress rate test the probability of fracture of occurrence is given by

$$\mu_m(t) = \beta_1 e^{\beta_2 \sigma_a} = \beta_1 e^{\beta_2 \dot{\sigma} t} \tag{5.21}$$

where σ_a is the applied stress, $\dot{\sigma}$ is the stress rate, t is time and β_1, β_2 are constants that are related to the material strength. Equation (5.21) predicts that the acceleration of the AE rate dN/dt can be very rapid if β_2 is large, as illustrated in figure 5.6.

However, in practice very little has been done to investigate the effect of strain rate on the AE activity in rocks. *Sano et al.* (1981) conducted uniaxial compression tests at strain rates ranging from 10^{-4} to 10^{-8} s^{-1} on Oshima granite. In his tests the AE event rate evolved in a similar manner to the inelastic volumetric strain rate: both parameters increased with increasing strain rate, as predicted by figure 5.1. On the basis of frictional sliding tests on Westerly granite, *Yabe* (2002) suggested that the rate dependence of AE event energy causes rate dependence of frictional properties, since AE activity is part of the frictional energy loss.

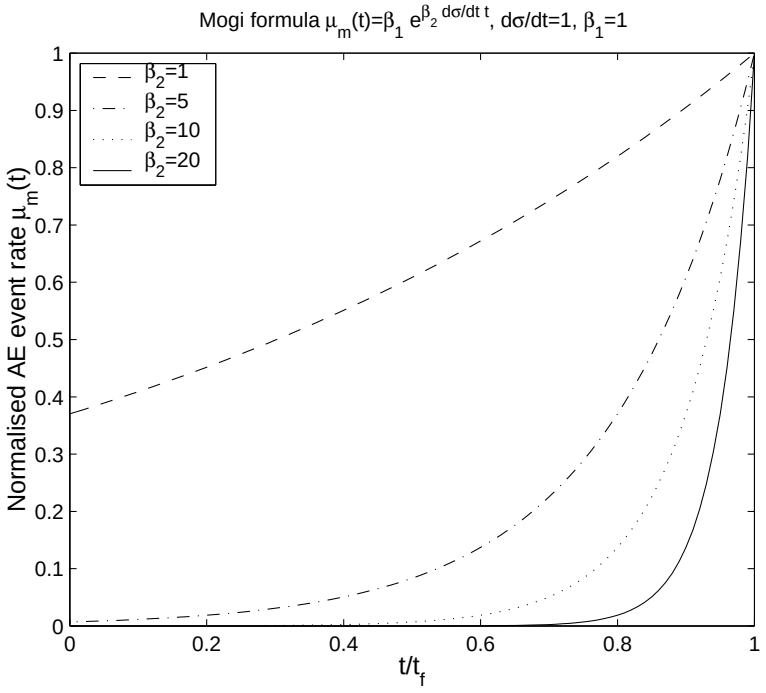

Figure 5.6. The dependence of AE event rate dN/dt on the deformation rate as predicted by the stochastic model of *Mogi* (1962). Here β_1 in (5.21) equals 1, $\dot{\sigma} = d\sigma/dt = 1$ and t=0-1, where t_f=1. β_2 takes values 1,5,10 and 20.

5.3 AE data

5.3.1 Introduction

The main reason why AE monitoring was used in this study was to obtain a reliable measure of the damage introduced by microcrack growth inside the test specimen. In this section I will first discuss some general features of the AE dataset and then proceed to quantify the damage due to microfracturing in terms of cumulative properties derived from the AE catalogue. Subsequently, the validity of the newly defined indicators of damage is assessed by stress history matching.

5.3.2 General characteristics of the AE data

Figures 5.7 and 5.8 illustrate the temporal evolution of the differential stress, AE event rate dN/dt and the seismic b-value (5.6) for two 80°C tests at a strain rate of 10^{-5} /s for the Clashach and Locharbriggs sandstones, respectively. For the Clashach sandstone (fig. 5.7) no distinct strain hardening phase was observed at a high strain rate of 10^{-5} /s, although significant AE activity began prior the peak stress was attained. However, the linearity in the stress versus time curve did not indicate an elastic (reversible) process: the AE activity accelerated rapidly up to the peak stress, indicating irreversible microfracturing inside the test specimen. After the peak stress was attained dN/dt decreased dramatically to a period of apparent quiescence, which can be attributed to critical crack coalescence (*Main et al.*, 1989). Dynamic instability was followed by a quick recovery in AE event rate and a subsequent decrease in a manner similar to earthquake aftershocks. The similarity in the temporal evolution of the AE foreshock and aftershock sequences with respect to specimen failure time was a characteristic feature of the Clashach tests. In contrast, the Locharbriggs sandstone (fig. 5.8) exhibited a more gradual acceleration of the AE event rate, followed by quiescence and a less pronounced aftershock activity.

It is possible that the quiescence, that was observed in both Clashach and Locharbriggs tests, is only apparent. Such apparent quiescence could be caused by the over-saturation of the measuring equipment because of the overlapping of small events in the high event rate period that precedes sample failure. As a consequence the AE event rate may underestimate the actual microcrack damage and this is why I also considered damage accumulation in terms of cumulative AE energy. This feature of the AE catalogue is further investigated in section 5.3.3.

The temporal evolution of AE activity exhibited a clear dependence on the applied loading rate. The acceleration of AE activity prior specimen failure became more rapid as the strain rate decreased. Figure 5.9 shows the AE event rate for the 80°C Clashach tests that were carried out at a strain rates ranging from 10^{-5} to 10^{-8} /s. The evolution of AE event rate in the Locharbriggs tests also displayed a similar strain rate dependence. This kind of behaviour is not predicted by the *Mogi* (1963) model (5.21). In my tests the stress rate is inversely proportional to the specimen failure time t_f (figure 4.9) and hence the *Mogi* formula (5.21)

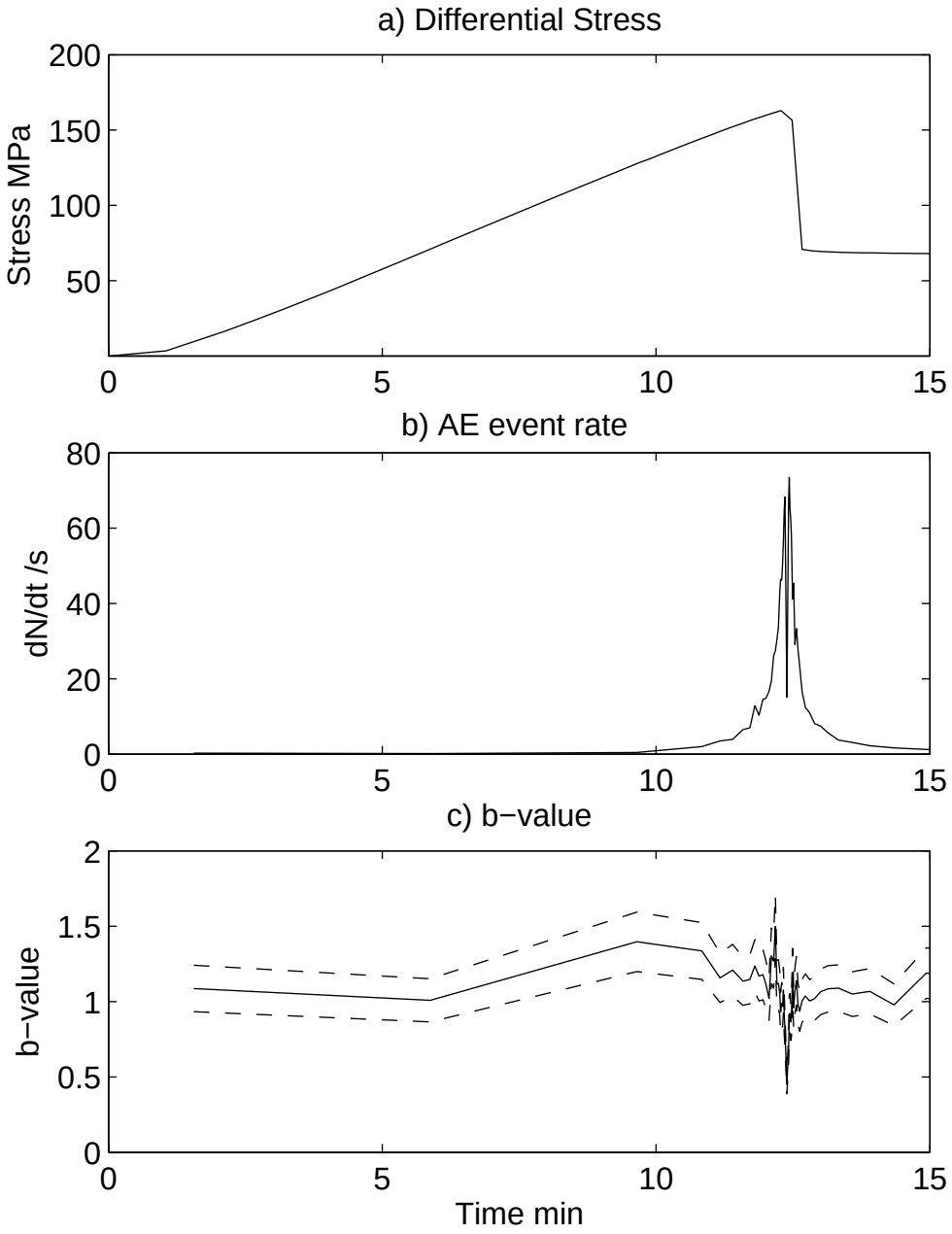

Figure 5.7. The temporal evolution of a) Differential Stress b) AE event rate dN/dt per minute and c) seismic b-value for a Clashach 80° C test that was carried out at a strain rate of 10^{-5} /s. The event rate and the b-value (6) were calculated in 50-event non-overlapping windows. The dotted line is the nominal 95% confidence limit (5.7).

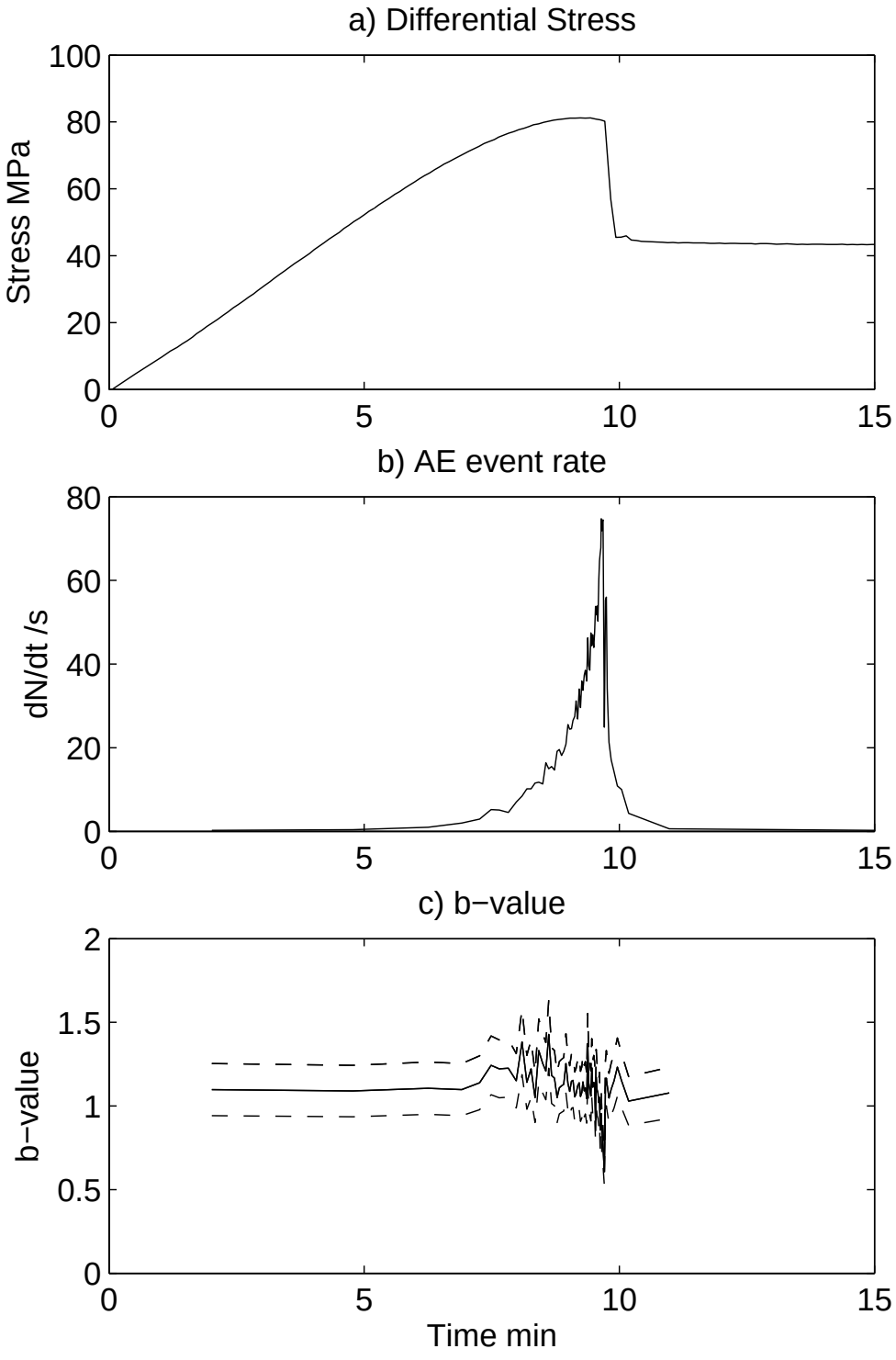

Figure 5.8. The temporal evolution of a) Differential Stress b) AE event rate dN/dt and c) seismic b-value for a Locharbriggs 80° C test that was carried out at a strain rate of 10^{-5} /s. The event rate and the b-value were calculated in 50-event non-overlapping windows. The dotted line is the nominal 95% confidence limit (5.7).

does not predict a strain rate dependence of AE activity. The deformation rate dependent evolution of AE activity illustrated in figure 5.9 suggests that specimen failure time becomes more difficult to predict as the strain rate decreases.

The temporal evolution for the seismic b-value as well as the b-values for each test (table 5.1.) were calculated using the maximum likelihood method (5.6) of *Aki* (1965). The temporal evolution of the b-value was characterised by a decrease in b-value with increasing stress. A b-value minimum b_f was observed immediately prior dynamic failure of the test specimen for both Clashach and Locharbriggs sandstones. The minima b_f ranged from 0.45 to 0.78 and from 0.61 to 0.96 for the Clashach and Locharbriggs sandstones, respectively, as shown in table 5.1. The calculated b-values ranged from 0.45 to around 1.5, hence suggesting that c^*=1.5 in (5.15).

Whether a double b-value anomaly was observed in any of these tests is debatable, since the evolution of the b-value depends somewhat on the bin size n used for the calculation. In other words, a local minimum that appears with n=50 may not be so well defined at n=200. This point is illustrated in figure 5.10., that shows the calculated b-values for n=50, 100, 150 and 200 for two 80°C Clashach tests. More importantly, the b-value itself also appears to be a function of bin size. The b-value minimum preceding specimen failure ranged from 0.60 to 0.85 for n=50 and n=100, respectively. However, for n=50 to 200 the calculated b-values were consistently between 0.6 and 1.5, hence suggesting a c^*-value of 1.5.

Although the magnitude of the b-value may depend on the bin size used for the calculation, relative b-values are nevertheless important in characterising the distribution of fracture sizes within a system. In my tests, the relative changes in the b-value minimum b_f and in the b-value b_t for the entire test were found to be correlated with deformation rate. Both b_f and b_t increased with decreasing strain rate (table 5.1.), hence suggesting a greater proportion of smaller events in the slow strain rate tests. For the Locharbriggs sandstone, the b-value for the individual tests was found to be a linear function of the logarithm of the strain rate, given by

$$b_t = 0.81 - 0.06 \log \dot{\varepsilon} \tag{5.22}$$

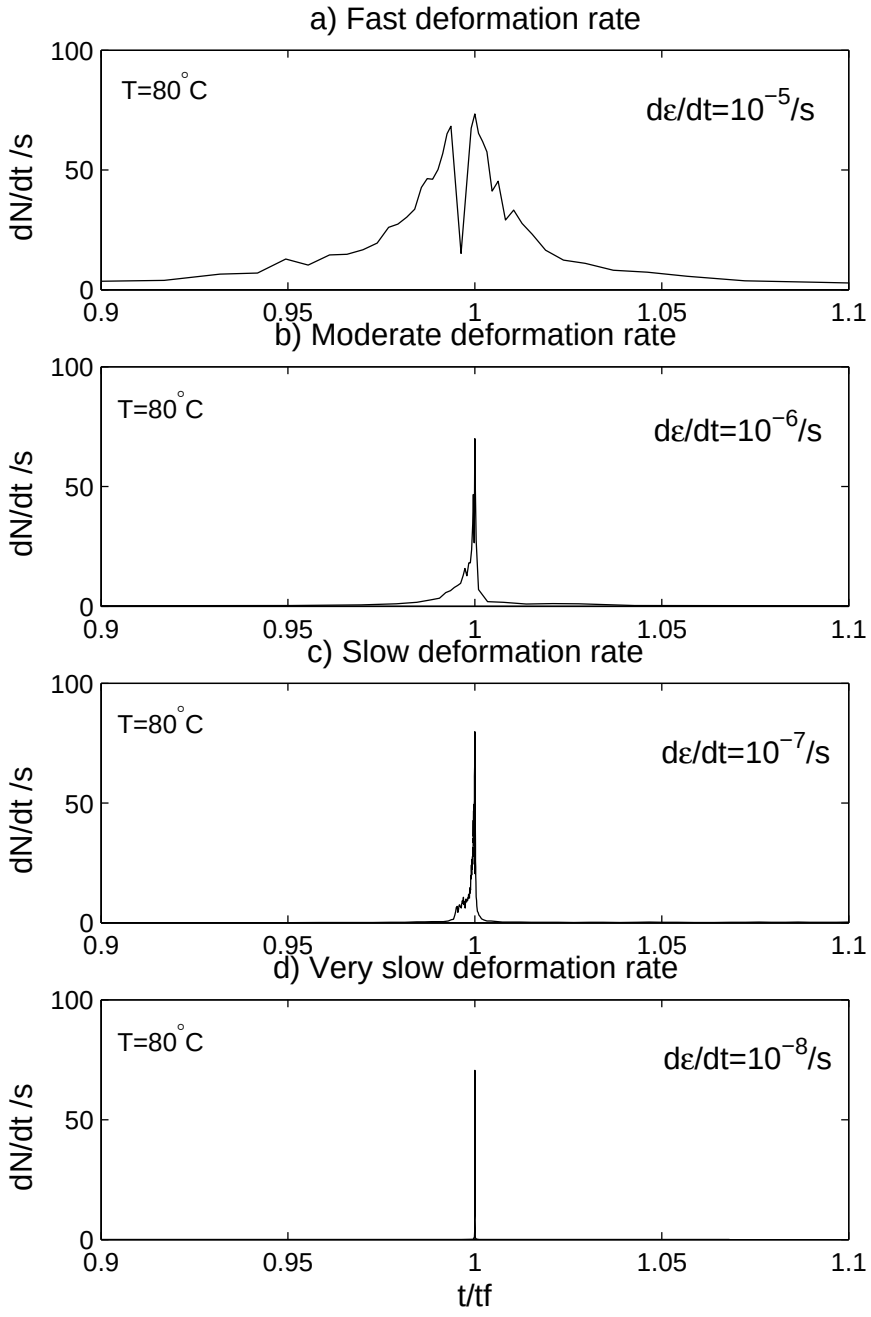

Figure 5.9. The evolution of AE event rate for the four 80°C Clashach tests from 10^{-5} to 10^{-8}/s. The AE activity exhibited a clear strain rate dependence, indicating that specimen failure becomes more difficult to predict as the strain rate decreases.

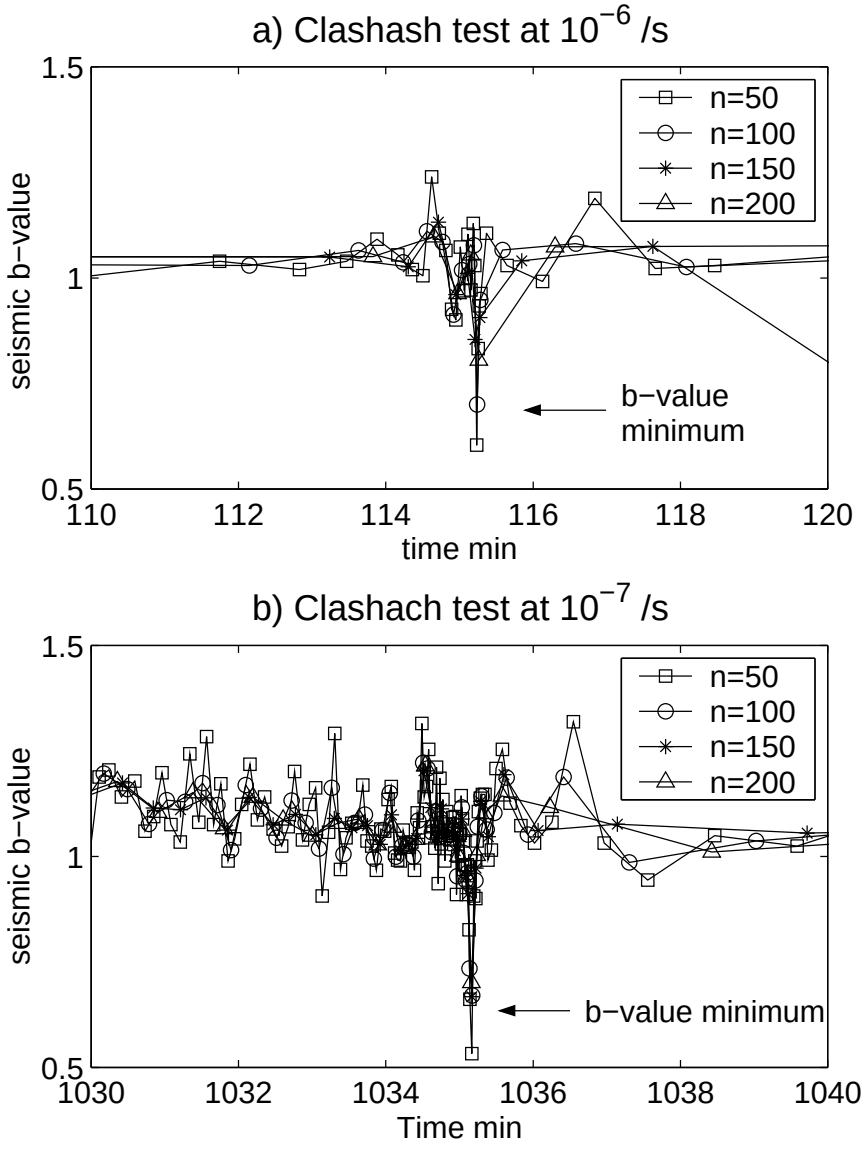

Figure 5.10. The temporal evolution of the seismic b-value for a 80°C Clashach test at 10^{-6} /s. The b-values were calculated using four different bin sizes: 50, 100, 150 and 200. The b-value was found to depend on the size of the bins.

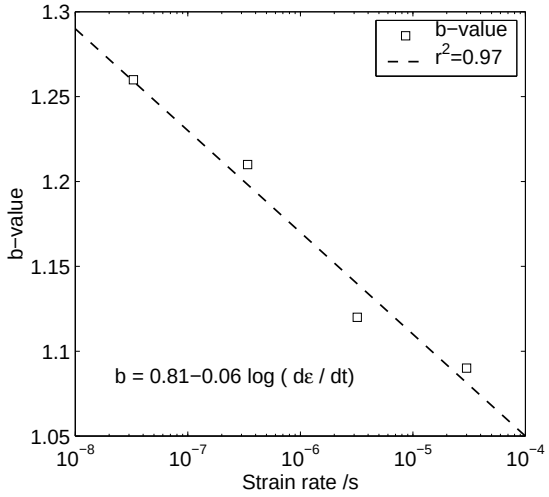

Figure 5.11. There calculated b-values for the entire deformation tests for Locharbriggs sandstone as function of the strain rate.

with an r-squared value of 0.97, as illustrated in figure 5.11. In addition, the maximum observed event amplitude A_{max} also decreased with the strain rate used for the test. The larger proportion of small events can be attributed to the greater importance of subcritical crack growth at slower strain rates.

The event rate statistics for all of the tests are summarised in table 5.1. There appears to be no correlation between the total number of recorded AE events N_t with lithology, strain rate or test temperature. This observation can be attributed to the different distribution of flaws inside the test specimen at the start of each test. In table 5.1., the total number of recorded AE events up to the peak stress and to the specimen failure are labelled as N_p and N_f, respectively. For all of the tests, majority of the AE events occurred after the peak stress had been attained. In addition, the proportion AE events that occurred after peak stress increased with decreasing strain rate. This observation can be attributed the more pronounced strain softening phase in the slow strain rate tests for both Clashach and Locharbriggs sandstones. There was slight correlation between specimen strength and the total number of recorded AE events, as shown in figure 5.12. Microfracturing is likely to be more intense in the specimen that sustained higher stresses, due to the exponential relationship between stress and the number of AE events (*Scholz*, 1968a).

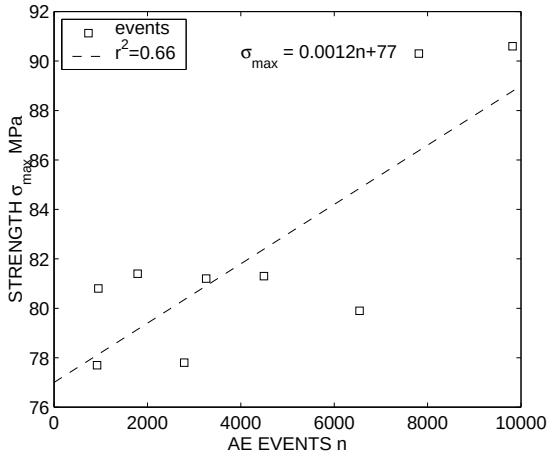

Figure 5.12. There is only a slight correlation between the total number of AE events and the specimen strength for the Locharbriggs sandstone.

5.3.3 AE source parameters

Although an array of AE transducers is required for comprehensive characterisation of the AE source physics, some general features of the AE sources can be derived from a two sensor dataset. For instance, assuming a self-similarity in AE the source function one would expect linear scaling at a log-log plot of duration versus event magnitude (*Kanamori and Anderson*, 1975; *Liakopoulou-Morris et al.*, 1994). Any events lying above the linear cluster can be deferred to as long duration low amplitude events, while those below the linear trend are of short duration and high amplitude. As shown in figure 5.13, the event duration and magnitude were approximately linearly related. However, events appeared to become longer in duration during the strain softening phase of deformation (5.13.b), which was maybe due to the high event rates that preceded sample failure. Instead of being recorded as individual events, small, otherwise unrelated events that overlap in time were summed up and appeared as long duration events in the AE catalogue (*Liakopoulou-Morris et al.*, 1994). This observation has important implications for any damage parameter that is derived from the AE catalogue: figure 5.13. clearly illustrates that damage is likely to be underestimated by the AE dataset immediately prior to sample failure due to the summing up of individual events. On the other hand, small duration, high amplitude events lying outside the linear cluster are likely to be caused by instrumental noise (*Cox and*

Table 5.1. Mechanical and AE data for the flow-through tests on Clashach (C) and Locharbriggs (L) sandstones. The b-values were calculated in 50-event non-overlapping windows in order to determine the b-value at specimen failure b_f. b_t is the seismic b-value for a whole test. N_p, N_f and N_t are the number of AE events up to the peak stress, to specimen failure and for the entire test, respectively.

Rock Type	$\dot{\varepsilon}$ s^{-1}	T °C	σ_{max} MPa	N_p	N_f	N_t	A_{max} dB	b_t	b_f
L	10^{-5}	80	81.2	1620	3257	3495	97	1.09	0.61
L	10^{-6}	80	80.8	191	948	987	96	1.13	0.94
L	10^{-7}	25	81.3	1186	4495	5035	81	1.21	0.83
L	10^{-7}	40	77.8	564	2788	3573	79	1.26	0.83
L	10^{-7}	60	81.4	713	1789	1922	97	1.24	0.96
L	10^{-7}	80	79.9	604	6541	6687	79	1.23	0.90
L	10^{-8}	80	77.7	177	922	1467	68	1.24	0.93
C	10^{-5}	80	162.8	997	1870	2495	98	1.03	0.45
C	10^{-6}	80	169.3	1294	1374	1603	97	1.01	0.60
C	10^{-7}	25	166.7	997	6185	8196	98	0.96	0.52
C	10^{-7}	40	140.4	852	2094	2496	97	1.04	0.45
C	10^{-7}	60	162.8	277	4200	5201	98	1.02	0.49
C	10^{-7}	80	134.6	518	5881	9881	95	1.08	0.53
C	10^{-8}	80	122.6	105	947	1616	97	1.09	0.78

Meredith, 1993). It was maybe due to the high amplitude threshold (50 dB) used for my tests that there were few such events. The higher amplitude threshold was used in order to save disk space, especially during the long duration, slow strain rate tests.

The recorded response of the AE sensors was investigated by plotting the event duration $\tau_d \sim L/v_r$ against rise time τ_r on a log-log scale. Figure 5.14(b) illustrates that most events lie in the region characterised by $\tau_r > T_0/\pi$ and $\tau_d > T_0/\pi$. Such relationship between τ_r and τ_d with respect to T_0/π suggests that $M_s \sim L$ for these tests, giving c^*=3 (fig. 5.5). This observation is not consistent with the calculated b-values in the region $0.45 < b < 1.5$ that suggest a c^*-value of 1.5. On the other hand, least squares fit to the event amplitude m in dB/20 versus log energy E_e plot (fig.5.14.a) yielded the following relationship

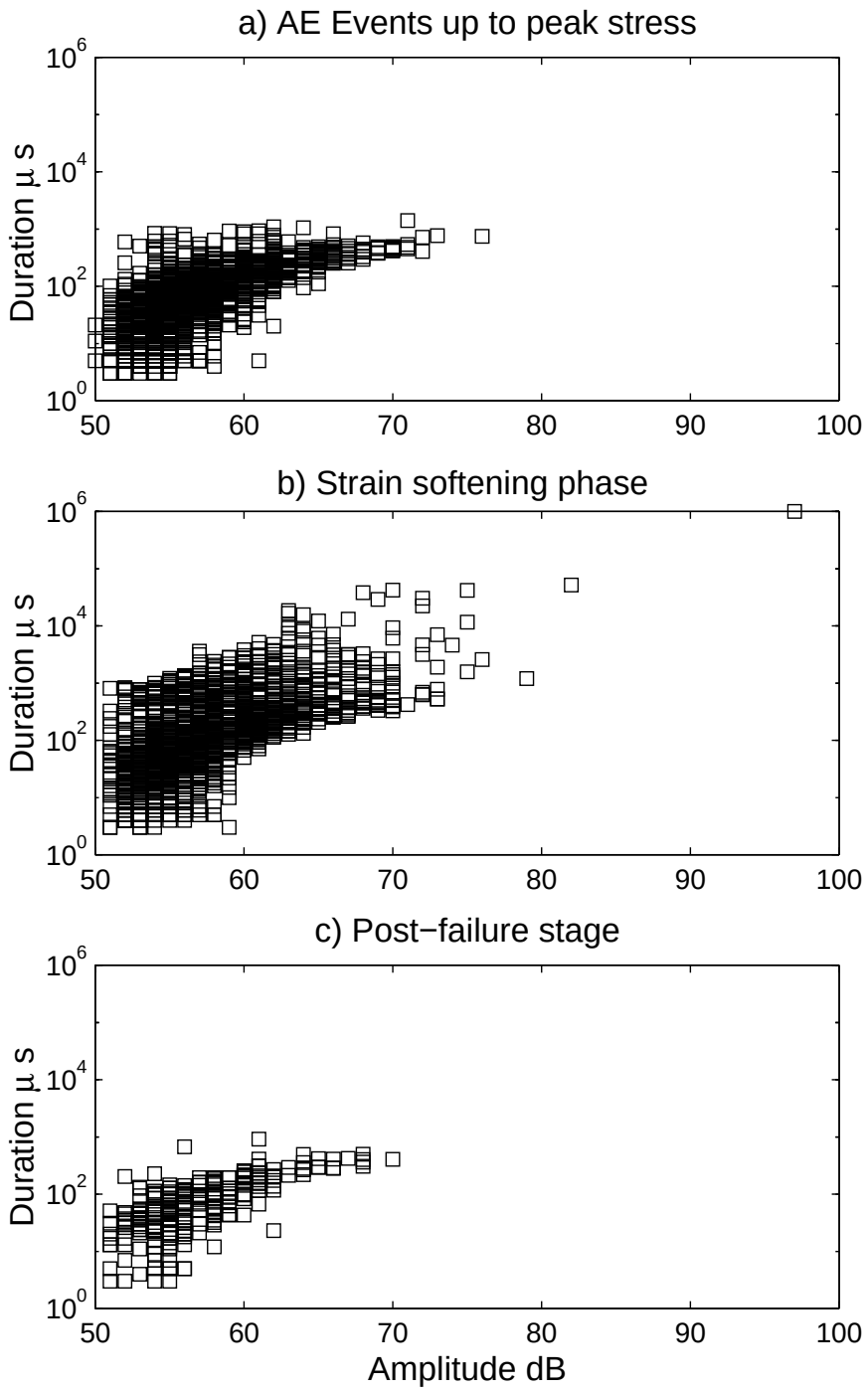

Figure 5.13. The AE event duration as a function of event magnitude (a) for the time interval preceding peak stress, (b) in the strain softening phase and (c) in the frictional sliding phase of the Locharbriggs 80°C test at a strain rate of 10^{-8}/s.

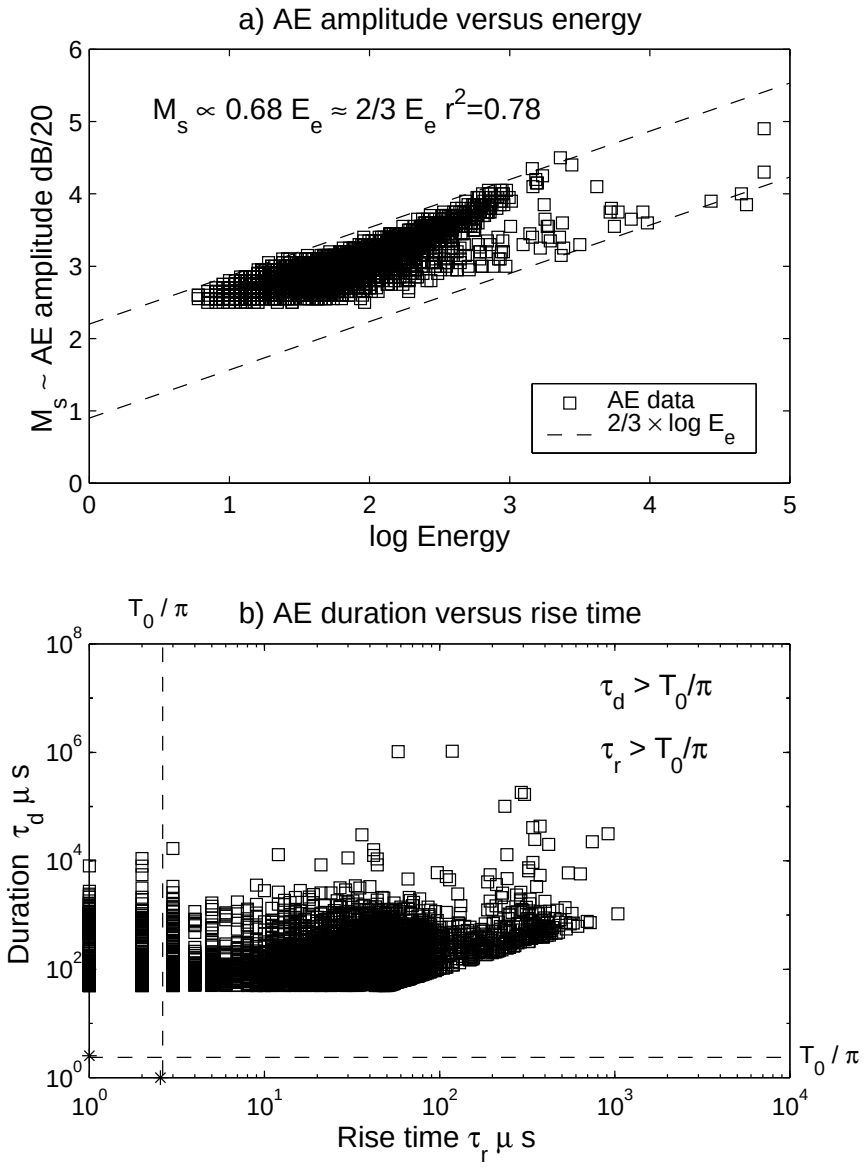

Figure 5.14. The AE event amplitude in dB/20 as a function of energy and rise time for the 25°C Clashach test at 10^{-8}/s. (a) The AE event amplitude in dB/20 as a function of logarithm of energy. It was assumed that the event magnitude M_s scales as amplitude in dB/20. The magnitude scales $M_s \propto 2/3$ log energy suggesting that $M_s \propto \log L^2$ and c^*=1.5. (b) The AE event duration L/v_r as a function of rise time τ_r for the same test. The natural period T_0 of the 125 kHz AE sensor was 8 μs. Most AE events lie in the region $\tau_r > T_0/\pi$ and $\tau_d > T_0/\pi$, hence suggesting that $M_s \propto \log L$ and that c^*=3. The diagonal lower cut-off results from the fact that event duration is always greater than the rise time. Similarly, event durations less than 30 μs cannot be measured because of instrument hit spacing (see section 3.5.3.)

$$m \propto 0.68 \log E_e \tag{5.23}$$

with an r-squared value of 0.78. Since the event amplitude in dB/20 is proportional to M_s, equation (5.22) suggests that $M_s \sim 2/3 \log E \sim \log L^2$ and that c^*=1.5 (Kanamori and Anderson, 1975). Hence, both c^*-value data and the inferred scaling relationship $M_s \sim 2/3 \log E_e$ indicate a value of c^*=1.5 for my tests. In addition, the calculated event duration τ_d for a trans-granular fracture event with L=0.2 mm and v_r=2000 m/s is 1 μs, which is less than T_0/π for the 125 kHz transducers that were used for the tests. Hence, majority of the AE data and the transducer specifications suggest a c-value of 1.5. This was the c-value that I used for calculating the damage parameters (section 3.5.3).

5.3.4 Temporal evolution of the AE event rate

The similarity of the recorded AE sequences to earthquake data was investigated by fitting the Omori formulae (5.1-5.2) to the AE event rate dN/dt, that was calculated for every ten consecutive events in the AE catalogue. The procedure for finding the optimum c-value is illustrated in figure 5.15. Firstly, $\log(dN/dt)$ was plotted against $\log(t_m - t)$ and $\log(t - t_m)$ for the foreshocks and aftershocks, respectively (fig. 5.15.a), with t_m considered to be known. On such plot, a rough estimate of the optimum c'-value is given by the break of slope in the AE event rate. Least-squares fits on $\log - \log$ plots of dN/dt versus $(c'+t-t_m)$ or $(c'+t_m-t)$ yielded the r-squared values for each tested c'-value. The c'-value yielding equally good fit to both fore- and aftershock data could then be determined from a plot of r^2 versus c' (fig. 5.15.b). Table 5.2. shows the c' values and the corresponding Omori law fits to the data. However, the values in table 5.2. do not represent the best fits of the Omori law to the fore- or aftershock data. Although the measured fore- and aftershock sequences were very similar, especially for the Clashach data, a constant c'-value could be imposed for each test, since the corresponding fit to the Omori law was only adequate.

The best fit to the Omori law was obtained by allowing c' to take different values for the fore- and aftershock sequences in each test, given by c_f and c_a, respectively.

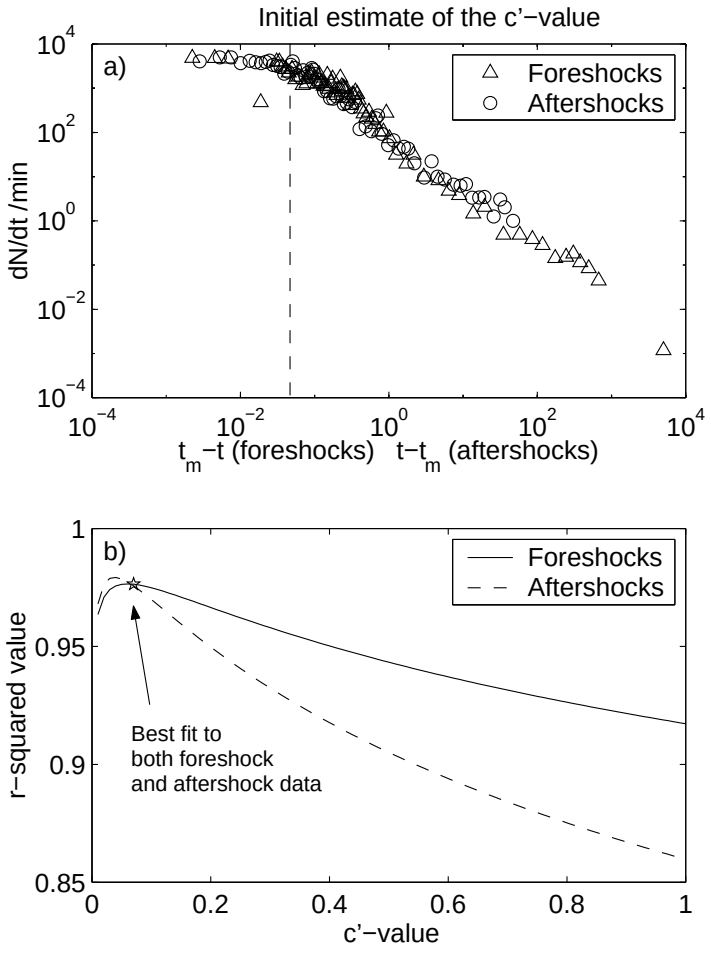

Figure 5.15. The procedure for finding the optimum c'-value for fitting the Omori law to the AE data. (a) log dN/dt was plotted against $\log(t_m - t)$ and $\log(t - t_m)$. The break in the slope provides a rough estimate of the c'-value. (b) The c'-value was estimated within 0.01 accuracy on a plot of c' versus the corresponding r-squared value indicating goodness of fit to the Omori law.

Table 5.2. The Omori law fits to the AE event rate dN/dt on Clashach (C) and Locharbriggs (L) sandstones. p is the exponent for aftershocks and p' is the exponent for foreshocks. The foreshock R_f and aftershock R_a rates scale as $R_f = e^{k_1}(c' + tm - t)^{-p'}$ and $R_a = e^{k_1}(c' + t - tm)^{-p}$, respectively. The event rate was calculated in 10 event bins per minute and the c' value is in minutes.

Rock	$\dot{\varepsilon}$	T	c'	p'	k_1	p	k_1	r^2
C	10^{-5}	80	0.44	2.45	6.68	1.90	6.35	0.936
C	10^{-6}	80	0.05	1.26	5.31	1.14	4.69	0.914
C	10^{-7}	25	0.50	1.22	7.70	1.14	6.11	0.858
C	10^{-7}	40	7.24	2.77	12.5	3.80	14.3	0.726
C	10^{-7}	60	0.37	1.28	7.23	1.74	6.93	0.858
C	10^{-7}	80	0.35	1.37	7.52	1.63	6.45	0.927
C	10^{-8}	80	0.07	1.33	4.92	1.37	4.82	0.976
L	10^{-5}	80	0.61	2.03	7.68	3.02	6.62	0.904
L	10^{-6}	80	0.18	1.40	5.43	1.82	4.33	0.927
L	10^{-7}	25	0.53	0.93	6.49	1.56	6.16	0.868
L	10^{-7}	40	0.11	0.89	5.94	1.47	4.41	0.925
L	10^{-7}	60	0.33	0.96	5.52	1.81	5.21	0.863
L	10^{-7}	80	0.31	0.86	6.68	2.17	4.78	0.880
L	10^{-8}	80	0.04	0.92	4.77	1.42	3.68	0.966

The optimal Omori law fits to the fore- and aftershock data are listed in table 5.3. For both sandstones the goodness of fit to the Omori formulae was best for the fore- and aftershock sequences that accompanied the very slow strain rate tests, at $10^{-8}\ s^{-1}$, as shown in figures 5.16. and 5.17. for the Clashach and Locharbriggs sandstones, respectively.

For some tests, single c'-value produced the best fit to both fore- and aftershock data. In such occasion the goodness of fit to the Omori law was better for the aftershocks than for the foreshocks. However, for most tests the c'-value that produced the best fit to the foreshock data was higher than the best-fitting c'-value for the corresponding aftershock sequence. This phenomenon is likely to be caused by the under-counting of small events in the high event rates that preceded specimen failure, since the c-value is a measure of the amount of missing events (*Utsu et al.*, 1995). A estimate for the proportion missing events as indicated by the c'-value is given by $100(1-2^{p'})\%$ at time t equals c'. For the Clashach tests, the inferred amount of missing events ranged from 85% at 0.56 mins and 44% at 0.01

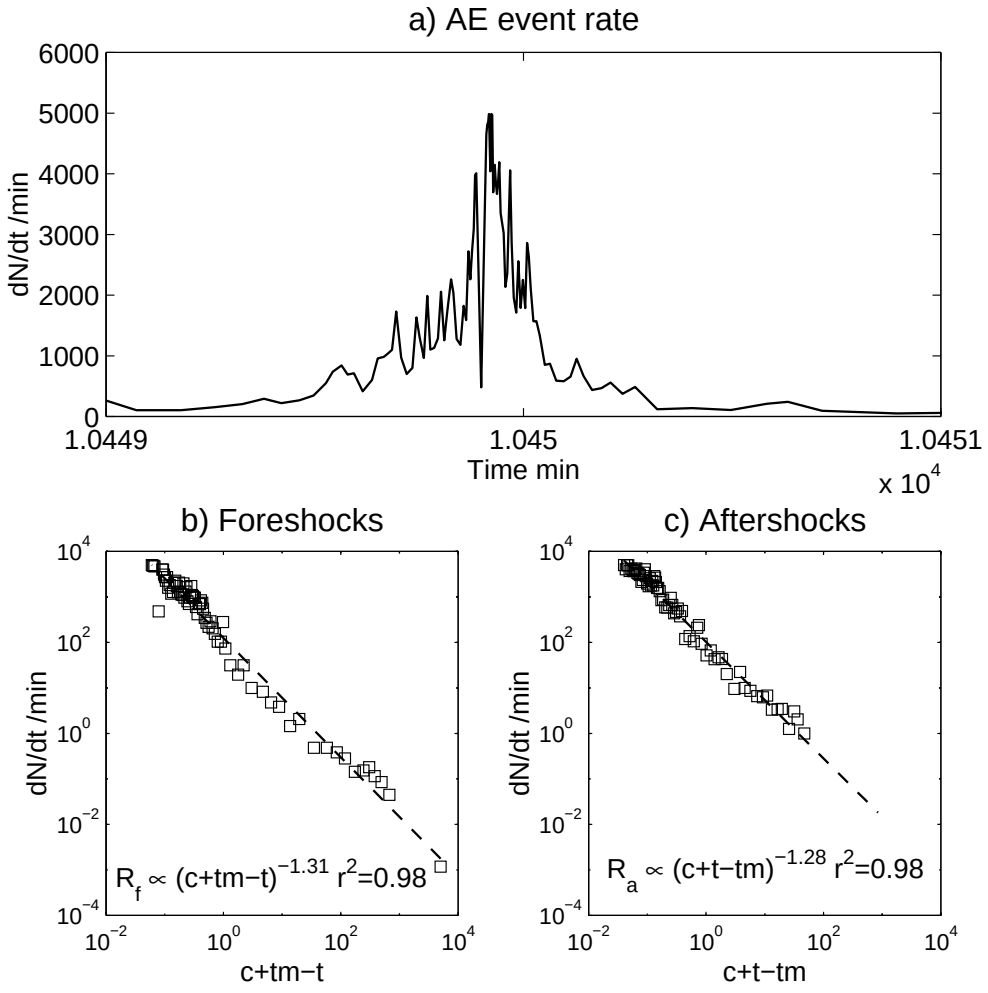

Figure 5.16. The (a) AE event rate, (b) foreshock sequence and (c) aftershock sequence for a 80°C Clashach test that was carried out at a strain rate of 3.1×10^{-8} s^{-1}. In (a) the event rate was calculated in 50-event bins. For the Omori law fits in (b) and (c) the event rate was calculated for every 10 events. It is important to note that the peak event rate of 5000 min^{-1} (83 s^{-1}) did not occur over a whole minute, but over few seconds prior to specimen failure.

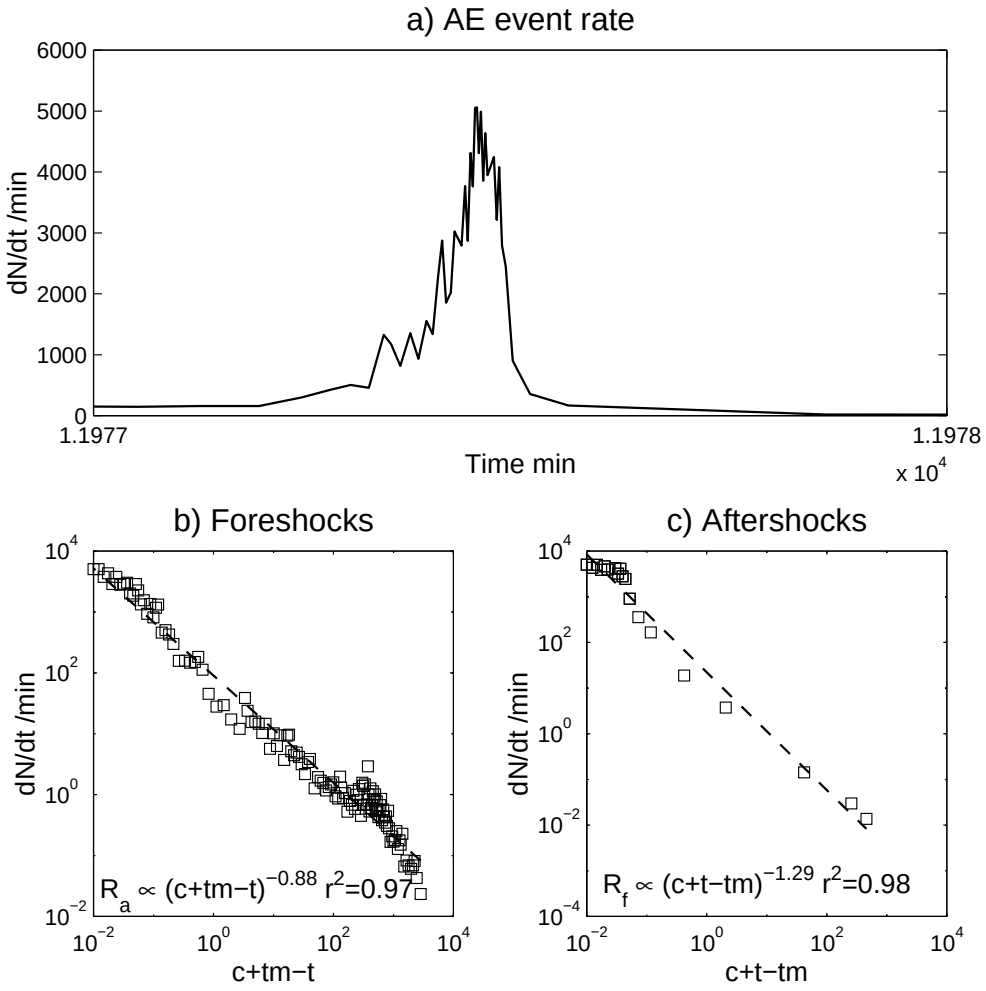

Figure 5.17. The (a) AE event rate, (b) foreshock sequence and (c) aftershock sequence for a 80°C Locharbriggs test that was carried out at a strain rate of 2.8×10^{-8} s^{-1}. In (a) the event rate was calculated in 50-event bins. For the Omori law fits in (b) and (c) the event rate was calculated for every 10 events. It is important to note that the peak event rate of 5000 min^{-1} (83 s^{-1}) did not occur over a whole minute, but over few seconds prior to specimen failure.

Table 5.3. Omori law fits to the AE event rate dN/dt on Clashach (C) and Locharbriggs (L) sandstones. The foreshock R_f and aftershock R_a rates scale as $R_f = e^{k_1}(c_f + tm - t)^{-p'}$ and $R_a = e^{k_1}(c_a + t - tm)^{-p}$, respectively.

Rock	$\dot{\varepsilon}$	T	c_f	p'	k_1	r^2	c_a	p	k_1	r^2
C	10^{-5}	80	0.56	2.71	7.04	0.937	0.11	1.26	5.60	0.958
C	10^{-6}	80	0.42	1.96	6.28	0.963	0.01	0.96	4.47	0.921
C	10^{-7}	25	4.27	2.14	10.8	0.892	0.01	0.79	5.05	0.954
C	10^{-7}	40	0.05	1.02	5.92	0.922	0.05	1.29	4.86	0.986
C	10^{-7}	60	0.01	0.83	6.23	0.911	0.02	1.20	5.69	0.927
C	10^{-7}	80	1.58	1.98	9.18	0.951	0.08	1.23	5.76	0.953
C	10^{-8}	80	0.06	1.31	4.86	0.977	0.04	1.28	4.66	0.979
L	10^{-5}	80	4.37	6.81	18.4	0.947	0.14	1.97	4.89	0.956
L	10^{-6}	80	0.33	1.63	5.80	0.928	0.01	1.30	2.95	0.990
L	10^{-7}	25	0.17	0.84	6.12	0.869	0.01	1.05	4.24	0.961
L	10^{-7}	40	0.19	0.93	6.07	0.927	0.01	1.13	3.74	0.966
L	10^{-7}	60	0.01	0.76	4.70	0.914	0.01	1.18	3.32	0.976
L	10^{-7}	80	0.11	0.80	6.42	0.883	0.02	1.37	3.22	0.971
L	10^{-8}	80	0.01	0.88	4.53	0.974	0.01	1.29	3.12	0.979

mins prior specimen failure. For the Locharbriggs tests the corresponding figures were 99% at 4.4 mins and 44% at 0.01 mins. The c'-values for the Locharbriggs foreshock sequences decreased with decreasing strain rate (table 5.3). It is possible that crack growth is inherently faster in the high strain rate tests, hence resulting a higher proportion of missing events in the fast loading rate tests.

Figures 5.18 and 5.19 illustrate the fore- and aftershock sequences and the corresponding fits to the Omori formulae for the Clashach and Locharbriggs $80°C$ tests that were carried out at four different loading rates. The exponent p' for foreshocks was found to decrease with decreasing strain rate for both sandstones. A smaller p' indicates a steeper acceleration of event rate prior specimen failure, which is also clearly observable in figure 5.9. For the very slow strain rate tests significant AE event rates were attained only few minutes prior dynamic failure of the test specimen, as shown in figures 5.16.a and 5.17.a. Since the total duration of the 10^{-8} s^{-1} tests was 8-9 days, this result represents a very steep acceleration of dN/dt prior dynamic instability.

For the Locharbriggs tests the decay rate of aftershocks correlated with test temperature. The exponent p was a function of test temperature and given by

$$p = 0.0055T + 0.90 \tag{5.24}$$

with an r-squared value of 0.934, as illustrated in figure 5.20. This observation is consistent with the higher p-values that have been obtained for earthquake data in areas with high heat flow (*Utsu et al.*, 1995).

5.3.5 Extraction of damage parameters from the AE catalogue

The damage caused by microcracking was quantified though various cumulative properties derived from the AE dataset. The damage parameter D, corresponding to χ' in (5.20), was calculated for c=1.5, in accordance with *Cox and Meredith (1993)*. While D can be considered to be proportional to the increase in fracture porosity (5.16), an additional surface area parameter S was also defined. In calculating S it was assumed that area scales logarithmically with respect to M_s, consistent with the dislocation theory of *Kanamori and Anderson* (1975). Hence, S is given by

$$S = \sum_{i=1}^{N} (10^{c^* m)^{2/3}} \tag{5.25}$$

where m is maximum event amplitude in dB/20 and c^*=1.5. It was assumed that S corresponds to the increase in surface area caused by the growth of microcracks inside the test specimen. Furthermore, the cumulative event number N and the cumulative AE energy E were also extracted from the AE catalogue. The damage parameters were calculated in one minute non-overlapping windows.

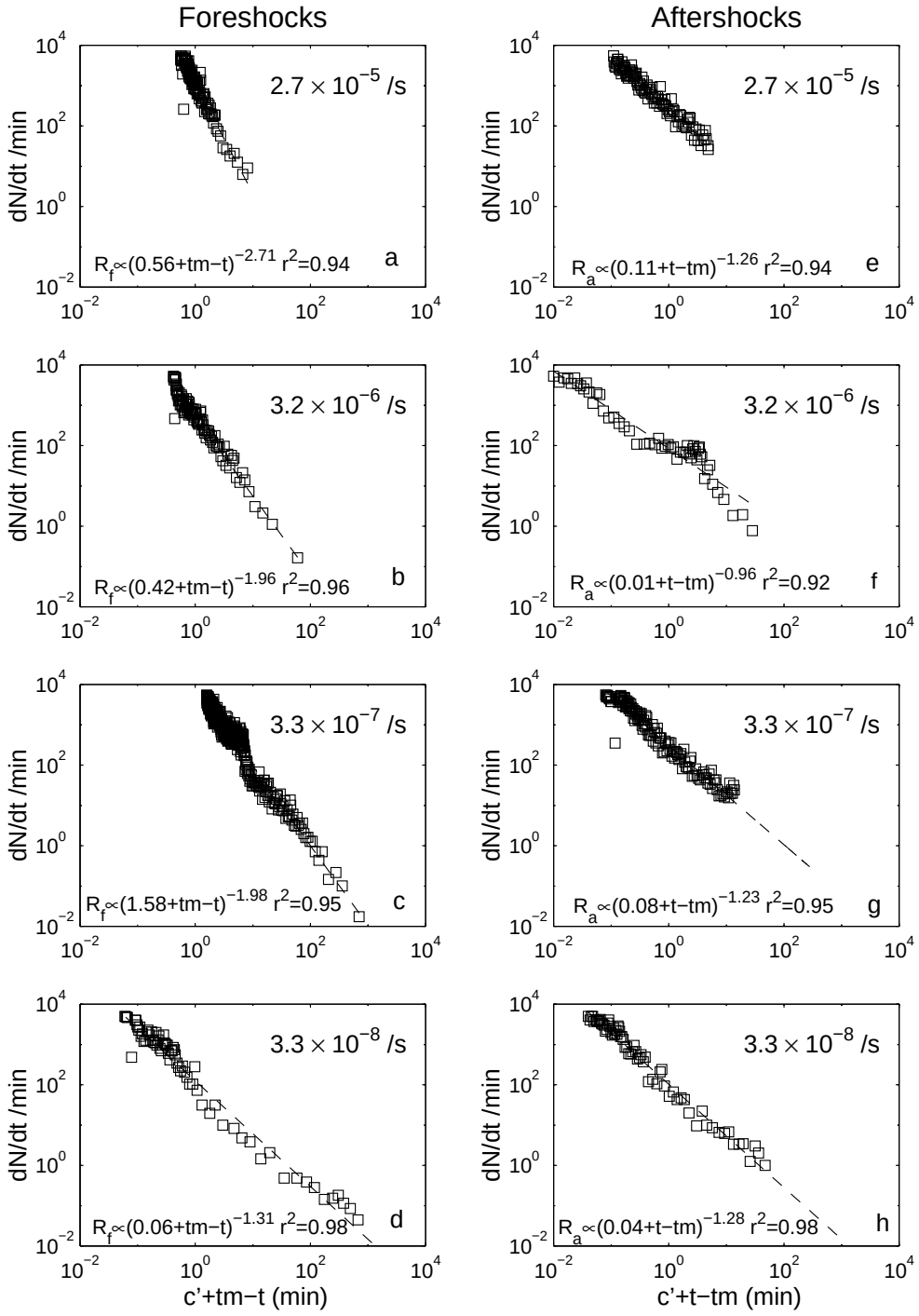

Figure 5.18. The foreshock (a,b,c,d) and aftershock (e,f,g,h) sequences for Clashach sandstone tests that were carried out at a four different strain rates.

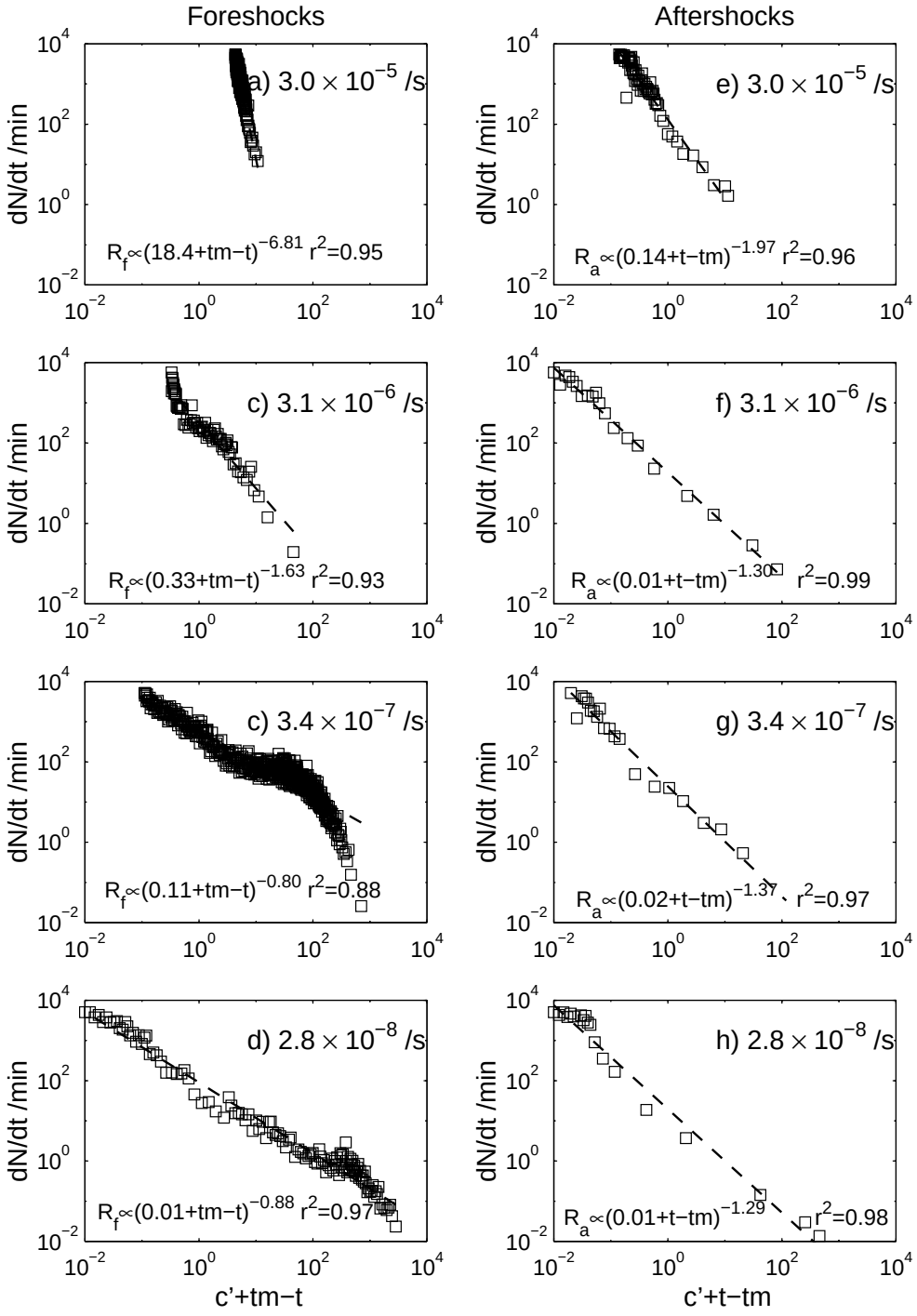

Figure 5.19. The foreshock (a,b,c,d) and aftershock (e,f,g,h) sequences for Locharbriggs sandstone tests that were carried out at a four different strain rates.

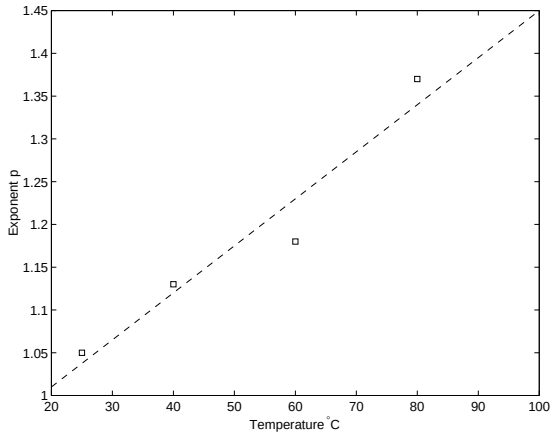

Figure 5.20. The exponent p for the aftershock sequences as a function of test temperature for the Locharbriggs tests at 10^{-7}/s. This observation is consistent with the higher p-values that have been observed in high heat flow areas (Utsu et al., 1995).

5.3.6 Correlation of AE damage with stress

In order to test the applicability of D,S,E and N, these newly defined damage parameters were used to invert the measured stress-strain curves according to *Cox and Meredith* (1993). Details of the theoretical basis of the inversion approach are given in section (5.2.7). The practical procedure for obtaining the inverted stress-strain curves is illustrated in figure 5.21. Firstly, least squares fit to the linear section of the stress-strain curve produced the secant modulus E_m and the origin strain value ε_0 (5.21.a). Secondly, the variation of the modified modulus E'/E_0 with time was determined from the measured stress-strain curve (5.21.b). Hence the scaling factors F' and G' were determined from plots of E_0/E' versus the working damage parameter χ' (5.21.c-d). Although the process of deriving the scaling factors was slightly circular, the derived values were unlikely to be wrong by more than a factor of two (*Cox and Meredith*, 1993). The damage parameters D, S, N and E were all used as the working damage parameter in the inversion procedure. Initially, the stress history matching exercise was carried out by using c-values ranging from 1.5 to 3.0 in calculating D and S. However, no consistent improvement in matching the measured data with the inverted data was attained by changing the c^*-value. Therefore, the best estimate of the c^*-value was assumed to be 1.5, in accordance with discussion in section 5.3.3.

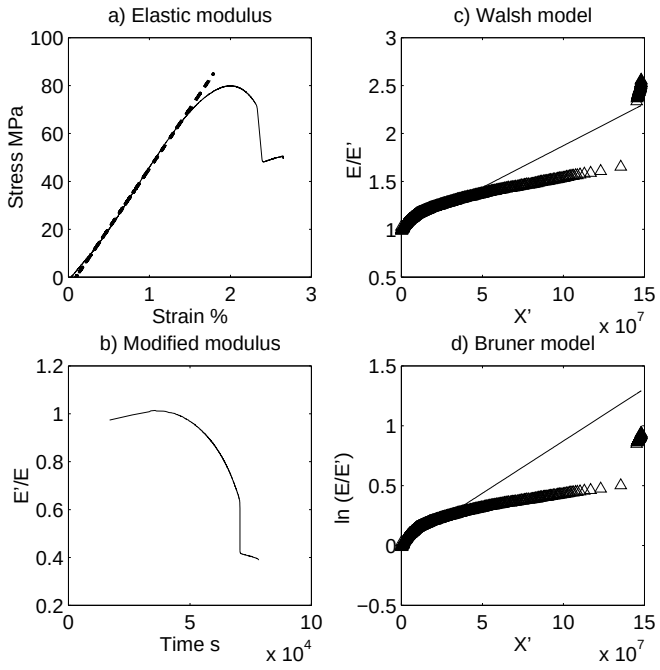

Figure 5.21. The procedure for stress history matching.

Figure 5.22 and 5.23 show typical inverted stress-strain curves for the Clashach and Locharbriggs sandstones, respectively. While *Cox and Meredith* (1993) used D to reconstruct the measured stress-strain curves, my results demonstrate that area S, cumulative event count N or cumulative event energy E can be used equally well in the inversion procedure. In fact, N and E produced a very good fit to the Clashach data (fig. 5.22), while the Locharbriggs stress history was best modelled by E (fig. 5.23). However, the main features of the stress-strain curves were produced by using both *Walsh* (1965) and *Bruner* (1976) models and all of the damage parameters. The fit to the Clashach data was excellent due to the lack of dominant strain softening or hardening phases. In other words, the isotropic damage parameters D, S, N and E performed well in describing the stress history of the Clashach sandstone due to the lack of non-linearity in the stress-strain behaviour. For the Locharbriggs sandstone both models consistently overestimated the peak stress, hence underestimating damage. The high crack concentrations and crack-to-crack interaction are the likely causes of the well developed non-linearity in the stress-strain curve for Locharbriggs sandstone. Such highly anisotropic crack distribution cannot be predicted well by using an

isotropic damage parameter. However, since the *Bruner* (1976) model includes a better treatment of crack interaction, the fit to the experimental data was better for this model. Damage is also likely to be underestimated due to the fact that AE is know to record only a fraction of cracks (*Lockner*, 1993a). However, all large events will trigger the recording system and the maximum recorded energy corresponds to these large events. This could be the reason why E is generally better in reproducing the measured stress-strain curves than N for the Locharbriggs tests.

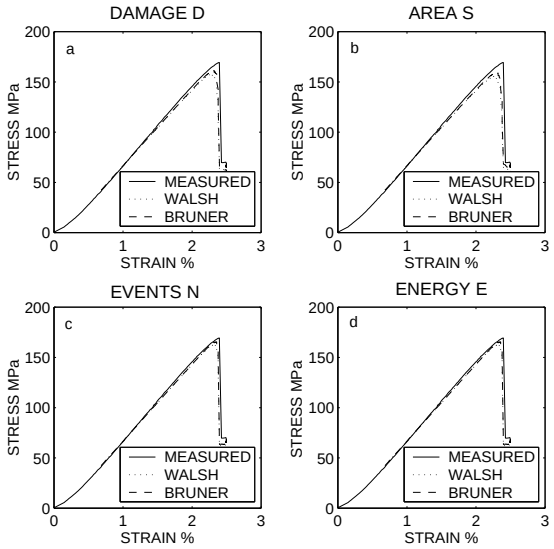

Figure 5.22. The inverted stress-strain curves for a 80°C Clashach test at 10^{-6} /s.

5.4 Discussion

My results demonstrate that the recorded AE activity for triaxial compression tests on Clashach and Locharbriggs sandstones bears many similarities to earthquake data. Namely, the data satisfies both Gutenberg-Richter and Omori formulae, in accordance with previous AE studies (*Mogi*, 1962, 1967; *Meredith and Atkinson*, 1983, *Hirata*, 1987, *Lockner*, 1993a, *Cox and Meredith*, 1993). Such scaling relationships are also observed for earthquakes (*Mogi*, 1967, *Frochlich and Davis*, 1993). Although AE studies are conducted on intact rock samples, while

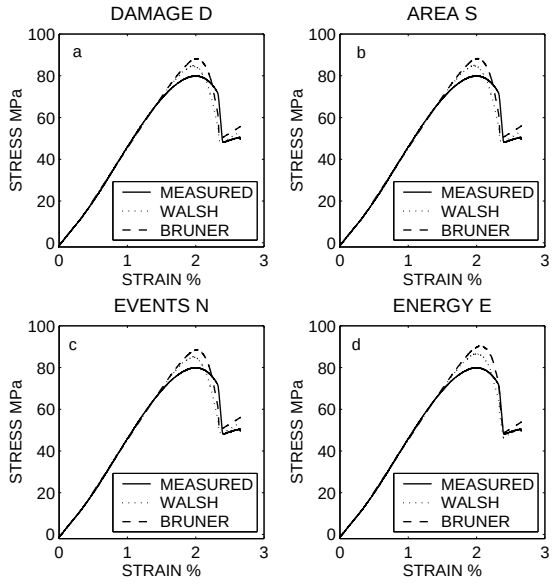

Figure 5.23. The inverted stress-strain curves for a 80°C Locharbriggs test at 10^{-7} /s.

earthquakes are thought to occur on pre-existing faults, the similarity in their statistical behaviour may be an indicator of the same underlying mechanism, that generates both of these phenomena. For instance, natural faults may heal and strengthen between earthquakes and therefore resemble the intact rock samples that were used in this study (*Lockner*, 1993a). On the other hand, the slip on faults is likely to involve the breaking of local asperities due to the roughness of fault surfaces. Moreover, the same micromechanical processes may contribute to rock fracture and fault slip (*Lockner*, 1993a).

In a typical test, specimen failure is preceded by a decrease in the seismic b-value followed by a recovery after faulting. A single b-value minimum is observed immediately before dynamic instability, in the fault nucleation stage. Such precursory changes in b-value have been reported for earthquakes (*Von Seggern*, 1980), volcanic events (*Vinciguerra*, 1999) and during the deformation of both intact and faulted rock specimen (*Main et al.*, 1989, 1992; *Sammonds et al.*, 1992; *Liankopoulou-Morris et al.*, 1994; *Zang et al*, 1996, 1998; *Lei et al.*, 2000). The temporal evolution of the seismic b-value for my tests is in agreement with the theory and observations of *Main and Meredith* (1989). Based on the assumption of increasing stress intensity factor as the sample approaches failure, they predicted a

drop in b-value in the pre-failure region followed by a recovery after faulting. This kind of pattern in the b-value evolution is typical for laboratory rock deformation tests (*Main et al.*, 1989; *Meredith et al.*, 1990).

The b-values for the different tests cluster around one, in accordance with the observed b-values for earthquakes (*Frochlich and Davis*, 1993). An interesting feature of the Locharbriggs tests is that the b-values increase systematically with decreasing deformation rate. In addition, the maximum recorded event amplitude decreases with strain rate. These observations suggest a higher proportion of smaller magnitude events in the slow loading rate tests. Some of these smaller magnitude events could be caused by subcritical crack growth by the stress corrosion mechanism, since stress corrosion is likely to be the dominant mechanism for crack growth in the slow strain rate tests.

The AE event rate exhibits distinct fore- and aftershock sequences associated with the dynamic failure of the tests specimen. Although aftershock sequences are not commonly recorded in laboratory tests, the temporal evolution of the AE event rate in my tests is very similar to the observations of *Meredith et al.* (1990) for Darley Dale sandstone. The AE event rate obeys the Omori formulae for fore- and aftershocks with high correlation coefficients. The Omori law exponents range from 0.83 to 2.71 and 0.76 to 6.81 for Clashach and Locharbriggs sandstones, respectively. However, the majority of the exponents are close to unity, as it is observed for earthquakes (*Utsu et al.*, 1995) and laboratory rock fracture (*Hirata*, 1987). In my tests, the exponent p' for foreshocks decreases with decreasing strain rate for both sandstones. This observation is not predicted by he stochastic model of *Mogi* (1962), which assumes that the fracture probability μ_m is a an exponential function of the stress rate and time (5.21). Instead, my observations suggest that the prediction of rock failure becomes increasingly difficult as the strain rate is decreased, as indicated by the steeper acceleration of AE event rate. Moreover, the Locharbriggs exponents p for aftershocks are consistently higher than the exponent p' for foreshocks. The higher p-values might be related to the fractured state of the rock specimen (*Mogi*, 1967).

It is maybe due to the narrow range of temperatures that was used for the tests that there are no distinct changes in the level of AE activity with test temperature. The only observable temperature effect is the correlation of the exponent p for aftershocks with test temperature. The formula that relates p

with test temperature (5.24) is similar to the regression $p = 0.692 + 0.000994T$ obtained for earthquake aftershocks in the Tohoku district of Japan (*Creamer and Kisslinger*, 1993). In my tests, however, the dependence of p on test temperature is more pronounced, since $p \propto 0.0055T$. It has been suggested that the positive correlation with surface heat flow and exponent p stems from a faster rate of stress relaxation in higher temperature areas (*Mogi*, 1967; *Utsu et al.*, 1995).

The close correlation of the statistical properties of AE and earthquake data suggest that both phenomena may be governed by similar source functions. Hence, the dislocation theory of *Kanamori and Anderson* (1975) was used to derive a damage parameter D as described in *Cox and Meredith* (1993). In addition, surface area parameter S, the cumulative AE count N and the cumulative AE energy E are used as measures of the damage caused by microcrack growth inside the test specimen. The damage parameters predict the stress-strain curves adequately, and hence can be considered as appropriate indicators of damage. However, for the Locharbriggs sandstone the microcrack damage is underestimated at a later stage of loading. This is probably due to the high crack concentrations that are not well modelled by using an isotropic damage parameter. In addition, the long event durations that are observed during the strain softening phase are likely to be due to the summing up of small, short events. Damage is also likely to be underestimated by the AE catalogue since not all microfracturing events are accompanied by a detectable AE (*Lockner*, 1993a; *Zang et al.*, 2000).

There appears to be some inconsistency in the c^*-value as it is inferred from the AE catalogue. It is certainly possible that this discrepancy has gone unnoticed for a considerable amount of time. Previous AE studies have invariably inferred the c-values from the b-values without considering the relationship of τ_r and τ_d to T_0/π in the recorded data (*Cox and Meredith*, 1993;*Main et al.*, 1989). Yet, my results indicate that seismic b-value depends on the size of the bins that were used in its calculation as well as on the distribution of fracture sizes within the deforming rock sample. Therefore, it may not be such a good indicator of the likely c^*-value for the experimental apparatus and the AE source parameters. For my tests the scaling of the maximum event amplitude versus energy suggests a c^*-value of 1.5, while the rise time duration data suggest that c^*=3. The event durations are of similar times to those reported by *Yanagidani et al* (1985). Yet, one might expect

that crack growth under compression is dominated by sharp rise time events with high propagation velocities (*Main et al.*, 1993), yielding c^*=1.5. The success of the stress history matching exercise suggests that c^*=1.5 could be the right value for my tests. On the other hand, c^*-value could be a function of M_s if different sized events produced elastic waves with different dominant frequencies (*Cox and Meredith*, 1983). A detailed study involving different frequency AE sensors and calibrated sources is required in order to clarify this issue.

5.5 Conclusion

The results of my triaxial compression tests demonstrate that sample failure is preceded by significant AE activity and followed by a subsequent decrease in in AE event rate. The foreshock and aftershock sequences are fairly symmetrical for the Clashach tests. The Locharbriggs tests display a more gradual acceleration of AE activity and a less pronounced aftershock sequences. The AE foreshock and aftershock sequences are well modelled by the Omori law for foreshocks (5.1) and aftershocks (5.2) (r^2=0.87-0.98). The exponent p' for the Locharbriggs aftershock sequences correlates with test temperature (r^2=0.93). This observation is in good agreement with the high p-values that have been observed for earthquakes in high heat flow areas.

Sample failure is also preceded by a decrease in seismic b-value. The magnitude of the b-value anomaly depends on the bin size that is used to calculate the b-values. Furthermore, The Locharbriggs b-values are proportional to the logarithm of strain rate (r^2=0.97). Similarly, the maximum recorded magnitude for each test A_{max} decreases with decreasing strain rate. Both of these observations suggest that smaller cracks are more abundant in the slow strain rate tests. The b-values and the Omori law exponents are close to unity just like the ones for crustal earthquakes.

Hence, both temporal and size distribution of the recorded AE activity exhibit distinct power-law scaling. This observation suggests a self-similarity in the AE source function. Since similar scaling relationships are also observed for earthquakes, fundamental empirical relations of earthquake seismology can be used to derive a damage parameter from the AE catalogue. Other cumulative

properties, such as the event energy, can also be used as indicators of damage. The damage parameters predict the recorded stress-strain behaviour for both rocks adequately. Hence, they are appropriate in quantifying the damage caused by microcrack growth inside the test specimen. In the next two chapters I will investigate how this microcrack damage is related to the evolution of permeability and pore fluid chemistry during the deformation tests.

Chapter 6

Stress corrosion crack growth

It seems ridiculous that the amount of chlorine in drinking water can cause the cracking of a thick stainless steel section in a few hours. Staehle (1969)

6.1 Introduction

Sample failure is preceded by time-dependent growth of microcracks, as evidenced by the AE activity. Furthermore, both specimen strength and elastic modulus are reduced on the application of a slower loading rate. These observations cannot be explained in terms of classic linear elastic fracture mechanics. In fact, time and rate dependence of brittle fracture properties are commonly ascribed to crack growth by the stress corrosion mechanism (*Anderson and Grew*, 1977; *Atkinson*, 1982, 1984; *Atkinson and Meredith*, 1987a; *Costin*, 1987). Environmentally assisted crack growth is likely to dominate fracture propagation rates in the slow strain rate tests since there is more time available for chemical reactions to occur. One might expect a geochemical signal associated with fracture growth due to active dissolution from growing crack tips, as suggested by *Dove* (1995). Alternatively, pore fluid chemistry could be affected by passive dissolution from the newly created fracture surfaces. The constant flow rate flow-through condition of my tests allowed these chemical effects to be investigated. The exit pore fluid was sampled at regular intervals and these samples were analysed for the

concentration of dissolved ions. In this chapter I will present the geochemical data collected during the triaxial compression tests on Clashach and Locharbriggs sandstones. I will first describe the evolution of pore fluid chemistry and AE damage with time in the Locharbriggs tests. The close correlation between chemistry and microseismic properties of brittle deformation in Locharbriggs sandstone has also been discussed in *Ojala et al.* (2003). Subsequently, I will describe the temporal evolution of the pore fluid chemistry in the Clashach tests. The final section deals with the evolution of damage and ion concentrations in terms of standard constitutive equations for subcritical crack growth.

6.2 The pore fluid chemistry in the Locharbriggs tests

6.2.1 The geochemical signal

Locharbriggs sandstone is mainly composed of quartz, so it is not surprising that a clear geochemical signal was recorded for the variation of dissolved silica in the exit pore fluid. Figure 6.1. illustrates the evolution of differential stress, cumulative AE count and pore fluid silica concentration with time during a 80°C Locharbriggs test at 10^{-8}/s. The variation in silica concentration correlated with the main deformation stages. During the early stages of loading the compaction of favourably oriented cracks lead to an exponential decrease in Si concentration in the exit pore fluid. It appears that the reduction in surface area due to crack closure is dominant over pressure solution, which might be expected to occur during compactive deformation at this temperature. There was no AE activity during this stage. During the linear elastic phase the Si concentration remained approximately constant at 3 ppm. This stage was also characterised by an intermittent low AE activity of one event per minute. Although both compactive and dilatant processes are likely to operate during this stage, the net increase in surface area is close to zero. Hence, both AE activity and Si concentration assumed constant values during this stage. The constant value of dissolved silica indicates a steady state in the dissolution reaction.

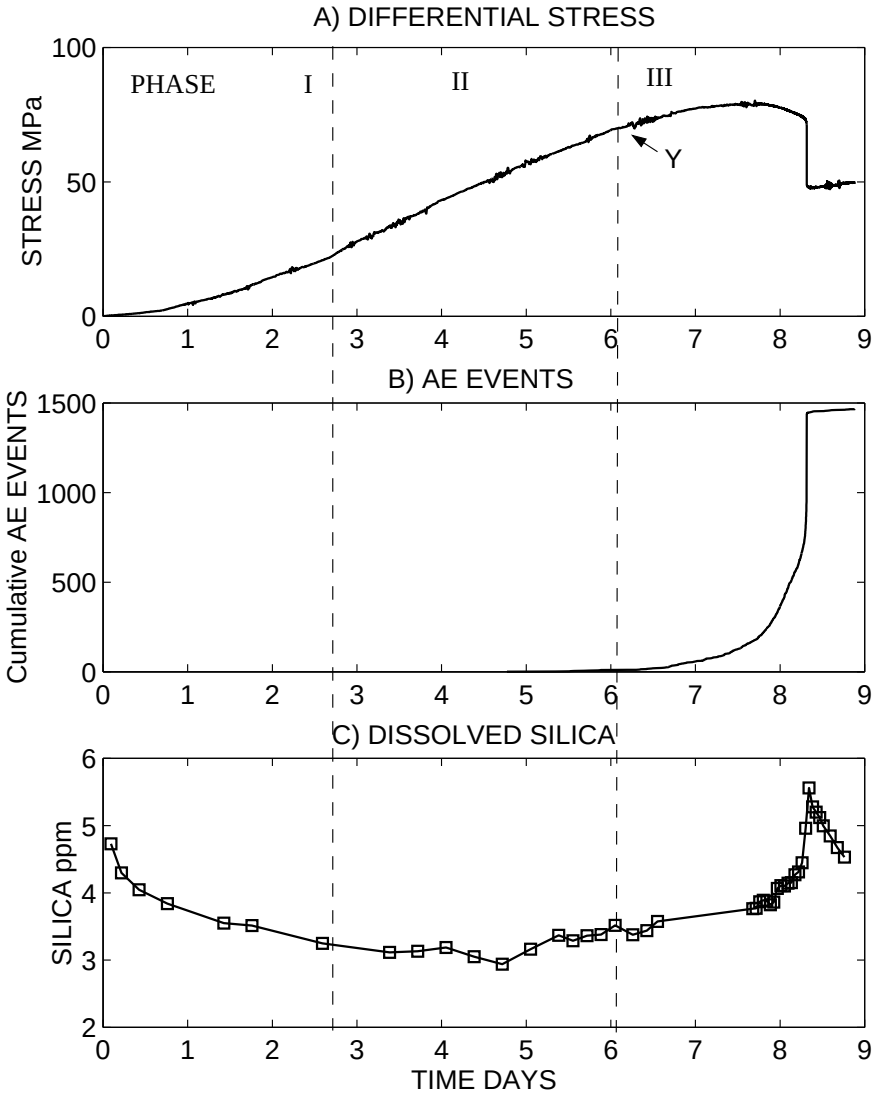

Figure 6.1. The measured a) stress, b) AE event rate and c) exit pore fluid silica concentration as a function of time during slow loading of Locharbriggs sandstone. The strain rate used was $2.8 * 10^{-8}$ /s. The amount of dissolved silica in the exit pore water correlates with the three phases of microfracturing. These are inferred compaction (I), linear elastic phase (II) and post-yield phase (III). Y indicates the yield point indicating the onset of nonlinearity in the stress-strain behaviour.

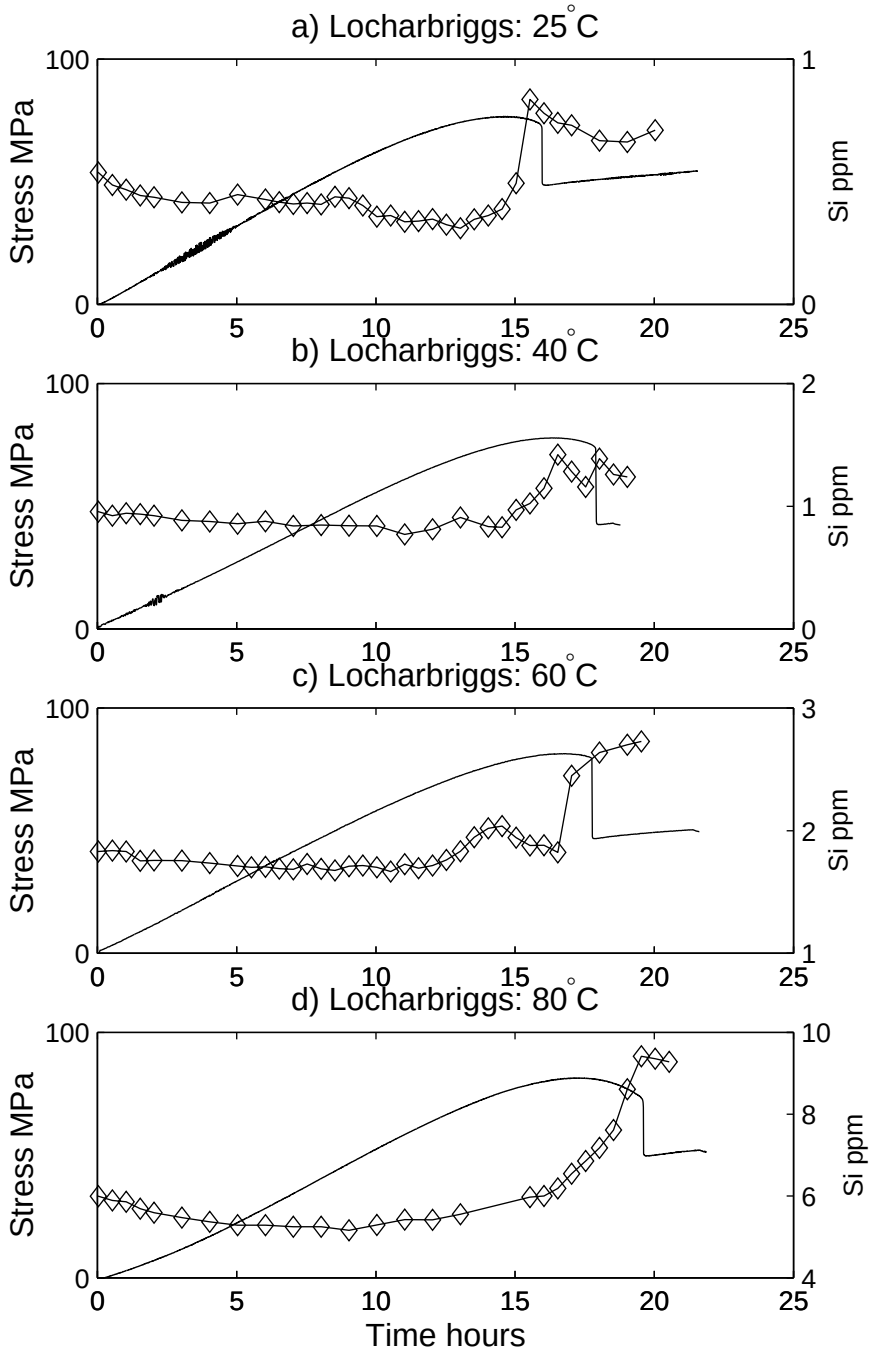

Figure 6.2. The silica signal in the Locharbriggs tests at 25-80°C. The amount of silica in the exit pore fluid increases with increasing temperature. Note that the y-axis scale is 0-2 ppm in (a) and (b), 0-4 ppm in (c) and 4-10 ppm in (d).

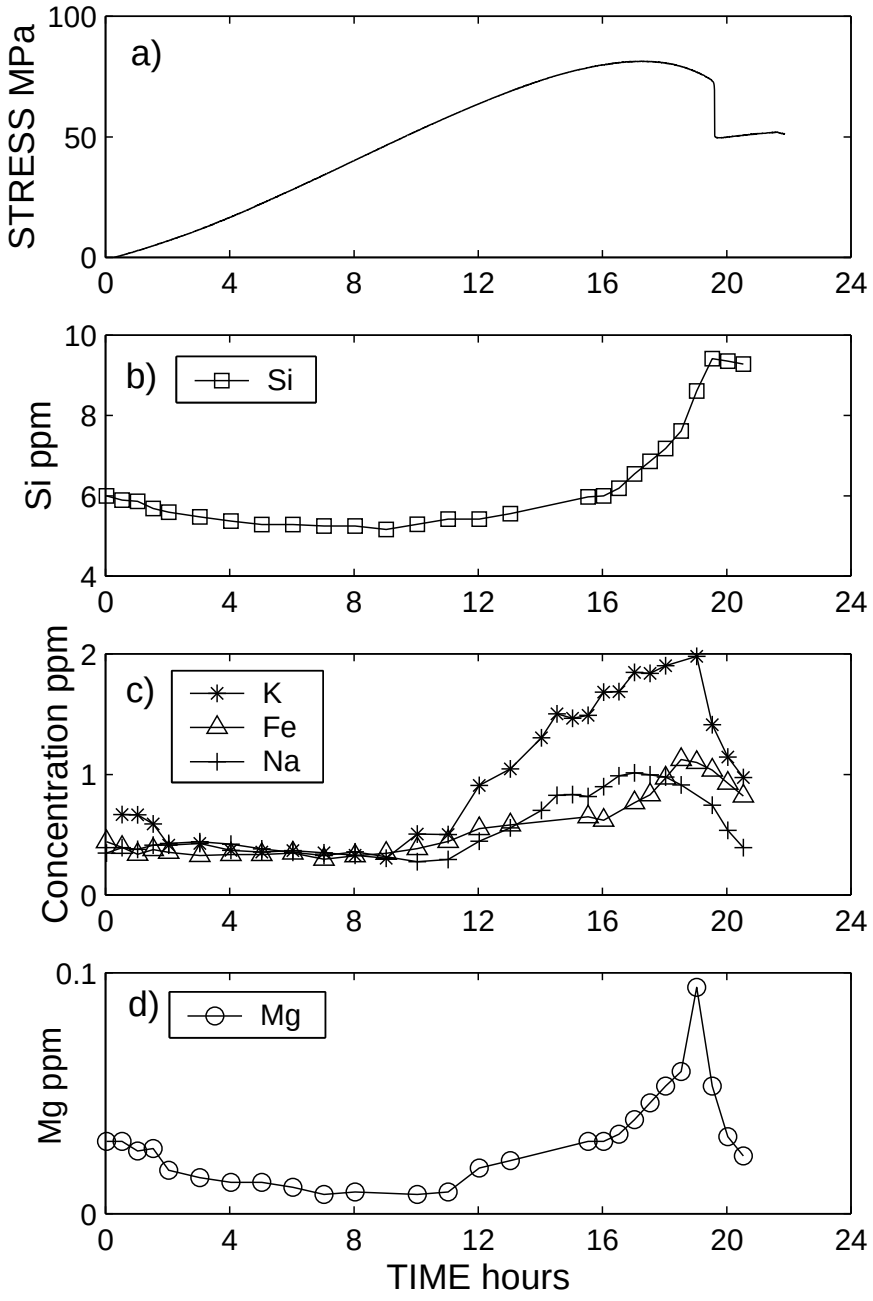

Figure 6.3. The measured a) differential stress and the exit pore fluid concentrations of dissolved b) silica, c) potassium, iron, sodium and d) magnesium for a test conducted at $80°C$ with a strain rate of $3.4 * 10^{-7}$ /s. These data can be attributed to dissolution from feldspar, quartz, hematite, dolomite and illite grains in the test specimen.

In the strain hardening phase of deformation both AE activity and Si concentration increased rapidly. The increased amount of silica in the exit pore water can be attributed to active dissolution from the growing crack tips or to passive dissolution from the newly created fracture surfaces. Peak stress was followed by a pronounced period of strain softening indicating quasi-static crack linkage that eventually lead to macroscopic failure and associated stress drop. Specimen failure was accompanied by a maximum of 5.5 ppm in the Si concentration. This silica peak occurs due to dissolution from the newly created fracture surface and gouge fill, as previously documented by *Ngwenya et al.*, (2000). Frictional sliding followed the macroscopic failure. During this stage the AE activity decreased to a constant level of one event per minute while the Si concentration decreased continuously.

Due to the requirement of 5ml of sample for the chemical analysis, changes in the pore fluid chemistry could only be monitored during the slow loading rate tests at 10^{-7} and 10^{-8} /s. The best signal to noise ratio was obtained for the 80°C tests due to the temperature dependence of the silica dissolution reaction (2.44). This observation is illustrated in figure 6.2, which shows the temporal evolution of the dissolved silica in the 25-80°C tests. In all of the slow strain rate Locharbriggs tests the variation of silica in the exit pore fluid corresponded to the main stages of deformation. Initial decrease was followed by a steady state concentration and a subsequent increase in the amount of silica in the strain hardening and softening phases of deformation. While the clearest geochemical signal as recorded for the concentration of silica, minor amounts of Fe, K, Na and Mg were also present in the pore fluid. The steady state and maximum recorded values for the concentrations of Si, Fe, K and Na for the Locharbriggs tests are listed in table 6.1. Figure 6.3 illustrates the typical evolution of the Si, K, Fe, Na and Mg concentrations during a 10^{-7} /s test. Although the signal was stronger after the yield point, the dissolution of Fe, K, Mg and Na was not directly correlated with the recorded AE. This could be an indication of a more complex chemical system or it may be caused by their higher surface area to volume ratio.

The presence of K, Fe, Na and Mg in the pore fluid can be attributed to dissolution from feldspar, illite, dolomite and diagenetic hematite.

Table 6.1. Chemical and AE data for the Locharbriggs tests. The exit pore water contains dissolved silica, sodium, potassium and iron. During the linear elastic phase of deformation the concentration of dissolved ions is approximately constant, indicating a steady state. C_{ss} is the measured steady-state value and dash indicates very low concentrations below 0.1 ppm. The majority of AE events occur after the peak stress has been attained.* This specimen was cut perpendicular to lamination, while the other specimen were cut parallel to lamination.

$\dot{\varepsilon}$ 1/s	T $^{\circ}C$	Value	Fe ppm	K ppm	Na ppm	Si ppm	% AE events after σ_{max}
3.3×10^{-7}	25	C_{ss}	0.1	-	0.8	0.3	74
		C_{max}	1.2	0.8	1.9	0.8	
2.8×10^{-7}	40	C_{ss}	0.1	-	0.4	0.8	80
		C_{max}	0.4	1.0	1.7	1.4	
3.1×10^{-7}	60	C_{ss}	1.0	0.5	0.8	1.7	60
		C_{max}	2.1	2.2	2.6	2.7	
3.4×10^{-7}	80	C_{ss}	0.3	0.4	0.3	5.0	81
		C_{max}	1.1	2.0	1.0	9.5	
2.8×10^{-8}	80	C_{ss}	0.1	0.6	0.5	3.0	91
		C_{max}	0.3	1.3	0.7	5.5	
3.1×10^{-8}*	80	C_{ss}	0.1	0.2	0.2	3.4	61
		C_{max}	0.1	1.7	1.0	6.7	

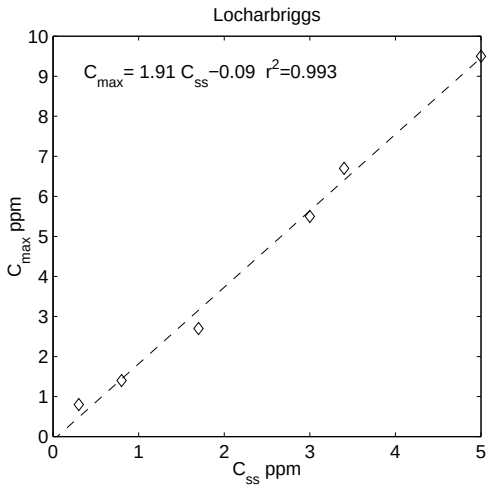

Figure 6.4. The maximum silica concentration C_{max} as a function of the steady-state value C_{ss} for the Locharbriggs tests. Both C_{ss} and C_{max} are listed in table 6.1.

6.2.2 The silica signal and its correlation with AE damage

In this section I will concentrate on the dissolution behaviour of the dominant mineral (silica) and its correlation with the measured AE damage. In order to allow for comparison between tests conducted at different strain rates and temperatures a parameter ΔC_{Si} was defined as

$$\Delta C_{Si} = C_{Si} - C_{ss} \tag{6.1}$$

where C_{Si} and C_{ss} are the outlet and steady state concentrations, respectively. The steady state values for all of the tests are listed in table 6.2. The maximum silica concentration C_{max}, which typically coincided with specimen failure, was a function of the steady state value C_{ss} and it was given by

$$C_{max} = 1.91 C_{ss} - 0.09 \tag{6.2}$$

with a high r-squared value of 0.993. The correlation between C_{max} and C_{ss} is shown in figure 6.4.

The normalised reactive surface area s_n corresponding to the steady-state value of 3 ppm of the 10^{-8}/s test was estimated from (*Kieffer et al.*, 1999)

$$s_n = \frac{\Delta C_{Si} Q_f}{k_+ V_{rock}} \tag{6.3}$$

where Q_f is the fluid flow rate, k_+ is the normalised dissolution rate constant (*Rimstidt and Barnes*, 1980) and V_{rock} is the volume of the rock sample. In comparison, a rough estimate of the specific surface area of the rock specimen s_v was obtained by assuming regular packing of identical spheres given by

$$s_v = \frac{6(1-\phi_i)}{D_p} \tag{6.4}$$

where ϕ_i is the interconnected porosity and D_p is the pore diameter (*Dullien*, 1979). For ΔC_{Si}= 3ppm, Q_f= 0.2 ml/min, k_+= 4.79×10^{-12}mol cm^{-2} s^{-1}, V_{rock}= 90.7 cm^3, ϕ_i= 16 % and D_p= 200 μm the calculated values for s_n and s_v are 0.38/cm and 252/cm, respectively. Hence, only a small fraction of the total surface area of the rock is likely to be contributing to the measured silica signal at this deformation stage. This observation rules out the hypothesis that silica is dissolving passively from the crack walls. In fact, the small reactive surface area is consistent with crack growth by the stress corrosion mechanism.

The geochemical signal was strongly correlated with the microfracturing damage derived from the AE data, as illustrated in figure 6.5. At 80°C the relationship between ΔC_{Si} and the damage parameters D, S, N and E was given by a power law of the form

$$\Delta C_{Si} \propto (D, S, N, E)^x \tag{6.5}$$

where x is the power-law exponent. The x-value in equation (6.5) ranged from 0.35 to 0.40 with high correlation coefficients of 0.94 and 0.96, respectively. Such a strong correlation between the silica signal and the microcrack damage is quantitatively consistent with the idea of progressive growth and linkage of microcracks by the stress corrosion mechanism. However, ΔC_{Si} is sensitive to the reactive, connected surface area traversed by the pore fluid, while S corresponds to the total increase in crack surface area. Since the magnitude of exponent x in (6.5) was consistently less than one, only a fraction of the accumulated microcrack damage was chemically reactive at any given time.

The measured silica signal also displayed a clear temperature dependence, as illustrated in figure 6.6. The steady-state concentration C_{ss} varied from 0.3 ppm at 25°C to 5.0 ppm at 80°C. In the 10^{-7} /s tests at 25-80°C both steady-state

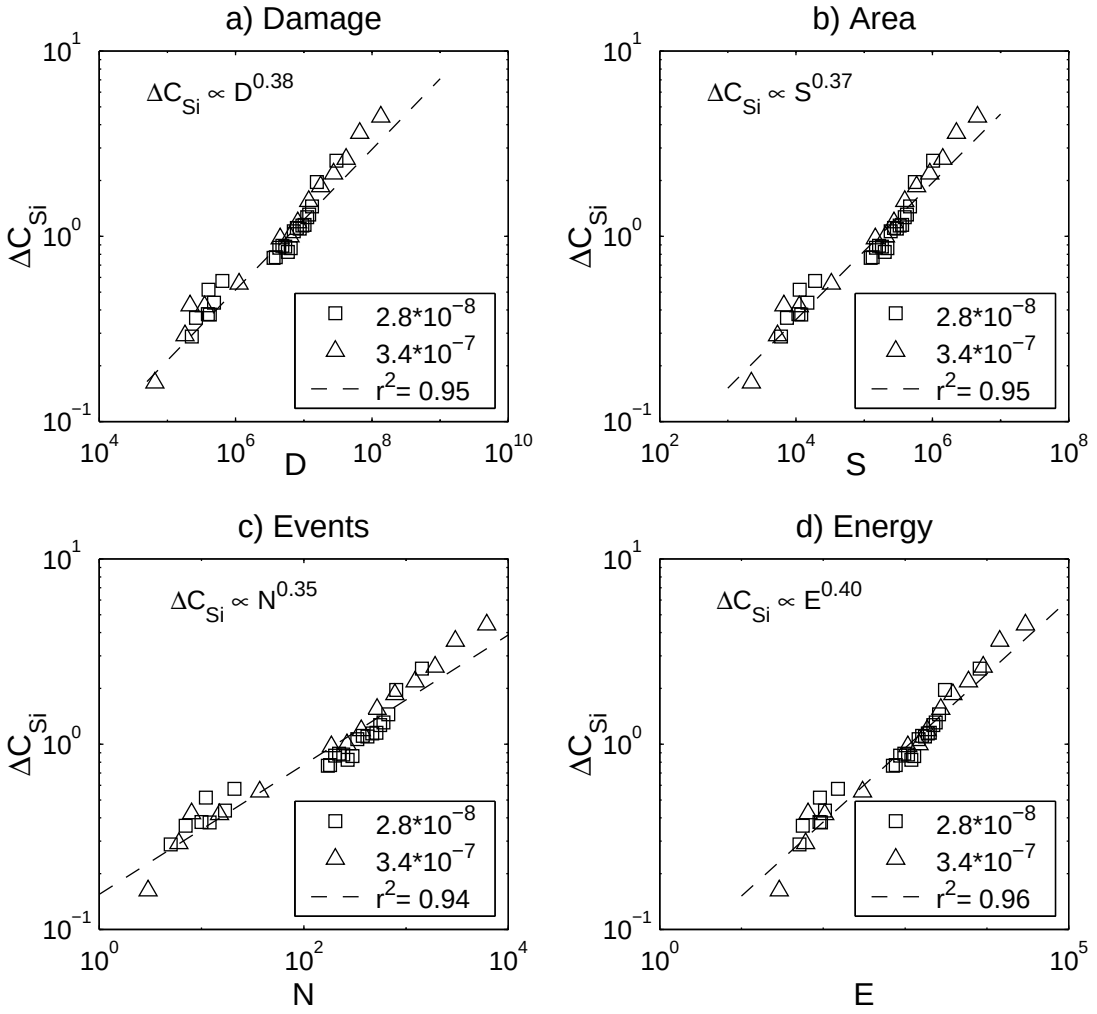

Figure 6.5. The measured amount of dissolved silica as a function of a) damage D, b) area S c) cumulative AE events N and b) cumulative AE energy E. The damage parameters derived from the AE data and the amount of dissolved silica in the exit pore fluid are correlated by a power-law relationship.

and maximum silica concentrations showed an Arrhenius (2.44) type temperature dependence given by

$$\ln C_{max} = 15.0 - 4587/T \quad (6.6)$$

$$\ln C_{ss} = 16.3 - 5209/T \quad (6.7)$$

with high r-squared values of 0.96 and 0.99, respectively and temperature T is in Kelvins. These observations suggest that reaction rates were also contributing to the measured silica signal. However, the steady state silica concentration at 80°C was not unique, since the C^{ss} was 5.0 and 3.0 for the 10^{-7} and 10^{-8} /s tests, respectively. The lower steady-state value at 10^{-8} /s could have been caused by a greater amount of initial compaction in the slower strain rate tests (*Sangha and Dhir*, 1972). Due to the high linear flow velocity of water, the Si concentrations were consistently below equilibrium concentrations in my tests, as shown in figure 6.6.

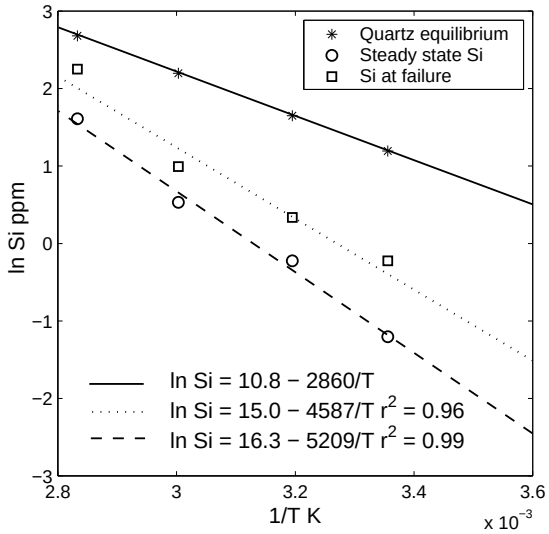

Figure 6.6. The steady state and peak silica concentrations for the slow strain rate as a function of inverse temperature for the slow strain rate tests at 10^{-7} s^{-1}. The concentrations display a clear temperature dependence. The equilibrium silica concentrations were calculated from *Rimstidt and Barnes* (1980).

6.3 Clashach sandstone pore fluid chemistry

A distinct geochemical signal was also recorded for the Clashach tests. Figures 6.7 and 6.8 show the measured silica signal for the 10^{-6} to 10^{-8}/s and 25-80°C tests. Because Clashach sandstone was twice as strong as the Locharbriggs one there was more time available for the collection of pore fluid samples. Hence, it was possible to resolve a silica signal also for the 10^{-6}/s test. In general, the measured silica signal was similar to that observed in the Locharbriggs tests. Initial decrease in the amount of dissolved silica was followed by an approximately constant value, indicating a steady state. However, any increase in Si concentrations in the strain hardening phase of deformation was confined to the immediate two hours that preceded specimen failure. The increase in Si concentrations prior macroscopic failure was therefore much sharper than that observed in the Locharbriggs tests. This observation is consistent with the considerably shorter strain hardening phase in the Clashach tests in comparison to the Locharbriggs tests. The measured silica signal was not correlated to the AE activity in the strain hardening phase of deformation, possibly due to a more complex chemical system in the Clashach tests. This is quite surprising since the Locharbriggs sandstone is mineralogically more complex.

The Clashach Si concentrations at failure were consistently higher than the Locharbriggs ones, as shown in table 6.2. They ranged from 10.4 to 409 ppm. The 40°C test was marked by extremely high concentrations amounting to several hundred ppm at specimen failure. However, the analytical errors (Appendix C) and the relative proportions of dissolved ions of the 40°C test were similar to those observed in the other tests. At 2.8-3.0 the steady state silica concentrations of the 80°C Clashach tests were close to the 3-5 ppm observed for the Locharbriggs sandstone. It was not possible to compare the results of the different temperature tests, since the Clashach Si concentrations did not display an Arrhenius type dependence on temperature. This observation suggests that the Clashach geochemical signal was dominated by the amount of reactive surface area rather than reaction rates.

There are several lines of evidence that suggest that the Clashach tests were characterised by a more complex chemical system than the Locharbriggs tests. The Clashach exit pore fluid contained a considerable amount of ions other than

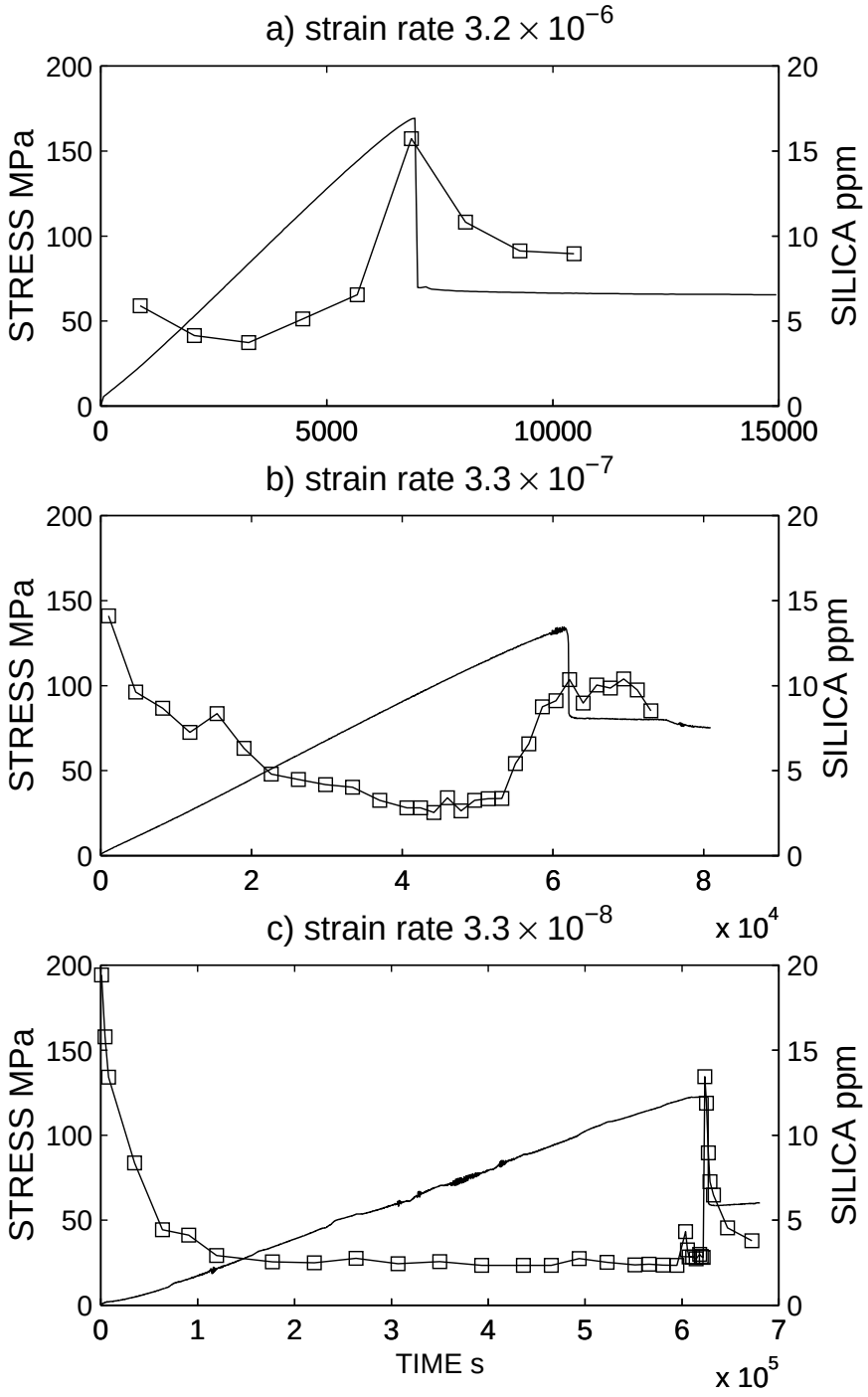

Figure 6.7. The silica signal in the Clashach 80°C tests at 10^{-5} to 10^{-8} /s .

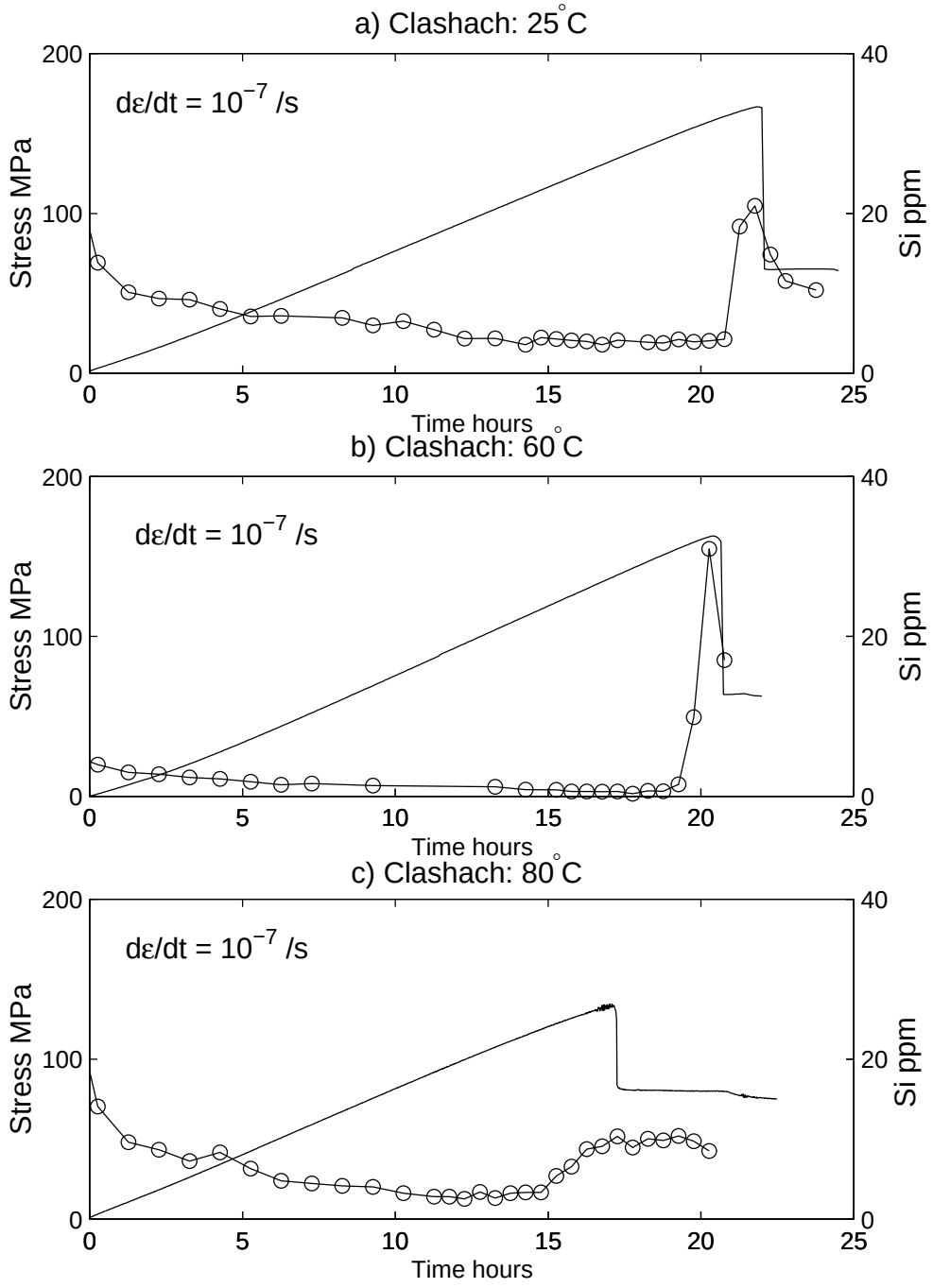

Figure 6.8. The silica signal in the 25-80°C Clashach tests at 10^{-7} /s.

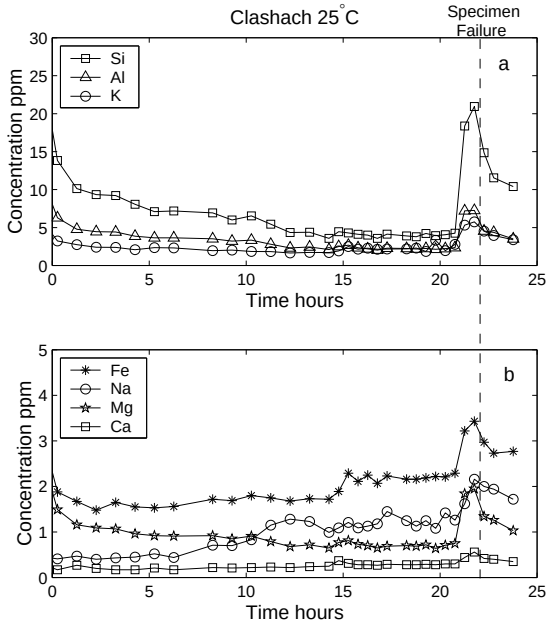

Figure 6.9. The concentrations of Si, K, Na and Al in the 25°C Clashach test at 10^{-7}/s. Following a sharp increase in the strain hardening phase, the ion concentrations peaked near the specimen failure.

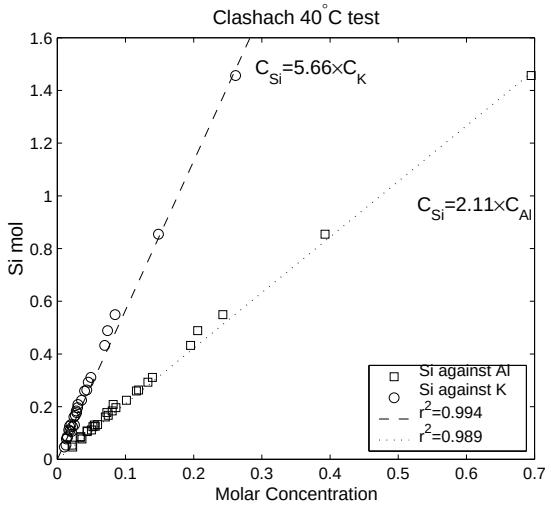

Figure 6.10. The ratios Si/Al and Si/K in the 40°C Clashach test. The Si/Ca ratio also remained constant at 218.7 (r^2=0.97) for this test.

silica, including Al, Ca, Fe, K, Mg and Na. Their presence in the pore water can be attributed to dissolution from quartz, feldspar, illite and diagenetic iron in the test specimen. The steady state and maximum values for Al, Ca, Fe, K, Mg and Na are listed in table 6.2. The concentrations of Al, K and Na were typically higher than that observed in the Locharbriggs tests. The most abundant ions were Si, Al and K, hence suggesting that a high proportion of the measured signal can be attributed to dissolution from quartz and alkali feldspar. The temporal evolution of Al, Ca, Fe, K, Mg and Na was similar to that of silica, as illustrated in figure 6.9. An initial decrease was followed by steady-state values and a subsequent increase prior macroscopic failure of the test specimen. The relative proportions of dissolved ions also stayed approximately constant, as shown in figure 6.10 for the 40°C test. In fact, for most tests the ratios Si/Al and Si/K remained constant at 2.2-3.7 and 5.7-6.7, respectively (table 6.3). The corresponding r-squared values were high at 0.96-0.99. Hence, a significant proportion of the recorded geochemical signal can be attributed to dissolution from alkali feldspar in the test specimen. Furthermore, the amount of Al present in the Clashach pore water was much greater than the amount of K relative to their stoichiometric ratios in the mineral. No such correlation between Si and other ions was observed in the Locharbriggs tests, although Locharbriggs sandstone contains more feldspar (16%) than Clashach (11%). The relative contribution of feldspar dissolution to the measured geochemical signal was therefore higher in the Clashach tests. Furthermore, in the 80°C test at 10^{-7}/s the concentrations of K, Na and Al actually peaked simultaneously before the dynamic failure of the test specimen, as illustrated in figure 6.11. Silica concentrations, however, reached their maximum at the time of the macroscopic failure. All of these observations suggest that the chemical system in the Clashach tests was a more complicated one than that in the Locharbriggs tests. Therefore, it is not surprising that no direct correlation between AE damage and ion concentrations was apparent in the recorded data.

6.4 Crack growth constitutive equations

A time to failure analysis of damage D, S, N and E (section 5.3.5) was carried out in order to quantify the evolution of the fracturing process in the Clashach

Table 6.2. The composition of the exit pore fluid in the Clashach tests. The pore fluid contained dissolved Al, Ca, Fe, K, Mg, Na and Si. The data for the 40°C test was quite noisy and the recorded concentrations were abnormally high. However, the relative proportions of dissolved ions in the the 40°C test were similar to that observed in the other tests.

$\dot{\varepsilon}$	T	value	Al	Ca	Fe	K	Mg	Na	Si
1/s	°C		ppm	ppm	ppm	ppm	ppm	ppm	ppm
2.5×10^{-7}	25	C_{ss}	2.2	0.2	1.8	1.7	0.7	1.2	4.1
		C_{max}	7.3	0.6	3.4	5.7	2.0	2.2	21.0
2.2×10^{-7}	40	C_{ss}	10	0.5	3	8	2	0.8	30
		C_{max}	187	3	0	102	33	1.5	409
2.7×10^{-7}	60	C_{ss}	0	0.1	0	0	0.1	0	0.6
		C_{max}	7.8	0.4	1.9	6.2	2.1	0.2	30.9
3.0×10^{-7}	80	C_{ss}	0.4	0	0.3	1.6	0.1	0.8	3.0
		C_{max}	1.1	0.2	1.2	5.9	0.4	2.4	10.4
3.1×10^{-8}	80	C_{ss}	0.2	0.1	0.3	0.8	0.1	0.3	2.8
		C_{max}	4.0	0.8	1.8	3.3	1.6	5.2	13.4

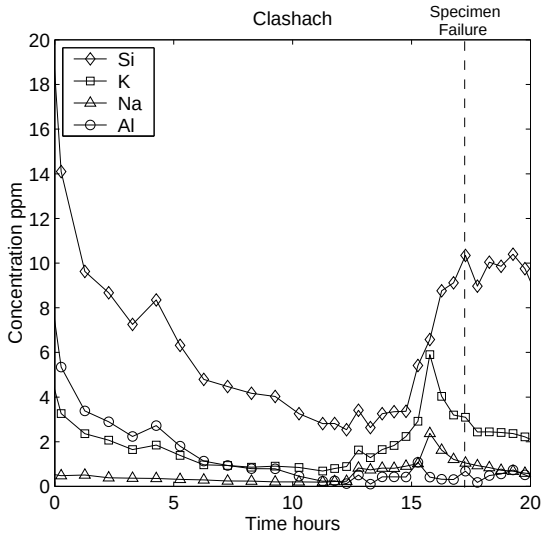

Figure 6.11. The concentrations of Si, K, Na and Al in the Clashach 10^{-7}/s test. The peak in the concentrations of K, Na and Al occurred prior specimen failure. This could be an indication of a more complex chemical system than in the Locharbriggs tests.

Table 6.3. The ratios of Si/Al, Si/K and Si/Ca ratios in the Clashach tests. These ratios remained constant throughout the tests listed below. The molar silica concentration C_{Si} is given by $C_{Si} = j_3 \times C_{Al,K,Ca}$.

$\dot{\varepsilon}$	T	Si/Al		Si/K		Si/Ca	
1/s	°C	j_3	r^2	j_3	r^2	j_3	r^2
2.5×10^{-7}	25	2.30	0.961	6.37	0.904	-	-
2.2×10^{-7}	40	2.11	0.998	5.66	0.994	218.7	0.974
2.7×10^{-7}	60	3.73	0.989	6.69	0.989	-	-
3.1×10^{-8}	80	2.19	0.988	5.88	0.978	-	-

and Locharbriggs tests. Assuming crack growth in a self-similar fashion, the parameters D and N can be considered as remote measures of the mean crack length. Similarly, the chemical reaction rate is also related to the mean crack length. For $n > 2$ the power law form (2.16) of the dependence of v on K (2.11) predicts that the acceleration of crack length c takes the form

$$c = c_0(1 - t/t_f)^z = c_0(1 - t/t_f)^{\frac{2}{2-n}} \tag{6.8}$$

where c_0 is the initial crack length at time t=0 and t_f is the failure time (*Das and Scholz*, 1981; *Main*, 1999). If the stress is increasing linearly, the resultant acceleration takes a similar form with a shorter acceleration for a given value of n (*Main*, 2000). It is interesting to note that power-law equations similar to (6.8) are used in statistical physics to describe the behaviour of two phase systems near the critical point (*Stanley*, 1971; *Stauffer*, 1985). The fracturing process of a rock sample during a laboratory test can be considered to be a similar system, consisting of two phases: the matrix and porosity (cracks) (*Chelidze*, 1982). Accordingly, the predominance of one phase (cracks) over another (rock matrix) can be described by an order parameter or $(1 - t/t_f)$ in (6.8).

The exponential formula (2.18) predicts a slightly different form. Combining equations (2.11) and (2.18) gives

$$\frac{dc}{dt} = v_0 \exp\left(\frac{c}{c^+}\right) \tag{6.9}$$

where $c^+ = (Y^2\sigma^2\varphi)^{-1}$ and φ is a constant. Equation (6.9) can also be written as

$$v_0 = \exp\left(-\frac{c}{c^+}\right)\frac{dc}{dt} \tag{6.10}$$

or, alternatively

$$v_0 = \frac{d}{dt}\left[-c^+ \exp\left(-\frac{c}{c^+}\right)\right] \tag{6.11}$$

and after integrating (6.11) I get

$$v_0 t = -c^+ \exp\left(-\frac{c}{c^+}\right) + zum \tag{6.12}$$

$$zum = c^+ \exp\left(-\frac{c_0}{c^+}\right) \tag{6.13}$$

where zum is a constant. Its value results from the fact that $c = c_0$ at $t = 0$. Substituting $t_f = c^+[\exp(c_0/c^+)V_0]^{-1}$ into (6.12) therefore gives

$$c = c_0 - c^+ \ln(1 - t/t_f) \tag{6.14}$$

Hence, (6.14) describes the evolution of crack length that is predicted by the exponential formula (2.18), which assumes that $v \propto \exp G$.

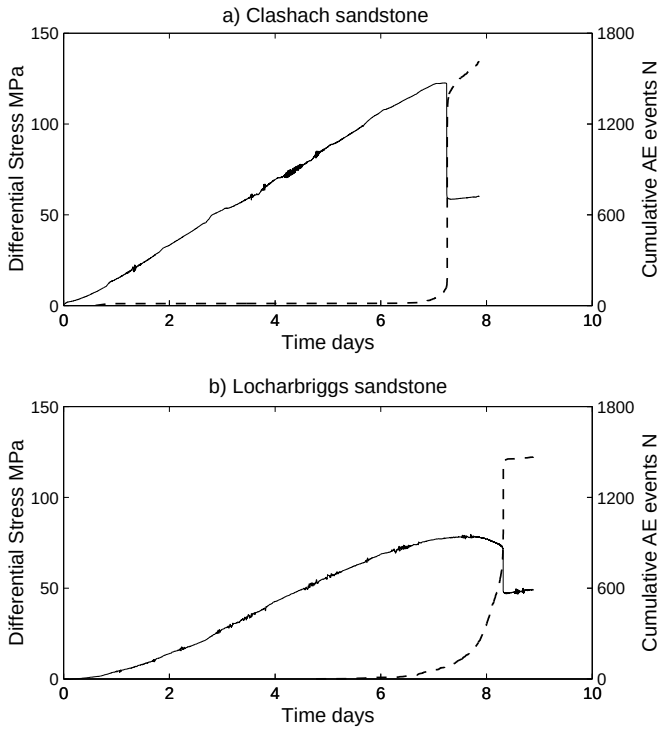

Figure 6.12. The differential stress and cumulative AE count N as a function of time for the a) 3.3×10^{-8} /s Clashach test and the b) 2.8×10^{-8} /s Locharbriggs test. Both experiments were carried out at a temperature of 80°C. The accumulation of damage was more gradual in the Locharbriggs test.

6.5 Accumulation of damage and Si dissolution

In this section I will investigate the temporal evolution of damage and pore fluid Si concentrations as predicted by the power law (6.8) and exponential formula (6.14). The evolution of damage and differential stress in the very slow strain rate tests at 10^{-8}/s is illustrated in figure 6.12 for both sandstones used in this study. While the total amount of damage, as indicated by the AE catalogue, was similar for both sandstones, the evolution of damage showed significant differences. For instance, in the 10^{-8}/s Locharbriggs test significant AE activity began over two days before the failure of the test specimen. However, in the Clashach 10^{-8}/s tests any significant AE activity was confined to the two hours that preceded specimen failure. Hence, the accumulation of damage was more gradual in the Locharbriggs tests.

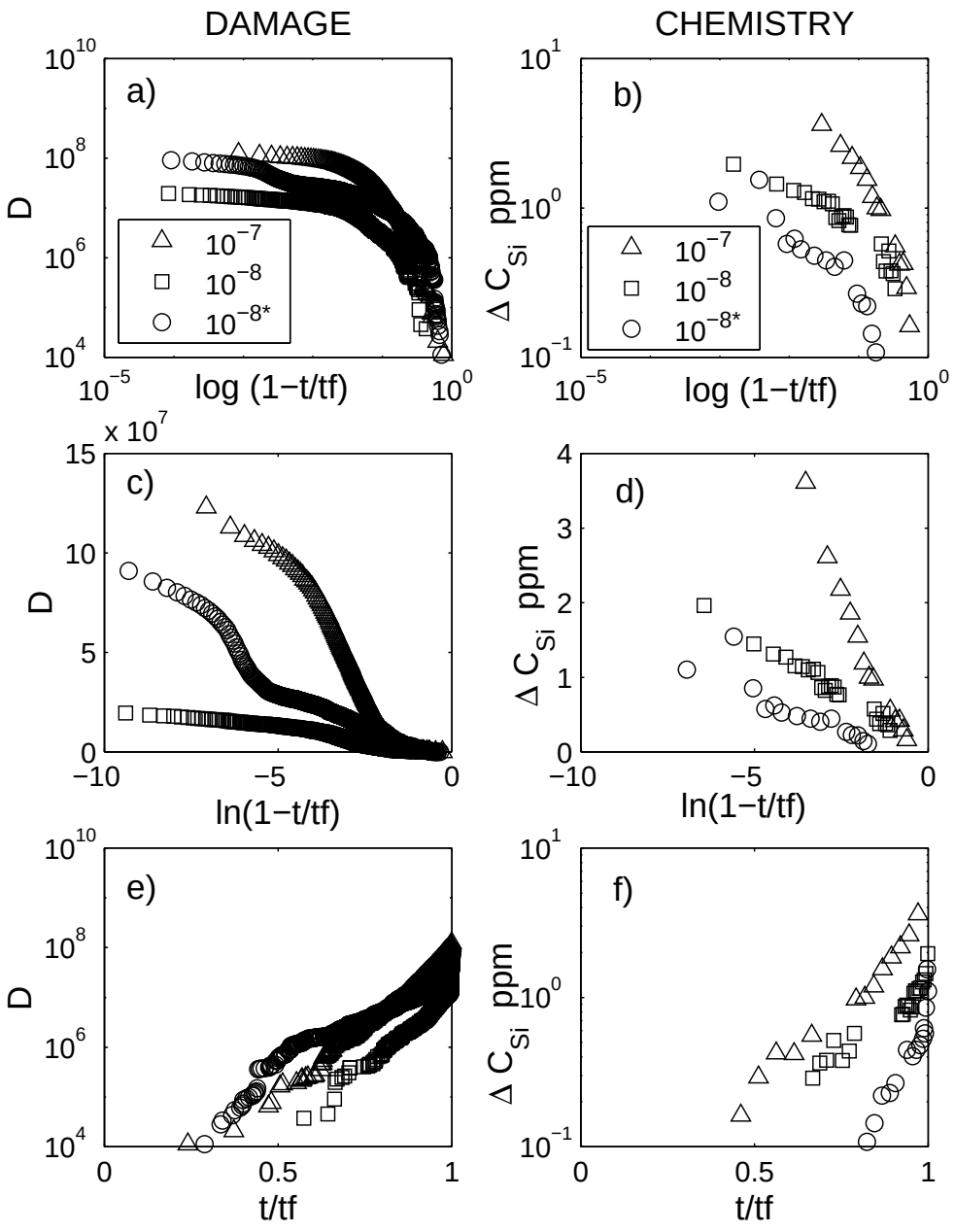

Figure 6.13. The temporal evolution of damage and silica in the Locharbriggs tests. (a,b) If we assume that crack velocity v scales with stress intensity K according to a power law (2.16) with n>2 one would expect a linear trend on a log D versus log (1-t/t_f) plot (6.8). (c,d) If the relationship between v and K was exponential (2.17) then D would be a linear function of ln (1-t/t_f) given by (6.14). The measured data shows that D is an exponential function of (t/t_f) given by (6.18) as indicated by the linear trends in (e) and (f).

Table 6.4. The fitted values for exponential formula (6.18) for the Locharbriggs tests. An exponential relationship is predicted assuming linear dependence of crack velocity v on stress intensity K. Here are the fitted values for the exponent q in equation (6.18) and the corresponding r-squared values for the different tests. * This specimen was cut perpendicular to lamination. All the other samples used were cut parallel to lamination.

$\dot{\varepsilon}$	T	ΔC_{Si}	r^2	D	r^2
1/s	$^\circ C$	q		q	
2.8×10^{-8}	80	4.26	0.904	14.4	0.982
3.1×10^{-8}*	80	11.4	0.874	8.13	0.958
3.4×10^{-7}	80	5.24	0.972	13.6	0.990
3.1×10^{-7}	60	8.25	0.786	3.51	0.811
2.8×10^{-7}	40	11.8	0.735	4.90	0.896
3.3×10^{-7}	25	22.0	0.950	6.01	0.938

The damage evolution in the Locharbriggs tests was investigated assuming that D and ΔC_{si} can be considered as indicators of the mean crack length c, as shown in figure 6.13. The chemical signal was well modelled assuming an exponential law (6.14), as indicated by the linear trend in figure 6.13d. However, the accumulation of damage was not well described by either power (6.8) or exponential (6.14) formulae. Instead, a good empirical fit was obtained by plotting $\log D$ versus t/t_f, as shown in fig. 613e. This kind of evolution of damage is also predicted by the constitutive equations for subcritical crack growth by setting $n = 2$ in the power law formula (2.16) and thus

$$v = v_0 \left(\frac{K}{K_0} \right) \tag{6.15}$$

Equation (6.15) indicates that the crack growth rate is directly proportional to crack length c via

$$\frac{dc}{dt} = v_0 \left(\frac{c}{c_0} \right) \tag{6.16}$$

After integration the crack length is given by

$$c = c_0 \exp\left(\frac{v_0 t}{c_0}\right) \tag{6.17}$$

Hence, assuming that the crack growth velocity v equals the Rayleigh wave velocity v_R the crack length c is given by

$$c = c_0 \exp\left(q\frac{t}{t_f}\right) \tag{6.18}$$

where q is a constant equal to $ln(v/v_R)$. The specimen failure time t_f was marked by a maximum in the AE event rate. Equation (6.18) provided the best fit to both the measured silica concentration and crack damage in the Locharbriggs tests. This is indicated by the linear trends in figure 6.13(e,f) and the high correlation coefficients in table 6.4 (r^2=0.74-0.99). The best fit was obtained for the 80°C tests, which had the highest signal-to-noise ratio of the measured geochemical data. In fact, it appears from figure 6.13d that the geochemical signal could be equally well described by an exponential formula (6.14). However, equation (6.14) did not provide a god fit to the crack damage, as illustrated in figure 6.13c. I believe that the differences between fig.6.13c and 6.13d can be attributed to the sampling frequency. While D was calculated from the AE event rate per minute, the geochemical data was sampled only every 30 min. Therefore the actual constitutive time to failure equation is more difficult to resolve from the geochemical data.

The accumulation of damage in all of the Locharbriggs tests was best described by an exponential formula (6.18), as illustrated in 6.14 for the 80°C tests at 10^{-5} to 10^{-8}/s. The left hand side shows log-log plots damage parameters D, S, N and E versus $(1 - t/t_f)$, while the right hand side gives D, S, N and E as a function of t/t_f. It appears that the 10^{-5} /s tests could have been equally well described by a power and an exponential formula. However, this could be an artifact of the 60s sampling frequency for the AE damage. The excellent fit obtained for the

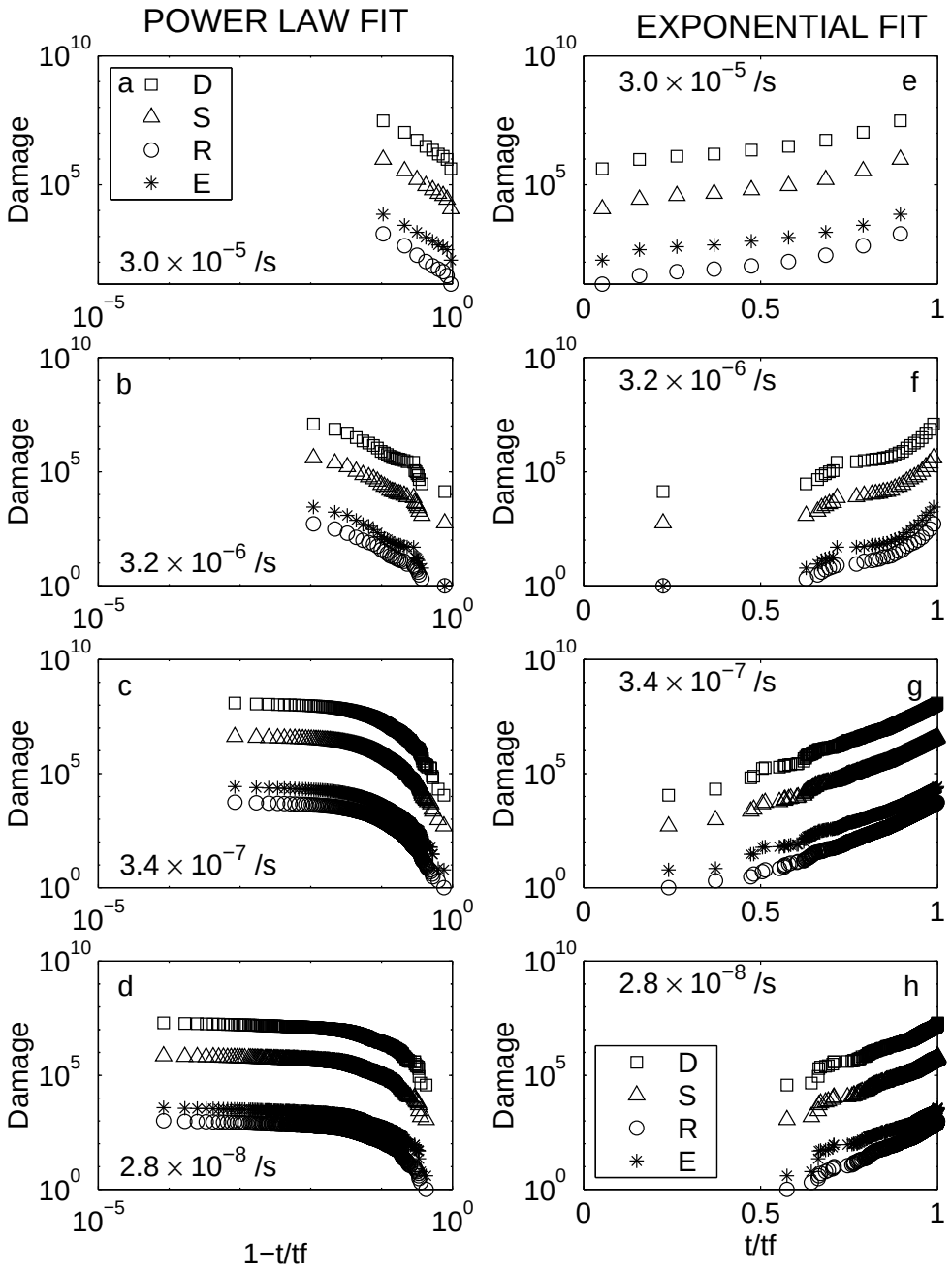

Figure 6.14. The evolution of damage parameters D, S, N, E in the 80°C Locharbriggs tests as a function of (a)-(d) log (1-t/t_f) and (e)-(h) t/t_f. The exponential law (6.18) predicts a straight line on (e)-(h), while the power law (6.8) predicts a straight line on (a)-(d). Hence, the exponential form provides the best fit to the data.

exponential law to the 10^{-8}/s Locharbriggs tests is illustrated in figure 6.15. The value of the exponent q in (6.18) ranged from 14.4-16.3 (r^2=0.98) for this test. In fact, the exponential formula (6.18) consistently outperformed the power law (6.8) with high r-squared values of 0.87-0.99, 0.85-0.99, 0.82-0.99 and 0.85-0.99 for the evolution of D, S, N and E, respectively. The fitted parameters and the corresponding r-squared values are listed in table 6.5. The exponent q in (6.18) also exhibited a clear strain rate dependence: it increased from around four to fourteen as the strain rate was decreased from 10^{-5} to 10^{-8}/s. This property of q is illustrated in figure 6.16. The observed reduction in q with increasing strain rate suggests that the acceleration to failure became steeper with decreasing strain rate.

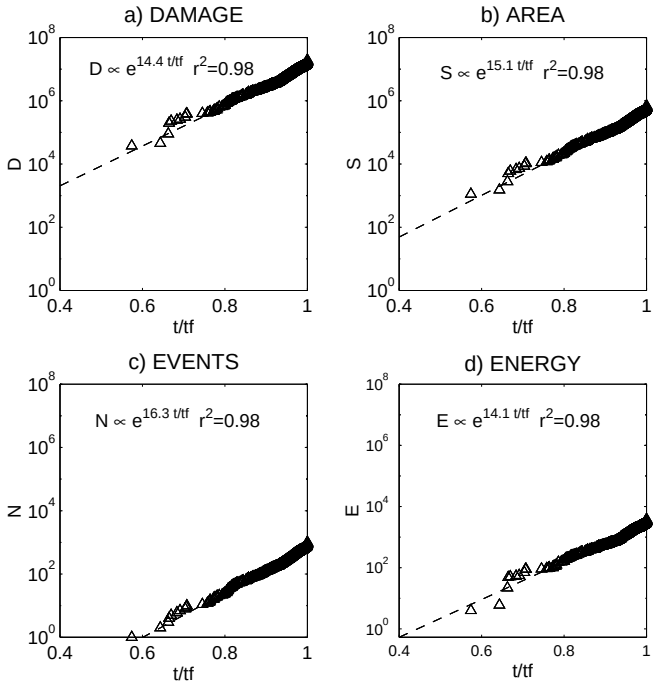

Figure 6.15. The evolution of damage (a) D, (b) S, (c) N and (d) E with time in the Locharbriggs test at 10^{-8} /s. The accumulation of damage was best described by an exponential law (6.18).

It is maybe due to the considerably shorter strain hardening phase in the Clashach tests, that the accumulation of damage was best described by a power law (6.8), as illustrated in figure 6.17. The linear trends on 6.17 (a-d) show that the power law provided a better fit than the exponential law (6.17e-h). Hence, the

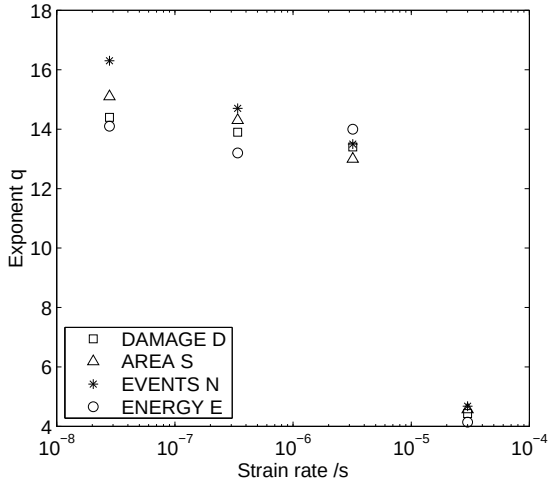

Figure 6.16. The exponential law (6.18) exponent q as a function of strain rate. There was a tendency for the exponent to increase with decreasing strain rate.

damage evolution was much sharper in the Clashach tests. All of the Clashach tests exhibited power law scaling; the fitted parameters and the corresponding r-squared values are listed in table 6.6. The goodness of fit to equation (6.8) ranged between 0.92-0.99, 0.85-0.99,0.67-0.98 and 0.67-0.99 for the evolution of D, S, N and E, respectively. For most of the tests the value of the critical exponent z in (6.8) was close to one, as illustrated in figure 6.18 for the 10^{-7}/s test. The exponent z also showed a clear strain rate dependence. The effect of decreasing strain rate was to decrease z, as illustrated in figure 6.19. As the strain rate was reduced from 10^{-5} to 10^{8} /s the critical exponent for D decreased from 1.45 to 0.14. A reduction in z with decreasing strain rate suggests a more sudden divergence in (6.8) near failure in the slow strain rate tests. This observations is in good agreement with the sharper acceleration to failure that was observed for the slow strain rate Locharbriggs tests.

The evolution of silica concentration prior to specimen failure was also very sharp in the Clashach tests. The acceleration of C_{Si} typically consisted of only three or four data points, due to the minimum sampling frequency of 30 min imposed by the sample volume considerations (section 3.5.5). Hence, the constitutive equation for the evolution of Si concentrations could not be resolved in the data. However, for the 10^{-7}/s test at 80°C the measured Si concentrations C_{Si} could be modelled either by power (6.19) or an exponential (6.20) law, given by

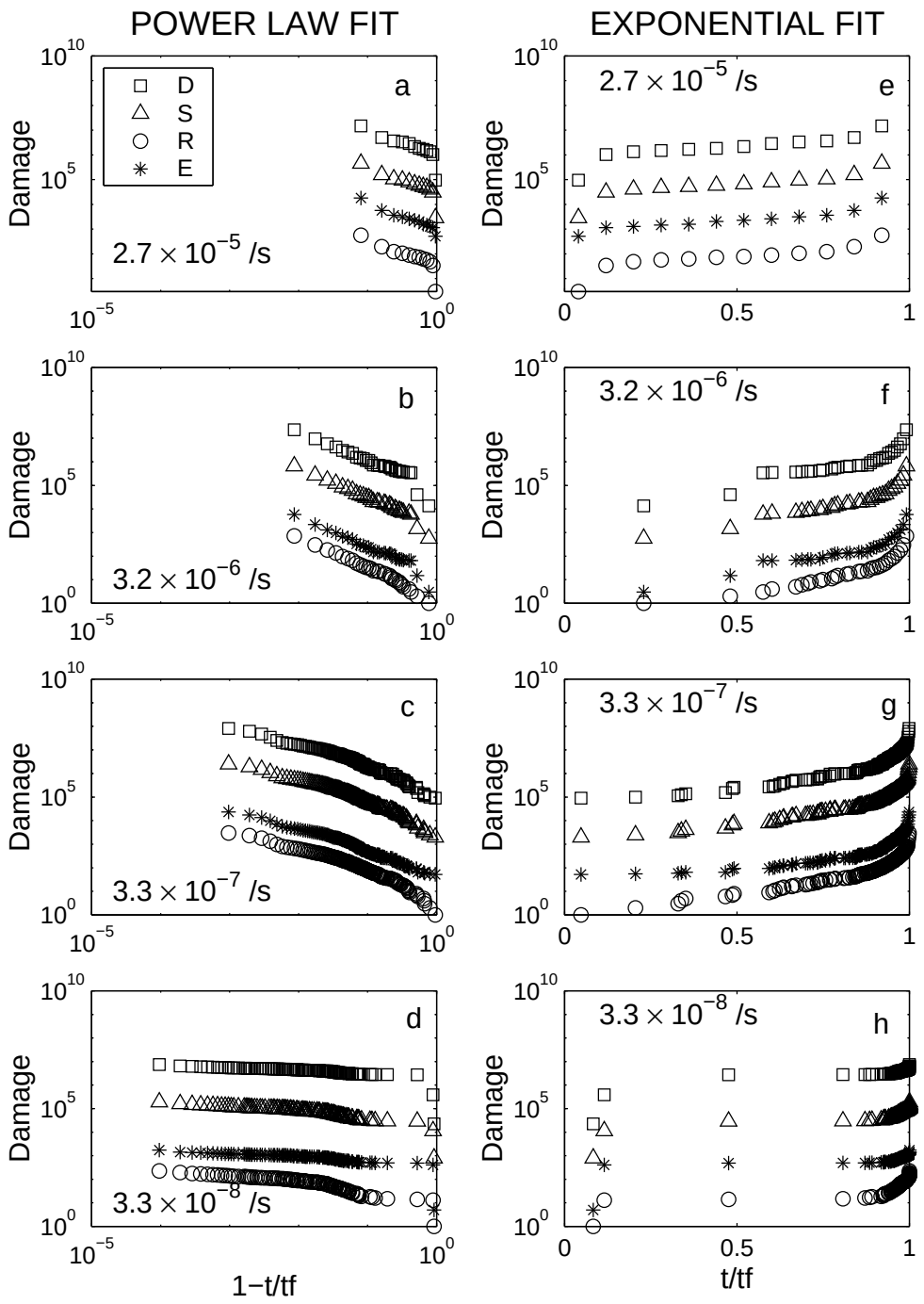

Figure 6.17. The evolution of damage parameters D, S, N, E in the 80°C Clashach tests as a function of (a)-(d) log (1-t/t_f) and (e)-(h) t/t_f. The exponential law (6.14) predicts a straight line on (e)-(h), while the power law (6.8) predicts a straight line on (a)-(d). Hence, the power law provides the best fit to the data.

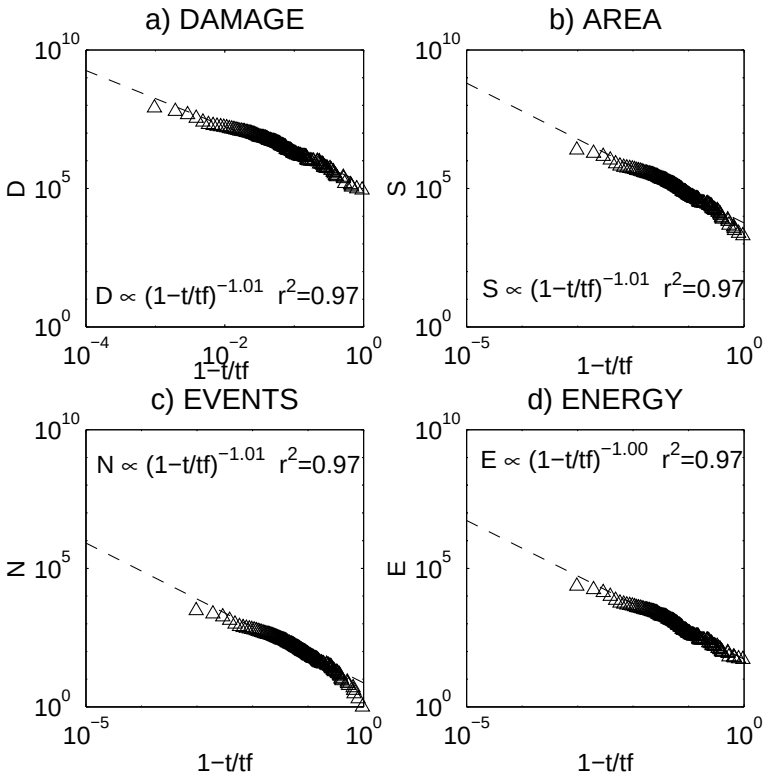

Figure 6.18. The evolution of damage parameters (a) D, (b) S, (c) N and E for the 80° Clashach test at 10^{-7} /s. The temporal evolution of damage is best described by a power law (6.8).

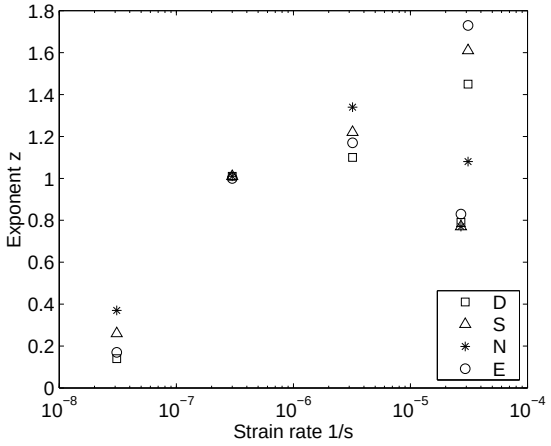

Figure 6.19. The power law exponent z (6.8) as a function of strain rate.

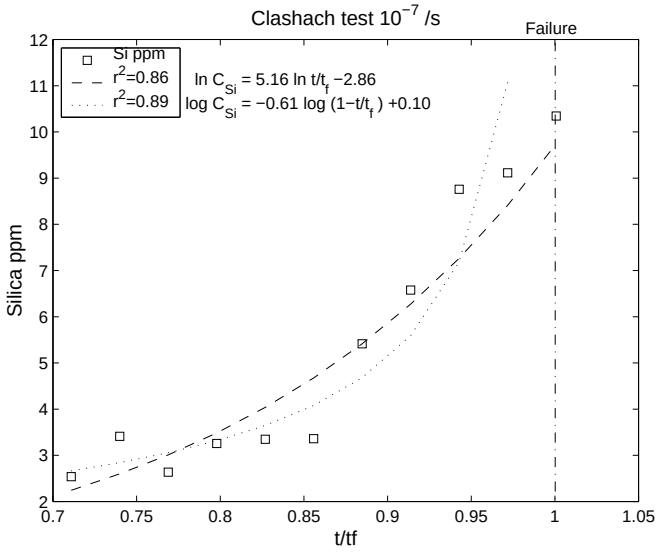

Figure 6.20. The increase in silica concentration in the 80° Clashach test at 10^{-7}/s as a function of time, compared to the two theoretical curves shown.

$$C_{Si} = 10^{0.1} \times (1 - t/t_f)^{-0.61} \quad (6.19)$$

$$C_{Si} = \exp(5.18\, t/t_f - 2.86) \quad (6.20)$$

with r-squared values of 0.89 and 0.86, respectively. Hence, the power law provided a better description of the evolution of Si concentrations in this test.

6.6 Discussion

The results of my experiments demonstrate that triaxial compression tests on Locharbriggs and Clashach sandstones are accompanied by a clear geochemical signal. Dissolution of silica from quartz grains dominates the observed signal, since quartz is the main mineral that makes up the rocks in this study. The geochemical signal that I observe follows the typical microfracturing domains of a stress-strain curve. Initially, the compaction of favourably oriented cracks leads to an exponential decrease in the concentration of silica in the exit pore

Table 6.5. The fitted values to the exponential formula (6.18) for the Locharbriggs tests. D, S, N and E are the damage parameters. Damage D in these tests is well modelled by $D = \exp(q\frac{t}{t_f} + j_1)$. d indicates a test that was carried out dry and * refers to a rock sample that was cut perpendicular to lamination.

$\dot{\varepsilon}$	T	parameter	q	j_1	r^2
3.0×10^{-5}	80	D	4.43	12.7	0.950
		S	4.58	9.15	0.949
		N	4.68	2.35	0.945
		E	4.14	4.70	0.949
3.1×10^{-6}	80d	D	17.2	-0.31	0.941
		S	16.6	-3.32	0.932
		N	16.1	-9.57	0.919
		E	17.4	-8.71	0.939
3.2×10^{-6}	80	D	13.4	1.96	0.917
		S	13.0	-1.06	0.912
		N	12.5	-7.27	0.910
		E	14.0	-7.08	0.906
3.3×10^{-7}	25	D	5.85	11.6	0.936
		S	6.08	7.93	0.936
		N	6.32	1.09	0.936
		E	5.52	3.46	0.916
2.8×10^{-7}	40	D	5.30	11.6	0.873
		S	5.30	8.14	0.851
		N	5.38	1.40	0.824
		E	4.75	3.72	0.853
3.1×10^{-7}	60	D	4.13	12.6	0.869
		S	4.07	9.28	0.855
		N	3.98	2.79	0.836
		E	3.78	4.50	0.867
3.4×10^{-7}	80	D	13.9	4.33	0.993
		S	14.3	0.64	0.993
		N	14.7	-6.34	0.995
		E	13.2	-3.39	0.990
2.8×10^{-8}	80	D	14.4	1.98	0.982
		S	15.1	-2.05	0.985
		N	16.3	-9.72	0.989
		E	14.1	-6.23	0.977
3.1×10^{-8}*	80	D	8.13	8.96	0.958
		S	8.32	5.51	0.966
		N	8.34	-0.79	0.969
		E	8.26	2.33	0.965

Table 6.6. The fitted values to the power law (6.8) Clashach tests. D, S, N and E are the damage parameters. The power law provides the best description of the temporal evolution of damage in the Clashach tests. Damage D in these tests is well modelled by $D = 10^{j_2} \times (1 - t/t_f)^z$.

$\dot{\varepsilon}$	T	parameter	z	j_2	r^2
3.1×10^{-5}	80	D	1.45	13.4	0.986
		S	1.61	9.34	0.969
		N	1.68	2.39	0.954
		E	1.73	5.81	0.968
2.7×10^{-5}	80	D	0.79	13.9	0.978
		S	0.77	10.4	0.985
		N	0.77	3.73	0.984
		E	0.83	7.00	0.983
3.2×10^{-6}	80	D	1.10	11.5	0.984
		S	1.22	7.55	0.996
		N	1.34	7.55	0.996
		E	1.17	2.87	0.984
2.5×10^{-7}	25	D	0.91	13.4	0.982
		S	0.91	9.71	0.983
		N	0.90	2.83	0.983
		E	0.96	5.97	0.987
2.2×10^{-7}	40	D	0.17	17.0	0.922
		S	0.53	10.9	0.849
		N	1.01	1.64	0.671
		E	1.02	3.65	0.669
2.7×10^{-7}	60	D	1.16	10.9	0.945
		S	1.17	7.28	0.954
		N	1.22	0.29	0.965
		E	1.28	3.53	0.967
3.0×10^{-7}	80	D	1.01	12.2	0.966
		S	1.01	8.67	0.969
		N	1.01	1.97	0.966
		E	1.00	3.95	0.974
3.1×10^{-8}	80	D	0.14	14.6	0.926
		S	0.26	10.0	0.889
		N	0.37	2.55	0.849
		E	0.17	5.99	0.885

water. In the linear elastic phase Si concentrations assume a constant value, hence indicating a steady state in the dissolution-precipitation reaction. The inferred dilatant microfracturing phase associated with strain hardening due to crack growth begins at the onset of significant AE activity. An associated increase in Si concentrations is observed during this deformation stage. For the Locharbriggs test, the measured geochemical and microseismic signal are strongly correlated by a power law relationship (6.5). Such a strong correlation suggests that stress corrosion crack growth is the mechanism by which microcracks are growing inside the test specimen. Hence, the environment and strain rate dependence of the Locharbriggs strength can be uniquely attributed to crack growth by the stress corrosion mechanism.

It is important to note, however, that the measured AE activity relates to the total increase in crack porosity, while the recoded geochemical signal is sensitive to the amount of interconnected pore space. Therefore the exponent x in (6.5) that relates the Si signal and microcrack damage need not be unity. This is what I observe. The power law exponent ranges from 0.35-0.40, hence suggesting that reactivity is not directly proportional to the crack surface area. In fact, the existence of two types of pore space was already verified by the initial porosity estimates (table 3.1), yielding 22% and 16% for the total and interconnected porosities in the Locharbriggs sandstone. Therefore some of the AE events may relate to the growth of microfractures from pre-existing flaws outside the interconnected pore space. More importantly, the AE catalogue is likely to underestimate the actual microcrack damage (*Lockner*, 1993a), since all microfracturing events may not be accompanied by a detectable AE and due to the higher than usual amplitude threshold of my tests. In addition, the overlapping of small events can cause them to be recorded as one long duration event, especially close to specimen failure when the event rates are high (section 5.3.3.). The stress matching exercise also demonstrated that damage is likely to be underestimated at a later loading stage (section 5.3.6). If a more realistic estimate of damage was available, one could expect a higher x-value linking microfracturing events to the measured silica signal.

The amount of silica in the exit pore water relates to the reactive surface area and dissolution-precipitation rates (section 2.4.5). Although the crack surface area parameter was estimated from the AE catalogue, it was not possible to determine

independently the evolution of the interconnected surface area during the triaxial compression tests. However, the very low estimate obtained for the geometric surface area (0.38/cm) and the strong temperature dependence Si concentrations (fig. 6.6) suggest that reaction rates could be dominating the measured silica signal. On the other hand, the Si signal at 80°C is not unique. In addition, both S and the Si concentrations evolve in a similar fashion during the strain hardening phase, indicating surface area control. Hence, the measured increase in Si concentrations during the dilatant microcracking phase can be attributed to changes in both surface area and reaction rates. However, the small surface area estimate and the strong quantitative relationship between damage and Si signal suggest that silica is actively dissolving from the tips of the growing cracks. Hence, my observations are in qualitative agreement with *Dove's* (1995) model, in which the crack growth velocity is governed by the quartz dissolution rate constant k_+. However, one could expect the effects of surface area and reaction rates to be intimately linked, since the creation of new surface area is a necessary consequence of crack growth by the bond breaking mechanism (*Dunning et al.*, 1994).

Much of the stress corrosion literature reviewed in chapter 2 is concerned with the propagation of a single, well defined crack in a double torsion type testing apparatus. In my tests, however, deformation proceeds by the propagation of several cracks. The microcrack damage and the Si concentrations are observed to increase in an exponential (6.18) fashion prior to the macroscopic failure of the Locharbriggs samples. This observation implies that both fracture rates and Si dissolution rates are accelerated during sample dilatancy. In fact, an increase in reaction rates during dilatancy is predicted by reaction rate theories of active crack growth (*Charles and Hillig*, 1962; *Wiederhorn and Boltz*, 1970; *Freiman*, 1984; *Atkinson and Meredith*, 1987a; *Lawn*, 1993) as well as due to the passive presence of dissolved constituents (section 2.4.5). In my tests the applied mean stress increases with time, and reaction rate theories predict that such condition is linked to exponentially increasing reaction and fracture rates. Therefore my observations are in good agreement with such theories. There are, however, various other factors that influence silica dissolution and fracture rates, whose relative contributions cannot be separated out by analysing experimental data. For instance, it is not possible to measure the activation entropy or to determine the abundance of reactive sites during a triaxial compression tests. Both of these

parameters are included explicitly in the *Dove's* (1995) model for stress corrosion crack growth by active dissolution (section 2.5). However, it is probable that the number of reactive sites increases during dilatancy due to the creation of new crack surface area.

For both sandstones, the acceleration of damage prior to specimen failure becomes sharper as the strain rate is decreased. This observation suggests that failure prediction becomes more difficult at slower strain rates. The temporal evolution of AE damage in the Clashach tests is best described by a power law (6.8). The period of rapid microcracking and the associated increase in Si concentrations is typically much shorter than in the Locharbriggs tests. Hence, it is not possible to resolve the exact form of the constitutive law from the temporal evolution of Si concentrations in the Clashach tests. However, in one test the Si signal is best modelled by a power law (6.8). The power law form exhibited by the damage and Si signal can be predicted from constitutive equations for subcritical crack growth (2.16). It is therefore likely that subcritical crack growth is the cause of the observed strain rate and environment dependence of strength in the Clashach tests. In fact, Clashach strength also decreases with strain rate according to a power law formula (Chapter 4). Such relationship between rock strength and deformation rate also results from crack growth according to the *Charles* (1958) power law (*Sano et al.*, 1981). Hence, many of my observations suggest that Clashach sandstone exhibits power law rheology in contrast to the exponential scaling observed for the Locharbriggs sandstone.

There are several reasons that could account for the lack of apparent correlation between AE damage and silica concentrations in the Clashach tests. For instance, the strain hardening phase is typically shorter and therefore the associated AE activity and silica increase are confined to narrower time window than in the Locharbriggs tests. It is possible that more frequent sampling of the exit pore fluid would have allowed me to establish a clear, quantitative relationship between the geochemical and AE data in the Clashach tests. The power law rheology and the smaller stress corrosion index (Chapter 4) also suggest that damage accumulation accelerates more rapidly in the Clashach tests. On the other hand, silica could be passively dissolving from the newly created crack surface area. In such case one would not observe corrosion products that are directly associated with the fracturing process. In fact, the lack of distinct temperature dependence of C_{max}

and C_{ss} also suggest that surface area dominates the measured geochemical signal over reaction rates. Furthermore, the ubiquitous presence of many dissolved ions including Al, Fe, Ca, K, Mg and Na could be indicative of a more complex geochemical system in the Clashach tests.

The increase in the Si concentrations during the strain hardening phase of the Clashach tests are consistent with the results of *Ngwenya et al.* (2000). They reported an increase in Si concentrations during tertiary creep of Clashach sandstone. In addition, the Clashach Si concentrations at failure were consistently higher than the Locharbriggs ones in their tests. This is also what I observe. However, the Locharbriggs data show significant differences to the creep tests of *Ngwenya et al.* (2000). They observed no increase in Si concentrations during the tertiary creep of Locharbriggs sandstone. The Locharbriggs tests were also associated with higher initial Si concentration than the Clashach tests. Neither of these findings agree with my observations. This discrepancy may have been caused by differences in the loading configuration or it could be due to different sampling intervals for the exit pore fluid. It is also possible that crack growth is inherently faster under constant strain rate loading when compared to creep loading (*Kranz*, 1979; *Rao and Kusunose*, 1985)

6.7 Conclusions

The results of my experiments demonstrate that brittle deformation in Clashach and Locharbriggs sandstone is associated with a distinct geochemical signal. The Locharbriggs pore fluid contains dissolved Si, Fe, K and Na and the Clashach pore water contains Si, Al, K, Fe, Mg, Na and Ca. Hence, much of the geochemical signal can be attributed to dissolution from quartz and feldspar grains in the test specimen. These are the main minerals that make up the rocks in this study.

The best signal to noise ratio is obtained for the variation of silica in the exit pore water. Due to the temperature dependence (r^2=0.96-0.99) and the small reactive surface area, the Locharbriggs silica signal is likely to be dominated by reaction rates. In contrast, the Clashach Si concentrations show no correlation with temperature and they are therefore likely to be more sensitive to changes in reactive surface area.

The temporal evolution of silica concentrations correlates with the characteristic microfracturing domains of a stress-strain curve. Initial Si reduction is followed by steady state values and a subsequent increase in the strain hardening phase. A strong power law correlation (r^2=0.94-0.96) exists between the Si concentrations and the AE damage in the Locharbriggs tests. The Si concentrations at failure are also strongly correlated to the steady state values (r^2=0.99). These observations suggest that crack growth occurs by the stress corrosion mechanism. Furthermore, my estimate of the reactive surface area is very small. This may be an indication that silica is dissolving actively from the growing crack tips. However, no distinct correlation between crack damage and Si concentrations is observed in the Clashach data. The ubiquitous presence of many dissolved ions, and the constant Si/Al (r^2=0.96-0.99), Si/K (r^2=0.90-0.99) and Si/Ca (r^2=0.97) ratios suggest that brittle fracturing of Clashach sandstone is associated with a more complex geochemical system than that in the Locharbriggs tests.

Furthermore, the evolution of damage and Si concentrations proceeds according to an exponential (r^2=0.82-0.99) or a power law (r^2=0.67-0.99) for Locharbriggs and Clashach sandstone, respectively. Both types of damage accumulation can be predicted from constitutive equations for subcritical crack growth by the stress corrosion mechanism.

In this chapter I have concentrated on the chemical content of the pore fluid, without referring to its ability to pass through the test specimen in the first place. This property of the percolating fluid is termed permeability: it is the subject of the next chapter.

Chapter 7

Strain rate dependence of Permeability

...there is no sensible relation between porosity and permeability.
Scheidegger (1974)

7.1 Introduction

A majority of previous experimental work on the coupling of fluid flow with brittle deformation has been conducted at a single strain rate of the order 10^{-5} to 10^{-6} /s (*Zhu and Wong*, 1997; *Main et al.*, 2000; *Ngwenya et al.*, 2003). Most of these studies have also been carried out at room temperature conditions. Consequently, little is known about the deformation rate and temperature dependence of fluid flow properties.

I have addressed the effect of loading rate and test temperature on the evolution of permeability during a triaxial compression test. It has already been established that the mechanical properties of the test specimens depend strongly on the applied loading rate (Chapter 4) and that such time dependent brittle deformation is likely to be caused by stress corrosion crack growth (Chapter 6). As a consequence, pore microstructure may be altered so extensively that the fluid flow properties also display a distinct time-dependence. Alternatively, compactive

processes or dissolution reactions may be enhanced at a higher test temperature or upon the application of a slower loading rate. These are the issues I will tackle in this chapter. The results presented in this chapter have also been published (*Ojala et al.*, 2004).

7.2 The importance of permeability

Rock permeability is an important scientific and economic interest in its own right. Moreover, fluid flow is strongly coupled with many mechanical, thermal and chemical processes operating in the crust. The porosity microstructure and hence the permeability of fault zones, hydrocarbon reservoirs and hydrothermal systems is continuously modified the movement of fluids in the subsurface. Similarly, both mechanical and seismic responses of the crust are strongly affected by the presence of fluids. In fact, any interest in fractures and fracture networks in oil reservoir economics stems from their ability to provide permeable pathways for the transport of hydrocarbons rather than from the bulk porosity that they possess. A potential hydrocarbon reservoir with a low permeability simply isn't a viable option.

Although a key material property, permeability is also notoriously difficult to estimate. The permeability of crustal rocks varies over ten orders of magnitude, as shown in figure 7.1 from *Brace* (1980). Sandstones exhibit permeabilities that range over four orders of magnitude. In addition, test specimens cut from the same block of rock may display widely varying permeabilities (*Brace*, 1980; *Guéguen and Palcianskas*, 1994; *Popp et al.*, 2001). Hence, it can be difficult to provide even an order of magnitude estimate of rock permeability. Furthermore, a wide range of temperature, pore pressure and differential stress conditions occur in the crust. All of these parameters may affect fluid flow properties significantly by modifying the pore microstructure (*Guéguen and Palcianskas*, 1994). The effect of lithostatic stress is to decrease permeability by closing off pores and cracks. In contrast, increasing pore pressure tends to open up pores and cracks and hence increase permeability. High temperatures and deviatoric stresses may induce microfracturing and increase permeability. Changes in permeability can also be induced by chemical reactions between the moving fluid and the wall

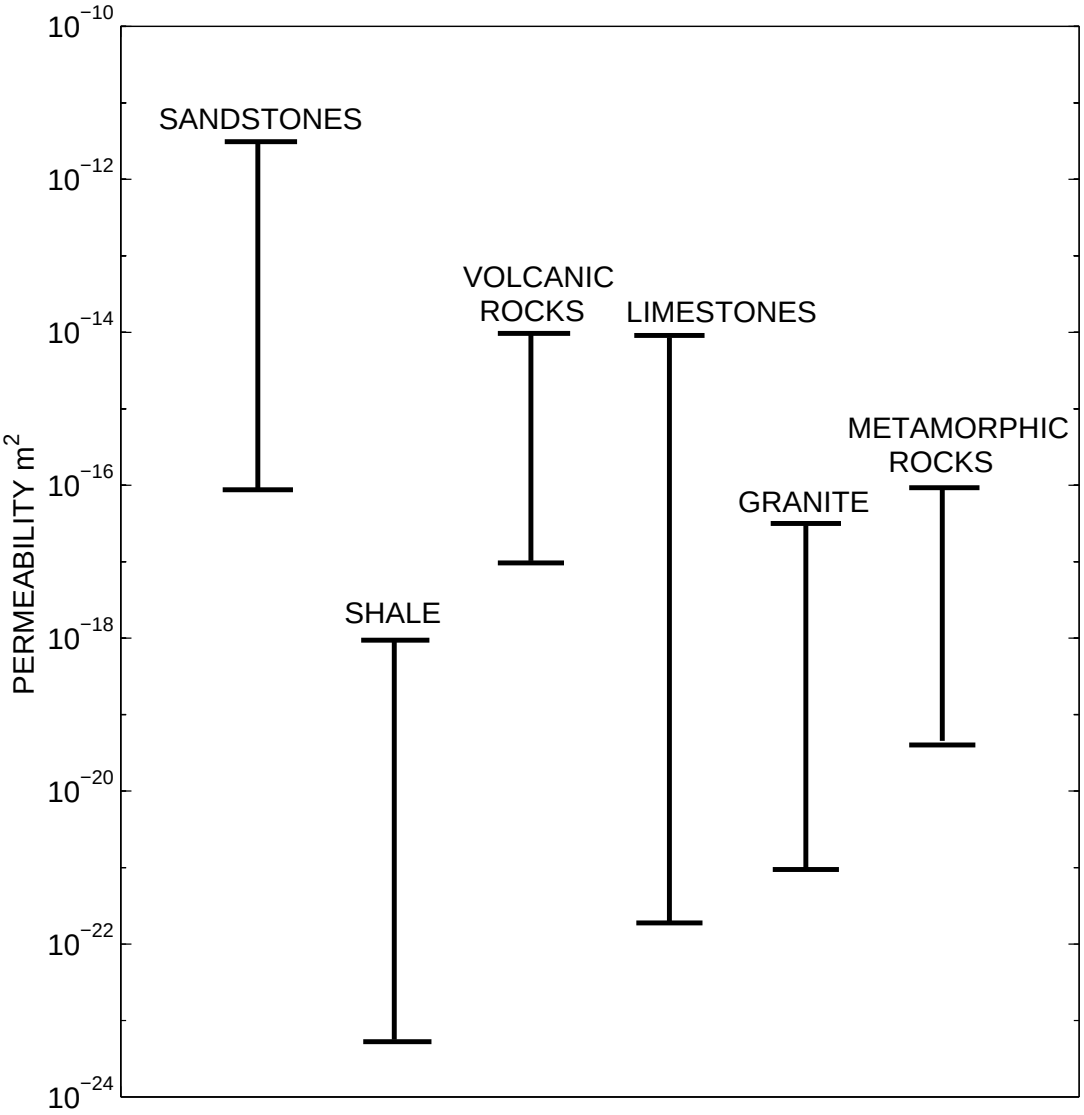

Figure 7.1. The measured permeabilities of various rocks at 25°C under hydrostatic conditions. Redrawn from *Brace* (1980).

rock. In general, dissolution increases permeability while precipitation leads to permeability reduction (*Tenthorey et al.*, 1998).

7.3 Previous Observations

Laboratory studies under controlled conditions provide an excellent opportunity to investigate the coupling of fluid flow properties with brittle deformation. The results of such studies have shown that dilatancy precedes failure by brittle faulting in both low and high porosity rocks (*Brace et al.*, 1966; *Scholz*, 1968a; *Zoback and Byerlee*, 1975). During the dilatant phase of deformation the growth of microcracks in the direction of maximum compressive stress causes the sample porosity to increase (e.g. *Tapponier and Brace*, 1976) In analysing permeability data, the effects of dilatancy and permeability change are expected to be coupled. Such an assumption stems from the idea that porosity and permeability are positively correlated (*Carman*, 1956; *Seeburger and Nur*, 1984; *Bourbie and Zinszner*, 1985; *Guéguen and Dienes*, 1989; *Bernabé*, 1995; *Zhu et al.*, 1999; *Simpson et al.*, 2001). In fact, a positive correlation has been observed for low porosity rocks, with permeabilities increasing by a factor of two to eight during the dilatant phase of deformation (*Zoback and Byerlee*, 1975; *Zhang et al.*, 1994; *Popp et al.*, 2001). However, it is debatable whether such correlation also holds for high porosity ($\phi > 15$ %) rocks.

The existing laboratory data on the interplay of fluid flow properties with brittle deformation in high porosity rocks is controversial. Previous studies have reported both increasing (*Mordecai and Morris*, 1971) and decreasing (*Zhu and Wong*, 1997) permeabilities during the dilatant phase of deformation. Furthermore, in the experiments of *Zhu and Wong* (1997) Darley Dale sandstone exhibited apparently contradictory behaviour: both increasing and decreasing permeabilities were recorded during dilatancy. Such differences in permeability evolution with brittle deformation can be explained using the parameter ξ that is given by

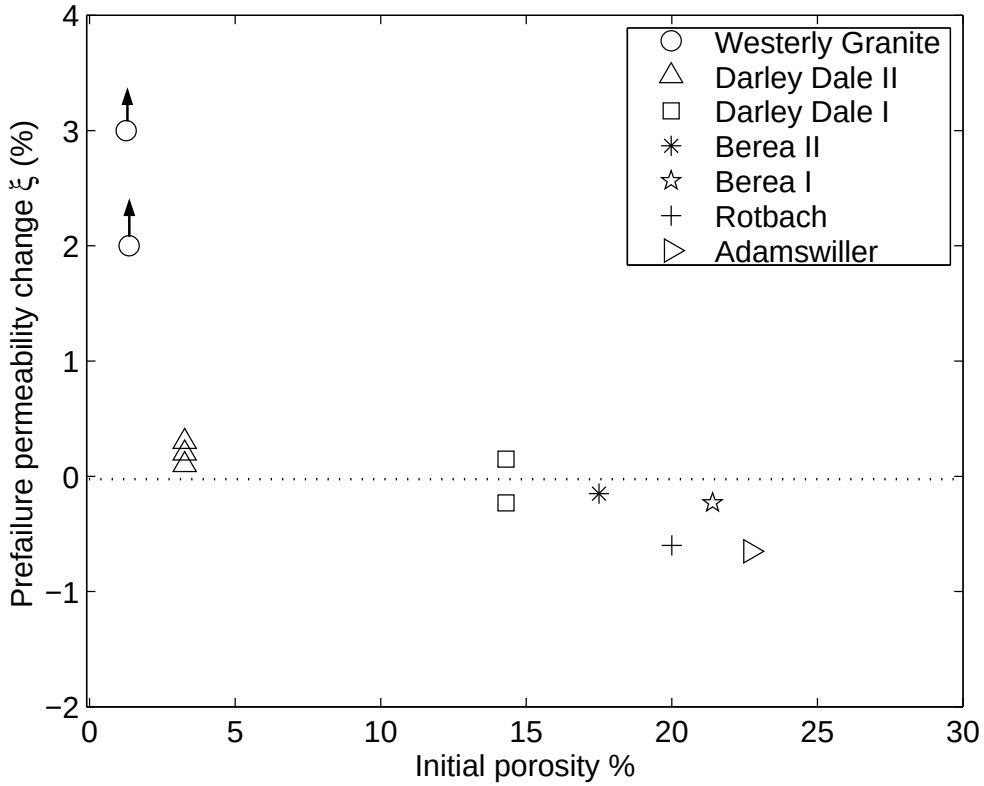

Figure 7.2. Pre-failure permeability change ξ as a function of initial porosity of various rock types that were deformed in a brittle regime. The data for Darley Dale II is from *Mordecai and Morris* (1977), Berea II is from *Gatto* (1984) and the Westerly Granite data are from *Zoback and Byerlee* (1975). All other data are from *Zhu and Wong* (1997). Arrows indicate the lower bounds of values. The multiple values for Darley Dale I and II, Westerly granite, and Berea I and II are from triaxial compression tests at different effective pressures. This figure is redrawn from *Zhu and Wong* (1997). On the basis of this diagram they suggested that the changeover from positive to negative correlation between dilatancy and permeability change occurs at rock porosity of 15 %.

$$\xi = \frac{k_{peak}}{k(C')} - 1 \tag{7.1}$$

where k(C') and k_{peak} are the permeabilities at the onset of dilatancy and peak stress, respectively (*Zhu and Wong*, 1997; *Wong and Zhu*, 1999). Whether porosity and permeability changes are positively or negatively correlated is indicated by the sign of the correlation parameter ξ, which itself is a function of porosity. The transition from positive to negative ξ occurs at ϕ =15%, as illustrated in figure 7.1 from *Zhu and Wong*, (1997). The observed positive and negative correlation between permeability change and dilatant microfracturing in low and high porosity rocks, respectively, can therefore be explained by using ξ. Hence, the different initial porosities of the test specimens provide an explanation for the contradictory behaviour observed for for Darley Dale sandstone (*Zhu and Wong*, 1997).

The negative correlation between permeability and porosity changes in high porosity rocks can be explained by using the equivalent channel model (*Paterson*, 1983; *Walsh and Brace*, 1984) given by

$$k = C\frac{r_h^2\,\phi_p}{\zeta} \tag{7.2}$$

where k is permeability, ϕ_p is porosity, r_h is the hydraulic radius, ζ is tortuosity, C is 1/2 and 1/3 for circular tubes and cracks, respectively. Hence, permeability may decrease in a dilating rock sample if the hydraulic radius is decreasing with progressively increasing tortuosity of the flow path (*Zhu and Wong*, 1996). Other workers are not entirely happy with the concept of tortuosity and its continued use in permeability estimation (*Clennell*, 1997). For instance, I. Gates wrote in a discussion of the work of *Fatt* (1956)

'The use of the network model eliminates the 'bugger factor', sometimes termed tortuosity, which is used to make theoretical calculations on the bundle of tubes to fit experimental data.'

Moreover, if rock porosity is considered to be fractal (*Thompson*, 1991), such an assumption precludes the use of an effective length scale that the concept of geometric tortuosity is based on. However, the problem of decreasing permeabilities with dilatancy and the associated need to introduce tortuous fudge factors is a direct consequence of the assumption that permeability and porosity are positively correlated. In fact, there may be no need to invoke a direct correlation between porosity and permeability (*Scheidegger*, 1974). In such case it is perfectly acceptable for permeability to decrease in a dilating rock sample.

Permeability is essentially a geometric parameter as it is measured in m^2. Hence, it is more likely that a relationship exists between permeability and structure rather than with permeability and porosity (*Scheidegger*, 1974; *Guéguen and Palcianskas*, 1994). Such an approach provides an alternative way to explain the observed permeability decrease during brittle deformation. It is assumed that, in a typical rock deformation experiment, the effect of increasing stress is to decrease permeability by progressive pore closure. Permeability is assumed to decrease exponentially according to

$$k = k_0 \exp\left[-\gamma_1 \left(\sigma_{eff} - \sigma_0\right)\right] \tag{7.3}$$

where σ_{eff} is the effective mean stress, σ_0 is its starting value and γ_1 is a coefficient (*Rice*, 1992). Recently, (*Wong and Zhu*, 1999) presented a compilation of the measured γ_1 values for different geomaterials. The stress sensitivity coefficient γ_1 takes values less than 2.0 MPa^{-1} for high porosity rocks, while fractured rocks and tight sandstones exhibit higher values of γ_1. However, other workers have suggested that permeability should be related to axial strain, rather than stress, since it is a geometric property (*David et al.*, 1994; *Main et al.*, 2000). In their models, axial strain replaces $\sigma_{eff} - \sigma_0$ and strain sensitivity coefficient γ_2 replaces γ_1 in (7.3).

Exponentially decreasing permeabilities have also been observed in the absence of significant porosity loss due to elastic compaction. In such case permeability decrease is attributed to changes in pore structure resulting from chemical reactions between pore fluid and the rock sample. Experimental work have demonstrated

that permeability reduction amounting to several orders of magnitude can occur due to the precipitation of authigenic phases (*Moore et al.*, 1983; *Small et al.*, 1992; *Main et al.*, 1994; *Scholz et al.*, 1995; *Tenthorey et al.*, 1998; *Morrow et al.*, 2001). Such experiments are typically carried out under constant pore pressure and differential stress, and hence any reduction in permeability cannot be attributed to mechanical compaction of cracks and pores. Nevertheless, both power law and exponential decrease of permeability with time have been observed (*Aharonov et al.*, 1998; *Morrow et al.*, 2001). The permeability reduction can be attributed to clogging of the pore throats by the newly precipitated minerals (*Tenthorey et al.*, 1998).

7.4 Results

7.4.1 Relationship between initial permeability and porosity

The initial permeabilities of the test specimens were measured at the start of each test run under hydrostatic conditions. The initial permeabilities and porosities are shown in figure 7.3. It is interesting to note that no clear correlation between sample permeability and porosity was observed. Instead, specimens with the same porosity had widely ranging permeabilities. The interconnected porosities varied from 10-12 % and 15-17% for the Clashach and Locharbriggs sandstones, respectively. However, the initial permeabilities ranged from 1.20 to 12.7 $\times 10^{-13} m^2$ and 0.53 to 17.9 $\times 10^{-13} m^2$ for the Clashach and Locharbriggs sandstones, respectively. Hence, the Locharbriggs sandstone permeabilities varied over two orders of magnitude. Such a large variation in initial permeabilities has also been observed in previous studies (*Popp et al.*, 2001). The large variation in the initial permeabilities of the test specimens is likely to be caused by normal variation in the sandstone formation. Although the Locharbriggs porosities were typically 5 % more than the Clashach ones, the recorded permeabilities were of similar magnitude.

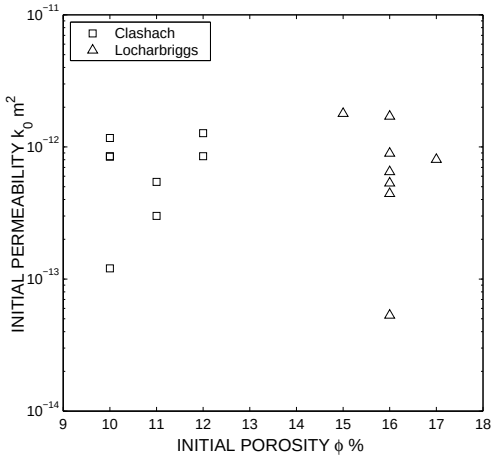

Figure 7.3. The initial permeability as a function of porosity. The axial permeability of the sandstone specimens may vary over two orders of magnitude for a given porosity value, possibly due to normal lithological variation.

Table 7.1. Mechanical and permeability data for the flow-through tests on Clashach and Locharbriggs sandstones. ϕ_i is the interconnected porosity, k_0 is the permeability at the test start and k_{peak} permeability at peak stress.

Rock type	T	$\dot{\varepsilon}$	ϕ_i	σ_{max}	k_0 $\times 10^{-13}$	k_{peak} $\times 10^{-13}$	k_{peak}/k_0
	$^\circ C$	1/s	%	MPa	m^2	m^2	%
Clashach	80	3.1×10^{-5}	10	168.5	11.7	14.3	122
Clashach	80	2.7×10^{-5}	11	162.8	5.44	6.93	127
Clashach	80	3.2×10^{-6}	10	169.3	8.50	7.28	86
Clashach	25	2.5×10^{-7}	10	166.7	8.44	5.47	65
Clashach	40	2.2×10^{-7}	12	140.4	12.7	10.4	82
Clashach	60	2.7×10^{-7}	10	162.8	1.20	0.73	61
Clashach	80	3.3×10^{-7}	12	134.5	8.52	4.16	49
Clashach	80	3.3×10^{-8}	11	122.6	3.01	0.75	25
Locharb.	80	3.0×10^{-5}	16	81.2	4.43	4.28	97
Locharb.	80	3.2×10^{-6}	16	80.8	5.33	6.70	126
Locharb.	25	3.3×10^{-7}	15	81.3	17.9	11.9	67
Locharb.	40	2.8×10^{-7}	16	77.8	6.49	3.13	48
Locharb.	40	3.3×10^{-7}	16	82.3	17.1	8.56	50
Locharb.	60	3.1×10^{-7}	17	81.4	8.04	5.72	66
Locharb.	80	3.4×10^{-7}	16	79.9	0.53	0.22	40
Locharb.	80	2.8×10^{-8}	16	77.7	8.96	2.98	33

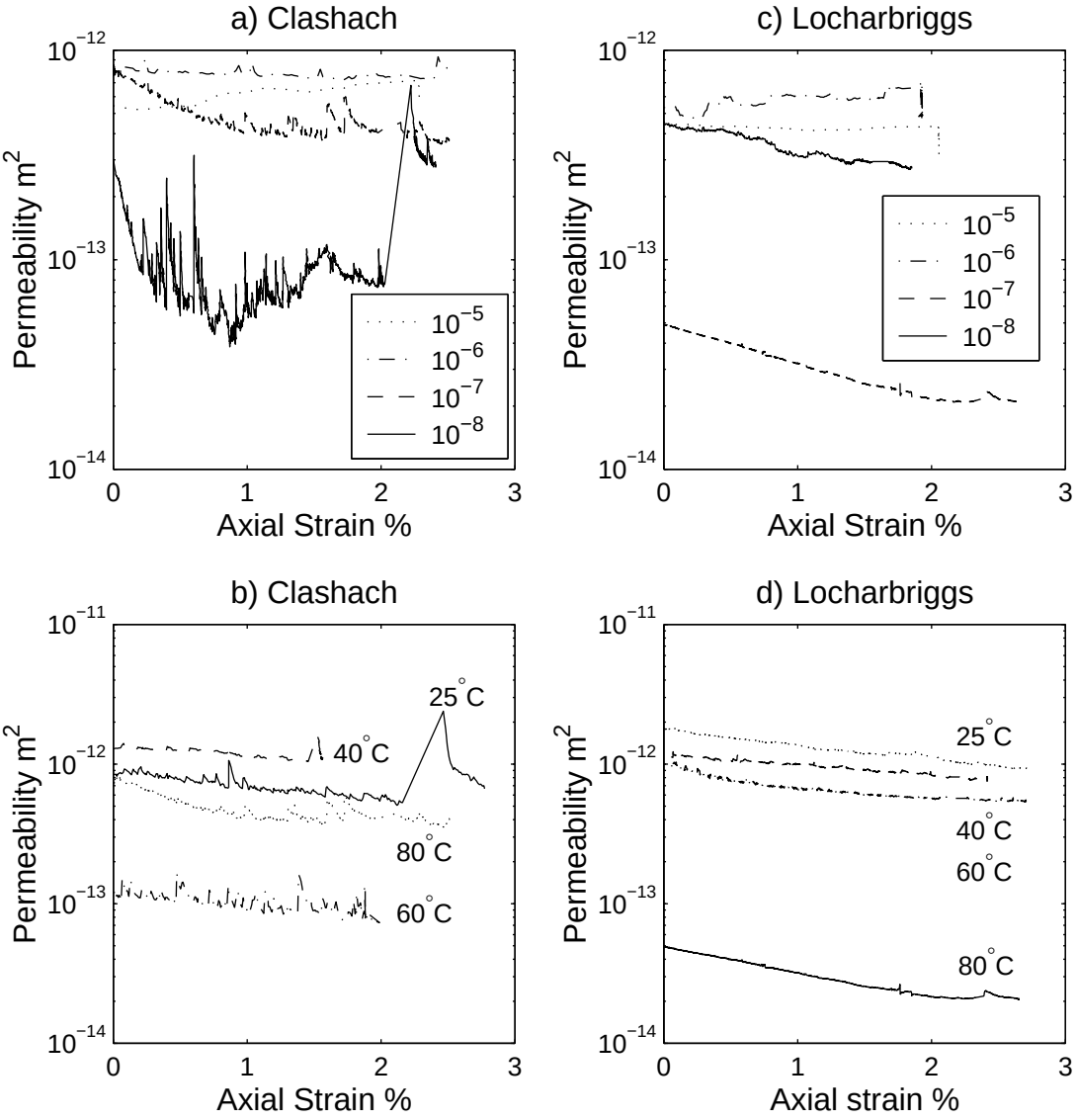

Figure 7.4. The evolution of permeability with axial strain for a) Clashach and c) Locharbriggs sandstone $80°C$ tests conducted at different strain rates and b) Clashach and d) Locharbriggs sandstone deformed at T=25-80°C using a strain rate of 10^{-7} /s.

7.4.2 The effect of loading rate on permeability evolution

The use of strain rates ranging over four orders of magnitude induced significant changes in the evolution of permeability with brittle deformation for both sandstones. The evolution of axial permeability with axial strain is illustrated in figure 7.4. Locharbriggs sandstone showed contrasting trends depending on the strain rate used. At high loading rates on the order of 10^{-5} to 10^{-6} /s the axial permeability increased in the dilatant phase of microcracking that preceded specimens failure. In contrast, slow loading rates of 10^{-7} and 10^{-8} /s resulted in continuously decreasing permeabilities. Following sample failure, permeabilities continued to decrease with increasing axial strain. For the 10^{-5} and 10^{-6} /s tests no appreciable strain occurred after specimen failure, but permeability kept decreasing.

For the Clashach sandstone, the effect of loading rate was to induce relative changes in permeabilities. Initial permeability decrease was followed by increasing permeabilities prior to specimen failure. The permeability reduction can be attributed to inferred compaction of favourably oriented cracks, while the subsequent enhancement in axial permeability is caused by microfracturing events, as evidenced by the AE activity. *Zhu and Wong* (1997) used parameter ξ to analyse the permeability evolution for their tests. However, since volumetric strain was not measured for my tests, the onset of dilatancy and hence ξ could not be determined. Instead, k_{min} was defined as the lowest recorded permeability value of the intact specimen for each test. Since all the Clashach tests were characterised by an initial permeability reduction, the ratio k_{min}/k_0, where k_0 is the initial permeability, could be used to compare the relative amount of permeability reduction for different tests. Figure 7.5.b illustrates the observed strain rate dependence of k_{min}/k_0 that is given by

$$k_{min}/k_0 = 28.2 \log \dot{\varepsilon} + 228 \tag{7.4}$$

where $\dot{\varepsilon}$ is the strain rate in 1/s and k_{min}/k_0 is given in per cent. Hence, the amount of initial permeability reduction as evidenced by the AE activity was proportional to the logarithm of strain rate with a high r-squared value of 0.962.

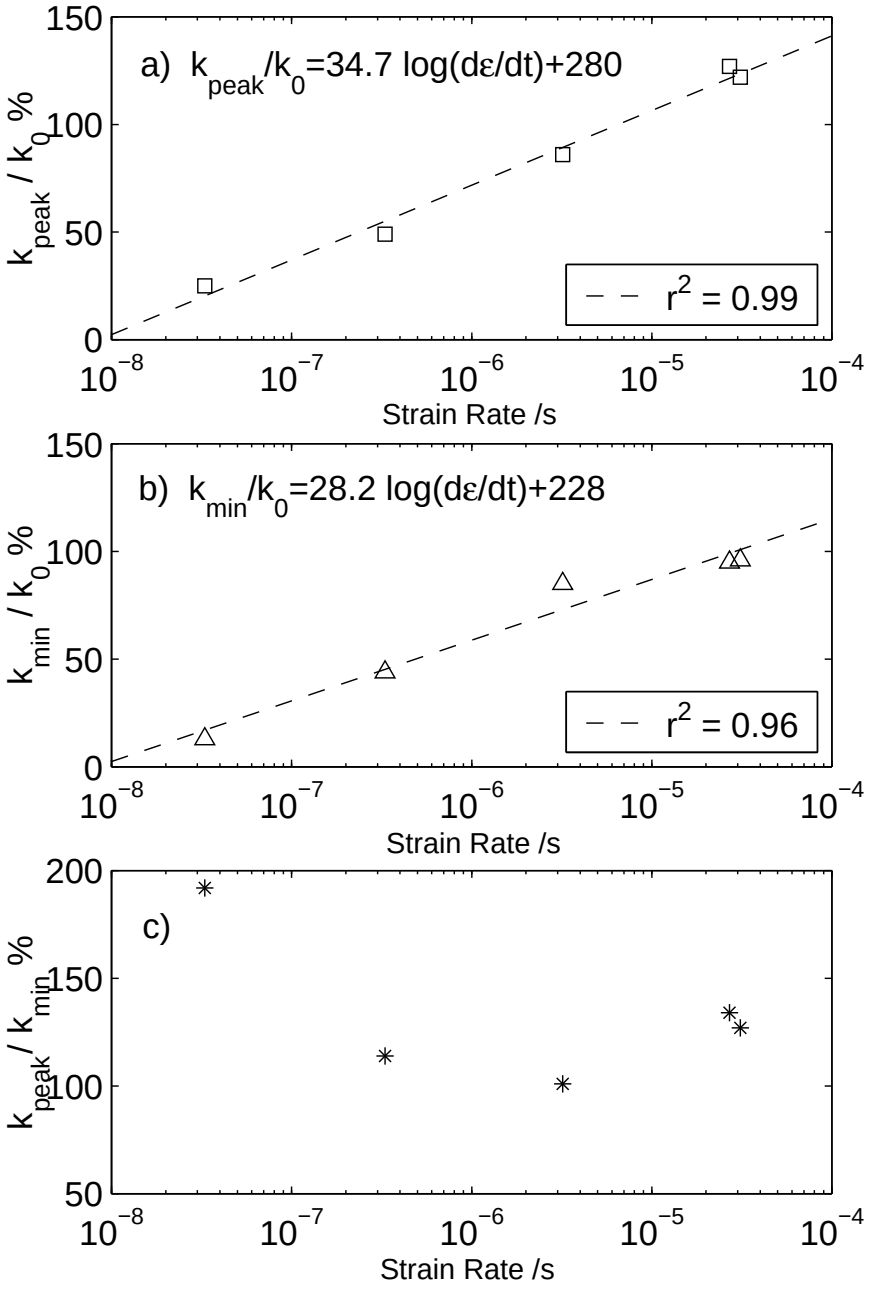

Figure 7.5. In the 80 °C Clashach tests the evolution of permeability depends on the applied strain rate. a) The ratio of permeability at peak stress k_{max} to initial permeability k_0 at the start of the test. b) The ratio of permeability minimum k_{min} to initial permeability k_0 at the start of the test. c) The ratio of k_{max} to k_0 did not display a systematic strain rate dependence

.

In slow deformation tests there is more time available for mechanical and chemical processes to occur, which may have caused a more efficient compaction and the observed greater reduction in permeability. Similar loading rate dependence was also observed for k_{peak}/k_0, where k_{peak} is the permeability at peak stress (figure 7.5.a). The ratio k_{peak}/k_0 was also a function of the logarithm of strain rate

$$k_{peak}/k_0 = 34.7 \log \dot{\varepsilon} + 280 \tag{7.5}$$

where the r-squared value was 0.987. At a high strain rate of 10^{-5} /s the peak stress permeability was 22-27 % higher than the initial permeability. In contrast, for the low strain rate test at 10^{-8} /s k_{peak} was only 25% of k_0. A similar distinct strain rate dependence of k_{peak}/k_0 was also observed for Locharbriggs sandstone, as shown in table 7.1, where the initial and peak permeabilities are tabulated for both rock types. Since the slopes of (7.4) and (7.5) are of similar magnitude, the observed loading rate effect may have been caused by the same underlying mechanism. It is possible that the k_{peak} values were masked by the initial permeability reduction due to inferred compaction. Moreover, the ratio k_{peak}/k_{min}, indicating inferred dilatancy, ranged from 101 to 192 % and did not display a strain rate dependence (fig 7.5c).

The transient increase in permeability at dynamic failure was more frequent for the Clashach tests than for the Locharbriggs tests. Only the 10^{-7} /s Locharbriggs test showed a transient increase in k at the time intervals used here. In contrast, all of the Clashach tests were characterised by a transient k increase associated with the formation of a through-going fault. Such transient permeability increase is predicted by the dilatant suction pump model of *Sibson*, (1994). This qualitative model was recently solved using the method of *Rudnicki and Chen* (1988) by *Grueschow et al.*, (2003) for aeolian sandstones similar to those used here. We therefore assume that the dynamic peak in permeability is only apparent. The apparent k increase at failure ranged from 0.2 to 18.6 $\times 10^{-13} m^2$. The relative change in permeability may, however, be a more appropriate measure of permeability since the absolute value of k was different for each test. The amount of permeability increase varied from 108 % for the 10^{-7} test to 887 % for the 10^{-8} /s test. However, there appeared to be no systematic variation between

Table 7.2. The fault angle, coefficient of internal friction μ_s (4.2), fault slip δ, shear stress drop $\Delta\tau$ and transient permeability increase Δk at failure for the Clashach tests. The slip δ was calculated from the axial strain drop $\Delta\varepsilon$ (mm) assuming that $2 \times \delta = \Delta\varepsilon / \cos\theta$ (*Rudnicki and Chen*, 1988).

$\dot{\varepsilon}$	Temp.	Fault angle θ	μ_s	δ	$\Delta\tau$	Δk_f
1/s	$^\circ C$	degrees		mm	MPa	%
3.2×10^{-6}	80	33	0.45	0.02	83.5	128
2.5×10^{-7}	25	26	0.78	0.17	90.8	452
2.2×10^{-7}	40	30	0.58	0.04	65.6	153
2.7×10^{-7}	60	25	0.84	0.11	86.7	140
3.3×10^{-7}	80	39	0.21	0.04	31.7	108
3.3×10^{-8}	80	26	0.78	0.11	54.4	887

the magnitude of the k increase with the amount of slip δ, the change in shear stress $\Delta\tau$ or the coefficient of internal friction μ_s (table 7.2). If we assume that the apparent permeability increase is due to the suction pump effect (*Grueschow et al.*, 2003) one would expect a correlation between δ and $\Delta\tau$. However, some of the Clashach data suffered from transient noise peaks due to electrical spikes or disturbances in the fluid flow through the sample. Both of these effects could contribute towards the apparent increase in permeability that I observe. More detailed modelling would be required to examine this question further.

7.4.3 Relationship between permeability, stress, strain and temperature

The slow strain rate tests at 10^{-7} and 10^{-8} /s on Locharbriggs sandstone were characterised by a strong dependence of permeability on stress and strain. Similar behaviour was also observed for the 25-60° tests at 10^{-7} /s that were conducted on Clashach sandstone. Hence, the lower temperature Clashach tests showed different behaviour to the 80° tests that are discussed in section 7.4.5. No such temperature dependent permeability evolution was observed for the Locharbriggs tests. Instead, the 25-80° /s tests conducted at 10^{-7} /s were all characterised by a similar permeability evolution, as shown in figure 7.6. The axial permeabilities decreased monotonically as a function of mean effective stress (fig. 7.6a) or strain

Table 7.3. For the slow strain rate tests, permeability k can be expressed in terms on increasing stress and strain according to equation 7.3. Least squares regression on plots of log k versus mean effective stress or axial strain yielded the stress sensitivity coefficient γ_1 and the strain sensitivity coefficient γ_2, respectively. The goodness of fit is indicated by the r-squared value. The values of the stress and strain sensitivity coefficients are of the same order as previously reported by *Main et al.*, (2000) and *Wong and Zhu*, (1999).

Rock	ε	T	γ_1	r^2	γ_2	r^2
	$1/s$	$^\circ C$	$10^{-2}MPa^{-1}$		m^2	
Clashach	3.2×10^{-7}	25	0.81	0.862	22.3	0.860
Clashach	3.3×10^{-7}	40	0.45	0.890	16.3	0.892
Clashach	3.3×10^{-7}	60	0.68	0.544	19.3	0.545
Locharbriggs	3.3×10^{-7}	25	1.56	0.988	25.4	0.984
Locharbriggs	2.8×10^{-7}	40	2.02	0.918	34.1	0.937
Locharbriggs	3.3×10^{-7}	40	0.99	0.953	16.1	0.967
Locharbriggs	3.1×10^{-7}	60	1.64	0.933	25.1	0.920
Locharbriggs	3.4×10^{-7}	80	2.77	0.995	42.0	0.997
Locharbriggs	2.8×10^{-8}	80	2.93	0.985	41.9	0.986

(fig. 7.6b). However, there was a tendency for the initial permeability to decrease with increasing test temperature for the Locharbriggs tests.

The continuously decreasing permeabilities were best described assuming an exponential dependence on mean effective stress or strain (*Rice*, 1992; *Main et al.*, 2000). The stress and strain sensitivity parameters, γ_1 and γ_2 were obtained by least-squares regression on log-linear plots of permeability versus stress or strain for the intact rock specimen (table 7.3). The r-squared values were similar for both parameters, thus suggesting that the exponential fit to both stress or strain data is equally good. The values of the stress sensitivity parameter γ_1 were consistently smaller for the Clashach (0.5-0.8) than for the Locharbriggs sandstone (1.0-2.8). Similarly, the strain sensitivity of permeability evolution as expressed by γ_2 was also smaller for the Clashach tests. While the permeability evolution of the slow strain rate tests on Locharbriggs sandstone was clearly controlled by stress and strain, the lower temperature Clashach tests showed only a moderate dependence of permeability on the applied load.

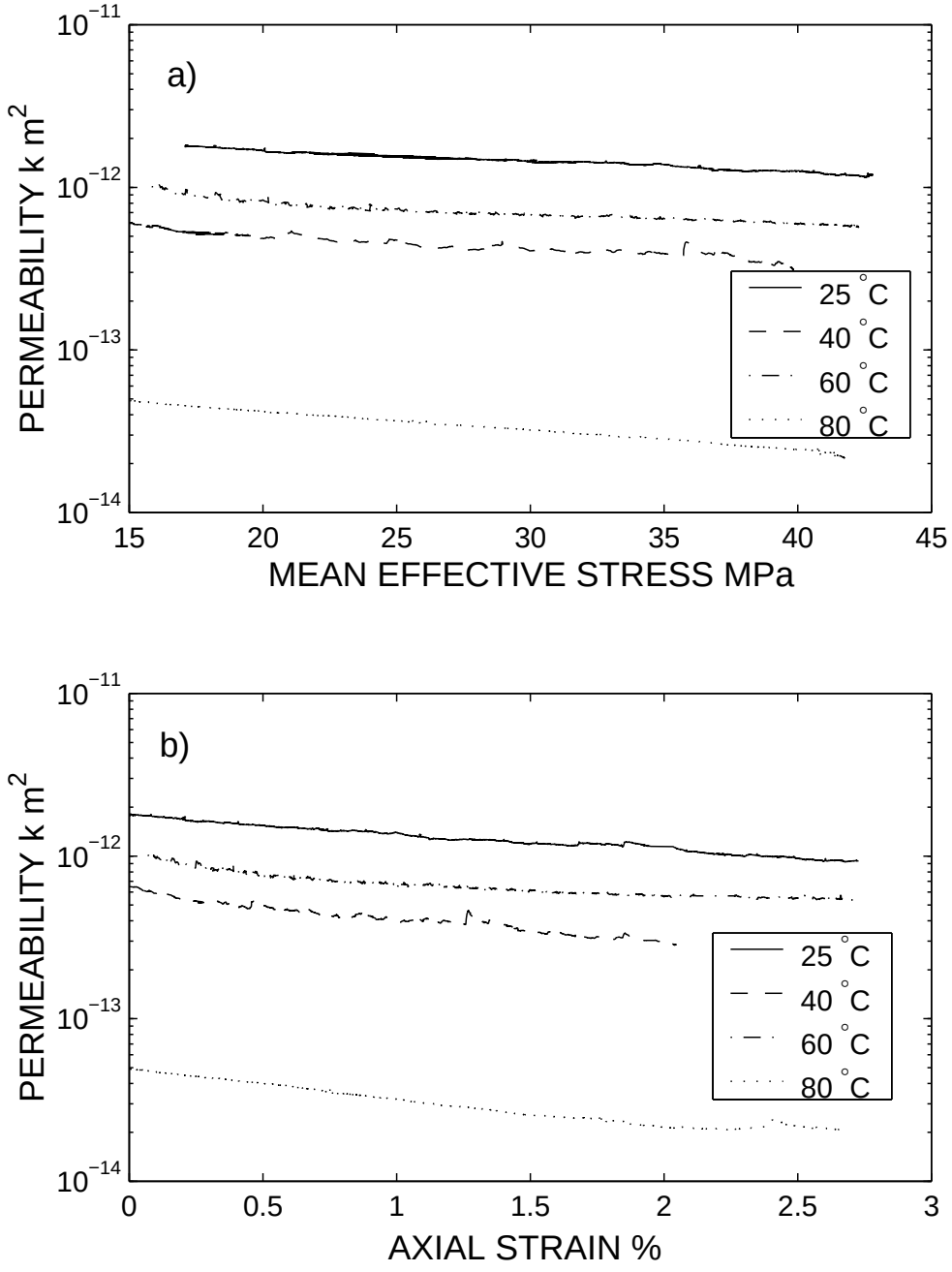

Figure 7.6. The axial permeability as a function of a) mean effective stress and b) axial strain for the Locharbriggs tests that were carried out at 3×10^{-7} /s. Permeabilities decrease as an exponential function of stress or strain.

7.4.4 Relationship between permeability and AE data

The high strain rate tests at 10^{-5} and 10^{-6} /s were characterised by a positive correlation between permeability and AE activity for both sandstones studied, as shown in figure 7.7. The initial permeability decrease due to compactive processes was more pronounced for the Locharbriggs sandstone. Following the onset of AE activity, the axial permeabilities started to increase. Permeability maximum was attained just after the formation of a though-going fault. The post-failure stage was marked by continuously decreasing permeabilities and negligible AE activity. Hence, permeability and AE activity no longer correlated in the frictional sliding phase.

The occurrence of AE can be related to microfracturing events (Lockner, 1993a), which may have caused the observed permeability increase by enhancing pore connectivity (*Tapponier and Brace*, 1976). Hence, the damage parameter N (section 5.3.5) was compared against the permeability data. For the 10^{-5} /s Clashach and Locharbriggs tests the N was directly correlated with permeability, as shown in figures 7.8(a) and 7.8(b), respectively. For the Clashach test the permeability increase Δk obeyed a power law with respect to N that is given by

$$\Delta k \propto N^{0.34} \tag{7.6}$$

with an r-squared value of 0.86. Δk is obtained by subtracting the permeability value at the onset of permeability increase from subsequent permeability values. Locharbriggs sandstone showed a relatively smaller increase in permeability and AE activity. Initially, permeability and AE activity were negatively correlated. Cumulative event count of 300 events defined a critical stage of damage, after which permeability and N were positively correlated. Such critical damage is probably related to the onset of dilatancy in the material. The Locharbriggs sandstone permeability k and AE events N were related by a log-linear relationship given by

$$k \propto 1.67 \times 10^{-14} \log N \tag{7.7}$$

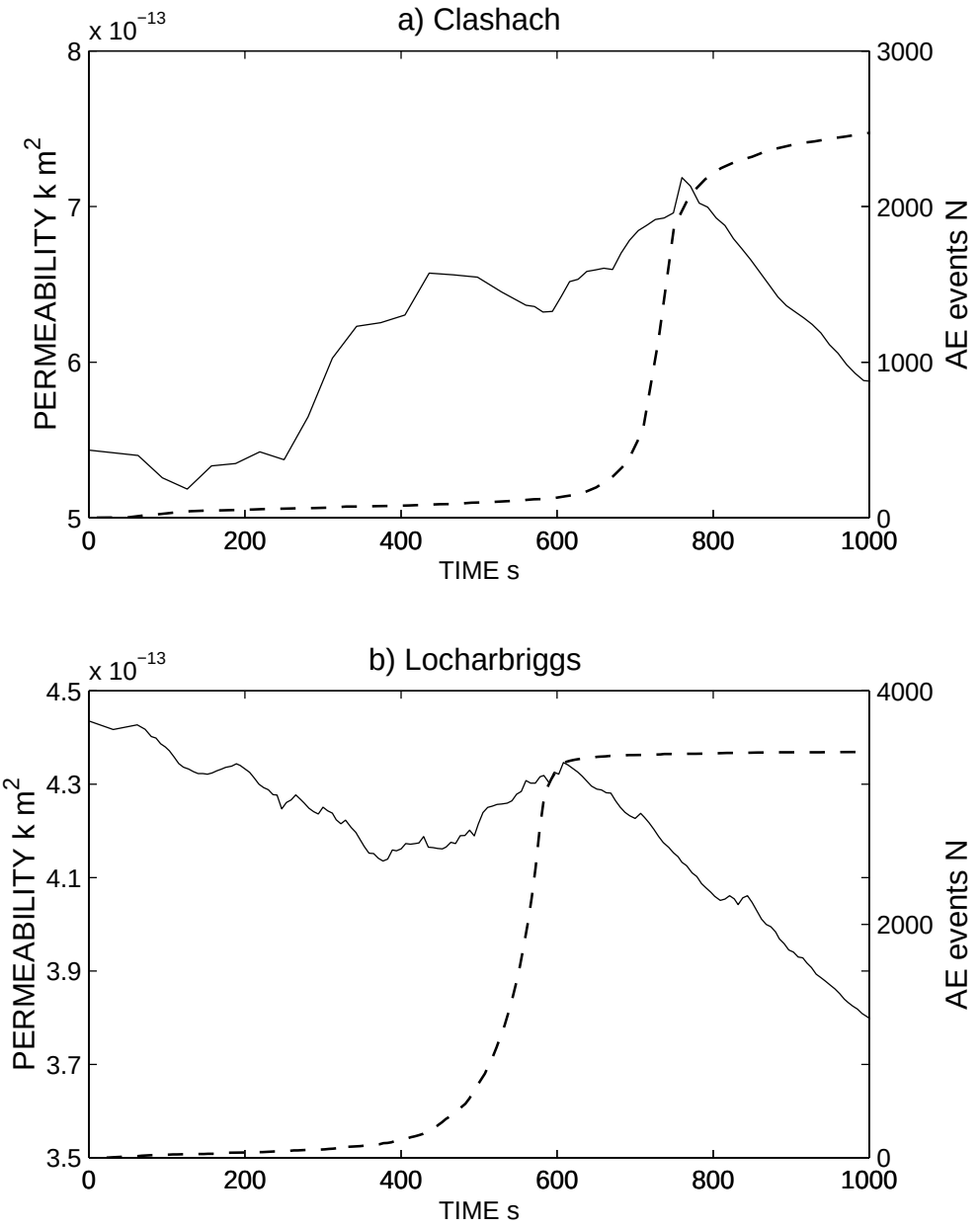

Figure 7.7. The evolution of permeability and stress as a function of time during two tests conducted at strain rates of a) 2.7×10^{-5} and b) 3.0×10^{-5} /s for Clashach and Locharbriggs sandstones, respectively. At high strain rates permeability increases during the dilatant phase of microcrack growth as evidenced by the AE activity. The dashed line is the cumulative AE count.

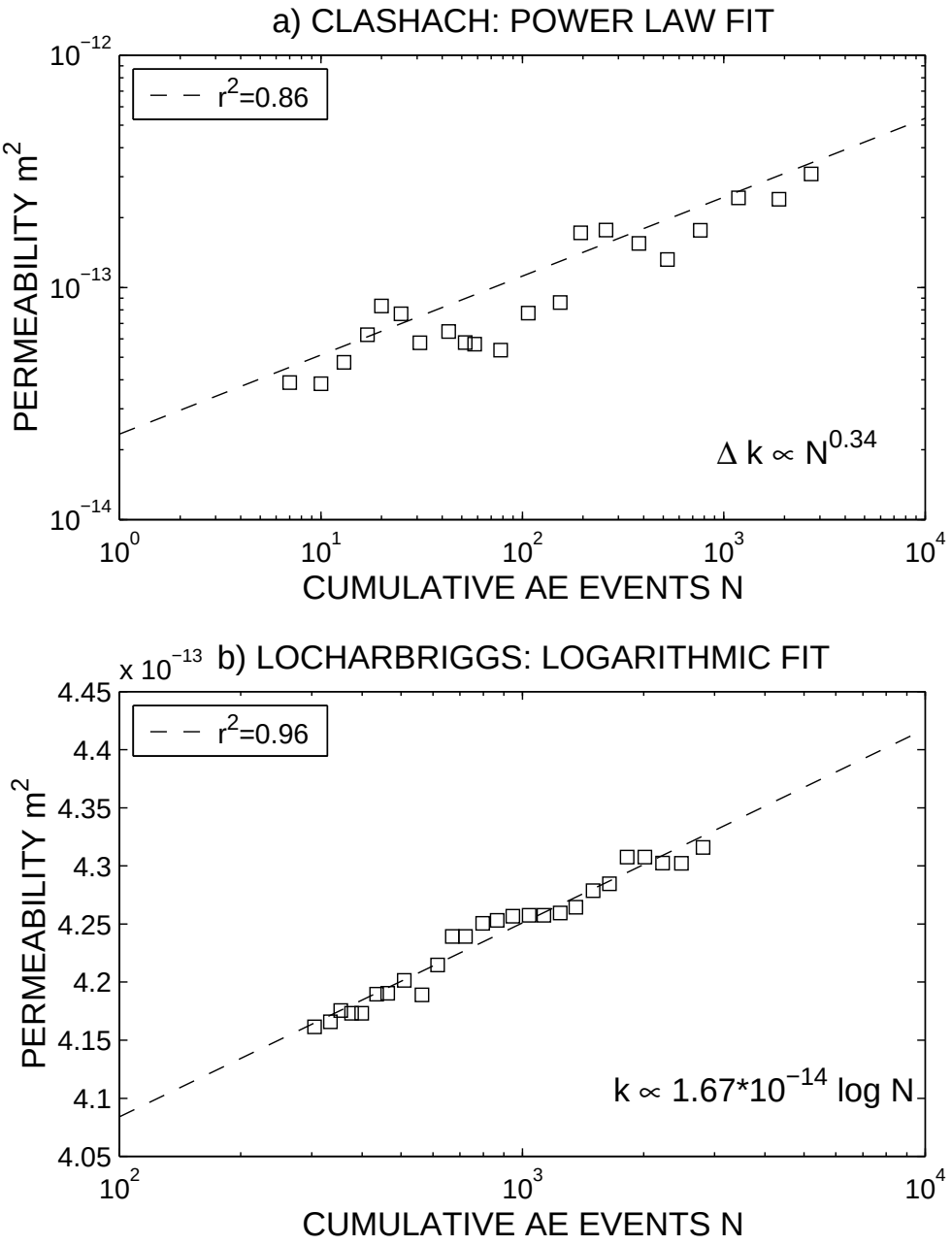

Figure 7.8. Permeability as a function of the cumulative AE event number N. a) The Clashach sandstone test at 2.7×10^{-5} /s is characterised by a power law relationship between Δk and N. b) For the Locharbriggs test at 3.0×10^{-5} /s test a logarithmic law gives a better description of the recorded data.

where the r-squared value was 0.96. It is possible that the data would also fit (7.6) but a wider bandwidth of N and k would be required to establish this formally. Assuming a direct proportionality between N and the change in volumetric strain (*Scholz*, 1968a; *Sano et al.*, 1981), equation 7.6 implies a power-law type dependence of permeability on porosity during the dilatant microcracking phase of deformation (*Carman*, 1956).

7.4.5 Relationship between permeability and chemical reaction

The permeability evolution in the 80° tests at 10^{-7} and 10^{-8} /s on Clashach sandstone did not correlate with AE activity or applied load, as illustrated in figure 7.9. Instead, the evolution of the fluid flow properties was related to the chemical state of the system. Initially, compactive processes caused a dramatic 75 % reduction in permeability while silica concentration decreased from 20 to 4 ppm. For the 5-day duration of the linear elastic phase silica concentration remained approximately constant, while permeability values showed a slight increase. After the peak stress has been attained, Si concentration peaked while permeability remained at the pre failure level. The formation of a through-going fault resulted in a transient increase in permeability due to the suction pump effect of *Rudnicki and Chen* (1988). During the frictional sliding phase both silica concentration and permeability decreased rapidly. The sample permeability was directly correlated with silica concentration up to the peak stress of the specimen as well as in the post-failure stage, as shown in figure 7.10. The absence of a clear correlation between permeability and dissolved ions at the strain softening region could be related to the onset of shear localisation, that may affect these properties differently.

The relation between permeability k and ion concentration C_i was best described by a linear law of the form

$$k = \beta_3 C_i + \beta_4 \tag{7.8}$$

where β_3 and β_4 are constants, k is in m^2 and C_i is in ppm. A linear dependence

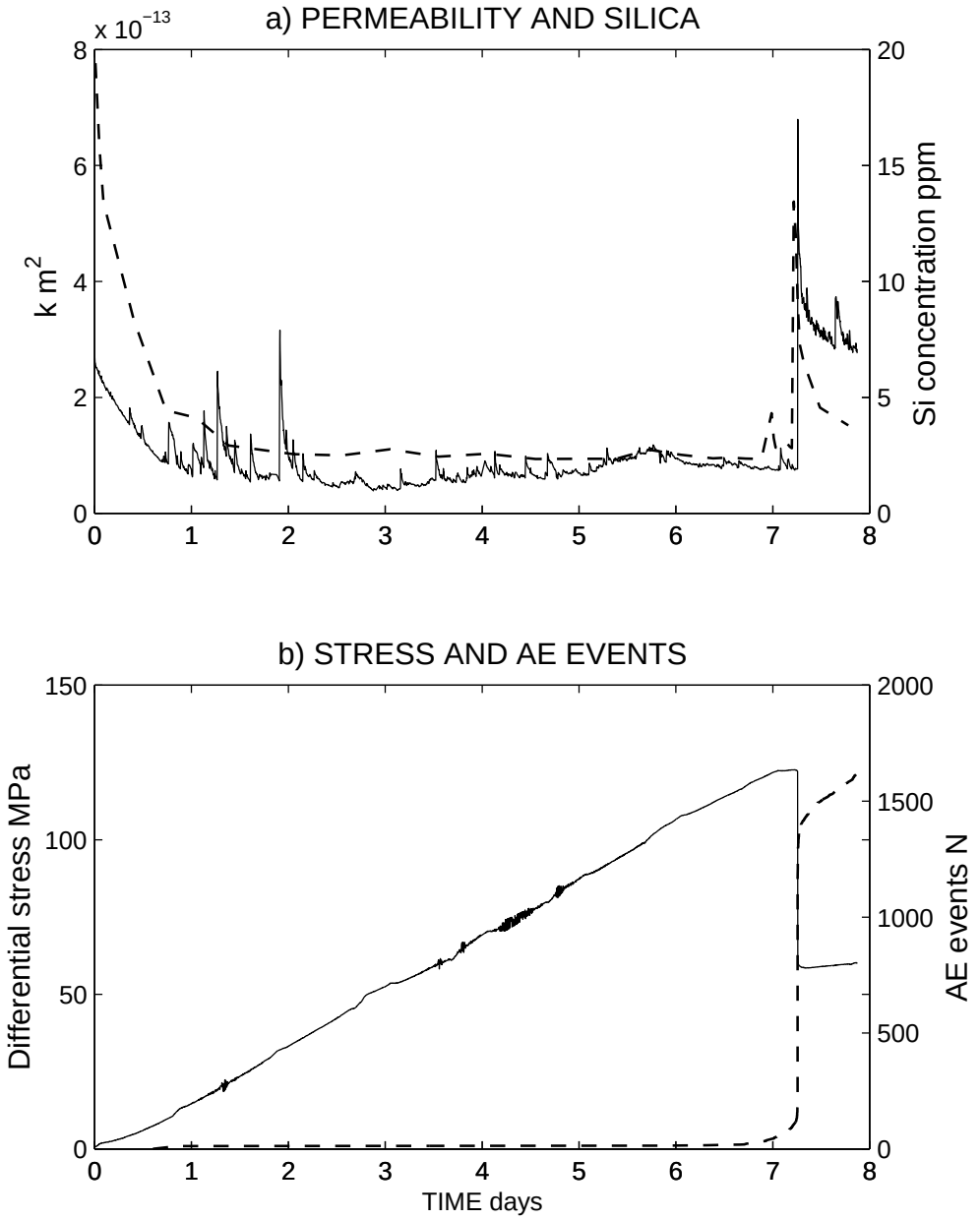

Figure 7.9. The evolution of a) permeability and silica concentration (dashed line) and b) differential stress and cumulative AE event count (dashed line) for a Clashach sandstone 80 °C test that was carried out at strain rate of 3.3×10^{-8}.

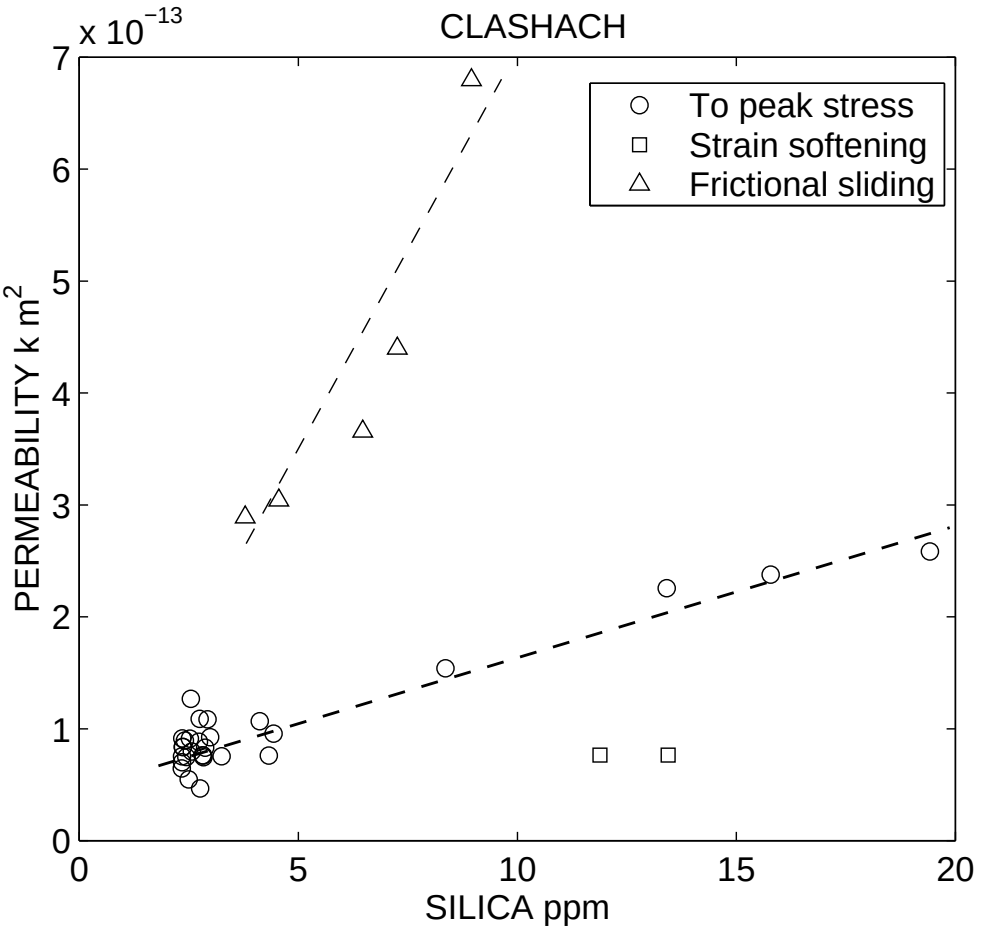

Figure 7.10. The evolution of permeability and silica concentration for a Clashach sandstone test conducted at a strain rate of 3.3×10^{-8} /s. The fluid permeability is a linear function of the concentration of dissolved silica in the exit pore fluid up to the peak stress. At the strain softening phase the silica concentration attains a maximum, but the sample permeability remains at a pre-failure level. After sample failure, the permeability and silica signal are again correlated by a linear law.

Table 7.4. Permeability of the intact rock specimen scales linearly with respect to the exit ion concentrations for the Clashach sandstone 80°C tests that were carried out at loading rate of 10^{-7} and 10^{-8} /s. The axial permeability is given by equation (7.8) in terms of exit ion concentration. The fitted values of β_3 were obtained using least-squared regression. The r-squared value indicates the goodness of fit of the model.

Test	Element	$\beta_3 \times 10^{-14}$	r^2
3.3×10^{-7}	Si	3.40	0.874
	Al	7.40	0.863
	K	10.9	0.539
	Fe	23.7	0.840
	Mg	39.3	0.868
3.3×10^{-8}	Si	1.14	0.895
	Al	2.92	0.887
	K	5.14	0.833
	Fe	6.87	0.803
	Mg	8.96	0.535

Table 7.5. The concentration of dissolved ions as a function of axial permeability for Locharbriggs sandstone during the initial compaction phase. Permeability can be expressed as $k = \beta_1 C_i + \beta_2$ where k is permeability in m^2 and C_i is ion concentration in ppm. For two tests, the concentrations of magnesium and iron also scale with permeability.

T	$\dot{\varepsilon}$	Ion	$\beta_3 \times 10^{-13}$	$\beta_4 \times 10^{-13}$	r^2
25	3.3×10^{-7}	Si	3.09	0.16	0.778
40	2.8×10^{-7}	Si	14.2	-7.58	0.843
		Mg	56.9	3.51	0.752
60	3.1×10^{-7}	Si	17.8	-2.38	0.738
80	3.4×10^{-7}	Si	0.27	-1.10	0.923
		Fe	1.58	-0.16	0.540
		Mg	8.10	0.25	0.646
80	2.8×10^{-8}	Si	2.03	-1.90	0.956

of permeability on ion concentrations was observed up to the peak stress σ_{max} and to 95 % of σ_{max} for the 10^{-8} and 10^{-7} /s tests, as shown in figure 7.11. For these tests, permeability correlated with the concentrations of Si, Al, K, Fe and Mg in the exit pore water. Least squares regression was used to obtain the β_3-values that are listed in table 7.4. The corresponding correlation coefficients ranged from 0.54 to 0.90. Although the numerical value of β_3 for each ion was different for the two tests, the relative change was similar, with Si, Al, K, Fe and Mg displaying increasing values of β_3 (in that order). Throughout the tests, Si displayed the highest concentrations while the Mg concentrations were the lowest, thus explaining the observed variation in β_3. The presence of Si, Al, K, Fe and Mg in the pore water can be attributed to dissolution from quartz, feldspar, illite and diagenetic iron in the test specimen. The positive correlation between axial permeability and ion concentration suggests that the processes of fluid flow and chemical reaction are interrelated.

In contrast, the Locharbriggs sandstone axial permeability and ion concentration were correlated only at the initial phase of inferred compaction, as illustrated in figure 7.12. The closure of favourably oriented microcracks may have resulted in smaller available surface area for dissolution, hence the decreasing concentrations. Both silica (fig. 7.13) and magnesium concentrations were found to obey a linear law (7.8) with respect to permeability during the mechanical compaction phase. The fitted coefficients and the associated correlation coefficients for the Locharbriggs tests are shown in table 7.5. The variation in Si, Mg and Fe concentrations in the exit pore water can be attributed to dissolution from quartz, illite and hematite.

7.5 Discussion

The results of my experiments demonstrate that lithology, temperature and deformation rate exert a strong influence on the way in which fluid flow properties evolve during a typical rock deformation test. Of particular importance is the notable dependence of permeability on the applied strain rate, since the majority of previous experiments have been carried out using a single deformation rate of the order of 10^{-5} to 10^{-6} /s. Yet, it is well known that the mechanical properties of rocks depend on the deformation rate (Chapter 4) and much of

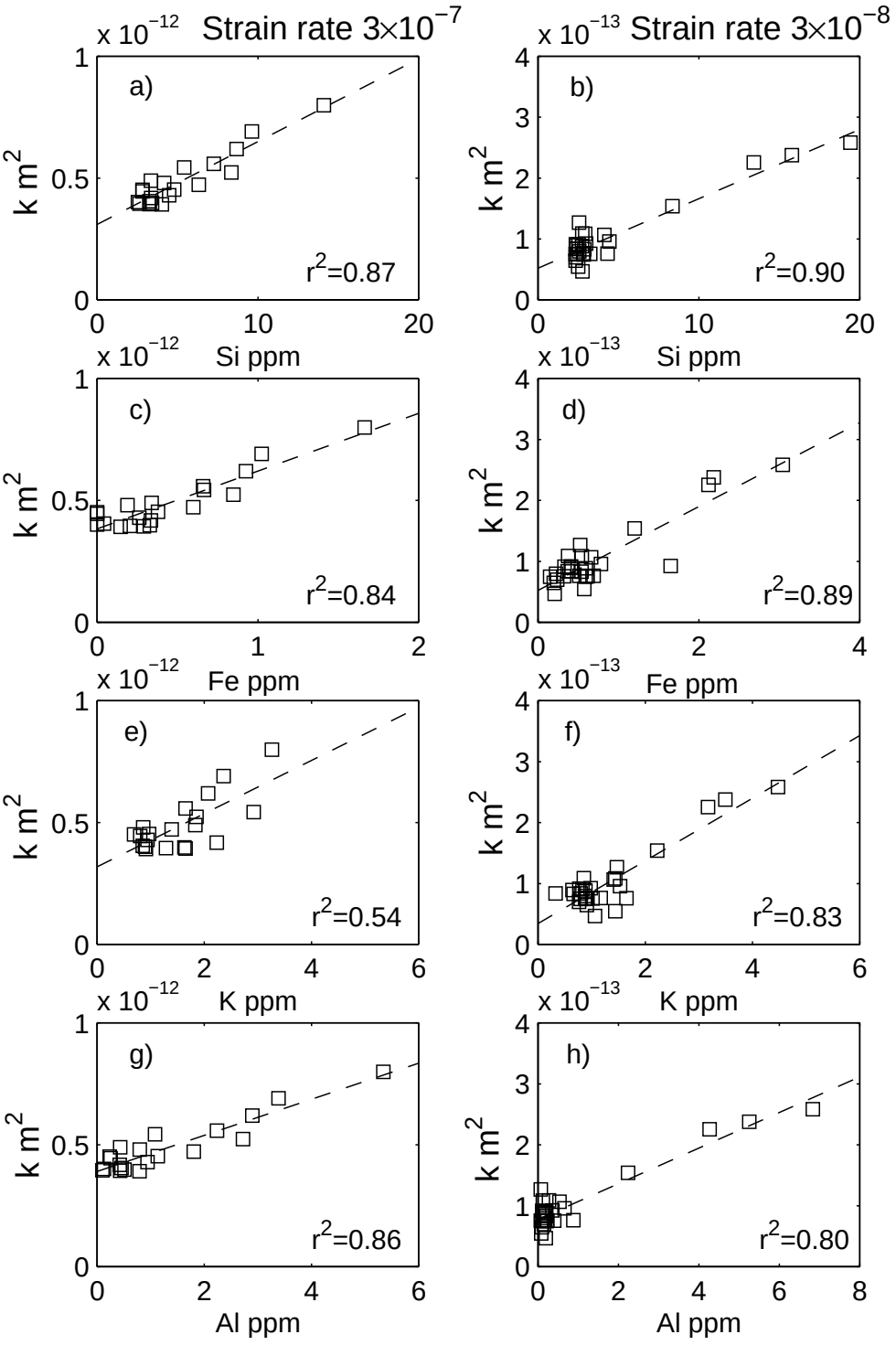

Figure 7.11. The concentration of dissolved ions as a function of permeability for Clashach sandstone. Axial permeability is a linear function of ion concentration.

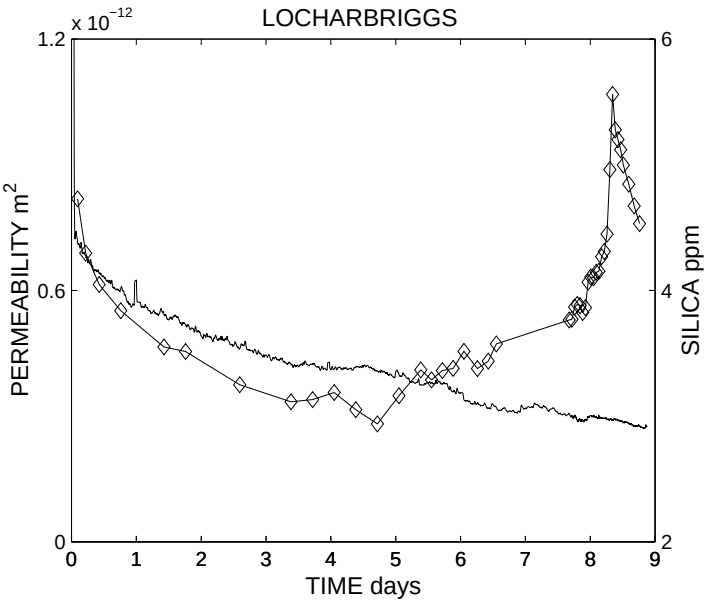

Figure 7.12. The evolution of silica dissolution and permeability for a 80°C Locharbriggs test at a strain rate of 2.8×10^{-8}/s.

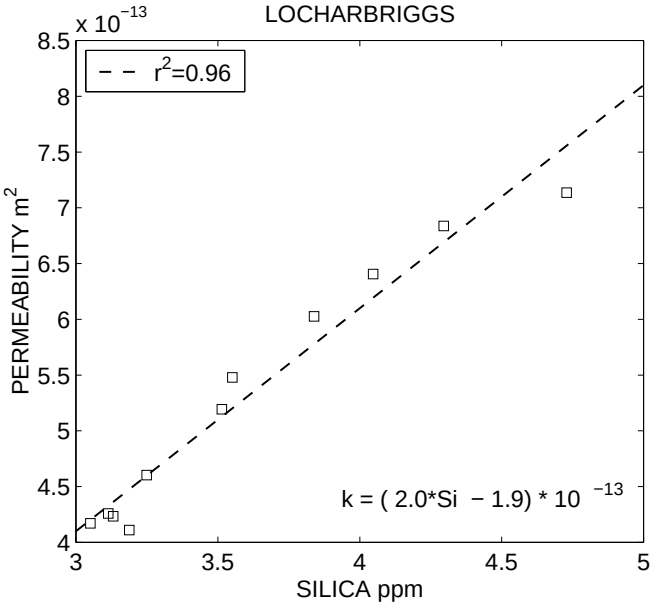

Figure 7.13. The concentration of silica as a function permeability for a 80°C Locharbriggs test at a strain rate of 3.4×10^{-7}/s.

this time-dependence can be attributed to subcritical crack growth by the stress corrosion mechanism (Chapter 6). Any changes in rock microstructure due to time-dependent fracturing are likely to result in concomitant changes in the fluid flow properties. This is because permeability is essentially a geometric property, as it is measured in m^2. Hence, one could expect a time-dependent component associated with rock permeability.

The effect of strain rate on permeability evolution has been previously reported by *Heiland* (2000), who carried out triaxial compression tests on low porosity (6-9%) sandstones. In their tests a strain rate of 10^{-6} /s or higher resulted in increasing permeabilities. In contrast, a strain rate of 10^{-7} /s or lower was associated with continuously decreasing permeabilities, although dilatancy occurred. My results for Locharbriggs sandstone are in excellent agreement with their observations. In the high strain rate tests, Locharbriggs permeability increases prior to specimen failure, while the slow strain rate tests are characterised by continuously decreasing permeabilities. However, such clear distinction in the permeability evolution is not observed for Clashach sandstone. At slow strain rates, test temperature exerts a significant effect on the way permeability evolves in Clashach sandstone. Hence, lithology, temperature and strain rate act together in determining the evolution of fluid flow properties in my tests.

Initially, all samples display a permeability decrease irrespect of the temperature or the deformation rate used for the test. This observation is agrees with *Zhu and Wong* (1997), who suggested that under moderate confining pressure, permeability and porosity decrease are correlated up to a point C' that marks the onset of dilatancy in a porous sandstone. Although the pore space of a clastic rock is made of three types of pores (nodal pores, tubular pores and cracks), it is the sheet like microcracks that close the most easily under the application of effective pressure (*Bernabé*, 1991; *Zhu and Wong*, 1996). Hence, the initial permeability reduction can be attributed to the closure of favourably oriented cracks. Although the volumetric strain was not measured in my tests, it is assumed that such compactive processes cause the initial reduction in axial permeability. This view is supported by the measured decrease in ion concentrations, since the effect of decreasing porosity is to reduce the available surface area for dissolution.

The initial permeability reduction is more pronounced for the slow strain rate tests than for the high strain rate tests. For both sandstones, the ratio of peak stress

permeability k_{peak} to initial permeability k_0 decreases with decreasing deformation rate. In addition, the amount of initial reduction in the axial permeability decreases systematically with the applied loading rate for the Clashach sandstone tests. Hence, my results agree with *Sangha and Dhir*, (1972) who observed a recovery in lateral strains in their 10^{-7} /s creep tests on Laurencekirk sandstone. They attributed this observation to a greater degree of mechanical compaction in the slow strain rate tests. It is certainly possible that the longer time available in the slow strain rate tests resulted in more efficient compaction. Alternatively, a greater initial compaction could have been caused by a more efficient precipitation of low temperature minerals in the slow strain rate tests (*Tenthorey et al.*, 1998). This hypothesis cannot be checked by SEM analysis of fresh surfaces, since the test specimen were impregnated with resin shortly after their removal from the experimental apparatus. However, the occurrence of any significant precipitation in my tests is unlikely due to the relatively low temperatures and short durations of the experiments.

Following the initial compaction phase, permeability evolution correlates with AE activity, mean effective stress or chemical content of the pore fluid. In the slow strain rate tests the permeability of Clashach sandstone increases prior faulting, while the Locharbriggs permeability decreases continuously. The contrasting permeability evolution might be explained by the deformation microstructures (section 4.6). The deformed Clashach specimens are characterised by pervasive microfracturing and grain crushing, suggesting a deformation style dominated by brittle fracturing. Locharbriggs sandstone shows more evidence of grain translation, which highlights the importance of compactive processes in modifying the pore space. The stress and strain sensitivity coefficients were also larger in the Locharbriggs tests than in the Clashach tests (table 7.3). Hence, the decreasing permeabilities in the Locharbriggs tests may be a result of a more efficient compaction when compared to the Clashach tests.

At high strain rates of 10^{-5} to 10^{-6} s^{-1} both sandstones exhibit increasing permeabilities prior to specimen failure. The cumulative AE event count N scales with permeability according to a power law (r^2=0.86) or a logarithmic law (r^2=0.96) for Clashach and Locharbriggs sandstone, respectively. Assuming that N is proportional to the increase in the inelastic volumetric strain (*Sano et al.*, 1981), the correlation between AE activity and axial permeability suggests

a positive power law (7.6) or logarithmic (7.7) dependence of permeability on porosity. The non-integer exponent in (7.6) indicates that porosity is a fractal object, in accordance with *Thompson* (1991). Equation (7.6) is similar to the famous Carman-Kozeny relationship (*Carman*, 1956) that predicts a power law dependence of permeability on porosity. Although a positive power-law correlation is observed in the high strain rate tests, it is unlikely that such relationship holds under crustal strain rates of 10^{-14} to 10^{-16} /s. In fact, in the slow strain rate tests there is no correlation between AE damage and sample permeability. Moreover, the initial permeabilities do not show any clear correlation with the sample porosity.

At slow strain rates of 10^{-7} and 10^{-8} /s the permeability of Locharbriggs sandstone decreases as an exponential function of the mean effective stress or the axial strain up to the dynamic failure of the test specimen. Similar behaviour is observed for the 25-60°C Clashach tests. My observations agree with those of *David et al.* (1994) and *Main et al.* (2000). The stress sensitivity coefficient ranges from 0.45 to 2.93×10^{-2} MPa^{-1}. Hence, for some of the tests, the stress sensitivity coefficient γ_1 is higher than the 2.0 MPa^{-2} limit for porous sandstones that was suggested by *Wong and Zhu* (1999). The higher γ_1 are likely to be a direct consequence of the greater temperature range and slower strain rates of my tests when compared to previous tests. The Locharbriggs sandstone displays this kind of pattern in the permeability evolution over the whole temperature range that was studied (25-80°C). Hence, temperature does not affect the pattern of permeability evolution in these tests. Furthermore, the fluid flow properties are not controlled by the AE damage (Chapter 5) or the pore fluid chemistry (chapter 6), since both of these parameters evolve in an opposing fashion to the sample permeability (fig. 7.12). Therefore, the permeability decrease is likely to be caused by mechanical compaction, such as the clogging of pore throats by fine particles. This view is supported by the triaxial compression tests of *Liakopoulou-Morris et al.* (1994) who demonstrated that purely mechanical processes can lead to continuously decreasing permeabilities in oil saturated Clashach sandstone. In contrast, *Main et al.* (1994) attributed decreasing permeabilities to chemical processes. In their triaxial tests on Dalquhandy sandstone oil-filled specimens exhibited increasing permeabilities while water saturated samples showed continuously decreasing permeabilities. It is therefore possible that chemical processes could

also contribute to the exponential permeability reduction in my tests. Hence, previous experimental data suggests that chemical or mechanical processes could be responsible for the observed permeability reduction in Locharbriggs sandstone.

In the slow strain, 80°C Clashach tests permeability correlates with the amount of dissolved ions in the exit pore fluid. The relationship between sample permeability and ion concentration can be described by a linear law. However, the direct correlation between permeability and fluid chemistry is dominated by the large initial reduction in both axial permeability and ion concentrations due to initial compaction (I) of the specimen. In the following linear elastic (II) and strain hardening phases (III), changes in permeability and chemical properties of the pore fluid are relatively small. It appears that the microstructural properties that control the fluid flow are not significantly altered during phases II and III. Although speculative, this may be an indication that the newly formed cracks are not efficiently incorporated into the interconnected pore space traversed by the pore fluid. This observation is consistent with the idea that permeability is not only a function of dilatancy but also of microcrack linkage (*Zoback and Byerlee*, 1975; *Zhu and Wong*, 1999; *Popp et al.*, 2001). Alternatively, only a small proportion of the pore space may dominate the fluid flow and the chemical signal that I observe.

One might expect permeability to be significantly modified by test temperature. An increase in temperature can induce microfracturing or accelerate dissolution rate and therefore enhance fluid flow properties. Alternatively, more abundant mineral precipitation at higher temperatures could decrease permeability. However, any thermally induced permeability changes that I observe are small, possibly due to the narrow range of temperatures used in my tests. For the Locharbriggs sandstone there is a tendency for the permeability to decrease with increasing temperature. However, this effect is not reproduced in all of my tests. It is more likely that the axial permeabilities vary over two orders of magnitude simply because of normal lithological variation. However, the Clashach permeabilities do appear to display a clear temperature effect. In the 25-60°C tests permeability decreases due to compactive processes, while in the 80°C it increases and correlates with the amount of dissolved silica. It is possible that the enhanced dissolution rate at 80 °C plays a dominant role in modifying pore microstructure and hence, permeability.

7.6 Conclusion

The results of my experiments on Clashach and Locharbriggs sandstone demonstrate that the permeability evolution during a triaxial compression test depends on the applied loading rate. This is not surprising because the mechanical properties of rocks (Chapter 4) and the AE activity (Chapter 6) also depend on the rate at which deformation occurs. Initially, all tests display a permeability decrease associated with the closure of favourably oriented microcracks. The amount of initial permeability reduction increases with decreasing loading rate. Furthermore, the permeability decrease is a linear function of the strain rate for the Clashach tests (r^2=0.96 to 0.99). These observations suggest that a greater degree of compaction was attained in the slower strain rate tests.

Following the initial permeability reduction fluid flow properties evolve as a function of mean effective stress (r^2=0.55 to 0.99), axial strain (r^2=0.55 to 0.99), AE damage (r^2=0.86 to 0.96) or the pore fluid chemistry (r^2=0.54 to 0.90) depending on test temperature and strain rate. In the high strain rate tests permeability increases as a power or a logarithmic function of the AE damage, hence suggesting that axial permeability and porosity are positively correlated.

At slow strain rates, Locharbriggs permeability decreases continuously as an exponential function of the mean effective stress or axial strain. The permeability reduction is likely to be caused by elastic pore closure. In contrast, the Clashach sandstone displays increasing permeabilities at slow strain rates. Hence, chemical reaction can also dominate the fluid flow properties, particularly at slow strain rates.

Chapter 8

Discussion

In reality, modern experiments are undertaken because one precisely recognises that nature is a poor experimenter. Gretener (1981)

8.1 Data synthesis

8.1.1 Introduction

It is fair to say that the complexity of natural geological processes cannot be duplicated in the laboratory. Any specific geological structure is a result of both fundamental processes and incidental conditions (*Gretener*, 1981). Since we have a fairly good idea of the fundamental processes, these are the ones that can be tested for in the laboratory. Trying to re-create both effects amounts to no more than reproducing '*both the signal and the noise*' Gretener (1981).

8.1.2 Stress corrosion crack growth

In this study the process of interest is subcritical crack growth by the stress corrosion mechanism. I set out to investigate this effect by carrying out nineteen triaxial compression tests in dry and wet environments and at four different temperatures and strain rates. The main findings of this study are summarised graphically in figures 8.1. and 8.2, for Locharbriggs and Clashach sandstones,

respectively. Because of the low confining pressure used (13.5 MPa), the failure of all rock samples occurred by brittle faulting and the microstructural observations also suggest the dominance of brittle fracturing in my tests. Furthermore, the strength of both sandstones was reduced in a wet environment and on the application of a slower loading rate. Since the strain rate and environment dependence of rock strength is commonly ascribed to stress corrosion fracturing (*Costin*, 1987), this is also the process by which cracks are likely to grow in my tests. This hypothesis was later verified by the close quantitative relationship that exists between microcrack damage and pore fluid chemistry in the Locharbriggs tests (*Ojala et al.*, 2003). Crack damage and pore fluid silica concentration are strongly correlated by a power law (r^2= 0.94-0.96) with an exponent x=0.35-0.40, which indicates that reaction rates are not uniform for cracks of different ages (table 8.1). Furthermore, the estimated reactive surface area (0.38/cm) is considerably smaller than the volume normalised surface area of the rock sample (252/cm). Hence, only a fraction of the total geometric surface area contributes to the geochemical signal that I observe. It is therefore likely that the measured silica signal represents dissolution from the newly created fresh fracture surfaces rather than passive dissolution from crack walls away from the crack tips. Furthermore, the Arrhenius-type temperature dependence of silica concentration demonstrates that reaction rates contribute towards the measured signal. This observation agrees with *Dove's* (1995) model that is based on reaction rate theory.

A wealth of geochemical, hydraulic, microseismic and mechanical data was collected during these tests. The four different types of recorded data are related to the applied strain rate and test temperature via 22 scaling relationships, that are listed in table 8.1. The evolution of microcrack damage, axial permeability and pore fluid chemistry are also interrelated during these tests, hence suggesting that brittle fracturing, fluid flow and chemical reaction are strongly coupled processes in the crust. It is interesting to note that many of the equations that describe the behaviour of Locharbriggs sandstone are exponential, while the scaling properties of Clashach sandstone are best expressed by power laws. This observation suggests that the accumulation of damage and the accompanying changes in permeability and pore fluid chemistry accelerate faster in the Clashach tests. It may be the reason why no direct correlation between chemistry and microseismic properties is observed in the Clashach tests, although both parameters increase during the relatively short strain hardening phase. The sampling frequency for the exit pore

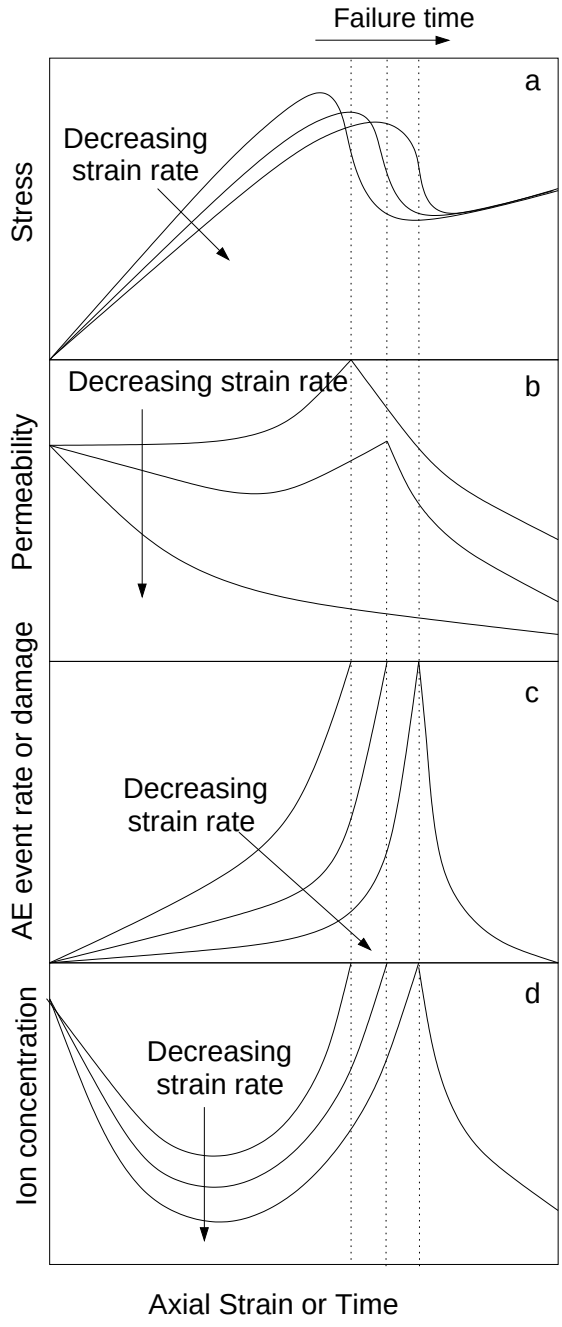

Figure 8.1. The effect of strain rate on the temporal evolution of hydraulic, microseismic and geochemical properties in Locharbriggs sandstone. a) This sandstone is weak and it exhibits distinct strain softening, that becomes more pronounced with decreasing strain rate. Strength and elastic modulus decrease systematically with decreasing strain rate. The predicted strength at a crustal strain rate (10^{-16}/s) equals 68 MPa. b) At high strain rate permeability increases continuously. At slow strain rate permeability decreases exponentially. c) Damage accumulates as an exponential function of time. Damage accumulation becomes steeper with decreasing strain rate. d) Pore fluid chemistry exhibits an exponential decrease followed by a quasi steady-state and an exponential increase prior to specimen failure. This kind of behaviour is typical for a poorly cemented sandstone.

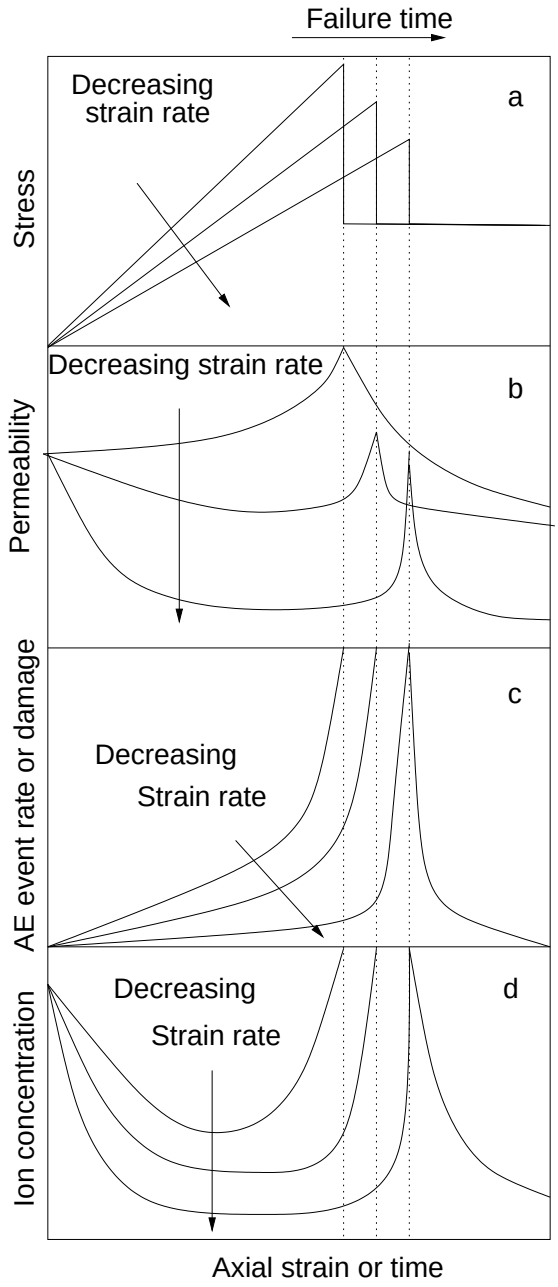

Figure 8.2. The effect of strain rate on the temporal evolution of hydraulic, microseismic and geochemical properties in Clashach sandstone. a) This sandstone is very strong and brittle. Both strength and elastic modulus decrease systematically with decreasing strain rate. The predicted strength at a crustal strain rate (10^{-16}/s) equals 50 MPa. b) At high strain rate permeability increases continuously. At slow strain rate an exponential decrease in permeability is followed by a quasi-static phase and an eventual increase. c) Damage accumulates as a power law function of elapsed time. Damage accumulation becomes steeper with decreasing strain rate. d) Pore fluid chemistry exhibits an exponential decrease followed by a quasi steady-state and an eventual sharp, power-law increase prior to specimen failure. This kind of behaviour is typical for a well-cemented sandstone.

Table 8.1. A summary of the scaling relationships that have been observed in this study. Peak stress scales as power (r^2=0.86) or a logarithmic (r^2=0.90) law. Elastic modulus is proportional to the logarithm of strain rate (r^2=0.89-0.92). Stress drop at failure is proportional to the peak stress (r^2=0.92). Locharbriggs Si concentrations scale with the AE damage (r^2=0.94-0.96) and test temperature T (r^2=0.96-0.99). Clashach Si concentrations are proportional to the concentrations of Al, K and Mg (r^2=0.90-0.99). Si concentrations and damage evolve according to a power(r^2=0.67-0.99) or an exponential law (r^2=0.82-0.99). The b_t-value is a logarithmic function of the strain rate (r^2=0.97). Omori decay parameter p is proportional to test temperature (r^2=0.93). In the high strain rate tests, permeability scales according to a power (r^2=0.86) or a logarithmic law (r^2=0.96). In the slow strain rate tests permeability is a function of mean effective stress (r^2=0.55-0.99) or ion concentrations (r^2=0.54-0.90).

Variable	Locharbriggs	Clashach
Peak stress σ_{max}	$\sigma_{max} = 1.11 \log(\dot{\varepsilon} \times E_m) + 82.4$	$\sigma_{max} = 281.8\, \dot{\varepsilon}^{0.047}$
Elastic modulus E_m	$E_m = 339.6 \log \dot{\varepsilon} + 7828$	$E_m = 777.7 \log \dot{\varepsilon} + 12687$
Stress drop $\Delta\sigma$	$\Delta\sigma \propto 0.77\sigma_{max}$	$\Delta\sigma \propto 0.77\sigma_{max}$
Silica concentration	$\Delta C_{Si} \propto (D, S, N, E)^x$ $C_{max} \propto \exp(-4587/T)$ $C_{ss} \propto \exp(-5209/T)$ $C_{Si} \propto \exp(qt/t_f)$	$C_{Si} = j_3 \times C_{Al,K,Ca}$ $C_{Si} \propto (1 - t/t_f)^z$
Damage	$D, S, N, E \propto \exp(qt/t_f)$	$D, S, N, E \propto (1 - t/t_f)^z$
b-value	b_t=0.81-0.06 log $\dot{\varepsilon}$	-
Omori law exponent p	p $\propto$ 0.0055T	-
Permeability k	$k \propto \log N$ k$\propto \exp(-\gamma_1 \sigma_{eff})$ $k = \beta_3 C_{Si,Fe,Mg} + \beta_4$	$\Delta k \propto N^{0.34}$ $k_{min}/k_0 = 28.2 \log \dot{\varepsilon}$+228 $k_{peak}/k_0 = 34.7 \log \dot{\varepsilon}$+280 $k = \beta_3 C_{Si,Al,Fe,K,Mg} + \beta_4$
Stress corrosion index n	124	21

fluid may have been too low to resolve any such signal. Alternatively, stress corrosion fracturing could proceed without the formation of distinct corrosion products in Clashach sandstone. Hence, the Clashach silica signal may have been dominated by passive dissolution from crack walls rather than active dissolution from the crack tips. The Clashach pore fluid also contains a considerable amount of other ions, such as Al, K, Fe, Mg, Ca and Na. For the Clashach experiments, the Si/Al and Si/K ratios remain constant throughout the deformation test (r^2=0.90-0.99). This could be an indication that the chemical system in the Clashach tests is more complex than what is observed for Locharbriggs sandstone.

In the previous chapters I have presented and discussed the temporal evolution of mechanical, microseismic, geochemical and fluid flow properties during the triaxial compression tests. It appears that both deformation rate and temperature induce significant changes in the way these petrophysical properties evolve during a typical test. The effect of test temperature and strain rate on the brittle deformation and fluid flow properties of Clashach and Locharbriggs sandstone are discussed in the next two sections.

8.1.3 The effect of test temperature

Stress corrosion crack growth is a thermally activated process. Hence one could expect fracture rates to be enhanced at a higher temperature. In fact, crack velocities in the quartz-water system have been observed to increase with temperature for a particular value of K or G (*Martin*, 1972; *Scholz*, 1972; *Meredith and Atkinson*, 1982; *Darot and Guéguen*, 1986). Although reaction rate theories of crack growth predict a change in slope on a $v - K$ plot associated with increased test temperature (*Wiederhorn and Boltz*, 1970; *Dove*, 1995), no such correlation has been observed for crack growth in the quartz water system at T=20-80°C (*Martin*, 1972; *Scholz*, 1972; *Darot and Guéguen*, 1986). Furthermore, the strength of quartz rich sandstones does not appear to be temperature dependent at T=26-204°C (*Serdengecti and Boozer*, 1961; *Blacid et al.*, 1981). In addition, *Fischer and Paterson* (1989) reported that the effect of test temperature on rock strength is smaller in sandstone than in calcite rocks. Due to the high temperatures (up to 400°C) a decrease in rock strength with increasing temperature was observable in their tests. However, in my tests the

temperature range is only 25-80°C. In the light of the previous observations, it is not surprising that the mechanical properties of Clashach and Locharbriggs sandstone do not display a clear temperature dependence. It is possible that the noise level imposed by sample variability is higher than the effect of test temperature on the short term strength of these rocks.

In contrast to the mechanical data, the microseismic activity, fluid flow properties and pore fluid chemistry all exhibit a clear temperature dependence (table 8.1). The AE foreshock and aftershock sequences are are well modelled by the Omori formulae with an exponent that is close to unity (r^2=0.87-0.98). For the Locharbriggs tests the Omori decay parameter p is a linear function of the test temperature (r^2=0.93). This observation is consistent with the high p-values that have been recorded in high heat flow areas in California and Japan (*Mogi*, 1967; *Creamer and Kisslinger*, 1993; *Utsu et al.*, 1995). It is possible that stresses relax faster in areas of high heat flow, thus explaining the faster aftershock decay rate (*Mogi*, 1967).

The geochemical data also exhibits a marked dependence on test temperature (table 8.1). Although the Si concentrations are consistently smaller than quartz equilibrium concentrations (*Rimstidt and Barnes*, 1980), both maximum and steady state Si concentrations obey an Arrhenius type temperature dependence (r^2=0.96-0.99). This observation suggest that reaction rates contribute towards the measured silica signal in the Locharbriggs tests. *Tenthorey et al.* (1998) reported a similar Arrhenius dependence of the post-experiment Si concentrations following a compaction experiment on quartz-feldspar sand. Due to the high pore and confining pressures and the higher feldspar content, the Si concentrations in their tests exceeded the quartz equilibrium values. However, no such temperature dependence is observed in the Clashach tests, possibly due to a greater surface area control on the measured geochemical signal.

Fluid flow properties appear to be affected by temperature in the Clashach tests. An increase in test temperature is associated with a lower initial permeability of the test specimen. Similar reduction in permeability with increasing temperature has also been observed for sand (*Tenthorey et al.*, 1998) and Gosford sandstone (*Fischer and Paterson*, 1989). In the triaxial compression tests of *Fischer and Paterson* (1989) the reduction in permeability was attributed to a decrease in initial accessible porosity with increasing test temperature. This may be the

reason for the temperature dependent permeabilities in my tests as well. The densification of test specimen with increasing temperature can be attributed to thermal expansion of quartz grains into the pore space (*Blacid et al.*, 1981) The evolution of permeability also exhibits a marked temperature dependence in the Clashach tests. In the low temperature tests at 25-60°C permeability is a function of the axial strain or applied mean stress. In the 80°C tests permeability correlates with the concentrations of dissolved ions (Si, Al, Fe, K, Mg) in the pore fluid. This could be due to the temperature dependence of dissolution rates (*Rimstidt and Barnes*, 1980; *Bevan and Savage*, 1989). Hence, it appears that the chemical evolution of the system dominates the fluid flow properties at high temperatures. This observation has important implications for modelling permeability evolution in crustal rocks. Since most permeability measurements are made at room temperatures, these values should be treated as upper limits for the rock type of interest.

8.1.4 The strain rate effect

The loading rate dependence of the mechanical properties of rocks has been confirmed in several studies (*Serdengecti and Boozer*, 1961; *John*, 1972; *Sangha and Dhir*, 1972; *Peng*, 1973; *Sano et al.*, 1981; 1982; *Costin*, 1987; *Masuda*, 2001). However, in my tests the evolution of AE activity, axial permeability and fluid chemistry also display a clear strain rate dependence. This is a very important observation because laboratory tests are typically carried out using high strain rates of the order of 10^{-5} to 10^{-6}/s. The slower strain rates used in my tests (10^{-7} to 10^{-8}/s) are likely to be more representative of crustal conditions. Geological strain rates range from 10^{-14} to 10^{-16}/s (*Barber*, 1990). It is not possible to attain such small strain rates in the laboratory.

Table 8.2 summarises the effect of strain rate on the various petrophysical properties as observed in this study. First of all, rock strength decreases with decreasing strain rate. The reduction in strength is best described by a power law (r^2=0.86) or a logarithmic law (r^2=0.90) for the Clashach and Locharbriggs sandstones, respectively. If a power law (r^2=0.81) is also used to describe the Locharbriggs data, the exponent n equals 124. For the Clashach sandstone, the stress corrosion index n=21. Hence, it appears that Locharbriggs sandstone has

Table 8.2. A summary of the effect of decreasing strain rate on rock properties, as observed in this study. The strength of Clashach and Locharbriggs sandstone decreases with decreasing strain rate. Microstructural and microseismic properties of these rocks indicate that microfracturing is more pervasive in the slow strain rate tests. The fluid flow properties suggest that a greater amount of initial compaction was attained in the slow strain rate tests.

Effect of decreasing $\dot{\varepsilon}$	Explanation
peak stress σ_{max} decreases	rock is weaker at slower $\dot{\varepsilon}$
linear crack density is is higher areal crack density is higher elastic modulus E_m decreases	more cracks at slower $\dot{\varepsilon}$ tests
higher b-value smaller A_{max}	more smaller cracks at slower $\dot{\varepsilon}$ tests
more pronounced strain softening phase higher proportion of AE events after σ_{max}	slower crack velocity, hence hence a more stable system
higher initial k drop smaller C_{ss}	more initial compaction
exponent p' for foreshocks decreases exponent z for damage decreases exponent q for damage increases	failure becomes less predictable

a greater resistance to subcritical crack growth than Clashach sandstone. Yet, both sandstones are composed of quartz and feldspar and one might expect that the susceptibility to chemical stress corrosion is similar for both rocks (*Swanson*, 1984). It is possible, however, that the resistance to subcritical crack growth is determined by rock microstructure. Locharbriggs sandstone has a higher proportion of feldspar (13%) than Clashach sandstone (11%). It also contains some diagenetic hematite on the grain surfaces. The greater heterogeneity of Locharbriggs sandstone could cause the crack paths to become more tortuous (*Atkinson and Meredith*, 1987a). As a consequence, its resistance for subcritical crack growth could be higher. Also, assuming that n is inversely proportional to grain size (*Atkinson and Meredith*, 1987a), one could expect a higher n-value for Locharbriggs sandstone. However, Clashach sandstone is twice as strong as Locharbriggs sandstone because of its pervasive quartz cement. This suggests that the resistance for crack growth is considerably higher for Clashach sandstone. One could expect a higher n-value associated with a greater amount of quartz cement, as was observed for Scioto sandstone by *Holder et al.* (2001). However, in my tests the well cemented Clashach samples exhibit a smaller n-value than the poorly cemented Locharbriggs sandstone. A more comprehensive testing programme would be required to resolve the controlling parameters (porosity, grain size, cementation) on subcritical crack growth parameters.

Microfracturing is more intense in the slow strain rate tests than in the high strain rate ones. Microstructural analysis indicates that both areal and linear crack densities are higher in the 10^{-8} /s test than in the 10^{-6} /s test for both sandstones. For Locharbriggs sandstone the crack density is considerably higher in the slow strain test. In addition, the elastic modulus E_m decreases with decreasing strain rate. The reduction in E_m with the applied loading rate can be described by a logarithmic law for both sandstones (r^2=0.89-0.92). Hence, my results agree with the observations of *Sangha and Dhir* (1972). In their uniaxial compression tests on Laurencekirk sandstone the the Young's modulus decreased with decreasing strain rate. Since the presence of cracks lowers the elastic modulus (*Costin*, 1987), the decrease in E_m with strain rate suggest that crack growth is more pervasive in the slow strain rate tests.

The relative proportion of smaller AE events also increases with decreasing strain rate. The maximum recorded amplitude A_{max} decreases with decreasing strain

rate in the Locharbriggs tests. Similarly, the seismic b-value increases as the loading rate is reduced. The b-value is a linear function of the applied strain rate (r^2=0.97). This observation is in good agreement with the uniaxial tests of *Sano et al.* (1982). They reported a decrease in b-value with decreasing volumetric strain rate. The higher proportion of smaller events suggest that small fractures dominate the brittle deformation properties at slow strain rates.

The slow loading rate tests exhibit more pronounced strain softening behaviour than the high strain rate tests. This is especially true for the Locharbriggs tests. Similarly, a greater proportion of AE events occur after the peak load has been attained if a slow strain rate is used. It is possible that cracks propagate faster in the high strain rate tests, which leads to uncontrollable behaviour of the machine-specimen assembly (*Paterson*, 1978). In contrast, fracture rates may be slower in a slow strain rate tests, causing the system to be more stable. In fact, *Serebrinsky et al.* (1999) reported a continuous decrease in stress corrosion crack velocity in brass, steel and silver alloys with decreasing strain rate. Smaller velocities for crack propagation could explain the higher proportion of small events that occur in the slow strain rate tests.

It appears that decreasing the applied strain rate favours a more compactive deformation style. The initial drop in the recorded axial permeability, as indicated by the k_{min}/k_0 ratio, is higher in the slower strain rate Clashach tests. Similarly, the ratio of the peak stress permeability k_{peak}/k_0 decreases with decreasing strain rate. Both k_{min}/k_0 and k_{peak}/k_0 are proportional to the logarithm on strain rate (r^2=0.96-0.99). However, k_{peak}/k_{min} does not display a clear strain rate dependence. Hence the observed decrease in k_{peak}/k_0 and k_{min}/k_0 is likely to be caused by the same underlying mechanism. I believe that initial compaction is more efficient in the slow strain rate tests. This view is supported by the fact that the measured steady-state Si concentrations also decrease with decreasing strain rate, indicating a smaller available surface area for dissolution. In their uniaxial compressions tests, *Sangha and Dhir* (1972) observed a recovery in lateral strain in the slow strain rate tests. Hence, they suggested that a greater degree of compaction was attained in the slow strain rate tests. If the volumetric strain had been measured also in my tests, this would have allowed a more quantitative analysis of the effect of strain rate on compactive processes.

The temporal evolution of AE activity also displays a marked dependence on the

applied strain rate. As the strain rate decreases the exponent p' for foreshocks decreases. Similarly, exponents z and q for damage decrease and increase, respectively. These observations suggest that the acceleration damage and AE activity is more rapid in the slow strain rate tests. Hence, prediction of sample failure becomes more difficult as the strain rate is reduced.

The stress drop at failure also decreases with decreasing strain rate for both rocks. I believe that this effect does not indicate an increased ductility, but that stress drop is linked to specimen strength. In fact, the stress drop for both rock types can be expressed by the same linear relation, as shown in table 8.1. (r^2=0.93). Although speculative, this could be the reason why stress drop in earthquakes is typically smaller (3-10 MPa) than what has been observed in laboratory studies (*Shearer*, 1999). Due to the smaller deformation rate rock strength is likely to be less in crustal conditions than in laboratory studies. Hence, one could expect smaller stress drops associated with earthquakes.

8.2 Potential applications

8.2.1 General applications

The results of my experiments are applicable to a wide range of time-dependent phenomena in the brittle crust. Crack growth by stress corrosion has been suggested as the possible mechanism for a variety of puzzling geophysical phenomena, including stability of hydrofractures, relaxation of internal stresses in rock (*Atkinson*, 1984), time dependent earthquake phenomena (*Scholz*, 1968b, *Anderson and Grew*, 1977; *Das and Scholz*, 1981; *Atkinson*, 1984; *Reuschlé*, 1990), linear chains of magmatic intrusions (*Anderson and Grew*, 1977; *Atkinson*, 1984) and the abnormally high strength of lunar rocks (*Anderson and Grew*, 1977; *Mizutani et al.* 1977). The observation that silica is actively dissolving during stress corrosion crack growth may have important implications for all of the above phenomena, since silica release is not commonly included in models for subcritical crack growth. Furthermore, knowledge of the long term evolution of fracture networks in reservoir rocks is essential for modelling the migration patterns of petroleum and geothermal fluids (*Dove*, 1995) as well as the flow of ground water and the

associated movement of contaminants. My results indicate that the evolution of fluid flow properties also exhibits a marked time dependence. This observation has important implications for modelling the long term hydraulic properties of faults and fractures (*Sausse et al.*, 2001).

While the strain rates operating in the crust are unattainable in laboratory conditions, a slower loading rate in a conventional test approaches creep strain rates and it is more representative of the crustal conditions. My results indicate that strain rate can have a significant effect on the evolution of AE activity and fluid flow properties during a conventional triaxial test. The deformation rate dependent permeability reduction and the smaller steady state Si concentrations also suggest that a greater degree of compaction was attained in the slow strain rate tests. However, rock deformation tests are typically carried out at a high strain rate of 10^{-5} to 10^{-6}/s to enable the test to be completed in one or a few days. Hence, care must be taken if the results of a high strain rate experiments are applied to crustal processes. It is very likely that the combined effects of time, deformation rate, temperature and chemical environment are even more pronounced in the crust than in my experiments. During natural geological processes, such as tectonic or sedimentary burial, several parameters are likely to change at once. In laboratory testing, the effects of any external parameters (confining pressure, pore pressure, T) must be studied separately in order to find their individual contributions (*Gretener*, 1981). This condition represents a fundamental difference between laboratory rock fracture and crustal deformation. Yet, under moderate confining pressure, the rock sample fails along a single, well defined plane that very much resembles a geological fault.

8.2.2 The resemblance of earthquake and AE foreshocks

The similarity of the statistical properties of AE activity and earthquake populations suggests that both phenomena could be caused by a similar mechanism (*Scholz*, 1968b). For instance, the slip on faults is likely to involve the breaking of local asperities because of the roughness of fault surfaces (*Lockner*, 1993a). Natural faults may heal and strengthen between earthquakes and thus resemble intact rock samples. In fact, the Omori law exponents are close to unity, just like the earthquake ones (*Utsu et al.*, 1995; *Ogata et al.*, 2003). However, the power

law exponents p and z decrease and the exponential law exponent q increases with decreasing strain rate. This observation highlights yet another reason why the results of high strain rate (10^{-5}-10^{-6}/s) tests should be treated with caution, if extrapolated to earthquake time-scales. Previous experiments at 2×10^{-5}/s have reported a more gradual acceleration of AE activity than earthquake foreshock sequences (*Liakopoulou-Morris et al.*, 1994), that has been considered typical of laboratory AE sequences (*Main*, 2000). My observations indicate that a gradual accelerations is a feature of the high strain rate tests, but the acceleration becomes steeper as the strain rate is reduced. In fact, the critical exponent z approaches zero in the very slow strain rate Clashach tests (z=0.14). Earthquake foreshocks also assume a value of z≈0 (*Main*, 2000). Hence, my observations suggest that rock failure becomes harder to predict as the strain rate decreases. Although speculative, this could be the reason why many large earthquakes lack a clearly recognisable foreshock sequence (*Mogi*, 1967). Yet, the statistical analysis of earthquake populations suggests that *foreshocks are genuine forerunners of large shocks* (*Helmstetter et al.*, 2003). As a consequence, one might expect foreshocks to precede earthquakes, although they may not be easily recognisable in the recorded data until after the event.

8.2.3 Temperature dependence of Omori decay parameter

The temperature dependence of AE aftershock decay rate is remarkably similar to that observed for earthquake aftershocks in Japan and in California (*Utsu et al.*, 1995). Already in (1967) *Mogi* noted that the geographic distribution of the exponent p of in the Omori formula resembles the geotectonic structure of the Japanese Islands. High p-values that indicate a rapid decay of aftershocks are generally observed in high heat flow areas. In my tests, p∝0.005T while *Creamer and Kisslinger* (1993) observed p∝0.00099T for aftershocks in the Tohoku district of Japan. However, in the earth's crust the seismogenic depth changes temperature. This is not the case for my tests. It is possible that the mechanism by which aftershock sequences are generated is affected by heat flow. In fact, in his aptly named article *Comparison of aftershocks of earthquakes and AE that occurs after turning out gas stove and so on* Ogasawara (1990) suggested that the occurrence of aftershocks maybe directly related to a diffusive

process that is equivalent to thermal diffusion. He observed that the decrease in temperature in the heating element of an electric cooking pot produces an AE sequence that resembles an earthquake aftershock sequence. It is therefore possible that the occurrence of earthquake aftershocks could be caused by pore fluid diffusion in the hypocentral area and that such diffusion is faster in a higher heat flow area. Alternatively, the greater ductility of rocks in a high heat flow area could cause the stresses to relax faster in the aftershock region (*Mogi*, 1967). It is clear, however, that laboratory tests can be used to investigate the temperature dependence of the aftershock activity. It would be interesting to know whether a positive correlation between p and T also exists for other lithologies. Furthermore, rock deformation tests could be used to study the effect of other parameters such as loading type and rock heterogeneity on the scaling constants in the Omori law. The Omori law remains one of the few established empirical formulae in seismology and it is therefore very important for modelling shallow seismicity (*Utsu et al.*, 1995; *Helmstetter et al.*, 2003; *Narteau et al.*, 2003).

8.2.4 Geochemical precursors of earthquakes

It has been suggested that '*distinguishing whether or not an aseismic slip leads to the rupture of asperity remains a further difficult research point in earthquake prediction*' (*Ogata et al.*, 2003). Strain and tilt meter data as well as GPS time series have revealed a number of silent earthquakes called aseismic slips that are not followed by subsequent large events in Japan (*Ogata et al.*, 2003). Similarly, a relative seismic quiescence is not always followed by a large earthquake (*Ogata*, 2001; *Ogata et al.* 2003). The geochemical signal that I observe could help to resolve this issue: one could expect an increase in ground water ionic concentrations prior to mechanical rupture. In such case, slow crack growth that is controlled by chemical reactions could take place without a measurable seismic activity (*Evans and Linzer*, 1973; *Anderson and Grew*, 1977). Alternatively, an increase in the fracture surface area or in the flow rate of pore water could induce changes in the ground water chemistry (*Anderson and Grew*, 1977). In fact, radon emissions have been observed to increase prior to earthquakes, possibly due to the formation of microcracks (*Scholz et al.*, 1973; *Igarashi et al.*, 1995; *Quattrocchi and Calcara*, 1998). In a recent study, *Tsunogai and Wakita* (1995)

analysed bottled water that was sourced near Kobe city. They observed an increase in Cl concentrations prior to the disastrous 1995 earthquake. The Cl signal that they measured is similar to the Si signal in my tests, although the peak in Cl occurred after the earthquake. However, since Cl was not present in the shallow strata below the sampling area, the Cl anomaly was attributed to increased ground water flow due to changes in tectonic stress or in permeability enhancement by microfracturing. Similarly, *Rojstaczer et al.* (1995) observed an increase in stream water flow and ionic concentrations after the 1989 Loma Pieta earthquake. They attributed these changes to an order of magnitude increase in permeability caused by the earthquake. These observations suggest that a regular sampling and analysis of ground water in seismically active areas could be used as a predictive technique, especially when there is no precursory activity, as it is often the case. However, more work is required to establish whether a geochemical method is useful for predicting earthquakes or volcano-seismic events (*King et al.*, 1995; *Quattrocchi and Calcara.*, 1998).

Similarly, fracturing and the subsequent generation of fresh, reactive surface area could enhance the reactivity of active faults. Structural and mineralogical textures in faulted rocks suggest that their deformation history was characterised by episodic fracturing followed by cementation and crack healing (*Hickman et al.*, 1995). As a consequence, the pore fluid in active faults might be associated with a different geochemical signature than the surrounding rocks (*Satake et al.*, 2003). Hence, sampling of ground water might also be used as a technique for differentiating between active and passive faults. Furthermore, chemical analysis of ground water could also provide means by which *in-situ* permeability could be estimated. In the slow strain rate Clashach tests permeability is directly proportional to the ion content of the exit pore water. It would be interesting to know whether such relationship also holds for other lithologies, such as calcite rocks. This is particularly intriguing, since the results of *Marone et al.* (1988) suggest that permeability and pore fluid concentrations are negatively correlated in a artificially jointed marble specimen. However, his test conditions were somewhat different: the confining pressures and pore fluid pressures were 600 MPa and 200 MPa, respectively. Hence, pressure solution was likely to dominate the deformation style.

8.2.5 The weakness of crustal faults

The geochemical data and the marked dependence of rock strength on the test environment might provide clues to the debate about the weakness of crustal faults (*Lockner and Byerlee*, 1993; *Scholz*, 2000; *Zoback*, 2000). Hydrolytic weakening or stress corrosion fracturing could be more pervasive in the fluid saturated rocks of the fault zone relative to the country rocks. If the pore fluid in active fault zones contains significant amounts of dissolved salts, this could accelerate the crack growth rates due to enhanced silica reactivity (*Dove*, 1995). Alternatively, fracturing of feldspar grains could lead to precipitation of phyllosilicates in the fault zone (*Hickman et al.*, 1995). The replacement of strong feldspar by weak clays could further weaken the rocks within the fault zone. In the Clashach tests, a considerable amount of dissolved ions originated from the feldspar grains. Hence, dissolution may occur preferentially from feldspar grains in a quartz rich sandstone. In fact, *Satake et al.* (2003) also observed a geochemical signal associated with feldspar grains in the groundwater in and around the Mozemu-Sukenobu fault zone in Japan. The rocks within the fault zone were characterised by a higher Na/Ca ratio than the surrounding country rocks. They attributed this observation to a more intense weathering of feldspar grains within the fault zone. Hence, pervasive microfracturing, the passive presence of electrolytes in the pore water and the enhanced breakdown rate of feldspar grains could all contribute to the weakness of crustal faults. My results demonstrate that all of these phenomena characterise the macroscopic failure of sandstone specimen in laboratory conditions.

8.2.6 The origin of silica for quartz cement

The results of this study could also be used to resolve some key issues regarding the origin of quartz cement in sandstones (*Bjørkum*, 1996; *Fisher and Knipe*, 1998; *Worden and Morad*, 2000). Knowledge of the distribution of quartz cement in a potential reservoir is a very important one, since *the presence, absence or precise quantity of of cement ... dictates whether a sandstone-hosted petroleum reservoir will prove economic* (*Worden and Morad*, 2000). Quartz cement is the most common pore-filling cement in sandstones that have been heated to at least

to 70-80°C (*Worden and Morad*, 2000) or above 90°C (*Fisher and Knipe*, 1998). However, there has been considerable debate whether the silica in the quartz cement is derived externally or internally. My results indicate that stress corrosion fracturing at 80°C or less can increase the amount of silica in the exit pore fluid and hence provide an internal source of silica for quartz cement. The fresh surfaces generated during microfracturing could also provide favourable sites for quartz precipitation. Assuming that the Si concentrations in excess of the steady-state values represent a degree of supersaturation with respect to the bulk rock grains (*Dewers and Hajash*, 1995), the elevated Si signal can be considered as a measure of the amount of diagenetic cement that the newly generated fault possesses to seal itself (*Ngwenya et al.*, 2000). Hence, my results also have important implications for the generation of impermeable seals during interseismic periods, as suggested by the fault-valve hypothesis of earthquake occurrence (*Sibson*, 1994; *Renard et al.*, 2000). Furthermore, microfracturing could also enhance the kinetic rates for pressure solution creep by increasing the surface area for dissolution (*Gratier et al.*, 1999). Ultimately, pressure solution and fracturing could act together in the crust and make it behave in both brittle and ductile manner (*Gratier et al.* 1999).

8.2.7 Crack growth on the Moon

It is highly likely that stress corrosion crack growth will not be taking place on the surface of the Moon, because of the lack of free flowing water in the 60 km thick crust (*Swindle*, 1998; *Shearer*, 1999). This assumption explains the anomalously high strength of lunar rocks, its non-hydrostatic shape and the deep foci of moonquakes (*Mizutani et al.*, 1977; *Atkinson*, 1982).

8.3 Outstanding questions

There is considerable evidence that reaction rates and surface area are dominating the Locharbriggs and Clashach silica signal, respectively. However, it is not possible to determine whether silica is dissolving actively from the growing crack tips of passively from the crack walls and hence to prove or disprove the Dove model (*Dove*, 1995). In fact, both of these processes may contribute to the

geochemical signal that I observe. In order to resolve this issue a more quantitative measure of the microcrack volume and surface area is required. Another puzzling feature of the geochemical data is the abundance of other dissolved ions than silica in the Clashach tests and the higher concentrations of dissolved ions relative to the Locharbriggs pore fluid.

Quite surprisingly, Clashach sandstone exhibits power-law rheology, while many of the empirical relationships for Locharbriggs sandstone are best described by an exponential or a logarithmic form. The subcritical crack growth index is also considerably different for these two rocks. Yet, both sandstones are relatively homogeneous and composed of quartz and feldspar. One could expect that their behaviour would be described through similar scaling laws. However, it is possible that the type of cement or the initial porosity controls the temporal evolution of mechanical, hydraulic and microseismic properties of these rocks. In particular, the cement type determine whether crack linkage or chemical reactions control the damage evolution, as indicated by the exponential and power law scaling, respectively. A more systematic study could help to pinpoint the controlling parameters (porosity, grain size, texture, type of cement) on the subcritical crack growth parameters in these rocks.

Since the volumetric strain was not measured it is not possible to determine whether dilatancy and permeability are positively or negatively correlated for these sandstones. Similarly, the reason why pore fluid chemistry and permeability are correlated remains unclear. Both of these properties could be controlled by surface area or by dissolution-precipitation reactions. The extent of mineral precipitation could not be determined for my tests, since the rock cores were impregnated with resin shortly after their removal from the experimental apparatus.

8.4 Recommendations for future work

I have demonstrated that microcrack damage and pore fluid Si content are strongly correlated during the strain hardening phase of deformation in Locharbriggs sandstone. It would be interesting to know whether such a correlation between fluid chemistry and damage accumulation also exists for other rock types. A double-torsion test could be carried out in order to determine whether dissolution is a precursor to (*Dove*, 1995) or a consequence of crack tip propagation. Since volcanic events are more likely to be preceded by measurable foreshock activity than large earthquakes, such a study could be particularly useful for understanding volcano dynamics. It has been suggested that slow crack growth by the stress corrosion mechanism is characteristic of the preparation stage for volcanic eruptions (*Anderson and Grew*, 1977; *Vinciguerra*, 1999).

Laboratory tests under controlled conditions should be carried out at relevant pore pressures and temperatures, and a wider range of strain rates or loading conditions could be used to establish a more quantitative relationship between chemistry and microcrack damage. For instance, an array of AE transducers could be arranged around the specimen so that each event could be located accurately. Alternatively, continuous recording of lateral as well as axial strain could provide a more reliable estimate of microcrack damage. Knowledge of the volumetric strain would also allow a more detailed analysis of the evolution of permeability with brittle deformation (*Wong and Zhu*, 1999).

Similarly, rock deformation experiments should be conducted under a wider range of temperatures in order to establish the effect of test temperature on the evolution of permeability and brittle fracturing properties in these, and other rocks. To date, stress corrosion fracturing has not been studied at temperatures above 80°C (*Dove*, 1995). A wider temperature range could be used to resolve whether reaction rates control the fracture propagation rates, as suggested by *Dove*'s 1995 model. It is anticipated, that post-test analysis of precipitation features would be required for the higher temperature tests.

The extent by which pore fluid percolates through a rock sample during a flow-through test should be investigated more fully. My measurements indicate that the size of the hole through which the fluid enters the rock sample affects the differential pressure reading. However, the pressure change is not consistent with

the Darcy formula (3.2), i.e. $dP \times A_s$ does not remain constant. More detailed study is required to understand this effect of the percolating fluid.

Finally, more experiments should be carried out under slow strain rate conditions. My experiments demonstrate that the evolution of microseismic and fluid flow properties with brittle fracturing can be significantly different, if a slow strain rate is used. Such tests are likely to be more representative of the slow loading conditions of the crust.

Chapter 9

Conclusions

This thesis presents laboratory research into the time-dependent deformation properties of porous sandstones. A series of flow-through compression tests were carried out to investigate this effect. The main findings of this study are as follows:

- The strength of porous sandstones depends systematically on the test environment and on the applied loading rate. The reduction of rock strength with decreasing strain rate is best described by a power law or a logarithmic law for the Clashach and Locharbriggs tests, respectively.
- Sandstones deformed at a slow strain rate exhibit higher crack densities than samples deformed at a high strain rate. In addition, the elastic modulus decreases systematically with decreasing strain rate. Hence, fracturing is more intense in the slow strain rate tests than in the high strain rate tests.
- The decrease in rock strength in the presence of water and on the application of a slower loading rate is caused by stress corrosion crack growth. This view is supported by the concomitant increase in silica concentrations indicating chemical corrosion and cumulative AE event rate indicating crack growth during the strain hardening phase of deformation.
- Locharbriggs sandstone exhibits an exponential increase in both AE damage and silica concentrations during the strain hardening phase. Microcrack damage and silica concentration are strongly correlated by a power law formulation. Only a small fraction of the sample surface area is contributing

towards this signal, hence suggesting that silica is dissolving actively from the growing crack tips.

- The AE damage increases according to a power law in the Clashach tests. There is no correlation between the silica concentrations and AE damage for the Clashach sandstone. This may be an indication that silica is dissolving passively from the crack walls.
- The Locharbriggs silica concentrations exhibit an Arrhenius type temperature dependence, hence suggesting that chemical reaction rates control the measured signal. Clashach sandstone does not exhibit such temperature dependence, hence suggesting that surface area controls the geochemical signal.
- The evolution of fluid flow properties during a typical test depends on the applied strain rate. At a high deformation rate, permeability evolution correlates with microcrack damage. At a slow deformation rate permeability correlates with mean effective stress or pore fluid chemistry.
- The evolution of AE activity during a typical test depends on the applied strain rate. The acceleration of AE damage becomes sharper as the strain rate decreases. Hence, rock failure becomes harder to predict as the strain rate decreases.
- The Omori law can be used to describe the AE foreshock and aftershock sequences with an exponent p that is close to unity. The Locharbriggs p-values depend systematically on the test temperature. These observations are in excellent agreement with the recorded earthquake data.
- The different behaviour exhibited by the two sandstones is likely to be caused by their differing porosity, composition and grain size.

Bibliography

Adams, F.D. & Nicholson, J.T. (1901). An experimental investigation of the flow of marble. *Phil. Trans. Roy Soc. London*, **195**, 363–401.

Aharonov, E., Tenthorey, E. & Scholz, C.H. (1998). Precipitation sealing and diagenesis 2. Theoretical analysis. *J. Geophys. Res.*, **103**, 23969–23981.

Aki, K. (1965). Maximum likelihood estimate of b in the formula log N=a-bm and its confidence limits. *Bull. Earthquake Res. Instit. Univ. Tokyo*, **43**, 237–239.

Aki, K. & Richards, P.G. (1980). *Quantitative seismology*. Freeman, San Francisco.

Anderson, O.L. & Grew, P.C. (1977). Stress corrosion theory of crack propagation with applications to geophysics. *Rev. Geophys. Space Phys.*, **15**, 77–104.

Ashby, M.F. & Hallam, S.D. (1986). The failure of brittle solids containing small cracks under compressive stress states. *Acta Metall.*, **34**, 497–510.

Atkinson, B.K. (1979). A fracture mechanics study of subcritical tensile cracking of quartz in wet environments. *Pure Appl. Geophysics*, **117**, 1011–1024.

Atkinson, B.K. (1980). Stress corrosion and the rate dependent tensile failure of a fine-grained quartz rock. *Tectonophysics*, **65**, 281–290.

Atkinson, B.K. (1982). Subcritical crack propagation in rocks: Theory, experimental results and applications. *J. Struct. Geology*, **4**, 41–56.

Atkinson, B.K. (1984). Subcritical crack growth in geological materials. *J. Geophys. Res.*, **89**, 4077–4114.

Atkinson, B.K. & Meredith, P.G. (1981). Stress corrosion cracking in quartz: a note on the influence of chemical environment. *Tectonophysics*, **77**, T1–T11.

Atkinson, B.K. & Meredith, P.G. (1987a). The theory of subcritical crack growth with applications to minerals and rocks. In B.K. Atkinson, ed., *Fracture mechanics of rock*, 111–166, Academic Press, London.

Atkinson, B.K. & Meredith, P.G. (1987b). Experimental fracture mechanics data for rocks and minerals. In B.K. Atkinson, ed., *Fracture mechanics of rock*, 477–525, Academic Press, London.

Barber, D.J. (1990). Régimes of plastic deformation - processes and microstructures: an overview. In D.J. Barber & P. Meredith, eds., *Deformation processes in minerals, ceramics and rocks*, 138–178, Unwin Hyman, London.

Barenblatt, G.I. (1962). The mathematical theory of equilibrium cracks in brittle fracture. *Adv. Appl. Mech.*, **7**, 55–129.

Barnett, R.L. & Kerrich, R. (1980). Stress corrosion cracking in biotite and feldspar. *Nature*, **283**, 185–187.

Baud, P. & Meredith, P.G. (1997). Damage accumulation during triaxial creep of Darley Dale sandstone from pore volumometry and acoustic emission. *Int. J. Rock Mech. MIn. Sci*, **34**, 371.

Becker, G.F. (1893). Finite homogeneous strain, flow and rupture of rocks. *Geol. Soc. Am. Bull.*, **4**, 13–90.

Bennett, P.C. (1991). Quartz dissolution in organic-rich aqueous systems. *Geochim. Cosmochim. Acta*, **55**, 1781–1797.

Berger, G., Cadore, E., Schott, J. & Dove, P.M. (1994). Dissolution rate of quartz in lead and sodium electrolyte solutions between 25 and 300 ° C. Effect of the nature of surface complexes and reaction affinity. *Geochim. Cosmochim. Acta*, **58**, 541–551.

Bernabé, Y. (1991). Pore geometry and pressure dependence of the transport properties in sandstones. *Geophysics*, **56**, 436–446.

Bernabé, Y. (1995). The transport properties of networks of cracks and pores. *J. Geophys. Res.*, **100**, 4231–4241.

Berner, E.K. & Berner, A.K. (1996). *Global environments*. Prentice Hall.

Berner, R.A. (1995). Chemical weathering and its effect on atmospheric CO_2 and climate. In A.F. White & S.L. Brantley, eds., *Chemical weathering rates of silicate minerals, Reviews in Mineralogy 31*, 565–583, Mineral. Soc. Am.

Bésuelle, P., Desrues, J. & Raynard, S. (2000). Experimental characterisation of the localisation phenomenon inside a Vosges sandstone in a triaxial cell. *Int. J. Rock Mech. Min. Sci.*, **37**, 1223–1237.

Bevan, J. & Savage, D. (1989). The effect of organic acids on the dissolution of K-feldspar under conditions relevant to burial diagenesis. *Mineralogical magazine*, **53**, 415–425.

Bieniawski, Z.T. (1966). Mechanism of brittle fracture of rock. CSIR Report RMEG 580, Pretoria.

Bjørkum, P.A. (1996). How important is pressure solution in causing dissolution of quartz in sandstones? *J. Sediment. Res.*, **66**, 147–154.

Bjørlykke, K. (1999). An overview of factors controlling rate of compaction, fluid generation and flow in sedimentary basins. In B. Jamtveit & P. Meakin, eds., *Growth, dissolution and pattern formation in geosystems*, 381–404, Kluwer Acad. Pub., Dordrecht, The Netherlands.

Blacid, J.D., Halleck, P.H., D'Onfro, P. & Riecker, R.E. (1981). Thermomechanical properties of Galesville sandstone. In N.L. Carter, M. Friedman, J.M. Logan & D.W. Stearns, eds., *Mechanical behaviour of crustal rocks*, vol. 24 of *Geophysical monograph series*, 153–159, American Geophysical Union, Washington D. C.

Blum, A.E., Yund, R.A. & Lasaga, A.C. (1988). The effect of dislocation density on the aqueous dissolution rate of quartz. *Geol. Soc. Am. Abstr. Prog.*, **20**, 290.

Bonnet, E., Bour, O., Odling, N.E., Davy, P., Main, I., Cowie, P. & Berkowitz, B. (2001). Scaling of fracture systems in geological media. *Rev. Geophysics*, **39**, 347–383.

Boozer, G.D., Hiller, K.H. & Serdengecti, S. (1963). Effects of pore fluid on the deformation behaviour of rocks subjected to triaxial compression. In C. Fairhurst, ed., *Rock Mechanics*, 579–624, 5th Symp. Rock Mechanics, Pergamon press, Oxford.

Bourbie, T. & Zinszner, B. (1985). Hydraulic and acoustic properties as a function of porosity in Fontainebleau sandstone. *J. Geophys. Res.*, **90**, 11,524–11,532.

Brace, W.F. (1980). Permeability of crystalline and argillaceous rocks. *Int. J. Rock Mech Min. Sci and Geomech Abstr.*, **17**, 241–251.

Brace, W.F. & Bombolakis, E.G. (1963). A note on brittle crack growth in compression. *J. Geophys. Res.*, **68**, 3709–3713.

Brace, W.F., Paulding, B.W. & Scholz, C.H. (1966). Dilatancy in the fracture of crystalline rocks. *J. Geophys. Res.*, **71**, 3939–3953.

Brady, P.V. & Walther, J.V. (1990). Kinetics of quartz dissolution at low temperatures. *Chemical Geology*, **82**, 253–264.

Brantley, S.L., Crane, S.R., Crerar, D.A., Hellman, R. & Stallard, R. (1986). Dissolution and dislocation etch pits in quartz. *Geochim. Cosmochim. Acta*, **50**, 2349–2361.

Brantley, S.L., Evans, B., Hickman, S.H. & Crerar, D.A. (1990). Healing of microcracks in quartz: Implications for fluid flow. *Geology*, **18**, 136–139.

Brunauer, S., Emmett, P.H. & Teller, E. (1938). Adsorption of gases in multimolecular layers. *J. Am. Chem. Soc.*, **60**, 309–319.

Bruner, W.M. (1976). Comment on 'Seismic velocities in dry and saturated cracked solids' by Richard J. O'Connell and Bernard Budiansky. *J. Geophys. Res.*, **81**, 2573–2578.

Budd, S.M. (1961). The mechanisms of chemical reaction between silicate glass and attacking agents. *Phys. Chem. Glasses*, **2**, 111–114.

Carman, P.C. (1956). *Flow of gases through porous media*. Butterworths, London.

Carroll, S.A., Maxwell, R.M., Bourcier, W., Martin, S. & Hulsey, S. (2002). Evaluation of silica-water surface chemistry using NMR spectroscopy. *Geochim. Cosmochim. Acta*, **66**, 913–926.

Casey, W.H. (1987). Heterogeneous kinetics and diffusion boundary layers: the example reaction in a fracture. *J. Geophys. Res.*, **92**, 8007–8013.

Chalmers, A.F. (1982). *What is this thing called science?*. Open University press, Milton Keynes.

Chang, C. & Haimson, B.C. (2000). True triaxial strength and deformability of the ktb deep hole amphibolite. *J. Geophys. Res.*, **105**, 18999–19013.

Charles, R.J. (1958). Static fatigue of glass. *J. Appl. Phys.*, **29**, 1549–1560.

Charles, R.J. & Hillig, W.B. (1962). Kinetics of glass failure of stress corrosion. In *Symposium sur la Résistance Mécanique du Verre et les Moyens de l'Ameliorer*, 511–527, Union Scientifique Continentale du Verre, Charleroi, Belgium.

Chelidze, T. (1982). Percolation and fracture. *Phys. Earth Planet. Int.*, **28**, 93–101.

Clennell, M.B. (1997). Tortuosity: a guide through the maze. In M.A. Lovell & P.K. Harvey, eds., *Developments in petrophysics*, vol. 122 of *Special Publications*, 299–344, Geological Society, London.

Cook, N.G.W. (1981). Stiff testing machines, stick slip sliding and the stability of rock deformation. In N.L. Carter, M. Friedman, J.M. Logan & D.W. Stearns, eds., *Mechanical behaviour of crustal rocks*, Geophysical monograph series, 93–102, American Geophysical Union, Washington D. C., 24th edn.

Costin, L.S. (1987). Time-dependent deformation and failure. In B.K. Atkinson, ed., *Fracture mechanics of rock*, 167–215, Academic press, London.

Coulomb, C.A. (1773). Sur une application des règles de Maximis et Minimis a quelques problèmes de statique relatifs à l'Architecture. *Acad. Roy. des Sciences Memoires de math. et physique par divers savants*, **7**, 343–382.

Cox, S.J. & Meredith, P.G. (1993). Microcrack formation and material softening in rock measured by monitoring acoustic emissions. *Int. J. Rock Mech. Min. Sci. and Geomech Abstr.*, **30**, 11–24.

Crampin, S., Chesnokov, E.M. & Hipkin, R.G. (1984). Seismic anisotropy - the state of the art II. *Geophys. J. R. Ast. Soc.*, **76**, 1–16.

Crawford, B.R. (1998). Experimental shear band permeability dependency on cataclastic fault gouge characteristics. In M.P. Coward, T.S. Daltaban & H. Johnson, eds., *Structural geology in reservoir characterization*, vol. 127 of *Special Publications*, 27–47, Geological Society, London.

Crawford, B.R., Smart, B.G.D., Main, I.G. & Liakopoulou-Morris, F. (1995). Strength characteristics and shear acoustic anisotropy of rock core subjected to true triaxial compression. *Int. J. Rock Mech. Min. Sci. and Geomech. Abstr.*, **32**, 189–200.

Creamer, F.H. & Kisslinger, C. (1993). The relation betwen temperature and the Omori decay parameter for aftershock sequences near Japan. *EOS*, **74**, No. 43, supplement 417.

Dana, J.D. (1884). On the decay of quartzyte, and the formation of sand, kaolin and crystallized quartz. *American J. Sci.*, **28**, 448–452.

Darcy, H. (1856). *Les fontaines publiques de la ville de Dijon*. Dalmont, Paris.

Darot, M. & Guéguen, Y. (1986). Slow crack growth in minerals and rocks: Theory and experiments. *Pageoph.*, **124**, 677–692.

Das, S. & Scholz, C.H. (1981). Theory of time-dependent rupture in the Earth. *J. Geophys. Res.*, **86**, 6039–6051.

David, C., Wong, T.F., Zhu, W. & Zhang, J. (1994). Laboratory measurements of compaction-induced permeability change in porous rocks: implications for the generation and maintenance of pore pressure excess in the crust. *Pure Appl. Geophys.*, **143**, 425–456.

De Vore, G.W. (1956). Surface chemistry as a chemical control on mineral association. *J. Geol.*, **64**, 31.

De With, G. (2002). Environment induced failure of brittle and quasi-brittle materials. *Materials chemistry and physics*, **75**, 229–234.

Dewers, T. & Hajash, A. (1995). Rate laws for water-assisted compaction and stress-induced water rock interaction in sandstones. *J. Geophys. Res.*, **100**, 13093–13112.

Dove, P.M. (1994). The dissolution kinetics of quartz in sodium chloride solutions at 25 to 300 ° C. *Am. J. Sci.*, **294**, 665–712.

Dove, P.M. (1995). Geochemical controls on the kinetics of quartz fracture at subcritical tensile stresses. *J. Geophys. Res.*, **100**, 22349–22359.

Dove, P.M. (1999). The dissolution kinetics of quartz in aqueous mixed cation solutions. *Geochim. Cosmochim. Acta*, **63**, 3715–3727.

Dove, P.M. & Crerar, D.A. (1990). Kinetics of quartz dissolution in electrolyte solutions using a hydrothermal mixed flow reactor. *Geochim. Cosmochim. Acta*, **54**, 955–969.

Dove, P.M. & Elston, S.F. (1992). Dissolution kinetics of quartz in sodium chloride solutions: Analysis of existinf data and a rate model for 25∘C. *Geochim. Cosmochim. Acta*, **61**, 3329–3340.

Dove, P.M. & Nix, C.J. (1997). The influence of alkaline earth cations, magnesium, calcium and barium ion dissolution kinetics of quartz. *Geochim. Cosmochim. Acta*, **61**, 3329–3340.

Dove, P.M. & Rimstidt, J.D. (1994). Silica-water interactions. In P.J. Heaney, C.T. Prewitt & C.V. Gibbs, eds., *Silica - physical behaviour, geochemistry and materials applications*, vol. 29 of *Reviews in Mineralogy*, 259–308, Mineralogical society of America, Washington D. C.

Doyen, P. (1988). Permeability, conductivity and pore geometry of sandstone. *J. Geophys. Res.*, **93**, 7729–7740.

Dugdale, D.S. (1960). Yielding of steel sheets containing slits. *J. Mech. Phys. Solids*, **8**, 100–115.

Dullien, F.A.L. (1979). *Porous media: Fluid transport and pore structure*. Academic Press, New York.

Dunning, J., Douglas, B., Miller, M. & McDonald, S. (1994). The role of the chemical environment in frictional deformation: stress corrosion cracking and comminution. *Pageoph.*, **143**, 151–178.

Dunning, J.D., Lewis, W.L. & Dunn, D.E. (1980). Geomechanical weakening in the presence of surfactants. *J. Geophys. Res.*, **85**, 5344–5354.

Dunning, J.D., Petrovski, D., Schuyler, J. & Owens, A. (1984). The effects of aqueous chemical environments on crack propagation in quartz. *J. Geophys. Res.*, **89**, 4115–4123.

Elias, B.P. & Hajash, A.J. (1992). Changes in quartz solubility and porosity due to effective stress: An experimental investigation of pressure solution. *Geology*, **20**, 451–454.

Elliot, H.A. (1958). Stress rupture of glass. *J. Appl. Phys.*, **29**, 224–225.

Evans, A.G. & Graham, L.J. (1975). A model for crack propagation in polycrystalline ceramics. *Acta Metall.*, **23**, 1303–1312.

Evans, A.G. & Linzer, M. (1973). Failure prediction in structural ceramics using acoustic emission. *J. Amer. Ceram. Soc.*, **56**, 575–581.

Ewalds, H.L. & Wanhill, R.J.H. (1991). *Fracture mechanics*. Edward Arnold, London.

Fatt, I. (1956). The network model of porous media. *Transactions, American institute of mining engineers*, **207**, 144–181.

Feng, X.T., Chen, S. & Li, S. (2001). Effects of water chemistry on microcracking and compressive strength of granite. *Int. J. Rock Mech. Min. Sci.*, **38**, 557–568.

Feynman, R.P. (1963). *The Feynman lectures on physics*, vol. 1. Addison-Wesley, London.

Fischer, G.J. & Paterson, M.S. (1989). Dilatancy during rock deformation at high temperatures and pressures. *J. Geophys. Res.*, **94**, 17607–17617.

Fisher, M.J. & Mudge, D.C. (1990). Triassic. In K.W. Glennie, ed., *Introduction to the petroleum geology of the North Sea*, 191–218, Blackwell scientific publications, Oxford.

Fisher, Q.J. & Knipe, R.J. (1998). Fault sealing processes in siliclastic sediments. In G. Jones, Q.J. Fisher & R.J. Knipe, eds., *Faulting, fault sealing and fluid flow in hydrocarbon reservoirs*, vol. 147 of *Special Publications*, 117–134, Geological Society, London.

Fournier, R.O. & Potter, R.W. (1982). An equation correlating the solubility of quartz in water from 25°C to 900°C at pressures up to 10000 bars. *Geochim. Cosmochim. Acta*, **46**, 1969–1973.

Fowles, J. & Burley, S. (1994). Textural and permeability characteristics of faulted, high porosity sandstones. *Marine and petroleum geology*, **11**, 608–623.

Franklin, S.P., Hajash, A., Dewers, T.A. & Tieh, T.T. (1994). The role of carboxylic acids in albite and quartz dissolution: an experimental study under diagenetic conditions. *Geochim. Cosmochim. Acta*, **58**, 4259–4279.

Freiman, S.W. (1984). Effects of chemical environments on slow crack growth in glasses and ceramics. *J. Geophys. Res.*, **89**, 4072–4076.

Frohlich, C. & Davis, S.D. (1993). Teleseismic b values: or, much ado about 1.0. *J. Geophys. Res.*, **98**, 631–644.

Gautier, J.M., Oelkers, E.H. & Schott, J. (2001). Are quartz dissolution rates proportional to B.E.T. surface areas? *Geochim. Cosmochim. Acta*, **65**, 1059–1070.

Glover, P.W., Baud, P., Darot, M., Meredith, P.G., Boon, S.A., LeRavalec, M., Zoussi, S. & Reuschlé, T. (1995). α/β phase transition in quartz monitored using acoustic emissions. *Geophys. J. Int.*, **120**, 775–782.

Gordon, J.E. (1976). *The new science of strong materials*. Penguin, Harmondsworth.

Grady, D.E. & Kipp, M.E. (1987). Dynamic rock fragmentation. In B.K. Atkinson, ed., *Fracture mechanics of rock*, 429–475, Academic Press, London.

Grandstaff, D.E. (1978). Changes in surface area and morphology and the mechanism of forsterite dissolution. *Geochim. Cosmochim. Acta*, **42**, 1899–1901.

Gratier, J.P., Renard, F. & Labaume, P. (1999). How pressure solution creep and fracturing process interact in the brittle crust to make it behave in both brittle and viscous manner. *J. Struct. Geol.*, **21**, 1189–1197.

Gretener, P.E. (1981). Reflections on the value of laboratory tests on rocks. In N.L. Carter, M. Friedman, J.M. Logan & D.W. Stearns, eds., *Mechanical behaviour of crustal rocks*, no. 24 in Geophysical monograph series, 323–326, American Geophysical Union, Washington D. C.

Griffith, A.A. (1920). The phenomena of rupture and flow in solids. *Phil. Trans. Roy. Soc. London*, **A221**, 163–198.

Griggs, D.T. (1936). Deformation of rocks under high confining pressures. *Jour. Geol.*, **44**, 541–577.

Griggs, D.T. (1940). Experimental flow of rocks under conditions favouring recrystallization. *Geol. Soc. Am. Bull.*, **51**, 1001–1022.

Griggs, D.T. & Bell, J.F. (1938). Experiments bearing on the orientation of quartz in deformed rocks. *Geol. Soc. Am. Bull.*, **49**, 1723–1746.

Griggs, D.T. & Handin, J. (1960). Observations on fracture and a hypothesis for earthquakes. In D.T. Griggs & J. Handin, eds., *Rock deformation*, 347–364, Geol. Soc. Am. Memoir no. 79.

Grueschow, E., Kwon, O., Main, I.G. & Rudnicki, J.W. (2003). Observation and modeling of the suction pump effect during a rapid dilatant slip. *Geophys. Res. Lett.*, **30**, 1226, doi:10.1029/2002GL015905.

Guéguen, Y. & Dienes, J. (1989). Transport properties of rocks from statistics and percolation. *Mathematical Geology*, **21**, 1–13.

Guéguen, Y. & Palcianskas, V. (1994). *Introduction to the physics of rocks*. Princeton Univ. Press, Princeton, New Jersey.

Guéguen, Y., Reuschle, T. & Darot, M. (1990). Single-crack behaviour and crack statistics. In D.J. Barber & P. Meredith, eds., *Deformation processes in minerals, ceramics and rocks*, 48–71, Unwin Hyman, London.

Gutenberg, B. & Richter, C.F. (1954). *Seismicity of the earth and associated phenomena*. Princeton University press, Princeton.

Haimson, B.C. & Chang, C. (2000). A new true triaxial cell for testing mechanical properties of rock and its use to determine rock strength ad deformability of Westerly granite. *Int. J. Rock Mech. Min. Sci.*, **37**, 285–296.

Haimson, B.C. & Chang, C. (2001). Mechanical behaviour of rocks subjected to true triaxial stresses: Are Mohr-type criteria adequate? In P. Särkkä & P. Eloranta, eds., *Rock Mechanics - a challenge for society*, 83–90, Proceedings of the ISRM regional symposium eurorock, Espoo, Finland.

Hajash, A. & Bloom, M.A. (1979). Marine diagenesis of feldspathic sands: a flow-through experimental study at 200°C, 1 kbar. *Chem. Geol.*, **89**, 359–377.

Handin, J. (1966). Strength and ductility. In S.P. Clark, ed., *Handbook of physical constants*, 97, 238–289, Geol. Soc. Am. Memoir no. 97.

Handin, J. (1969). The Coulomb-Mohr failure criteria. *J. Geophys. Res.*, **74**, 5343–5348.

Heard, H.C. (1976). Comparison of the flow properties of rocks at crustal conditions. *Phil. Trans. Royal Soc. London Ser. A*, **283**, 173–186.

Heiland, J. (2000). Permeability in triaxially stressed sandstone. In *Thermo-hydro-mechanical coupling in fractured rock*, 3rd Euroconference on rock physics and rock mechanics, Bad Honnef, Germany.

Helgeson, H.C., Murphy, W.M. & Aargaard, P. (1984). Thermodynamic and kinetic constraints on reaction rates among minerals and aqueous solutions. II. Rate constants, effective surface area and the hydrolysis of feldspar. *Geochim. Cosmochim. Acta*, **48**, 2405–2432.

Helmstetter, A., Sornette, P. & Grasso, J.R. (2003). Mainshocks as aftershocks of conditional foreshocks: How do foreshock statistical properties emerge from aftershock laws. *J. Geophys. Res.*, **108**, 2046, doi:10.1029/2002JB001991.

Henderson, J.H., Syier, J.K. & Jackson, M.L. (1970). Quartz dissolution as influenced by pH and the presence of disturbed surface layer. *Israel J. Chem.*, **8**, 357–372.

Hickman, S., Sibson, R. & Bruhn, R. (1995). Introduction to special section: Mechanical involvement of fluids in faulting. *J. Geophys. Res.*, **100**, 12831–12840.

Hillig, W.S. & Charles, R.J. (1965). Surfaces, strain-dependent reactions and strength. In V.F. Zachey, ed., *High strength materials*, 682–705, John Wiley, New York.

Hirata, T. (1987). Omori's power law aftershock sequences of microfracturing in rock fracture experiment. *J. Geophys. Res.*, **92**, 6215–6221.

Hirata, T., Satoh, T. & Ito, K. (1987). Fractal structure of spatial distribution of microfracturing in rock. *Geophys. J. R Astr. Soc.*, **90**, 369–374.

Hirschwald, J. (1912). *Handbuch der bautechnischen Gesteinsprufung*. Gebr. Borntraeger, Berlin.

Holder, J., Olson, J.E. & Philip, Z. (2001). Experimental determination of subcritical crack growth parameters in sedimentary rock. *Geophys. Res. Lett.*, **28**, 599–602.

Holdren, G.R. & Berner, J.R. (1979). Mechanism of feldspar weathering, I. experimental studies. *Geochim. Cosmochim. Acta*, **43**, 1161–1171.

Holdren, G.R. & Speyer, P.M. (1987). Reaction rate-surface area relationships during the early stages of weathering II. Data on eight additional feldspars. *Geochim. Cosmochim. Acta*, **51**, 2311–2318.

Hurd, D.C. (1973). Interactions of biogenic opal sediment and seawater in the central equatorial Pacific. *Geochim. Cosmochim. Acta*, **37**, 2257–2282.

Icenhower, J.P. & Dove, P.M. (2000). The dissolution kinetics of amorphous silica into sodium chloride solutions: Effects of temperature and ionic strength. *Geochim. Cosmochim. Acta*, **64**, 4193–4203.

Igarashi, G., Saeki, S., Takahita, N., Sumikawa, K., Tasaka, S., Sasaki, Y., Takahashi, M. & Sano, Y. (1995). Ground-water radon anomaly before the Kobe earthquake in Japan. *Science*, **269**, 60–61.

Inglis, C.E. (1913). Stresses in a plate due to the presence of cracks and sharp corners. *Trans. Inst. Naval Archit.*, **55**, 219.

Irwin, G.R. (1958). Fracture. In S. Flügge, ed., *Handbuch der Physik*, vol. 6, 551–590, Springer-Verlag, Berlin.

Jaeger, J.C. & Cook, N.G.W. (1976). *Fundamentals of rock mechanics*. Chapman and Hall, London.

John, M. (1972). The influence of loading rate on the mechanical properties and fracture processes in rock. *CSIR Rep. ME*, **1115**.

Jones, A., Duck, R., Reed, R. & Weyers, J. (2000). *Practical skills in environmental science*. Prentice Hall, England.

Kamiya, H. & Shimokata, K. (1976). The role of salts in the dissolution of powdered quartz. In J. Cadek & T. Păces, eds., *Proceedings of the international symposium on water-rock interaction*, Czechoslovakian geological survey, Prague.

Kanamori, H. & Anderson, D.L. (1975). Theoretical basis of some empirical relations in seismology. *Bull. Seism. Soc. Am.*, **65**, 1073–1095.

Kay, M. (2001). *Physico-chemical mechanisms of fault sealing: an experimental study*. Ph.D. thesis, University if Edinburgh.

Kemeny, J.M. & Cook, N.G.W. (1987). Crack models for the failure of rocks in compression. In *Proc 2nd Int. Conf. on Constitutive laws for Engineering Materials*, 879–887, Tucson, AZ.

Kieffer, B., Jove, C.F., Oelkers, E.H. & Schott, J. (1999). An experimental study of the reactive surface area of the Fontainebleau sandstone as a function of porosity, permeability and fluid flow rate. *Geochim. Cosmochim. Acta*, **63**, 3525–3534.

King, C.Y., Koizumi, N. & Kitagawa, Y. (1995). Hydrogeological anomalies and the 1995 Kobe earthquake. *Science*, **269**, 38–39.

Kirby, S.H. (1984). Introduction and digest to the special issue on chemical effects of water on the deformation and strengths of rocks. *J. Geophys. Res.*, **89**, 3991–3995.

Knauss, K.G. & Wolery, T.J. (1988). The dissolution kinetics of quart as a function of pH and time at 70 °C. *Geochim. Cosmochim. Acta*, **52**, 43–53.

Knott, J.F. (1973). *Fundamentals of fracture mechanics*. Butterworths, London.

Kranz, R.L. (1979). Crack growth and development during creep of Barre granite. *Int. J. Rock Mech. Min. Sci. Geomech. Abs.*, **16**, 23–35.

Kranz, R.L. (1983). Microcracks in rocks: a review. *Tectonophysics*, **100**, 449–480.

Krausz, A.S. (1978). The deformation and fracture kinetics of stress corrosion cracking. *Int. J. Fracture*, **14**, 5–15.

Krausz, A.S. & Eyring, H. (1975). *Deformation kinetics*. Wiley-Interscience, New York.

Kronenberg, A.K. (1994). Hydrogen speciation and chemical weakening of quartz. In P.J. Heaney, C.T. Prewitt & C.V. Gibbs, eds., *Silica - physical behaviour, geochemistry and materials applications*, 123–175, Mineralogical society of America, Washington D. C.

Kusunose, K. (1995). Fracture mechanics of rocks. *J. Phys. Earth*, **43**, 479–504.

Labuz, J.F., Shah, S.P. & Dowding, C.H. (1985). Experimental analysis of crack propagation in granite. *Int. J. Rock Mech. Min. Sci and Geomech. Abstr.*, **22**, 85–98.

Lankford, J. (1981). The role of tensile microfracture on the strain rate dependence of compressive strength of fine-grained limestone - analogy with strong ceramics. *Int. J. Rock Mech. Min. Sci & Geomech Abstr.*, **18**, 173–175.

Lasaga, A.C. (1981). Transition state theory. In A.C. Lasaga & R.J. Kirkpatrick, eds., *Kinetics of geochemical processes*, vol. 8 of *Reviews in Mineralogy*, 135–139, Mineralogical Society of America, Washington D. C.

Lasaga, A.C. (1984). Chemical kinetics of water-rock reactions. *J. Geophys. Res.*, **89**, 4009–4025.

Lasaga, A.C. (1990). Atomic treatment of mineral-water surface reactions. In M.F. Hochella & A.F. White, eds., *Mineral-water interface chemistry*, vol. 23, 17–85, Mineralogical society of America, Washington D. C., reviews in mineralogy edn.

Lasaga, A.C. & Blum, A.E. (1986). Surface chemistry, etch pits and mineral-water reactions. *Geochim. Cosmochim. Acta*, **50**, 2363–2379.

Lawn, B. (1993). *Fracture of brittle solids*. Cambridge University Press, Cambridge, 2nd edn.

Lawn, B.R., Roach, D.H. & Thomson, R.M. (1987). Thresholds and reversibility of brittle cracks: an atomistic surface model. *J. Mater. Sci.*, **22**, 4036.

Lee, M.R., Hodson, M.E. & Parsons, I. (1998). The role of intragranular microtextures and microstructures in chemical and mechanical weathering: Direct comparison of experimentally and naturally weathered alkali feldspars. *Geochim. Cosmichim. Acta*, **62**, 2771–2788.

Lei, X., Kusunose, K., Rao, M.V.M.S., Nishizawa, O. & Satoh, T. (2000). Quasi-static fault growth and cracking in homogeneous brittle rock under triaxial compression using acoustic emission monitoring. *J. Geophys. Res.*, **105**, 6127–6139.

Liakopoulou-Morris, F., Main, I.G., Crawford, B.R. & Smart, B.G.D. (1994). Microseismic properties of a homogeneous sandstone during fault nucleation and frictional sliding. *Geophys. J. Int.*, **119**, 219–230.

Lockner, D. & Byerlee, J. (1977). Acoustic emission and creep in rock at high confining pressure and differential stress. *Bull. Seism. Soc. Am.*, **67**, 247–258.

Lockner, D.A. (1993a). The role of acoustic emission in the study of rock fracture. *Int. J. Rock Mech. Min. Sci. Geomech. Abs.*, **30**, 883–899.

Lockner, D.A. (1993b). Room temperature creep in saturated granite. *J. Geophys. Res.*, **98**, 475–487.

Lockner, D.A. & Byerlee, J.D. (1993). How geometrical constraints contribute to the weakness of mature faults. *Nature*, **363**, 250–252.

Lockner, D.A., Byerlee, J.D., Kuksenko, J.D., Ponomarev, V. & Sidorin, A. (1991). Quasi-static fault growth and shear fracture energy in granite. *Nature*, **350**, 39–42.

Lovell, J.P.B. (1983). Permian and Triassic. In G.Y. Graig, ed., *Geology of Scotland*, 325–342, Scottish academic press, Edinburgh.

Main, I. (2000). A damage mechanics model for power law creep and earthquake aftershock and foreshock sequences. *Geophys. J. Int.*, **142**, 151–161.

Main, I.G. (1988). Prediction of failure times in the earth for a time-varying stress. *Geophys. J.*, **92**, 455–464.

Main, I.G. (1991). A modified Griffith criterion for the evolution of damage with a fractal distribution of crack lengths: application to seismic event rates and b-values. *Geophys. J. Int.*, **107**, 353–362.

Main, I.G. (1999). Applicability of time-to-failure analysis to accelerated strain before earthquakes and volcanic eruptions. *Geophys. J. Int.*, **139**, F1–F6.

Main, I.G. & Meredith, P.G. (1991). Stress corrosion constitutive laws as a possible mechanism for intermediate-term and short-term seismic quiescence. *Geophys. J. Int.*, **107**, 363–372.

Main, I.G., Meredith, P.G. & Jones, C. (1989). A reinterpretation of the precursory seismic b-value anomaly from fracture mechanics. *Geophys. J.*, **96**, 131–138.

Main, I.G., Meredith, P.G. & Sammonds, P.R. (1992). Temporal variations in seismic event rate and b-values from stress corrosion constitutive laws. *Tectonophysics*, **211**, 233–246.

Main, I.G., Sammonds, P.R. & Meredith, P.G. (1993). Application of a modified Griffith criterion to the evolution of fractal damage during compressional rock failure. *Geophys. J. Int.*, **115**, 367–380.

Main, I.G., Smart, B.G.D., Shimmield, G.B., Elphick, S.C., Crawford, B.R. & Ngwenya, B.T. (1994). The effects of combined changes in pore fluid chemistry and stress state on permeability in reservoir rocks: Preliminary results from analogue materials. In *North Sea oil and gas resevoirs III*, 357–370, Kluwer Acad., Norwell, Mass.

Main, I.G., Kwon, O., Ngwenya, B.T. & Elphick, S.C. (2000). Fault sealing during deformation-band growth in porous sandstone. *Geology*, **28**, 1131–1134.

Mair, K. (1997). *Experimental studies of fault zone development in a porous sandstone*. Ph.D. thesis, University of Edinburgh.

Mair, K., Main, I. & Elphick, S. (2000). Sequential growth of deformation bands in the laboratory. *J. Struct. Geology*, **22**, 25–42.

Marone, C., Rubenstone, J. & Engelder, T. (1988). An experimental study of permeability and fluid chemistry in an artificially jointed marble. *J. Geophys. Res.*, **93**, 13763–13775.

Martin, R.J. (1972). Time-dependent crack growth in quartz and its application to the creep of rocks. *J. Geophys. Res.*, **77**, 1406–1419.

Martin, R.J. & Durham, W.B. (1975). Mechanisms of crack growth in quartz. *J. Geophys. Res.*, **80**, 4837–4844.

Masuda, K. (2001). Effects of water on rock strength in a brittle regime. *J. Struct. Geology*, **23**, 1653–1657.

Meredith, P.G. (1990). Fracture and failure of brittle polycrystals: an overview. In D.J. Barber & P. Meredith, eds., *Deformation processes in minerals, ceramics and rocks*, 5–47, Unwin Hyman, London.

Meredith, P.G. & Atkinson, B.K. (1982). High temperature tensile crack propagation in quartz: experimental results and application to time-dependent earthquake rupture. *Earthquake Pred. Res.*, **1**, 377–391.

Meredith, P.G. & Atkinson, B.K. (1983). Stress corrosion and acoustic emission during tensile crack propagation in Whin Sill dolerite and other basic rocks. *Geophys. J. R. astr. Soc.*, **75**, 1–21.

Meredith, P.G., Main, I.G. & Jones, C. (1990). Temporal variations in seismicity during quasi-static and dynamic rock failure. *Tectonophysics*, **175**, 249–268.

Michaelske, T.A. (1983). Crack arrest in glass: the blunt truth. *Frac. Mech. ceram.*, **V**, 277–289.

Michaelske, T.A. & Freiman, S.W. (1982). A molecular interpretation of stress corrosion in silica. *Nature*, **295**, 511–512.

Mikumo, T. & Miyatake, T. (1979). Earthquake sequences in a frictional fault model with non-uniform strengths and relaxation times. *Geophys. J. Royal Astron. Soc.*, **59**, 497–522.

Miller, M.E. & Dunning, J.D. (1985). Evidence for a coordinated attack of H, OH in water weakening of quartz. *Eos Trans. AGU*, **66**, 1065.

Miretzky, P., Conzonno, V. & Cirelli, A.F. (2001). Geochemical processes controlling silica concentrations in groundwaters of the Salado River drainage basin, Argentina. *J. Geochem. Exploration*, **73**, 155–166.

Mizutani, H., Spetzler, H., Getting, I., III, R.J.M. & Soga, N. (1977). The effect of outgassing upon the closure of cracks and the strength of lunar analogues. *Proc. Lunar Sci. Conf.*, **8**, 1235–1248.

Mogi, K. (1959). Experimental study of deformation and fracture of marble. I. On the fluctuation of compressive strength of marble and the relation to the rate of stress application. *Bull. Earthquake Res. Inst. Tokyo Univ.*, **37**, 155–170.

Mogi, K. (1962). Study of elastic shocks caused by the fracture of heterogeneous materials and its relation to earthquake phenomena. *Bull. Earthquake Research Institute Tokyo Univ.*, **40**, 125–173.

Mogi, K. (1967). Earthquakes and fractures. *Tectonophysics*, **5**, 35–55.

Mogi, K. (1972). Fracture and flow of rocks. *Tectonophysics*, **13**, 541–568.

Moore, D.E. & Lockner, D.A. (1995). The role of microcracking in shear-fracture propagation in granite. *J. Struct. Geol.*, **17**, 95–114.

Moore, D.E., Morrow, C.A. & Byerlee, J.D. (1983). Chemical reactions accompanying fluid flow in granite held in a temperature gradient. *Geochim. Cosmochim. Acta*, **47**, 445–453.

Mordecai, M. & Morris, L.H. (1971). An investigation into the changes of permeability in a sandstone when failed under triaxial stress conditions. In *Proc. U. S. Rock Mech. Symp.*, 221–239.

Morrow, C.A., Moore, D.E. & Lockner, D.A. (2001). Permeability reduction granite under hydrothermal conditions. *J. Geophys. Res.*, **106**, 30551–30560.

Murrell, S.A.F. (1965). The effect of triaxial stress systems on the strength of rocks at atmospheric temperatures. *Geophys. J. R. Astr. Soc.*, **10**, 231–281.

Murrell, S.A.F. (1990). Brittle-to-ductile transitions in polycrystalline non-metallic materials. In D.J. Barber & P.G. Meredith, eds., *Deformation processes in minerals, ceramics and rocks*, 109–137, Unwin Hyman, London.

Narteau, C., Shebalin, P., Hainzl, S., Zöller, G. & Holschneider, M. (2003). Emergence of a band-limited power law in the aftershock decay rate of a slider-block model. *Geophys. Res. Lett.*, **30**, 1568, doi:10.1029/2003GL017110.

Newman, K. & Newman, J.B. (1969). Failure theories and design criteria for plain concrete. In *Proceedingd of the international conference on structure, solid mechanics and engineering design in civil engineering*, Southampton University.

Ngwenya, B.T., Elphick, S.C. & Shimmield, G.B. (1995). Reservoir sensitivity to water flooding: an experimental study of seawater injection in a North Sea reservoir analog. *AAPG Bulletin*, **79**, 285–304.

Ngwenya, B.T., Elphick, S.C., Main, I.G. & Shimmield, G.B. (2000). Experimental constraints on the diagenetic self-sealing capacity of faults in high porosity rocks. *Earth Planet. Sci. Lett.*, **183**, 187–199.

Ngwenya, B.T., Kwon, O., Elphick, S.C. & Main, I.G. (2003). Permeability evolution during progressive development of deformation bands in porous sandstones. *J. Geophys. Res.*, **108**, 2343, doi:10.1029/2002JB001854.

Obert, L. & Duvall, W. (1942). Use of subaudible noises for the prediction of rock bursts, Part II. *U.S. Bur. Mines Report 3654*.

Obreimoff, J.W. (1930). The splitting strength of mica. *Proc. Roy. Soc. London*, **A127**, 290–302.

O'Day, P.A., Chisholm-Brause, C.J., Towle, S.N., Parks, G.A. & Jr., G.E.B. (1996). X-ray adsorption spectroscopy of Co(II) sorption complexes on quartz (α-$Si0_2$) and rutile (TiO_2). *Geochim. Cosmochim. Acta*, **61**, 2515–2532.

Ogasawara, H. (1990). Comparison of aftershocks of earthquakes and AE that occurs after turning out gas stove and so on. In *Progress in Acoustic emission, Proceedings of the 10th international Acoustic Emission Symposium*, 266–272, The Japanese Society for NDI, Sendai, Japan.

Ogata, Y. (2001). Increased probability of large earthquakes near aftershock regions with relative quiescence. *J. Geophys. Res.*, **106**, 8729–8744.

Ogata, Y., Jones, L.M. & Toda, S. (2003). When and where the aftershock activity was depressed: Constrasting decay patterns of the proximate large earthquakes in Southern California. *J. Geophys. Res.*, **108**, 2318, doi:10.1029/2002JB002009.

Ohnaka, M. & Mogi, K. (1982). Frequency characteristics of acoustic emission in rocks under uniaxial compression and its relation to the fracturing process to failure. *J. Geophys. Res.*, **87**, 3873–3884.

Ojala, I.O., Ngwenya, B.T., Main, I.G. & Elphick, S.C. (2003). Correlation of microseismic and chemical properties of brittle deformation in Locharbriggs sandstone. *J. Geophys. Res.*, **108**, 2268, doi:10.1029/2002JB002277.

Ojala, I.O., Ngwenya, B.T. & Main, I.G. (2004). Loading rate dependence of permeability evolution in porous aeolian sandstones. *J. Geophys. Res.*, **109**, B01204, doi:10.1029/2002JB002347.

Orowan, E. (1944). The fatigue of glass under stress. *Nature*, **154**, 341–343.

Ovid (1990). *P. Ovidi Nasonis ex Ponto libri quattuor*. Teubner, Leipzig.

Parks, G.A. (1984). Surface and interfacial free energies of quartz. *J. Geophys. Res.*, **89**, 3997–4008.

Paterson, M.S. (1978). *Experimental rock deformation - the brittle field*. Springer Verlag, New York.

Paterson, M.S. (1983). The equivalent channel model for permeability and resistivity development in synthetic salt rock: A reappraisal. *Mech. Mat.*, **2**, 345–352.

Paul, B. & Gangal, M. (1967). Initial and subsequent fracture curves for biaxial compression of brittle materials. In C. Fairhurst, ed., *Failure and breakage of rock*, 113–141, Proc. Eight Symposium on Rock Mechanics, University of Minnesota.

Peng, S.S. (1973). Time-dependent aspects of rock deformation as measured by a servo controlled hydraulic testing machine. *Int. J. Rock Mech. Min. Sci.*, **10**, 235–246.

Pollock, A.A. (1989). Acoustic emission inspection. In *Metals handbook*, vol. 17, 278–294, ASM international, 9th edn.

Popp, T., Kern, H. & Schulze, O. (2001). Evolution of dilatancy and permeability in rock salt during hydrostatic compaction and triaxial deformation. *J. Geophys. Res.*, **106**, 4061–4078.

Quattrocchi, F. & Calcara, M. (1998). Test sites for earthquake prediction experiments within the Colli Albani region. *Phys. Chem. Earth*, **23**, 915–920.

Rao, M.V.M.S. & Kusunose, K. (1995). Failure zone development in andesite as observed from acoustic emission locations and velocity changes. *Phys. Earth Planet. Int.*, **88**, 131–143.

Renard, F., Gratier, J.P. & Jamtveit, B. (2000). Kinetics of crack sealing, intergranular pressure solution and compaction around active faults. *J. Struct. Geol.*, **22**, 1395–1407.

Renshaw, C.E. & Pollard, D.D. (1994). Numerical simulation of fracture set formation: A fracture mechanics model consistent with experimental observations. *J. Geophys. Res.*, **99**, 9359–9372.

Reuschlé, T. (1990). Slow crack growth and aftershock sequences. *Geophys. Res. Lett.*, **17**, 1525–1528.

Reuschlé, T., Darot, M. & Guéguen, Y. (1989). Mechanical and transport properties of crustal rocks: from single cracks to crack statistics. *Phys. Earth Planet. Int.*, **55**, 353–360.

Rice, J.D. (1992). Fault stress states, pore pressure and the weakness of the San Andreas fault. In B. Evans & T.F. Wong, eds., *Fault mechanics and transport properties of rocks*, 475–504, Academic Press.

Rice, J.R. (1978). Thermodynamics of the quasi-static growth of Griffith cracks. *J. Mech. Phys. Solids*, **26**, 61–78.

Rimstidt, J.D. & Barnes, H.L. (1980). The kinetics of silica-water interactions. *Geochim. Cosmochim. Acta*, **44**, 1683–1699.

Robertson, E.C. (1955). Experimental study of the strength of rocks. *Bull. Geol. Soc. Am.*, **66**, 1275–1314.

Rojstaczer, S., Wolf, S. & Michel, R. (1995). Permeability enhancement in the shallow crust as a cause of earthquake induced hydrological changes. *Nature*, **373**, 237–239.

Rose, A.W. & Burt, D.M. (1979). Hydrothermal alteration. In H.L. Barnes, ed., *geochemistry of hydrothermal ore deposits*, 173–235, John Wiley and Sons, 2nd edn.

Rudnicki, J. & Chen, C.H. (1988). Stabilization of rapid frictional slip on a weakening fault by dilatant hardening. *J. Geophys. Res.*, **93**, 4745–4757.

Sammonds, P., Meredith, P., Gomez, J. & Main, I. (1994). The interaction between pore fluid pressure changes and crack damage evolution in rocks and subsurface rock structures modelled from acoustic emission data. In T. Kishi, Y. Mori & M. Enoki, eds., *Progress in Acoustic emission*, 249–254, Proceedings of the 12th International acoustic emission symposium, The Japanese society for non-destructive inspection, Sapporo, Japan.

Sammonds, P.R., Meredith, P.G. & Main, I.G. (1992). Role of pore fluids in the generation of seismic precursors to shear fracture. *Nature*, **359**, 228–230.

Sangha, C.M. & Dhir, R.K. (1972). Influence of time to the strength, deformation and fracture properties of a lower Devonian sandstone. *Int. J. Rock Mech Min. Sci. and Geomech. Abstr.*, **9**, 343–354.

Sangha, C.M. & Dhir, R.K. (1975). Strength and deformation of rock subject to multiaxial compressive stresses. *Int. J. Rock Mech. Min. Sci.*, **12**, 277–282.

Sano, O., Ito, I. & Terada, M. (1981). Influence of strain rate on dilatancy and strength of Oshima granite under uniaxial compression. *J. Geophys. Res.*, **86**, 9299–9311.

Sano, O., Terada, M. & Ehara, S. (1982). A study of the time-dependent microfracturing and strength of Oshima granite. *Tectonophysics*, **84**, 343–362.

Satake, H., Murata, M. & Hayashi, H. (2003). Chemical characteristics of groundwater around the Mozumi-Sukenobu fault zone and the implications for fault activity. *Geophys. Res. Lett.*, **30**, 1356, doi:10.1029/2002GL015239.

Satoh, T., Shivakumar, K., Nishizawa, O. & Kusunose, K. (1996). Precursory localization and development of microfractures along the ultimate fracture plane in amphibolite under triaxial creep. *Geophys. Res. Lett.*, **23**, 865–868.

Sausse, J., Jacquot, E., Fritz, B., Leroy, J. & Lespinasse, M. (2001). Evolution of crack permeability during fluid-rock interaction: Example of the Brézouard granite (Vosges, France). *Tectonophysics*, **336**, 199–214.

Scheidegger, A.E. (1974). *The physics of flow through porous media*. University of Toronto press, Toronto.

Schlegel, M.L., Nagy, K.L., Fentier, P. & Sturcio, N.C. (2002). Structures of quartz $(10\bar{1}0)$- and $(10\bar{1}1)$ -water interfaces determined by X-ray reflectivity and atomic force microscopy of natural growth surfaces. *Geochim. Cosmochim. Acta*, **66**, 3037–3054.

Scholz, C.H. (1968a). Experimental study of the fracturing process in brittle rock. *J. Geophys. Res.*, **73**, 1447–1454.

Scholz, C.H. (1968b). Microfractures, aftershocks and seismicity. *Bull. Seism. Soc. Am.*, **58**, 1117–1130.

Scholz, C.H. (1968c). Microfracturing and the inelastic deformation of rock in compression. *J. Geophys. Res.*, **73**, 1417–1432.

Scholz, C.H. (1972). Static fatigue of quartz. *J. Geophys. Res.*, **77**, 2104–2114.

Scholz, C.H. (1990). *The mechanics of earthquakes and faulting*. Cambridge University Press, Cambridge.

Scholz, C.H. (2000). Evidence for a strong San Andreas fault. *Geology*, **28**, 163–166.

Scholz, C.H., Sykes, L.R. & Aggarwal, Y.P. (1973). Earthquake prediction: a physical basis. *Science*, **181**, 803–810.

Scholz, C.H., Léger, A. & Karner, S.L. (1995). Experimental diagenesis: Exploratory results. *Geophys. Res. Lett.*, **22**, 719–722.

Schott, J., Berner, R.A. & Sjoberg, E.L. (1981). Mechanism of pyroxene and amphibole weathering. 1. Experimental studies of iron-free minerals. *Geochim. Cosmochim. Acta*, **45**, 2123–2135.

Schultz, M.S. & White, A.F. (1999). Chemical weathering in a tropical watershed: Luquillo mountains, Puerto Rico II: Quartz dissolution rates. *Geochim. Cosmochim. Acta*, **63**, 337–350.

Schultz, R.A. (2000). Growth of geologic fractures into large-strain populations: review of nomenclature, subcritical crack growth and some implications for rock engineering. *Int. J. Rock Mech. Min. Sci.*, **37**, 403–411.

Schwartzentruber, J., Furst, W. & Renon, H. (1987). Dissolution of quartz into dilute alkaline solutions at 90 °C. *Geochim. Cosmochim. Acta*, **51**, 1867–1874.

Scott, D.R., Marone, C.J. & Sammis, C.G. (1994). The apparent friction of granular fault gouge in sheared layers. *J. Geophys. Res.*, **99**, 7231–7246.

Seeburger, D.A. & Nur, A. (1984). A pore space model for rock permeability and bulk modulus. *J. Geophys. Res.*, **89**, 527–536.

Segall, P. (1984). Rate dependent extensional deformation resulting from crack growth in rock. *J. Geophys. Res.*, **89**, 4185–4195.

Serdengecti, S. & Boozer, G.D. (1961). The effects of strain rate and temperature on the behavior of rocks subjected to triaxial compression. In *Proceedings of the Fourth Symposium on rock mechanics*, 83–97.

Serebrinsky, S.A., Duffo, G.S. & Galvele, J.R. (1999). Effect of strain rate on stress corrosion crack velocity: difference between intergranular and transgranular cracking. *Corrosion science*, **41**, 191–195.

Shah, K.R. & Labuz, J.F. (1995). Damage mechanisms in stressed rock from acoustic emission. *J. Geophys. Res.*, **100**, 15527–15539.

Shearer, P.M. (1999). *Introduction to seismology*. Cambridge University Press, Cambridge.

Sibson, R.H. (1994). Faulting and fluid flow. In J. Parnell, ed., *Geofluids: Origins, migration and evolution of fluids in sedimentary basins*, vol. 78 of *Special Publications*, 69–84, The Geological Society, London.

Simpson, G., Gueguen, Y. & Schneider, F. (2001). Permeability enhancement due to microcrack dilatancy in the damage regime. *J. Geophys. Res.*, **106**, 3999–4016.

Small, J.S., Hamilton, D.L. & Habesch, S. (1992). Experimental simulation of clay precipitation within reservoir sandstones 1. techniques and examples. *J. Sediment. Petrol.*, 508–519.

Sondergeld, C.H. & Estey, L.H. (1981). Acoustic emission study of microfracturing during the cyclic loading of Westerly granite. *J. Geophys. Res.*, **86**, 2915–2924.

Sornette, D. (1999). Earthquakes: from chemical alteration to mechanical rupture. *Physics reports*, **313**, 237–291.

Speidel, M.O. & Hyatt, M.V. (1972). Stress corrosion cracking in high strength aluminium alloys. *Advances in corrosion Sci. Technology*, **2**, 115–135.

Staehle, R.W. (1969). Comments on the history, engineering and science of stress corrosion cracking. In R.W. Staehle, ed., *Fundamental aspects of stress corrosion cracking*, 3–14, National association of corrosion engineers, Houston, Texas.

Stanley, H.E. (1971). *Introduction to phase transitions and critical phenomena*. International series of monographs in physics, Oxford University Press, Oxford.

Stauffer, D. (1985). *Inroduction to percolation theory*. Taylor and Francis, London.

Swanson, P.L. (1984). Subcritical crack growth and other time and environment-dependent behavior in crustal rocks. *J. Geophys. Res.*, **89**, 4137–4152.

Swanson, P.L. (1987). Tensile fracture resistance mechanisms in brittle polycrystals: an ultrasonics and in-situ microscopy investigation. *J. Geophys. Res.*, **92**, 8015–8036.

Swindle, T.D. (1998). Water amongst the rock. *Nature*, **395**, 549–550.

Tapponier, P. & Brace, W.F. (1976). Development of stress-induced microracks in Westerley Granite. *Int. J. Rock Mech. Min. Sci. and Geomech. Abstr.*, **13**, 103–112.

Tenthorey, E., Scholz, C.H. & Aharonov, E. (1998). Precipitation sealing and diagenesis 1. Experimental results. *J. Geophys. Res.*, **103**, 23951–23967.

Terzaghi, K. (1945). Stress conditions for the failure of saturated concrete and rock. *Proc. Am. Soc. Test Mat.*, **45**, 777–792.

Tester, L.M., Worley, W.G., Robinson, B.A., Grigsby, C.O. & Feerer, J.L. (1994). Correlating quartz dissolution kinetics in pure water from 25 to 625 °C. *Geochim. Cosmochim. Acta*, **58**, 2407–2420.

Thompson, A.H. (1991). Fractals in rock physics. *Annual reviews in earth and planetary science*, **19**, 137–262.

Timoshenko, S.P. (1953). *History of strength of materials*. McGraw-Hill, London.

Tsonogai, U. & Wakita, H. (1995). Precursory chemical changes in groundwater: Kobe earthquake, Japan. *Science*, **269**, 61–63.

Tuncay, K., Puckett, J., Al-Shaeib, Z. & Ortoleva, P. (2002). Pits, outgrowths and inclusions as coated grain kinetic instabilities. *Geochim. Cosmochim. Acta*, **66**, 3901–3912.

Turner, F.J., Griggs, D.T., Clark, R.H. & Dixon, R.H. (1956). Deformation of Yule marble. Part VII: Development of oriented fabrics at 300°-500°c. *Bull. Geol. Soc. Am.*, **67**, 1259–1294.

Utsu, T., Ogata, Y. & Matsu'ura, R.S. (1995). The centenary of the Omori formula for a decay law of aftershock activity. *J. Phys. Earth*, **43**, 1–33.

Van Lier, J.A., De Bruyn, P.L. & Overbeek, J.T.G. (1960). The solubility of quartz. *J. Phys. Chem.*, **64**, 1675–1682.

Vinciguerra, S. (1999). Seismic scaling exponent as a tool in detecting stress corrosion crack growth in the September-October 1989 flank eruption in Mt. Etna volcano. *Geophys. Res. Lett.*, **26**, 3685–3688.

Von Karman, T. (1911). Festigkeitsversuche unter allseitigem Druck. *Z. Ver. Dtsch. Ing.*, **55**, 1749–1757.

Von Seggern, D. (1980). A random stress model for seismicity statistics and earthquake prediction. *Geophys. Res. Lett.*, **7**, 637–640.

Walsh, J.B. (1965). The effect of cracks on the compressibility of rock. *J. Geophys. Res.*, **70**, 381–389.

Walsh, J.B. & Brace, W.F. (1984). The effect of pressure on porosity and the transport properties of rock. *J. Geophys. Res.*, **89**, 9425–9431.

Walsh, J.N. (1997). Inductively coupled plasma-atomic emission spectrometry (ICP-AES). In R. Gill, ed., *Modern analytical geochemistry*, 41–66, Longman, Essex, England.

White, A.F. & Brantley, S.L. (1995). Chemical weathering rates of silicate minerals: an overview. In A.F. White & S.L. Brantley, eds., *Chemical weathering rates of silicate minerals, Reviews in Mineralogy 31*, 1–22, Mineral. Soc. Am.

Wiederhorn, S.M. (1967). Influence of water vapour on crack propagation in soda-lime glass. *J. Am. Ceram. Soc.*, **50**, 407–414.

Wiederhorn, S.M. (1969). Fracture of ceramics. In *Mechanical and thermal properties of ceramics*, National Bur. Stand. Pub. 303, Washington D.C.

Wiederhorn, S.M. (1978). Mechanisms of subcritical crack growth in glass. In R.C. Bradt, D.P.H. Hasselman & F.F. Lange, eds., *Fracture mechanics of ceramics*, 549–580, Plenum, New York.

Wiederhorn, S.M. & Boltz, L.H. (1970). Stress corrosion and static fatigue of glass. *J. Am. Ceram. Soc.*, **53**, 543–548.

Wiederhorn, S.M. & Johnson, H. (1973). Effect of electrolyte ph on crack propagation in glass. *J. Amer. Ceram. Soc.*, **56**, 192–197.

Wiederhorn, S.M. & Johnson, H. (1980). Micromechanisms of crack growth in ceramics and glasses in corrosive environments. *Metal Sci.*, **14**, 450–458.

Wiederhorn, S.M., Johnson, H., Dienes, A.M. & Heuer, A.H. (1974). Fracture of glass in vacuum. *J. Amer. Ceram. Soc.*, **57**, 336–341.

Wiederhorn, S.M., Freiman, S.W., Fuller, E.R.J. & Simmons, C.J. (1982). Effects of water and other dielectrics on crack growth. *J. Mater. Sci.*, **17**, 3460–3478.

Winter, R.B. (1983). Bruchmechanische gesteinuntersuchungen mit dem bezug zu hydraulischen frac-versuchen in tiefbohrungen. *Reihe A Nr. 13*, ber. Instit. fur Geophys. Ruhr Univ. Bochum, W. Germany.

Wollast, R. (1967). Kinetics of the alteration of K-feldspar in buffered solutions at low temperature. *Geochim. Cosmochim. Acta*, **31**, 635–648.

Wong, T.F. & Wu, L.C. (1995). Tensile stress concentration and compressive failure in cemented granular material. *Geophys. Res. Lett.*, **22**, 1649–1652.

Wong, T.F. & Zhu, W. (1999). Brittle faulting and permeability evolution: Hydromechanical measurement, microstructural observation, and network modeling. In *Faults and subsurface fluid flow in the shallow crust*, vol. 113 of *Geophysical Monograph series*, 83–99, American Geophysical Union, Washington D. C.

Worden, R.H. & Morad, S. (2000). Quartz cementation in oil field sandstones: a review of the key controversies. *Spec. Pub. Int. Ass. Sediment.*, **29**, 1–20.

Yabe, Y. (2002). Rate dependence of AE activity during frictional sliding. *Geophys. Res. Lett.*, **29**, 1388, doi:10.1029/2001GL014369.

Yanagidani, T., Ehara, S., Nishizawa, O., Kusunose, K. & Terada, M. (1985). Localization of dilatancy in Ohshima granite under constant uniaxial stress. *J. Geophys. Res.*, **90**, 6840–6858.

Yokoyama, T. & Banfield, J. (2002). Direct determinations of the rates of rhyolite dissolution and clay formation over 52000 years and comparison with laboratory measurements. *Geochim. Cosmochim. Acta*, **66**, 2665–2681.

Zang, A., Wagner, C.F. & Dresen, G. (1996). Acoustic emission, microstructure and damage model of dry and wet sandstone stressed to failure. *J. Geophys. Res.*, **101**, 17507–17521.

Zang, A., Wagner, F.C., Stanchits, S., Dresen, G., Andresen, R. & Haidekker, M.A. (1998). Source analysis of acoustic emissions in AUE granite cores under symmetric and asymmetric compressive loads. *Geophys. J. Int.*, **135**, 1113–1130.

Zang, A., Wagner, F.C., Stanchits, S., Janssen, C. & Dresen, G. (2000). Fracture process zone in granite. *J. Geophys. Res.*, **105**, 23651–23661.

Zhang, S., Cox, S.F. & Paterson, M.S. (1994). The influence of room temperature deformation on porosity and permeability in calcite aggregates. *J. Geophys. Res.*, **99**, 15761–15775.

Zhu, W. & Wong, T.F. (1996). Permeability reduction in a dilating rock: Network modeling of damage and tortuosity. *Geophysical Research Letters*, **23**, 3099–3102.

Zhu, W. & Wong, T.F. (1997). The transition from brittle faulting to cataclasic flow: Permeability evolution. *J. Geophys. Res.*, **102**, 3027–3041.

Zhu, W. & Wong, T.F. (1999). Network modeling of the evolution of permeability and dilatancy in compact rock. *J. Geophys. Res.*, **104**, 2963–2971.

Zhu, W., Evans, B. & Bernabé, Y. (1999). Densification and permeability reduction in hot-pressed calcite: A kinetic model. *J. Geophys. Res.*, **104**, 25501–25511.

Zoback, M.D. (2000). Strength of the San Andreas. *Nature*, **405**, 31–32.

Zoback, M.D. & Byerlee, J.D. (1975). The effect of microcrack dilatancy on the permeability of Westerly granite. *J. Geophys. Res.*, **80**, 752–755.

Appendix A

Instructions for loading a rock sample

A.1 Preparing the Cell

1. Place the black rubber sleeve inside the cell.
2. Slide the rock sample into the rubber jacket, into the cell.
3. Spray *BWC anti-seize thread lubricant* into long metal screws before putting them into cell ends.
4. Attach the cell ends to the main body of the cell using the screws.
5. Tighten the screws using a **20 kN** spanner so that opposite pairs of screws are tightened one after another.

A.2 Preparing the sample stack

1. The sample stack consists of two steel mushroom shaped platens (i.e. end pieces), 2 translucent melinex sheets, 2 circular nylon sheets, 2 circular metallic spacers (for the sample ends), the main body of the cell (including the rock sample), 2 wooden spacers and 2 metallic spacer.

2. Make two circular *melinex* sheets that have the same diameter as the sample. For flow through tests a 3 mm hole is required in the middle of the melinex sheet.

3. Put the melinex sheets into a jar of distilled water.

4. Grease the piston end with *multipurpose LM2 grease or vaseline*. Do not grease the ends if fluid is to be flown through the sample.

5. Take out one melinex sheet with a pair of tweezers.

6. Set a metallic spacer onto the lower mushroom shaped platen.

7. Set the melinex sheet on top of the metallic spacer.

8. Set the nylon sheet on top of the melinex sheet.

9. Arrange gray spacers on to the lower platen.

10. Slide the main body of the cell on top of the lower platen.

11. Use a transparent plastic bar to push sample as far as possible inside the cell.

12. Set the nylon sheet on top of the rock sample.

13. Take out another melinex sheet from the jar using tweezers.

14. Set the melinex sheet, followed by the metallic spacer on top of the rock specimen.

15. Slide the upper platen inside the cell.

16. Place the sample stack on top of metallic and a wooden spacers. The metallic spacer needs to be under the wooden one as it will attach to the magnetic base.

17. Slide the whole assembly inside the load frame.

18. Centre the cell at top and bottom.

19. Arrange a plastic and a metallic spacer on top of the cell assembly, depending on how much room there is between the top platen and the ram actuator. Remember that the metallic sheet is always used as a spacer as it is required for axial strain measurement.

A.3 Pressurising the rock sample to hydrostatic conditions

1. Bring the ram down so that it touches the top of the sample stack. Having closed **2**, open **3, 5 and 6** in the upper ram circuit (figure 3.2). Keep other valves closed.
2. Set the pump to deliver **400 ml/h**. Open **9** slowly.
3. Check whether the sample stack moves under the ram. As soon as the sample stack is secured in its place switch off the pump and close **9**.
4. Open confining pressure valves (lower set of valves in figure 3.2) **5&7**, close **1**. Keep other valves closed.
5. The **Pc** reading on testpoint screen indicates the pressure in the accumulator. The value is given in Volts - to convert from Volts to psi you'll need to multiply the reading by **1012.65**.
6. If the accumulator pressure equals the confining pressure to be used in the experiment close **7**. Otherwise leave **7** open.
7. Reduce the pressure on line. Close **2,3 & 6**, open **1**. Open **2** slowly.
8. Close **2**, leaving **1&3** open.
9. Take the confining pressure cable. Check that there is oil coming out of the cable by opening **4** while pumping the hand pump on the right hand side of the ram.
10. Close **3**. Tighten the confining pressure cable to the side of the cell using a spanner. Open **3** and **4**.
11. Pump the confining pressure to **100 psi** using hand pump. Close **4**.
12. Open **2** to let the air out. Observe the testpoint screen - the confining pressure P_{conf} value drops. Close **2**. Open **4**.
13. Pump the confining pressure to **100 psi** using hand pump.
14. Open **2** to let the air out. Observe the testpoint screen - the P_{conf} value drops. Close **2**. Open **4**.
15. Pump the confining pressure to **100 psi** using hand pump.
16. Close **4**.
17. Take the gray spacers out.
18. Bring the ram down. Close **2,7,8,10,11 and 12**. Open **3,5,6**.

19. Check that the pump is filled with oil and that the right hand side valve is open, while left hand side valve is closed.
20. Check that the pump is set to deliver mode with a flow rate of **400 ml/h**.
21. Switch the pump on. Observe the pressure in the pump. Once the pressure is about 800 psi, open **9** in the upper ram circuit.
22. Observe the ram pressure on testpoint screen. The measured pressure is shown in volts. *100 psi equals 0.003 Volts.* If the pressure doesn't rise markedly after connecting the pump, the pump may have been filled with air. In this case the pump needs to be emptied of air and filled with oil instead.
23. Increase the ram pressure to **100 psi**.
24. The sample is now in hydrostatic pressure of **100 psi**. Using instructions given above, increase P_{conf} and ram pressure to **400, 1000, 1600, 2000 psi** in turns.
25. Set the band and cartridge heaters to the required temperature for the test. The controls are found on the side of the rig.
26. Attach the permeameter to the top and bottom platen by using two small spanners. You will need an adjustable spanner for this job.
27. Attach the data logging cable to the left hand side of the permeameter.
28. Close the two valves located above and below the differential pressure transducer in the permeameter. Otherwise the small particles that are liberated during the initial 24 hour flushing may damage the diaphragm.
29. Switch the water pump on, delivering **0.37 ml/h**.
30. Attach a plastic tube on the permeameter top permeameter outlet. Place the other end of the tube in a suitable empty container. This will ensure that the lab is not flooded when you come back the next day.
31. Leave the system to equilibrate for approximately 24 hours.

A.4 Pressurising the ram

1. Before pressurising the ram set the testpoint software ready for logging at the required rate. If you are recording AE, you will need to do this for the AE recording software (MISTRAS or MI-TRA) as well.

2. If AE activity is being recorded, remember to attach the AE cable to (a) the amplifier and (b) to the back of the MISTRAS computer.
3. Open **3,5,6**, keep other valves closed.
4. Switch the pump on deliver mode with the required flow rate for the test. The required flow rate depends on the desired strain rate. For a strain rate of the order of 10^{-5}, 10^{-6}, 10^{-7} or 10^{-8} /s you will need to use a pump rate of 400, 40, 15, 1.5 ml/min, respectively. Make sure that the pump is filled with oil and not with air, for instance.
5. After the pump pressure has increased to **800 psi**, open **9**.
6. This is the start of the test. You will need to start logging the data at this moment. Change the testpoint program into logging mode. If you are also recording AE by using MISTRAS, press enter now to start logging the AE activity.
7. Observe ram voltage on screen. The pressure should start rising.

A.5 Filling the pump

1. Switch pump on refill mode with **400 ml/h** flow rate.
2. Open the pump valve that has a plastic tube leading to the oil reservoir.
3. Make sure that the plastic refill tube is in oil and not in air.
4. Switch the pump on.
5. Once the pump is filled with oil, switch the pump off and close the pump valve leading to the oil reservoir.

A.6 Stopping a test

1. Valves **2, 6, 8, 10** are closed while **3, 5, 6, 9** are open in the ram circuit.
2. Valves **1, 3, 5, 7** are open while **2, 4, 6** are closed in the lower, confining pressure circuit.
3. Open **7** to reduce ram Pressure to hydrostatic pressure. The **2000** psi hydrostatic pressure corresponds to **0.0746** Volts on the testpoint screen

4. In order to reduce the hydrostatic pressure the confining pressure circuit valve **7** needs to be closed. Open **2** to let pressurised oil out.
5. Reduce both oil and ram pressure in steps to **100** psi.
6. Lift ram up. Keeping other valves closed, open **2** and **5**.
7. Set the pump to pump oil at **400 ml/h**. Open **9**.
8. Take the confining pressure connection out.
9. Take the band heaters off using a special spanner.
10. Disconnect the AE cable. Take the cell out.

Appendix B

Preparation of standard solutions

Many instruments (such as the Thermo Jarrell Ash Iris ICP-AES) require a calibration phase. In this phase the technique is tested using known amounts of analyte, usually referred to as standard solutions. The calibration procedure involves obtaining a graphical relationship between the instrument response and the known concentration of the standard. Hence, unknown samples can be determined by reference to this relationship (*Jones et al.*, 2000). This appendix gives instructions for preparing standard solutions for chemical analysis.

These stock standard solutions are kept in the laboratory fridge. They are usually 1000 ppm solutions. However,the geochemical signal from a rock dissolution experiments typically involves concentrations in the 1-20 ppm range (*Ngwenya et al*, 2000). It is important to have standard solutions that bracket the anticipated concentrations. For instance, for analysing concentrations in the 1-20 ppm range one would require 1 ppm, 10 ppm and 20 ppm standard solutions of the analyte. Listed below are instructions for preparing a 50 ml of silica standard. The instructions for making other standards (Al, Fe, K, Mg, Ca, Na) are exactly the same, except for the stock standard that is used for preparing the standard solution. Three standards and a blank sample were used for calibrating the ICP instrument. Typical concentrations of Al, Fe, K, Mg, Ca, and Na in the standards are listed in table B.1. The standards were also acidified with 1% HCl, just like the pore fluid samples.

Table B.1. The standards that were used for the calibration of the ICP instrument. Three standards and a blank sample were used to calibrate the instrument.

Standard no.	Al ppm	Ca ppm	Fe ppm	K ppm	Mg ppm	Na ppm	Si ppm	HCl %
Blank	0	0	0	0	0	0	0	1
1	1	1	5	5	1	5	1	1
2	2	5	10	10	2	10	10	1
3	5	10	20	20	5	20	20	1

B.1 Making standards for silica analysis

1. Take out the 1000 ppm silica stock standard.
2. Use the equation $C1 * V1 = C2 * V2$ to calculate how much of the stock standard is required for making the appropriate standard. $C1$ and $C2$ are the concentrations for the stock standard and required standard, respectively. $V2$ is the amount of standard solution that is being prepared. $V1$ is the amount of stock standard solution that is needed for making this standard. For instance, when making 100 ml of 2 ppm silica standard the required amount is $V1$(ml)= (2ppm*100ml)/1000ppm.
3. Start making the standards from the lowest concentration required.
4. Insert a plastic end piece to the pipette.
5. Program the pipette to take out the required amount of silica stock standard.
6. Put the pipette into the standard solution. Press the button once.
7. Insert the pipette into a 100 ml plastic bottle. Press the button once.
8. Remember not to touch the bottle with the pipette.
9. Squeeze some distilled water into the 100 ml bottle.
10. Put a cap on the 100ml bottle and then shake it.
11. Fill up to the 100ml line with distilled water from the squeezy bottle.
12. Pour some of the standard in the 100 ml bottle into a 50 ml plastic bottle. Rinse the 50 ml bottle with the standard.
13. Fill the 50ml bottle with the newly made standard.
14. Add 500 μl of HCl into the 50 ml bottle of the newly made standard with the

pipette. The 500 μl of HCl represents 1%. This procedure should be carried out in the fume cupboard.

15. Make the other standards as described above.
16. The standard will keep up to 2 weeks if kept in the fridge.

Appendix C

ICP-AES

C.1 Introduction

The identification of different ions in the pore fluid samples was carried out using Thermo Jarrell Ash Iris Inductively Coupled Plasma-atomic emission spectrometer (ICP-AES) (*Walsh*, 1997). The ICP technique has many advantages over traditional methods for chemical analysis, such as the atomic absorption spectroscopy. Since the background signal from the argon plasma is relatively low, the technique has good, low detection limits (0.2-100 parts per billion). The ICP method is also very fast: up to 60 elements can bee screened during a sample run lasting less than one minute. The ICP technique enjoys a freedom from interferences, since chemical bonds cannot survive ICP. Furthermore, the technique gives long linear calibration ranges over several orders of magnitude: this feature represents a great advantage for multi-element work where different elements can be encountered at varying concentrations. On the downside, the ICP instrument costs more to run than traditional methods for chemical analysis.

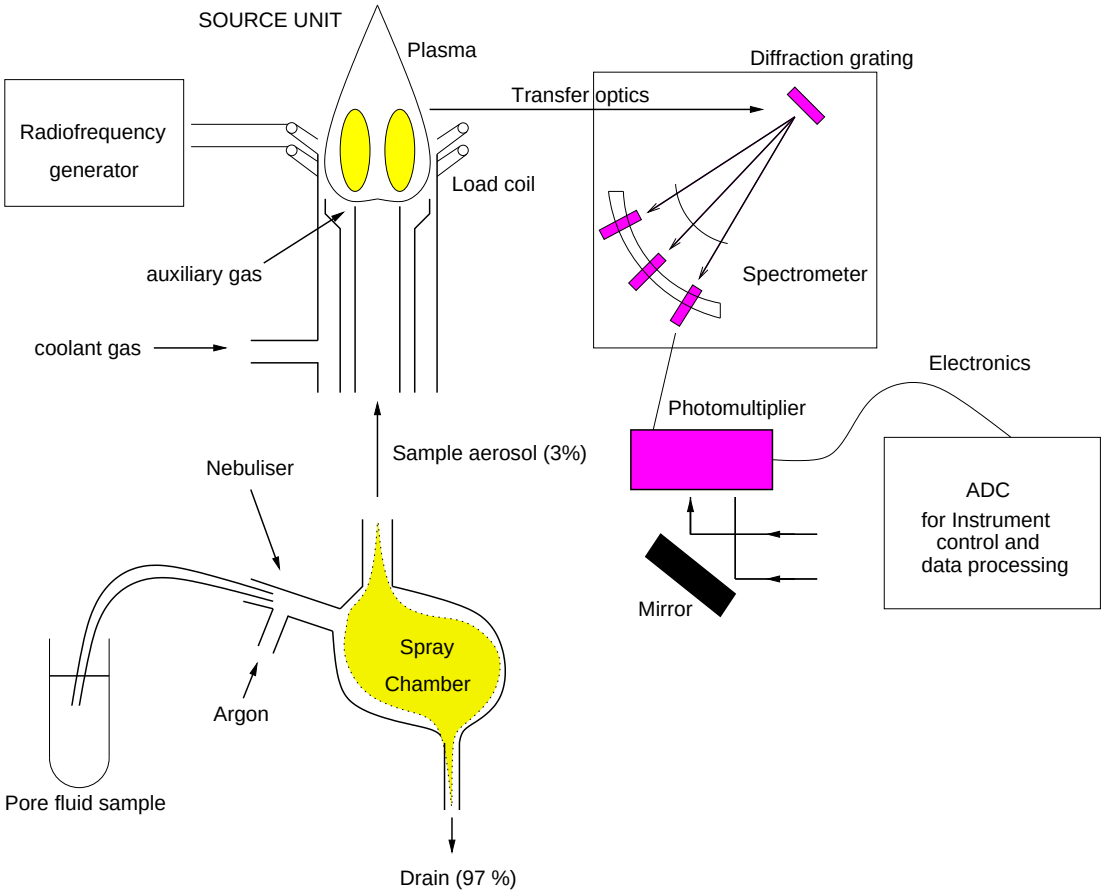

Figure C.1. The major components of a multi-element ICP-AES system. The sample is introduced into the plasma as an aerosol suspended in an argon gas. The elements present in the plasma emit light and a multi-channel optical spectrometer resolves this light into its component wavelengths. The intensity of the wavelength is measured by a photo-multiplier tube. The voltage produced in the photo-multiplier is converted to a digital signal in an analogue to digital converter (ADC). The measured signal can then be processed by using a computer. Redrawn from *Walsh* (1997).

C.2 The ICP-AES instrument

The ICP-AES instrument consist of three essential units: the source unit (the ICP torch), the spectrometer and the computer as illustrated in figure C.1 from *Walsh* (1997). The energy required for the emission spectral lines is provided by the source unit. The spectrometer resolves and separates these lines. It also measures the signal strength. The signal is converted to a numerical measurement by using a computer.

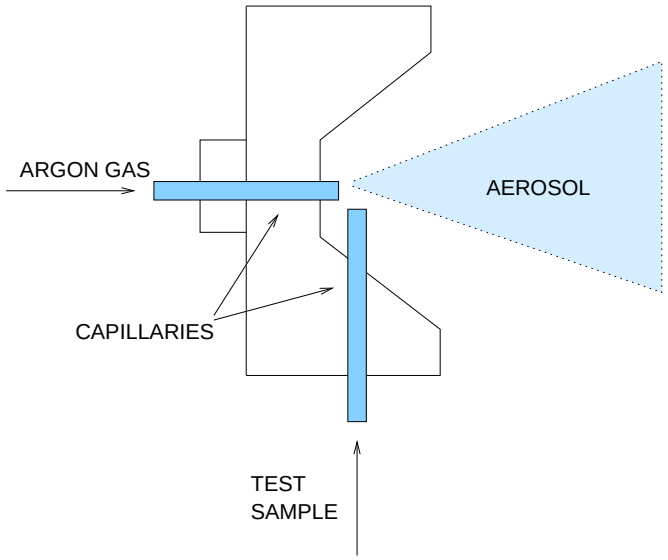

Figure C.2. A simple cross-flow nebuliser that can be used to produce an aerosol of the liquid sample that is being analysed. This requires that the two capillary tubes are carefully aligned and set at right angles. Redrawn from *Walsh* (1997).

Sample introduction is carried out by using a pneumatic nebuliser. Figure C.2 from *Walsh* (1997) illustrates a typical cross-flow nebuliser. The sample that is being analysed is pumped through a capillary tube into the nebuliser. Another capillary tube oriented at right angles to the sample tube carries argon gas to the nebuliser. This arrangement converts the liquid sample into a gas. However, only a few percent of the solution is converted into aerosol, while most of the solution is lost via a drain (fig. 4.1). Separation of larger droplets from the fine aerosol mist is carried out in the spray chamber. The fine aerosol mist travels up to the plasma and is used for analysis. The reproducibility and efficiency of sample nebulisation is a critical part of quantitative ICP analysis. Since only a

small proportion of the sample reaches the ICP any changes in the nebulisation process will change the emission signal significantly (*Walsh*, 1997). This is why it is important to check that the drain tube is functioning properly when carrying out the analysis. Another important consideration of the sample introduction is the clean-out rate between sample analysis. Typical analysis requires a flush time of 30-45 s between samples (*Walsh*, 1997). I used a flush time of 30 s when carrying out the ICP analysis.

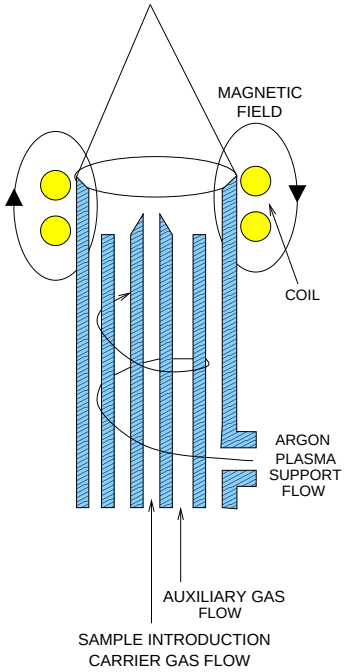

Figure C.3. Co-axial design of an ICP torch. Redrawn from *Walsh* (1997).

The fine sample mist travels into an ICP torch that generates the plasma for ICP analysis. Figure C.3. from *Walsh* (1997) illustrates a typical co-axial torch that is used for most systems. The torch consists of three co-axial tubes. The innermost tube carries the sample as an aerosol with argon gas. The intermediate tube may be used as an auxiliary gas supply in order to lift the sample higher and away from the injector gas tube. The argon gas that supports the plasma enters the outermost tube via a T-junction and and travels up the torch in a spiral pattern. The plasma is produced as the *coolant* or *plasma* gas flows through a two- or a three-turn load coil that is connected to a 27-40 MHz generator. Conduction in the coolant gas is initiated by an electrical spark (this is termed igniting the

torch). The movement of conducting gas across a magnetic field generates eddy currents that bring about intense Ohmic heating. As a consequence, the argon gas reaches a temperature of about 10000 K. The hollow load coil is continuously cooled by water that runs through it while the outer part of the *coolant* gas cools the quartz glass torch (*Walsh*, 1997).

The sample is introduced through a central injector tube that punches a hole into the plasma (*Walsh*, 1997). As a consequence the plasma forms a doughnut shape around the sample is it is being introduced. The sample is heated progressively from outside inwards. This is why the ICP method produces linear calibration lines over four to five orders of magnitude (*Walsh*, 1997). Heating from outside inwards decreases the levels of self-adsorption and self-reversal. Since the sample is heated to temperatures above 7000 K desolvation, vaporisation, dissociation, ionisation and excitation are almost instantaneous (*Walsh*, 1997).

The mechanism by which atomic emission spectral lines are generated is illustrated in figure C.4. The intense heat can cause electrons to jump temporarily to a higher orbital with an energy level E_j. However, as the atom moves higher in the ICP tail frame it cools and the electron may drop back to its ground state with a lower energy level E_i. In doing so it sends out a photon. The wavelength λ emitted by these electron transitions is inversely proportional to E_j-E_i, which in turn, is related to the atomic number Z. Hence, different atoms emit different wavelengths and the resulting spectral lines are characteristic of the emitting atom or ion. In a high energy source such as the ICP several electron transitions can take place and hence atomic or ionic species may generate a series of lines (*Walsh*, 1997).

The spectrometer separates the emitted radiation into discrete spectral lines. The light emitted by the tail frame of the ICP is dispersed into its constituent wavelengths in a diffraction grating and the intensity of the signal is measured by photo-multipliers (*Walsh*, 1997). The signal intensity is a measure of the concentration of a particular element. The voltage produced by the photo-multipliers is converted into a digital signal that can be processed by a computer.

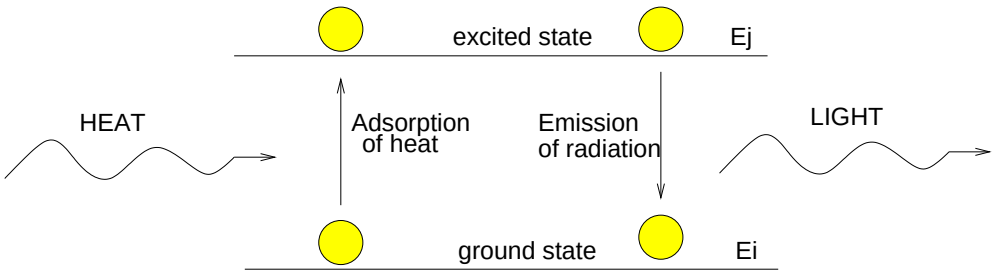

Figure C.4. The generation of atomic emission in an ICP instrument. The intense heat causes the electron to jump temporarily to a vacant orbital at a higher energy E_j. As the atom moves to a lower energy state (lower temperature region in the flame) an electron will fall to a lower energy level at E_i. In doing so it sends out a photon. The frequency and the wavelength of this emission depends on difference between these two energy levels. The wavelength of this emission reveals the identity of the atom. This phenomenon is fundamental to all spectral methods of chemical analysis.

C.3 Analysis

The ICP-AES instrument was calibrated before each analysis session. Ideally, the geochemical signal would be measured after subtracting the background emission line for each sample. However, in practice this is not possible. Hence, a blank solution (table B.1) was run prior instrument calibration. The blank solution was analysed for three times and the average signal was used as a background. This is clearly less than ideal since it is unlikely that the blank will contain the same matrix elements than the pore fluid samples (*Walsh*, 1997). However, it is the most widely used method for estimating the background value.

The calibration was carried out using three standard solutions with known concentrations of Si, Fe, Mg, Na, Ca, K and Al (table B.1.). The standards were run at an order of increasing concentrations and the recorded signal was the average of three runs. Subsequently, the sample concentrations were interpolated from a calibration curve that was drawn up by the computer software after analysing the standards. While the best calibration curve would have a slope equal to one, a slope of 0.995 was deemed accurate enough for analysis. However, for most tests the slopes of the calibration lines were 0.999.

Having calibrated the instrument a standard solution was analysed as a sample

of unknown concentrations. The same standard was run as an unknown sample every 30 mins in order to correct for instrumental drift. It was assumed that the instrumental drift is linear with respect to time. All samples were analysed for the concentrations of Mg, Na, Ca, Fe, Al, Si and K three times and the average of three concentrations was recorded. The ICP-AES instrument was calibrated every 2 hours.